

Toward Switching Cyanide- and Thiocyanate- Bridged Compounds Derived from Mononuclear Building Blocks

Von der Naturwissenschaftlichen Fakultät der
Gottfried Wilhelm Leibniz Universität Hannover

zur Erlangung des Grades

Doktor der Naturwissenschaften

(Dr. rer. nat.)

genehmigte Dissertation von

Dominik Aljoscha Florian Natke, M. Sc.

2021

Referent: Prof. Dr. techn. et rer. nat. habil. Franz Renz

Korreferent: Prof. Dr.-Ing. Ralf Franz Sindelar

Korreferentin: Prof. Dr. rer. nat. Nadja-C. Bigall

Tag der Promotion: 01.10.2021

Abstract

Bistable compounds which exhibit reversible phase transitions under external stimuli accompanied by changes of physical properties are excellent candidates for multifunctional electronic molecular devices and nano-sensors. In this regard, coordination complexes switchable between two or more different electronic states offer great potential due to their flexible design and adjustable properties. Transition metal complexes, mostly containing iron, cobalt, or manganese, can show a spin crossover (SCO). This is a reversible switching between the low and high spin state through physical and chemical stimuli. Additionally, cyanide-bridged complexes can show a reversible electron transfer coupled with a spin transition/SCO (ETCST) between two redox-active transition metals with mixed-valences. Therefore, cyanide-bridged molecular complexes and coordination polymers are of great interest in current research.

This dissertation continues the investigations for new switchable complexes. Therefore, novel cyanide-bridged multinuclear complexes and thiocyanate-bridged frameworks were synthesized and characterized. For this purpose, different new and known mononuclear complexes were analyzed in terms of their suitability as building blocks. Appropriate building blocks were combined to form multinuclear complexes, some of them with switching (SCO or ETCST) behavior. The presented results are discussed in four chapters according to the used building blocks and resulting complexes.

After a short introduction, the Current State of Research is summarized in Chapter 2. The Chapters 3 and 4 deal with the synthesis of distinct mixed-valence complexes using certain iron and cobalt complexes with pentadentate Schiff base ligands. Dinuclear, trinuclear, and pentanuclear complexes were obtained of which some show SCO and likely ETCST behavior. In Chapter 5, an ETCST-active tetranuclear square complex was used to build up 1D chains through hydrogen bonds with a co-crystallized organic molecule. Significant alterations of the structure were observed in solid-state. Chapter 6 is about the formation of a new kind of coordination framework derived from a thiocyanate-based Prussian blue analog. The aggregation of the building blocks to different framework structures was investigated as well as their properties and how an SCO behavior might be introduced. The analyzed compounds show potential as chemical sensors, and the building blocks might lead to new spin state based electronics.

Keywords: coordination compounds, molecular switches, mixed-valent, spin crossover, electron transfer, spin transition, cyanide, thiocyanate, iron, cobalt

Zusammenfassung

Bistabile Verbindungen, deren physikalische Eigenschaften durch externe Stimuli geändert werden können, sind hervorragende Anwärter für multifunktionale elektronische Anwendungen und Nanosensoren. Übergangsmetallkomplexe, die zwischen zwei oder mehreren elektronischen Zuständen wechseln können, bieten aufgrund ihrer Designvielfalt und Anpassungsmöglichkeiten dahingehend großes Potential. Solche Komplexe beinhalten häufig Eisen, Cobalt oder Mangan und können einen Spin Crossover (SCO) zeigen. Dies bezeichnet den durch chemische oder physikalische Änderungen induzierten reversiblen Übergang vom Low in den High Spin Zustand. Zusätzlich kann in cyanidverbrückten Komplexen ein reversibler Elektronenübertrag mit gekoppeltem Spinübergang/SCO (ETCST, engl. electron transfer coupled spin transition) zwischen zwei redoxaktiven Übergangsmetallen verschiedener Valenzen stattfinden. Aus diesem Grund befasst sich die aktuelle Forschung intensiv mit cyanidverbrückten molekularen Komplexen und Koordinationspolymeren.

Diese Dissertation führt die Forschungen zu neuen molekularen Schaltern fort. Es werden die Ergebnisse der Synthesen und Charakterisierungen von verschiedenen cyanidverbrückten molekularen Komplexen und thiocyanatverbrückten Koordinationsnetzwerken diskutiert. Zu diesem Zweck wurden bereits bekannte und neuartige mononukleare Komplexe bezüglich ihrer Eignung als Bausteine analysiert. Ausgewählte Bausteine wurden im Anschluss zu multinuklearen Komplexen kombiniert, von denen einige schalten können (SCO oder ETCST). Die Ergebnisse sind, entsprechend der verwendeten Bausteine und den daraus resultierenden Komplexen, in vier Kapitel unterteilt.

Nach einer kurzen Einleitung ist der aktuelle Stand der Forschung in Kapitel 2 zusammengefasst. Die Kapitel 3 und 4 befassen sich mit der Synthese von molekularen Komplexen, die verschiedene Valenzen aufweisen. Zu diesem Zweck wurden ausgewählte Eisen und Cobalt Komplexe mit fünfzähligen Schiff'schen Base Liganden verwendet, um eine Reihe von di-, tri- und pentanuklearen Komplexen herzustellen, von denen einige einen SCO und wahrscheinlich ETCST zeigen. In Kapitel 5 wurde eine 1D Kettenstruktur durch Wasserstoffbrücken zwischen einem ETCST-aktiven tetranuklearen Komplex und einem organischen Molekül erzeugt, in der signifikante Strukturänderungen zu beobachten sind. Kapitel 6 handelt von neuartigen Netzwerkstrukturen, die von Thiocyanat-basierten Berliner Blau Analogon abgeleitet wurden. Es wurde untersucht, wie die Aggregation der einzelnen Bausteine beeinflusst werden kann, welche Eigenschaften die resultierenden Verbindungen aufweisen und ob ein SCO in diesem System möglich ist. Die untersuchten Verbindungen zeigen großes Potential für die Verwendung als chemische Sensoren und die einzelnen Bausteine können zur Entwicklung neuartiger, auf dem Spinzustand beruhender, Anwendungen beitragen.

Schlagwörter: Koordinationsverbindungen, molekulare Schalter, gemischte Valenzen, Spin Crossover, Elektronenübergang, Cyanid, Thiocyanat, Eisen, Cobalt

Danksagung/Acknowledgment

Mein besonderer Dank gilt zuallererst meinem Doktorvater Professor Dr. Franz Renz, der mir während meiner Zeit an der Universität vieles ermöglicht hat. Angefangen von meiner Bachelorarbeit, über die Anfertigung meiner Masterarbeit in Japan bis hin zu dieser Doktorarbeit. Durch seine Unterstützung konnte ich mit vielen Freiheiten an meinem Thema forschen, mir ein Netzwerk auf zahlreichen internationalen Konferenzen aufbauen und drei weitere Forschungsaufenthalte in Japan absolvieren.

Mein weiterer Dank gilt dem Stipendienprogramm *Hannover School for Nanotechnology* (HSN) und dessen Leiter Dr. Fritz Schulze-Wischeler für die Finanzierung des größten Teils meiner Doktorarbeit und der Konferenzbesuche. In diesem Zusammenhang möchte ich auch Professor Dr. Ralf Sindelar von der Hochschule Hannover für die gute Kooperation im HSN-Umfeld und die Übernahme des Korreferats danken. Ebenso danke ich Professorin Dr. Nadja Bigall vom Institut für Physikalische Chemie der Leibniz Universität Hannover für die Übernahme des weiteren Korreferats und des Prüfungsvorsitzes. Professor Dr. Christoph Tegenkamp von der TU Chemnitz möchte ich für die Zusammenarbeit im Rahmen des HSN-Programms danken. Des Weiteren wurden einige meiner Austausche mit der Slowakei und Japan durch die Graduiertenakademie und den DAAD gefördert. Auch dafür vielen Dank.

Bedanken möchte ich mich auch bei meinen (ehemaligen) Kollegen aus dem AK-Renz, den anderen Arbeitskreisen, der Verwaltung, dem akademischen Mittelbau und den chemisch-technischen Assistenten und Assistentinnen des Instituts für Anorganische Chemie. Vielen Dank für die zahlreichen anregenden Diskussionen, für die Hilfe bei Messungen, die gute Arbeitsatmosphäre und die schöne Zeit. Ganz besonders bedanke ich mich bei Annika, die nicht nur durch ihre genaue und kritische Art einige Verbesserungsmöglichkeiten für meine Ideen und Abstracts fand, sondern auch eine gute Freundin wurde, mit zwei fantastischen Aufenthalten in Japan, und die immer ein offenes Ohr für mich hatte. Stephen danke ich für die zahlreichen fachlichen Diskussionen seit meiner Bachelorarbeit und unsere grandiosen zwei Monate in Tsukuba. Nicht zu vergessen sind in meiner Danksagung Börst, Moritz, Kirsten und die ehemaligen Masteranden und jetzigen Doktoranden Kevin, Arthur und Justus. Weiterhin den Mitarbeitern unseres Instituts, Marvin (Lietzow), Andy und Marc, sowie den ehemaligen Praktikanten, Bacheloranden und Austauschstudierenden, unter anderem Renee, Christoph, Max und Jules, die ich betreuen durfte.

I want to thank especially Professor Dr. Hiroki Oshio for the possibilities of staying in his lab and everything he taught me during my three stays in Tsukuba. The discussions were tough, but I learned a lot from them. On the other hand, I enjoyed our talks and dinners in particular the Curry Udon at Zeyo. Furthermore, I am very thankful for my introduction to Professor Dr. Masaaki Ohba who I want to thank for our good cooperation and my great stay at his lab in Fukuoka despite the starting Corona-pandemic. Not to forget all lab members I met in Japan and in particular Professor Dr. Masayuki Nihei, Associate

Professor Dr. Takuya Shiga, Associate Professor Dr. Ryo Ohtani and Assistant Professor Benjamin Le Ouay, thank you for the discussions and great talks. A special thanks goes to my Japanese friends with whom I worked together in the labs of Prof. Oshio and Prof. Ohba. Thank you, Marina, Nibe, Yuta, Haruchan, Takayama, Sato, Kenta and Saiki, to name some of them, for the great time and all the help especially with translations. I would also like to thank our partners in Slovakia, especially Professor Dr. Roman Boca and Cyril for the scientific exchange, measurements, and nice evenings.

Zu guter Letzt danke ich noch meiner Familie, meinen Freunden und Freundinnen, die mir während der Doktorarbeit und des vorangegangenen Studiums stets ein Anker waren. In diesem Zusammenhang möchte ich besonders meine Mutter Charlotte, meinen Vater Thomas und meinen besten Freund Patrick nennen. Meiner Tante Arbana möchte ich besonders dafür danken, meine Arbeit gegengelesen zu haben, genau wie Jojohannes und Anica.

List of Abbreviations

1	$[\text{Co}(\text{L}^1)\text{-CN-Fe}(\text{tp})(\text{CN})_2](\text{BF}_4) \cdot \text{H}_2\text{O}$
2	$\text{Fe}(\text{pztp})(\text{CN})_2(\text{BF}_4) \cdot \text{C}_2\text{H}_3\text{N}$
3	$[\text{Fe}(\text{L}^2)\text{-CN-Fe}(\text{L}^2)](\text{PF}_6)_3 \cdot 3 \text{C}_2\text{H}_3\text{N}$
+I effect	inductive effect (electron releasing)
+M effect	mesomeric effect (electron releasing)
-I effect	inductive effect (electron withdrawing)
-M effect	mesomeric effect (electron withdrawing)
ABA	<i>p</i> -aminobenzoic acid
B1	$\{\text{Co}^{\text{II}}_2[\text{Bi}(\text{SCN})_6]_2\text{Co}^{\text{II}}(\text{H}_2\text{O})_2\} \cdot 2 \text{Et}_2\text{O}$
B2	$\text{K}[\text{Bi}(\text{SCN})_6\text{Co}^{\text{II}}(3\text{-cyanopyridine})_2] \cdot 3 \text{acetone}$
B3	$\text{Bi}_2(\text{SCN})_{12}\text{Co}^{\text{II}}_3(3\text{-cyanopyridine})_6 \cdot 2 \text{H}_2\text{O}$
B4	$\text{Na}[\text{Bi}(\text{SCN})_6\text{Co}^{\text{II}}(3\text{-cyanopyridine})_2] \cdot 2 \text{acetone}$
B5	$\text{K}[\text{Bi}(\text{SCN})_6\text{Fe}^{\text{II}}(3\text{-cyanopyridine})_2] \cdot 3 \text{acetone}$
B6	$\text{K}[\text{Bi}(\text{SCN})_6\text{Ni}^{\text{II}}(3\text{-cyanopyridine})_2] \cdot 3 \text{acetone}$
bpy*	4,4'-dimethyl-2,2'-bipyridine
Bu ₄ N ⁺	tetrabutylammonium
CTIST	charge transfer induced spin transition
CV	Cyclic voltammetry; Cyclic voltammogram
D1	dinuclear compound 1: $[\text{Co}(\text{L}^1)\text{-CN-Fe}(\text{tp})(\text{CN})_2](\text{ClO}_4) \cdot \text{H}_2\text{O}$
D2	dinuclear compound 2: $[\text{Co}(\text{L}^1)\text{-CN-Fe}(\text{tp}^*)(\text{CN})_2](\text{ClO}_4) \cdot 2(\text{C}_2\text{H}_3\text{N})$
DTA	differential thermal analysis
ETCST	electron transfer-coupled spin transition
Et ₂ O	diethyl ether
HB	hydrogen bonding

HT phase	high temperature phase
L ¹	symmetric pentadentate Schiff base ligand
L ²	asymmetric pentadentate Schiff base ligand
LIESST	light induced excited spin state trapping
LMCT	ligand-metal charge transfer
LT phase	low temperature phase
MMCT	metal to metal charge transfer
MMET	metal to metal electron transfer
P1(acetone)	$\{[\text{Mo}(\text{CN})_8][\text{Fe}(\text{salpet}_{\text{H},\text{NO}_2})_4] \cdot 8(\text{C}_3\text{H}_6\text{O}) \cdot 9(\text{H}_2\text{O})$
P1	$\{[\text{Mo}(\text{CN})_8][\text{Fe}(\text{salpet}_{\text{H},\text{NO}_2})_4] \cdot 6(\text{C}_7\text{H}_5\text{N}) \cdot 11(\text{H}_2\text{O})$
P2	$\{[\text{W}(\text{CN})_8][\text{Co}(\text{salpet}_{\text{H},\text{NO}_2})_4] \cdot 10(\text{C}_7\text{H}_5\text{N}) \cdot 9(\text{H}_2\text{O})$
PBA	Prussian blue analogs
phen	1,10-phenantroline
pztp	tetrakis(pyrazolyl)borate
RT	room temperature
salpet	<i>N,N'</i> -bis(2-hydroxybenzylidene)-1,6-diamino-3-azahexane
SB1	$\{\text{Co}^{\text{II}}[\text{Bi}(\text{SCN})_6][\text{Co}^{\text{II}}(\text{acetone})(\text{H}_2\text{O})_2]\} \cdot 2 \text{ acetone} \cdot 1 \text{ Et}_2\text{O}$
SB2	$\text{K}[\text{Bi}(\text{SCN})_6\text{Co}^{\text{II}}]_2$
SB3	$\{[\text{Bi}(\text{SCN})_6]_2[\text{Co}^{\text{II}}(\text{H}_2\text{O})_2]_3\}[\text{Co}(\text{NCS})_2(\text{H}_2\text{O})_4] \cdot 4 \text{ H}_2\text{O}$
SB4	$\{[\text{Bi}(\text{SCN})_6]_2[\text{Co}^{\text{II}}(4\text{-cyanopyridine})_2]_3\}$
SB5	$(H\text{-isoquinoline})_3\{[\text{Bi}(\text{SCN})_6][\text{Co}^{\text{II}}(\text{isoquinoline})_2]\}[\text{Co}(\text{NCS})_4]$
SB6	$\text{Na}\{[\text{Bi}(\text{SCN})_6][\text{Ni}^{\text{II}}(3\text{-cyanopyridine})_2]\} \cdot 2 \text{ acetone}$
SCE	saturated calomel electrode
SCO	spin crossover
SQ1 _{solv}	$[\text{Co}_2\text{Fe}_2(\text{bpy}^*)_4(\text{CN})_6(\text{tp}^*)_2](\text{PF}_6)_2 \cdot 2\text{ABA} \cdot 4\text{benzonitrile} \cdot 2\text{diisopropyl ether}$

SQUID	superconducting quantum interference device
T1	{[Co(salpet _{H,H})CN] ₂ [Co(phen) ₂]}[BF ₄] ₂ · solvent
TIS	temperature-independent susceptibility
TG	thermogravimetry
tp	tris(pyrazolyl)borate
tp*	potassium hydrotris(3,5-dimethylpyrazol-1-yl)borate
UV-Vis	ultraviolet-visible
X	monodentate ligand such as: halides and pseudohalides
XRD	X-ray diffraction
ZFS	zero-field splitting

Table of Content

Abstract.....	I
Zusammenfassung.....	III
Danksagung/Acknowledgment.....	IV
List of Abbreviations.....	VI
Table of Content.....	X
1. Introduction.....	1
2. Current State of Research.....	5
2.1 Spin Crossover in Mononuclear Complexes with Penta-N ₃ O ₂ -dentate Schiff Base Ligands.....	5
2.1.1 Spin Crossover.....	5
2.1.2 Complexes with Penta-N ₃ O ₂ -dentate Schiff Base Ligands.....	11
2.2 Electron Transfer Coupled Spin Transition in Prussian Blue Analogs.....	13
2.2.1 From Mononuclear Building Blocks to Molecular and Bulk Prussian Blue Analogs.....	13
2.2.2 Electron Transfer Coupled Spin Transition.....	14
2.2.3 Dinuclear and Tetranuclear ETCST Complexes.....	18
2.3 Potential Applications for Spin State Switching Materials.....	21
3. Dinuclear Cyanide-Bridged Complexes.....	23
3.1 Co(II) and Fe(II) Schiff Base Complexes in Dinuclear Prussian Blue Analogs.....	24
3.2 Derivatives of [FeCo]-Complexes.....	35
3.2.1 Experimentals.....	35
3.2.2 Results and Discussion.....	36
3.2.3 Conclusion and Outlook.....	40
4. Spin Crossover Building Blocks and its Derivatives.....	41
4.1 Structural, Magnetic and Electrochemical Characterization of Iron(III) and Cobalt(III) Complexes with Penta-N ₃ O ₂ -dentate Ligands.....	42
4.2 Angled Trinuclear Cobalt Complex.....	59
4.2.1 Experimentals.....	59

4.2.2 Results and Discussion.....	60
4.2.3 Conclusion and Outlook.....	63
4.3 Switchable Pentanuclear Complexes.....	64
4.3.1 Experimentals.....	64
4.3.2 Results and Discussion.....	66
4.3.3 Conclusion and Outlook.....	77
5. Co-Crystallization of Tetranuclear [Co ₂ Fe ₂]-Complexes.....	79
6. Framework Structures Emerged from Thiocyanate-Based Prussian Blue Analogs.....	89
6.1 Thiocyanate-Based Coordination Compounds with Co, Fe, and Ni.....	90
6.1.1 Experimentals.....	90
6.1.2 Results and Discussion.....	93
6.2 How to Control the Aggregation of Bi-NCS Coordination Frameworks.....	111
6.2.1 Experimentals.....	111
6.2.2 Crystal Structures.....	113
6.3 Conclusion and Outlook.....	120
7. General Conclusion and Outlook.....	123
8. Appendix.....	127
8.1 Novel Dinuclear Cyanide-Bridged Complexes.....	128
8.2 Derivatives of Spin Crossover Complexes as Building Blocks.....	140
8.3 Co-Crystallization of Tetranuclear [Fe ₂ Co ₂]-Complexes.....	152
8.4 Framework Structures of Fe, Co, and Ni with [Bi(SCN) ₆] ³⁻	159
9. References.....	163
10. Curriculum Vitae and List of Publications.....	173

1. Introduction

In the year 1997, the world chess champion Garry Kasparov lost for the first time a six-game match against the specially developed chess computer *Deep Blue* from IBM. Nowadays the strongest chess-playing programs are running on ordinary computers and are far superior to world champions.^[1,2] This exemplary development demonstrates the progress made within 20 years in the calculating abilities and artificial intelligence based on the enhancement of integrated circuit technologies. The infamous Moore's Law (in 1965 by Intel co-founder Gordon Moore) embodies this technological evolution with the often-cited doubling of transistors in leading-edge integrated-circuits every two years. It is based on economical rather than scientific principles and it provides an efficient size-scaling of integrated-circuits through assessing the decreasing transistor sizes with good product yields and reliability.^[2] However, the development of better integrated circuit technologies is increasingly constrained by fundamental physical limits, some even speak of a "post-Moore world". To prevent stagnation, new technologies such as spintronics (or spin electronics) might complement established semiconductor-based electronics.^[2-5] Common spintronic devices are fabricated from only a few inorganic materials such as metals and semiconductors. In contrast to these materials, magnetic molecules have the advantage of flexible structures, quantized energy levels, and tunable magnetic properties.^[6] Exceptional examples for magnetic molecules are transition metal complexes with a $3d^4 - 3d^7$ electron configuration that can be switched by external stimuli between the low spin (LS) and the high spin (HS) state, the so-called spin crossover (SCO).^[6]

SCO complexes consist mostly of iron(II), iron(III), or cobalt(II) ions that are coordinated by one or multiple organic and inorganic ligands. They can be switched between two or more different magnetic states - for iron(II) even between diamagnetic and paramagnetic behavior. The switching is controlled by external stimuli such as temperature, light, pressure, and in specific cases by protonation, electric fields, and magnetic fields.^[7,8] With the change of spin state, the d-electron related physical properties such as magnetic moments, coordination bond lengths, color, and sometimes electrical conductivity change as well. The transition can be measured e.g., by XRD, SQUID magnetometry, Mössbauer spectroscopy, and UV-Vis spectroscopy.^[8,9] These switchable properties make SCO materials promising candidates, not only for spintronics but also for nanoscopic multi responsive applications such as display devices, high-density data storages, sensors and micromechanics.^[6,10-14] A closely related and therefore also highly investigated switching phenomenon is the electron transfer coupled spin transition (ETCST). It occurs in mixed-valence cyanide-bridged compounds and describes an electron transfer between two redox-active metal ions induced by temperature, light, pressure, or protonation

that is coupled with an SCO. Common ETCST complexes are [CoFe] Prussian blue analogs (PBAs) that switch from the $[\text{Co}^{\text{II}}_{\text{LS}}\text{Fe}^{\text{II}}_{\text{LS}}]$ low temperature phase to the $[\text{Co}^{\text{II}}_{\text{HS}}\text{Fe}^{\text{II}}_{\text{LS}}]$ high temperature phase.^[15,16]

Molecular design is the key to control the switching behavior. While the SCO properties can directly be influenced through changing the ligand field splitting between the LS and HS state, the ETCST transition depends on the redox potentials of the ETCST ion-couple. Both conditions heavily depend on the used metal ions and ligands. In addition, the intermolecular interactions in solid-state are crucial for the transition behavior.^[8,9,15,17] Therefore, design and synthesis of new SCO and ETCST compounds are an ongoing challenge. The past research resulted in several compounds with outstanding properties, such as multistability,^[18-20] switchable second harmonic generation effects,^[21] and an ETCST coupled change between a semiconducting and an insulating phase.^[22]

In this thesis, the scope was to synthesize new switchable multinuclear compounds via cyanide and thiocyanate bridging using a building block approach. These building blocks are mononuclear complexes that were analyzed with regard to their potential for synthesizing SCO and ETCST complexes. After the 1. Introduction and the 2. Current State of Research, the results are summarized within four chapters according to the used building blocks.

In Chapter 3 a series of dinuclear $[\text{Co}^{\text{II}}_{\text{HS}}\text{Fe}^{\text{III}}_{\text{LS}}]$ complexes based on a penta- N_5 -dentate Schiff base ligand that stabilizes cobalt(II) ions in combination with common iron(III) cyanometalates is presented. Even though dinuclear cyanide-bridged complexes are especially interesting due to a potentially electron transfer induced molecular polarity,^[23] only a few examples showing ETCST behavior were reported yet.^[24,25] To obtain a macroscopic polarization, a predominant direction of the molecules needs to exist within the crystal structure, which is not the case for the known compounds.

Chapter 4 covers the development of new multinuclear complexes from known iron(III) SCO and cobalt(III) complexes with asymmetric penta- N_3O_2 -dentate Schiff base ligands. These building blocks were extensively investigated within the last years,^[26-34] but no detailed investigation that included the iron(III) redox potentials was reported, nor attempts of synthesizing ETCST complexes from them. Therefore, the redox potentials were analyzed, and suitable building blocks were combined obtaining two new trinuclear $[\text{Co}^{\text{III}}_2\text{Co}^{\text{II}}]$ complexes and two new pentanuclear complexes, $[\text{Mo}^{\text{IV}}\text{Fe}^{\text{III}}_4]$ and $[\text{WCo}_4]$.

For some tetranuclear $[\text{Co}_2\text{Fe}_2]$ square PBAs an ETCST can be induced in solution by protonation of the terminal (non-bridging) cyanide ions coordinated to the iron moiety.^[18,35] In Chapter 5 this was mimicked in solid-state by the co-crystallization of a $[\text{Co}_2\text{Fe}_2]$ square complex with the bifunctional hydrogen bonding donor molecule 4-aminobenzoic acid (aba). With this approach it is possible to control the ETCST behavior of this complex through cyanide-aba hydrogen bonding interactions of different strengths (carboxylic acid and amino group) and a controlled aggregation.

1. Introduction

In Chapter 6, previously reported thiocyanate-based PBA^[36,37] were developed to new mixed-valence thiocyanate-based frameworks with bismuth(III), cobalt(II), iron(II) and nickel(II) ions. Previous investigations in our group found a thermochromic behavior in these compounds that might derive from an SCO.^[38] Furthermore, the aggregation behavior and how to control the resulting structures were investigated.

2. Current State of Research

The title of this thesis *Toward Switching Cyanide- and Thiocyanate-Bridged Compounds Derived from Mononuclear Building Blocks* implies the bottom-up approach of synthesizing multinuclear compounds from mononuclear building blocks. However, already the mononuclear complexes can show interesting properties including switching behavior. Therefore, the first part of this chapter (Chapter 2.1) is dedicated to the current research of iron(III) and cobalt(III) complexes with penta- N_3O_2 -dentate Schiff base ligands and their switching properties. The second part of this chapter reviews the current research about the actual cyanide-bridged multinuclear complexes and especially the resulting material class of Prussian blue analogs and its building blocks. Additionally, the bridging of mixed-valence transition metal ions leads to a relatively new kind of molecular switches, of which current trends are presented (Chapter 2.2). In the last part of this chapter, an overview of potential applications for these spin state switches is given (Chapter 2.3).

2.1 Spin Crossover in Mononuclear Complexes with Penta- N_3O_2 -dentate Schiff Base Ligands

2.1.1 Spin Crossover

Molecular compounds can show a variety of different switching mechanisms. This involves structural isomerization such as cis-trans and ring-opening/closing isomerization, valence tautomerism, and a change of the spin states.^[7,8,16,39-42] Coordination compounds with d^{4-7} transition metal ions that are octahedrally coordinated can exist in two stable spin states, the high spin (HS) and the low spin (LS) state (Figure 1a). A transition between both spin states is called spin crossover (SCO, Figure 1b).^[8]

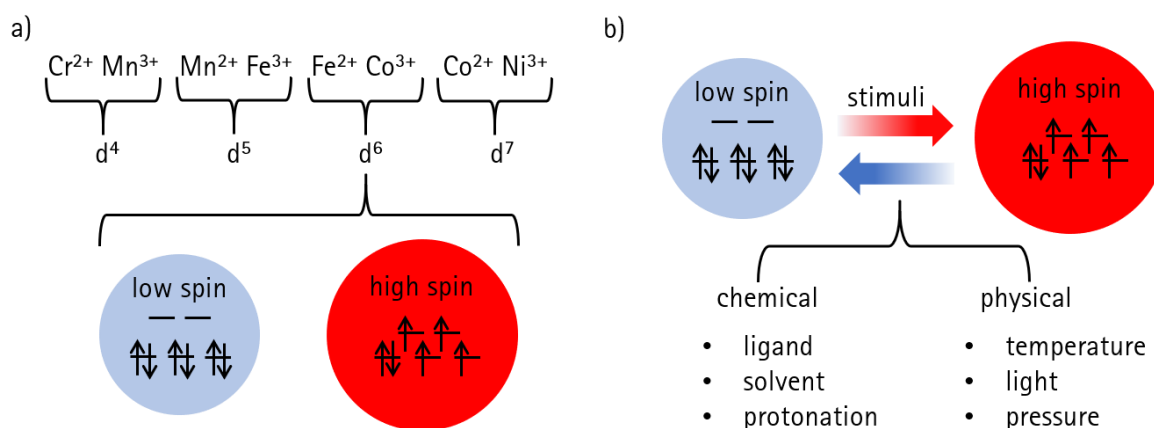


Figure 1: a) Octahedrally coordinated $3d^{4-7}$ transition metal ions and the HS and LS configuration for d^6 ions. b) SCO of a octahedrally coordinated d^6 ion with possible stimuli.

A complex occupies the LS or HS state if the ligand field splitting is stronger or weaker than the spin pairing energy, respectively. A thermally induced SCO can occur if the difference of the Gibbs free energy ($\Delta G_{\text{HL}} = \Delta H_{\text{HL}} - T\Delta S_{\text{HL}}$) of the HS and LS state is within the range of thermal energy ($k_{\text{B}}T$, Figure 2a).^[8,43] The ligand field splitting depends on the metal cation, the ligands, and the chemical environment. These parameters can be changed to control the spin state and SCO behavior.^[8,9,44] In order to roughly describe how large the ligand field splitting for particular metal ions and ligands is, the spectrochemical series can be used. For the most common SCO ions, the order is from larger to smaller ligand field splitting: $\text{Co}^{3+} > \text{Fe}^{3+} > \text{Fe}^{2+} > \text{Co}^{2+}$.^[44] The most SCO complexes are known for iron(II) despite the fact that its octahedral LS state is maximally stabilized. However, for the other d^6 ion, cobalt(III), only very few compounds in the HS state or with SCO behavior are known, due to its large ligand field splitting. Iron(III) complexes slightly favor the LS state as well, but nevertheless, many compounds, which show SCO or are only in the HS state, are known (Chapter 2.1.2). Note that some iron(III) complexes in HS state tend to hydrolyze. Cobalt(II) complexes tend to occupy the HS state, with many known SCO examples.^[45] For ions of a higher period than the 3d transition metals only the LS state is expected, with a few exceptions, since the ligand field splitting increases by about 50 % from 3d to 4d and from 4d to 5d elements.^[8,43]

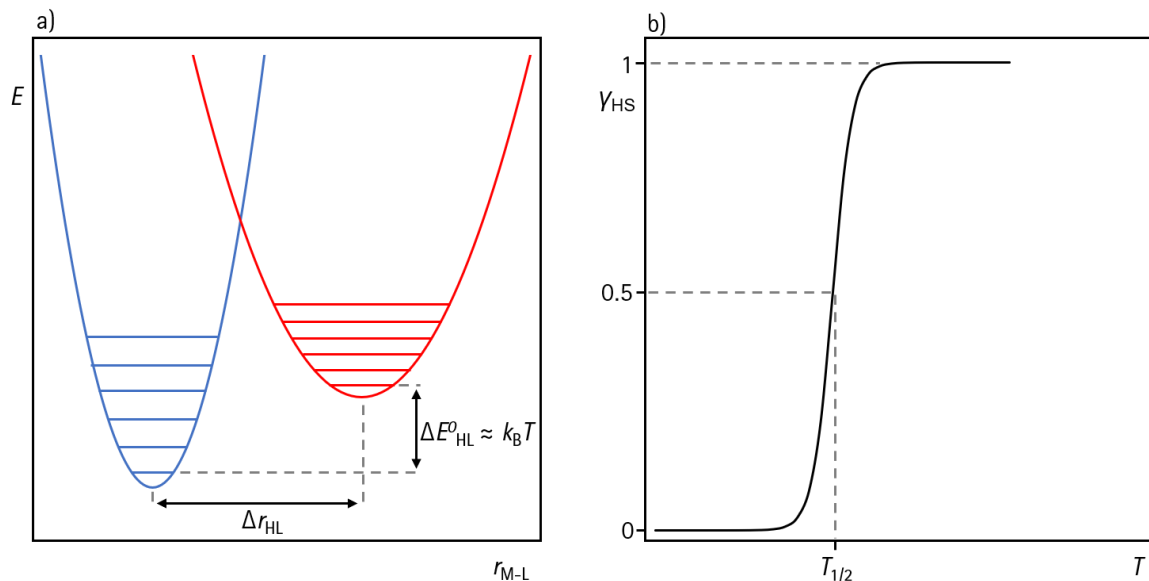


Figure 2: a) Standard potential well model of octahedrally coordinated $3d^{4-7}$ ions in the LS (blue) or HS (red) state, $r_{\text{M-L}}$ is the metal-ligand distance. b) Spin transition type SCO behavior. Adapted from Ref.^[8].

The SCO is an entropy-driven process with $\Delta S > 0$ and $\Delta H > 0$, which can show different thermally induced transition behaviors. If the HS (Y_{HS}) and LS ratio (Y_{LS}) is one ($Y_{\text{HS}}/Y_{\text{LS}} = 1$), the Gibbs free energy is 0 ($\Delta G_{\text{HL}} = 0$) and the temperature $T_{1/2}$ can be described as $T_{1/2} = \Delta H \cdot \Delta S^{-1}$, preferring the HS state above $T_{1/2}$.^[8,43] Oshio et al. proposed that the SCO behavior can be classified into a spin transition type for an abrupt change between the HS and LS state within a few K and a spin equilibrium type for

gradual changes over a wider temperature range.^[9] The type of SCO can be described by the domain model and is therefore strongly dependent on intermolecular interactions. An abrupt spin transition type SCO (Figure 2b) derives from strong interactions with larger domain sizes, while a spin equilibrium type SCO occurs in compounds with smaller domains and weaker intermolecular interactions. Due to the different kinds of interactions and the smooth transition between both types of SCO, the resulting SCO behaviors include also incomplete transitions, transitions with hysteresis, and multistable behavior.^[8,9]

An SCO can be triggered not only thermally, but also by further physical and chemical stimuli. Of these physical stimuli such as pressure, magnetic fields, or electric fields, electromagnetic radiation is very well investigated and bears great potential for applications. Many compounds are known in which a spin change can be induced at low temperatures by visible light of a defined wavelength. This phenomenon is referred to as light induced excited spin state trapping (LIESST), because the excited spin state is stable at low temperatures. Note that this is not an entropy-driven process. It is also possible to change induce a transition back to the ground state, the reverse-LIESST. Furthermore, a several similar effects were discovered, such as the hard X-ray induced excited spin state trapping (HAXIESST) by Renz et al., which are described in the literature.^[7,46,47] On the chemical side, the spin state can be changed through exchanging or modifying the ligand.^[26-28] This approach is very useful for molecular design. However, the need of additional synthesis and purification steps makes it less feasible for reversible switching. Further approaches are to induce an SCO through solvent exchange and host-guest interactions,^[48-50] ligand isomerization, and bond breaks.^[7]

The change of spin state is accompanied by a change of properties that are depending on the d-electron configuration, which makes it not only possible to measure and quantify the SCO behavior, but also to use it for applications. Coordination bond lengths increase in the HS state due to the additional occupation of the antibonding orbitals (Figure 1a), which can be measured by vibrational spectroscopy and XRD methods. Any change of spin state results in a different number of unpaired electrons within the d-Orbitals. The magnetic moment resulting from this spin configuration can be measured by SQUID magnetometry, which is commonly utilized to determine the thermal SCO behavior (Figure 2b). Also, NMR (nuclear magnetic resonance) and EPR (electron paramagnetic resonance) spectroscopy can be utilized to determine the magnetic behavior and therefore the spin state of coordination compounds. The spin state itself can be confirmed by the gamma-ray-based Mössbauer spectroscopy, which is extremely sensitive especially for iron compounds. However, the measurement periods are relatively long, and the resulting spectrum can be impaired by other atoms that unspecifically absorb the radiation as well. Furthermore, SCO compounds often show reversible thermochromic behavior induced by the spin change observable by optical spectroscopy. Another way of characterizing the SCO behavior

is by heat capacity measurements. As previously stated, an SCO is an entropy-driven process, which can be determined by its heat capacity. While the magnetic contribution is about 20 % - 25 % of the entropy changes, the larger part is caused by intermolecular and intramolecular vibrations.^[8,9,47]

Following, selected examples of SCO complexes are presented that strongly influenced the research field and show new possibilities of controlling the SCO behavior and the resulting properties. M. Seredyuk and J. A. Real et al. synthesized four iron(II) complexes with two asymmetric, 1,10-phenantroline-based ligands. The spin states and SCO behavior upon ligand modifications and deprotonation of the ligand were investigated. They found a compound showing thermally induced two step SCO behavior between 150 K and 250 K and a further compound showing a partial SCO induced by pressure.^[51] In a cooperation together with T. Shiga, G. N. Newton and H. Oshio et al. we extended this research using the asymmetric tridentate ligand 2-[5-phenyl-1H-pyrazole-3-yl] 6-benzimidazole pyridine (H_2Bip). Due to the asymmetric character of the ligand, the deprotonation steps can be separated resulting in two iron(II) and three iron(III) complexes with different protonation and spin states, which could be isolated (Figure 3). These results showed a general trend that a higher charge density, through the protonation, results in a larger ligand field splitting. The five isolated states showed apart from different spin states also different magnetic behavior, color, and electrochemical properties. In addition, the compound $[Fe^{II}(H_2Bip)_2](BF_4)_2$ exhibits a thermally induced abrupt SCO with a small hysteresis. Furthermore, an SCO can even be triggered in solid-state by protonation through acid and basic vapors. These tunable properties are a promising strategy for the development of smart molecular devices.^[52]

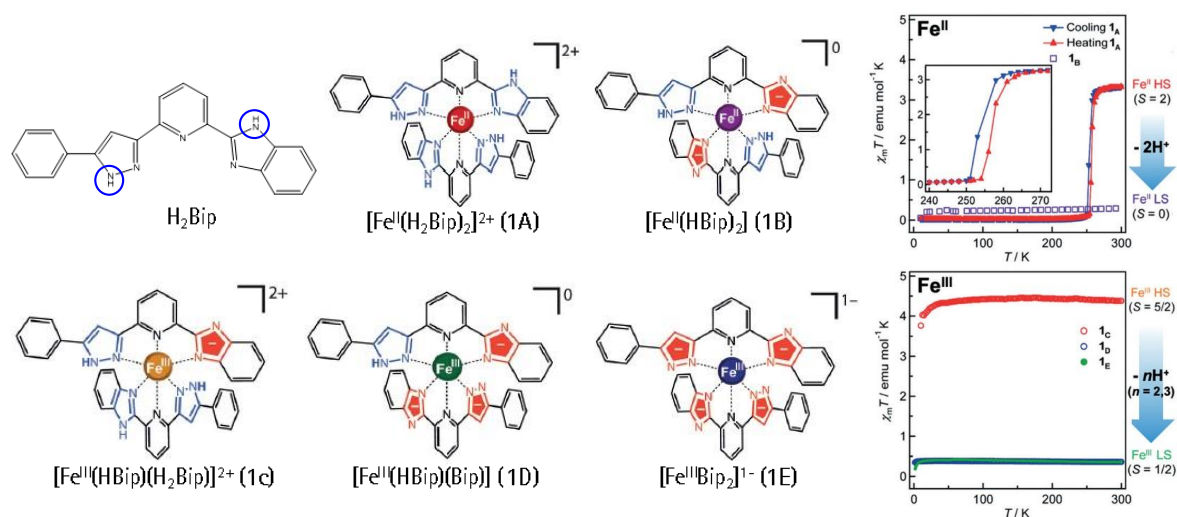


Figure 3: Five synthesized iron complexes based on the Ligand H_2Bip and their temperature-depending magnetic behavior. The color of each ion in the complexes corresponds to its crystal color. The red parts of the ligand visualize its deprotonation. Reprint with permission from Ref.^[52]. Copyright Wiley-VCH.

H. Oshio et al. synthesized a tetranuclear $[\text{Fe}^{\text{II}}_2\text{Fe}^{\text{III}}_2]$ grid complex, which just shows a partial SCO up to 300 K but can be switched between three different spin states at low temperatures with lasers of different wavelengths. Green light (532 nm) caused a LIESST transition for one iron(II), while red light (808 nm) caused a LIESST transition for one iron(III). This was the first observation of a site-selective SCO. These multistable compounds bear the potential for nano-scaled logical and light-programmable devices.^[20]

Further ways of modifying the ligand field splitting are changing substituents at the ligand. D. Müller et al. showed that it is possible to adjust $T_{1/2}$ for an iron(II) tetrazole system between 120 K and 200 K by using different halogen substituents. In this specific case, the shift of $T_{1/2}$ was only influenced by the changed steric demand caused by the halogen substituents and not by a changed coordination sphere or electronic structure.^[53]

The properties of iron(II) SCO 1D coordination polymers, which arise from the Fe-Fe bridging by three N^1, N^2 -1,2,4-triazole derivatives (Figure 4), are very unique due to their flexibility. $T_{1/2}$ can be adjusted between 100 K and 385 K through the introduction of substituents and exchanging the counter ions. Furthermore, these compounds show desired properties such as abrupt SCO and hysteresis near RT. Simple preparation, chemical stability, and easy processability make these compounds promising candidates for applications. Due to the polymeric character of these complexes, the synthesis of gels, films, liquid crystals, nanoparticles, and composite materials is possible.^[54,55]

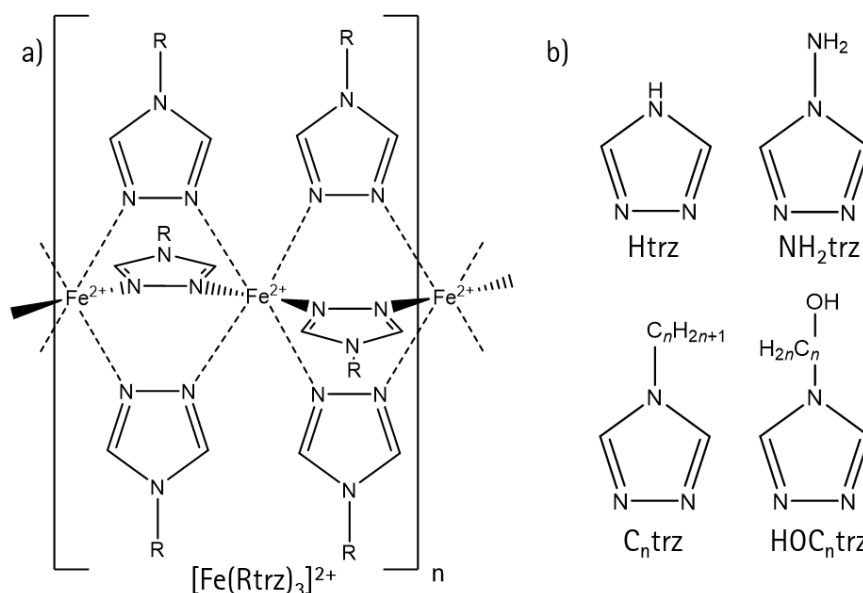


Figure 4: a) Scheme of the iron(II) 1D triazole-based coordination polymer. b) Examples of triazole derivatives.

SCO nanoparticles are especially interesting for miniaturized electronic devices. Therefore, the inverse micelle technique is used to synthesize triazole-based nanoparticles. E. Coronado et al. described the parameters, which are important for the synthesis of reproducible particle sizes and properties.^[56] We

synthesized polymer fiber composite materials through electrospinning of the nanoparticles while maintaining the SCO behavior.^[57] I. A. Gural'skiy et al. synthesized chiral triazole nanoparticles through the addition of the chiral anion camphorsulfonate, which was published in 2015. Its chiral properties such as circular dichroism is coupled to the spin state and can therefore be switched.^[58]

Especially for optical applications such as magneto-optical memory and optoelectronics, multifunctional materials with switchable optical properties are highly attractive.^[21,59] The first evidence of a correlation between the spin state in an SCO compound and its nonlinear optical properties was published by V. Rodriguez et al. in 2012.^[59] S. Ohkoshi et al. reported a 3D chiral coordination network of cyanide-bridged niobium and iron(II) that shows an SCO induced change of its second-harmonic generation optical properties, a LIESST effect including reversible switching between two HS phases by light, and an SCO induced long-range magnetic ordering. The change of spin state in this compound switches the polarization plane of the output second-harmonic generation light by about 90°, which is caused by the crystal structure and light induced magnetization. This cutting-edge study might lead to further developments in the field of optical materials.^[21] Furthermore, 3D coordination frameworks have the great advantage of possible host-guest interactions. M. Ohba, J. A. Real, S. Kitagawa et al. synthesized a platinum-iron(II) SCO framework that showed guest induced SCO^[48,50] which is discussed in Chapter 6.

Combined SCO and optical properties can also simplify the detection of the spin state. Instead of introducing additional nonlinear optical properties to an SCO complex, B. Weber et al. combined the SCO properties of an 1D iron(II) coordination polymer with fluorescent properties. The emission spectra of this compound in solid-state change from a greenish color in the LS state to a yellow color in the HS state. Alongside the SCO, also a phase transition appears in the same temperature region, which might be the reason for the large hysteresis of 48 K. However, it cannot clearly be stated if the change of emission spectra is caused by the phase transition or SCO.^[60]

All mentioned examples contain iron(II) or iron(III) as SCO-active ion. For this reason, the following examples are based on other metal ions. The first cobalt(II) SCO complex was published in 1961 by R. C. Stouffer et al., which is two years earlier than the first report of an iron(II) SCO compound.^[61,62] However, the variety of cobalt(II) SCO compounds with unique properties, as discussed above, is much smaller than for iron compounds. Their SCO behavior is often gradual, the influence of the chemical environment is weaker and the photo-induced population of the HS state is not very efficient.^[62] S. Hayami et al. discovered two cobalt(II) SCO coordination polymers, which differ by their coordinated chloride and bromide anions. The compounds show a gradual SCO and adsorption and desorption for water and CO₂. The magnetic susceptibility of the bromide compounds is more sensitive to the

adsorption and desorption of water molecules than iron(II) and iron(III) compounds. It can therefore be for chemical responsive materials.^[49]

For manganese(III) even fewer SCO complexes are known, compared to cobalt(II). However, the Jahn-Teller effect in the manganese(III) HS state is of interest because it offers different kinds of SCO behavior. G. G. Morgan et al. published the first manganese(III) complex that shows an abrupt thermal SCO with an 8 K hysteresis. The manganese ion is coordinated by a hexa- N_4O_2 -dentate Schiff base ligand resulting in a chiral crystal structure. The research regarding SCO in d^4 compounds will likely be encouraged by these results.^[63]

In 2015 two independent reports of photo-induced magnetization of molybdenum(IV) in multinuclear octacyanomolybdat ($[Mo^{IV}(CN)_8]^{4-}$) complexes were published, even though molybdenum is a 4d element. This LIESST effect was firstly confirmed by V. Marvaud et al. Note that the molybdenum(IV) ion has no octahedral coordination sphere, resulting in a different ligand field splitting. The published $[MoZn_2]$ complex showed diamagnetic behavior up to the irradiation with blue light (405 nm), when it switched to the paramagnetic HS phase.^[64] O. Stefanczyk, C. Mathoniere, and B. Sieklucka et al. published the second molybdenum(IV) complex showing photo-induced magnetization in 2015. The 1D $[MoCo_2]$ ribbon compound showed a magnetization by irradiation of green and polychromatic white light. However, it could not clearly be determined, if an SCO or a metal-metal charge transfer (MMCT) caused magnetization.^[65] Especially the first example shows that even beyond the 3d elements an SCO is possible This leads to new possibilities for future molecular design.

2.1.2 Complexes with Penta- N_3O_2 -dentate Schiff Base Ligands

Schiff bases (imines) were firstly synthesized by H. Schiff in 1864^[66] and are of great importance in the current field of chemistry due to their use in many organic syntheses, as biological-active species, and in metalorganic complexes. The most common synthesis is a condensation reaction of an aldehyde or ketone with primary amine. This simple synthesis procedure makes it possible to create a wide variety of different Schiff base ligands with good modifiability.^[67] Therefore, SCO iron(III) Schiff base complexes are well established and, according to H. Oshio et al., can be categorized into four groups. The four groups are symmetric or asymmetric Schiff base ligands, which are derived from salicylaldehyde or acetylacetone.^[9] Below, mainly asymmetric penta- N_3O_2 -dentate salicylaldehyde-based Schiff base complexes are discussed. Already in 1985, the SCO complex $[Fe_{(3,3)salpet_{(H,H)}}X]$ ($_{(3,3)H_2salpet_{(H,H)}}$: 4-azaheptamethylene-1,7-bis(salicylideneiminat); X: monodentate ligand) with a symmetric Schiff base ligand was reported by N. Matsumoto (Figure 5). Through varying the monodentate ligand, the spin state and SCO behavior could be changed.^[68] However, a detailed investigation of mononuclear complexes with the asymmetric version of the salpet ($H_2salpet$: N,N -bis(2-hydroxybenzylidene)-1,6-

diamino-3-azahexane) ligand began 24 years later. R. Boca et al. synthesized the three mononuclear complexes $[\text{Fe}(\text{salpet}_{\text{H,H}})\text{Cl}]$, $[\text{Fe}(\text{salpet}_{\text{H,H}})\text{CN}]$, and $[\text{Fe}(\text{salpet}_{\text{tert-butyl,Me}})\text{Cl}]$.^[26] In the following years, a wide variety of salpet-based iron(III) complexes were synthesized, often with different substituents at the R^1 and R^2 positions and with chloride, pseudohalides, or organic molecules as exchangeable monodentate ligand. A general trend could be observed for the spin state dependency on the monodentate ligand. While a cyanide ion (C-bonded) always resulted in an LS complex, for all chloride and most pseudohalide complexes an HS state was observed. However, some of these complexes mostly with NCS^- , NCS^- , N_3^- and organic ligands showed an SCO, which was often gradual.^[26-32] This year R. Boca et al. published the complex $[\text{Fe}(\text{salpet}_{\text{Cl,Cl}})\text{NCS}]$, which shows an abrupt SCO with a 24 K hysteresis.^[34] Cyanide-bridged multinuclear complexes of $[\text{Fe}(\text{salpet}_{\text{R}^1,\text{R}^2})\text{NC}]_Y\text{-R}^3$ (R^3 : bridging complex between the $[\text{Fe}(\text{salpet}_{\text{R}^1,\text{R}^2})\text{NC}]$ building blocks; cyanide N-bonded), can show an SCO as well^[69-71] and are discussed in Chapter 2.2.1. Besides the large number of iron(III) salpet complexes, only a few mononuclear $[\text{Co}(\text{salpet}_{\text{R}^1,\text{R}^2})\text{X}]$ complexes have been synthesized and characterized. Even though cobalt(III) usually doesn't show an SCO, the complexes might be used as building blocks for multinuclear complexes as well.^[33]

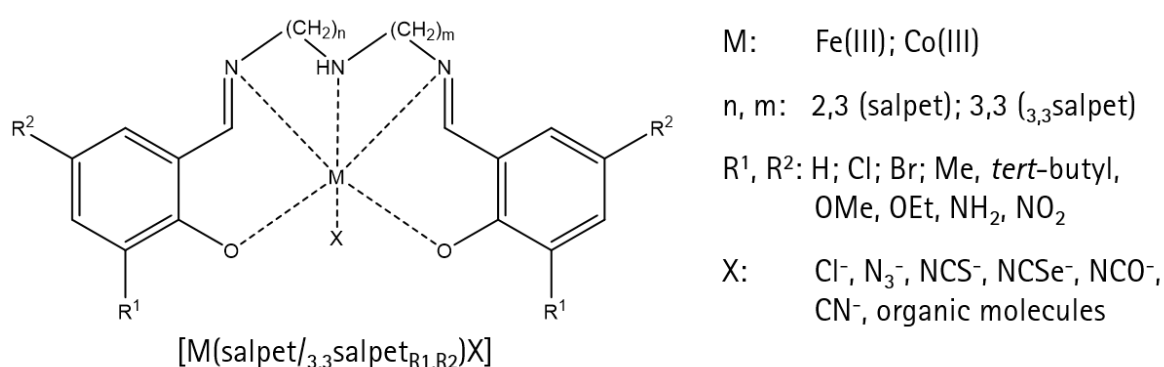


Figure 5: General scheme of salicylaldehyde-based penta- N_3O_2 -dentate Schiff base complexes.

The salpet complex can only stabilize cobalt(III) and iron(III) ions under aerobic conditions. If cobalt(II) ions should be stabilized, e.g. as building block for multinuclear complexes, the Schiff base ligand needs to be modified. Such ligands were synthesized by A. Panja^[72] and S. N. Dhuri et al.^[73] and the corresponding cobalt(II) complexes were investigated. While A. Panja exchanged the salicylaldehyde with 2-pyridinecarbaldehyde to synthesize symmetric Schiff base ligands,^[72] S. N. Dhuri et al. added a further step to reduce the imines to secondary amines.^[73] Both investigated the electrochemical properties. These results show great potential for these complexes as building blocks for MMCT compounds. This is discussed in Chapter 2.2.2 and Chapter 3 and Chapter 4.

2.2 Electron Transfer Coupled Spin Transition in Prussian Blue Analogs

2.2.1 From Mononuclear Building Blocks to Molecular and Bulk Prussian Blue Analogs

Prussian blue already caught general and scientific attention in the 18th century due to its intense blue color. The color is caused by an MMCT between the cyanide-bridged alternating iron(II) and iron(III) coordination centers, which build up a 3D network. Different redox potentials of the iron ions are derived from the asymmetric cyanide ion. The direction, $\text{Fe}^{2+}\text{-C}$, and $\text{Fe}^{3+}\text{-N}$ can be explained by the strong π -acceptor abilities of the carbon atom, which stabilizes the lower oxidation state, and the moderate σ -donor abilities of the nitrogen atom, preferable to iron(III), respectively. Inclusion of other heterometals, instead of one or both iron species, leads to Prussian blue analogs (PBAs), whose electronic structure and properties depend on the present combination. In general, PBAs are synthesized from different building blocks, which are based on cyanometalates and solvated metal ions. To prevent polymerization, capping ligands can be introduced to isolate OD fragments of PBAs called molecular PBAs (Figure 6). The shape and dimensionality can be controlled by the number and position of the available binding sites. Furthermore, the physical properties of molecular PBAs, such as redox potential and electronic states, can be changed by the choice of building blocks. Typical capping ligands are for example bidentate bipyridine derivatives and tridentate tris(pyrazolyl)borate derivatives.^[15,74]

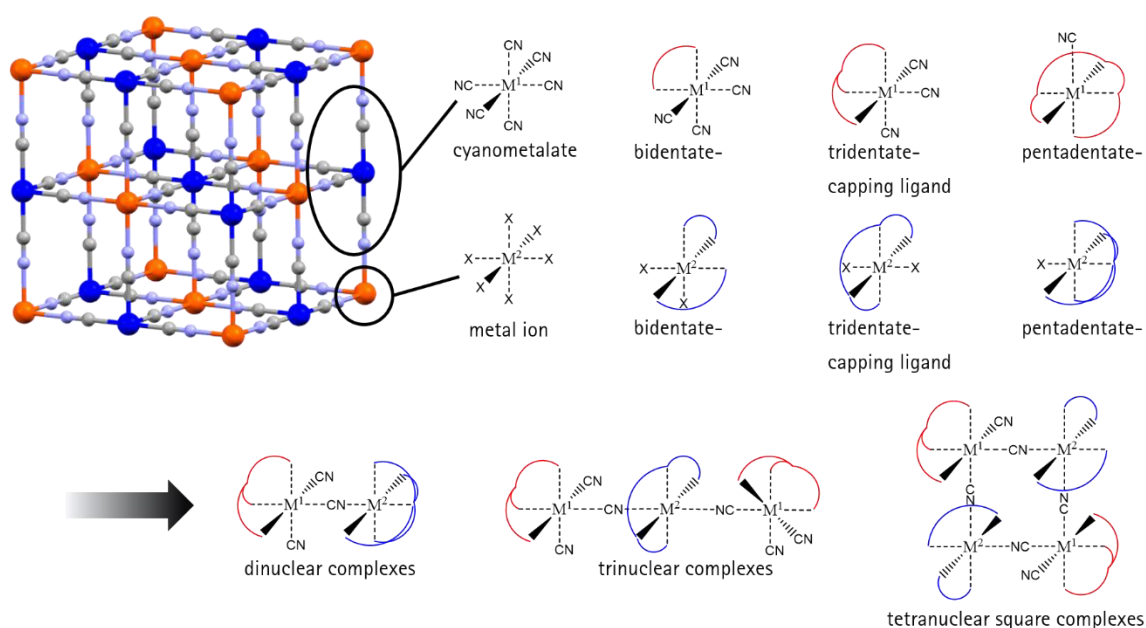


Figure 6: Bulk PBA and examples of building blocks and the resulting PBAs. M^1 and M^2 are heterometals, red and blue lines correspond to multidentate ligands, X are coordinating solvate molecules or anions.

H. Oshio et al. published in 1999 and 2000 five cyanide-bridged iron-iron, iron-copper, and iron-cobalt complexes with bipyridine capping ligands resulting in a square shape.^[75,76] Further molecular PBAs can be synthesized using the previously presented $[\text{Fe}(\text{salpet}_{3,3}\text{H})\text{Cl}]$ and $[\text{M}(\text{salpet}_{R1,R2})\text{Cl}]$ (M: iron(III),

cobalt(III)) complexes as building blocks. In 2004, R. Herchel and F. Renz et al. published a mixed-valence $[\text{Cr}^{\text{III}}\text{Fe}^{\text{III}}_3]$ PBA, which was synthesized through the simple reaction of $[\text{Fe}(\text{salpet}_{\text{H,H}})\text{Cl}]$ with $\text{K}_3[\text{Cr}(\text{CN})_6]$. The resulting T-shaped tetranuclear complex (charge-neutral) showed a thermally induced gradual incomplete SCO.^[77] Furthermore, four $[\text{Fe}^{\text{II}}\text{Fe}^{\text{III}}_6]$ star-shaped complexes based on penta- N_3O_2 -dentate Schiff base ligands were published by R. Boca, I. Salitros, and F. Renz et al. in 2010 and 2012. While the compound $\{\text{Fe}^{\text{II}}(\text{CN})_6[\text{Fe}(\text{salpet}_{\text{H,H}})]\}\text{Cl}_2$ also showed a thermally induced gradual incomplete SCO, the other three compounds remained in the HS state from 5 K to 300 K.^[69,70] I. Salitros et al. published in 2020 two tetranuclear $[\text{Co}^{\text{III}}\text{Fe}^{\text{III}}_3]$ complexes, the first with an asymmetric and the second with a symmetric penta- N_3O_2 -dentate Schiff base ligand. The reaction of the Schiff base complex with the $[\text{Co}(\text{CN})_6]^{3-}$ building block resulted in a mixed-valence complex in which the facial-like coordinated iron(III) complexes are linked via the cobalt(III) ion. Gradual SCO could be observed for the complex with the asymmetric Schiff base complex, while the second complex remained in the HS from 5 K to 300 K.^[71] These results show that it is possible to obtain different molecular shapes with similar building blocks. Therefore, the shape does not only depend on the available binding sites but also depends on the synthesis procedure, charges, electronic states, and inter and intramolecular interactions.

These presented PBAs, which are derived from different symmetric and asymmetric derivatives of the salpet complexes, represent the solvated metal ions with capping ligands and were combined with different cyanometalates. Even though it is possible to synthesize the mononuclear cyanometalate $[\text{Fe}(\text{salpet}_{\text{R}_1,\text{R}_2})\text{CN}]$, no mixed-valence compound could be synthesized from it,^[26-34,69-71,77] which is discussed in Chapter 4. However, it is possible to obtain mixed-valence complexes from $[\text{Co}(\text{salpet}_{\text{R}_1,\text{R}_2})\text{CN}]$, demonstrated by Z. Travnicek et al. in 2013 and 2016^[78,79] and in Chapter 4 by our group. Travnicek et al. synthesized one $[\text{Co}^{\text{III}}\text{Fe}^{\text{II}}]$ complex, two $[\text{Co}^{\text{III}}\text{Mn}^{\text{III}}]$ complexes, and two $[\text{Co}^{\text{III}}_2\text{Mn}^{\text{III}}]$ complexes from $[\text{Co}(\text{salpet}_{\text{H,OEI}})\text{CN}]$ and a similar tetra- N_2O_2 -dentate Schiff base ligand for iron and manganese. The anions chloride and bromide coordinate to one iron/manganese site as monodentate capping ligand. Formation of the trinuclear $[\text{Co}^{\text{III}}_2\text{Mn}^{\text{III}}]$ complex is possible because the anions iodide and nitrate are not coordinating at the sixth manganese site. The spin states of the metal ions do not change up to 300 K.^[78,79] M. J. Cliffe and P. Grey et al. claimed that PBAs do not necessarily need to have cyanide bridges. They published the first thiocyanate-based PBA in 2019,^[36] which is discussed in Chapter 6.

2.2.2 Electron Transfer Coupled Spin Transition

Prussian blue demonstrates that cyanide bridges enable electron transfers between mixed-valence redox-active metal ions. In 1996 A. Fujishima and K. Hashimoto et al. reported a photoinduced magnetization at low temperatures in the PBA $\text{K}_{0.2}[\text{Fe}(\text{CN})_6\text{Co}_{1.4}] \cdot 6.9\text{H}_2\text{O}$. However, the magnetization was not caused by the LIESST effect but by a charge transfer from the iron(II) to the cobalt(III), which

induced a spin transition from the LS to the HS state of the cobalt.^[80] This new effect was later named CTIST (charge transfer induced spin transition) and can be separated in the light induced charge transfer process from the $[\text{Co}^{\text{III}}_{\text{LS}}\text{Fe}^{\text{II}}_{\text{LS}}]$ state to the $[\text{Co}^{\text{II}}_{\text{LS}}\text{Fe}^{\text{III}}_{\text{LS}}]$ state and the following change of spin state from the $[\text{Co}^{\text{II}}_{\text{LS}}\text{Fe}^{\text{III}}_{\text{LS}}]$ state to the $[\text{Co}^{\text{II}}_{\text{HS}}\text{Fe}^{\text{III}}_{\text{LS}}]$ state.^[74] During the following years, further bulk [CoFe] PBAs were reported showing CTIST not only induced by light but also thermally.^[81,82] Hereinafter, the $[\text{Co}^{\text{II}}_{\text{LS}}\text{Fe}^{\text{III}}_{\text{LS}}]$ state is referred to as low temperature (LT) phase and the $[\text{Co}^{\text{II}}_{\text{HS}}\text{Fe}^{\text{III}}_{\text{LS}}]$ state is referred to as high temperature (HT) phase. The first molecular PBA showing thermally induced CTIST was synthesized from the building blocks $[\text{Fe}(\text{CN})_6]^{3-}$ and a cobalt(II)-phenanthroline derivative and was reported in 2004.^[83] In contrast to the light induced CTIST, the thermally induced transition is analog to the SCO an entropy-driven process. Therefore, it cannot be separated into multiple steps and the term *induced* is less accurate than *coupled*. Furthermore, the term *charge transfer* can be misunderstood as delocalized charge instead of an actual occurring electron transfer. For these reasons, Oshio et al. proposed in 2011 that ETCST (electron transfer coupled spin transition) is a more suitable term for this phenomenon and should be used instead of CTIST for the thermally and light induced process in molecular PBA (Figure 7a).^[74] Recently, ETCST was also used for this phenomenon in bulk PBAs.^[16] Consequently, in this thesis, ETCST is used not only for [CoFe] pairs but also for further transition metal combinations showing a similar switching mechanism.

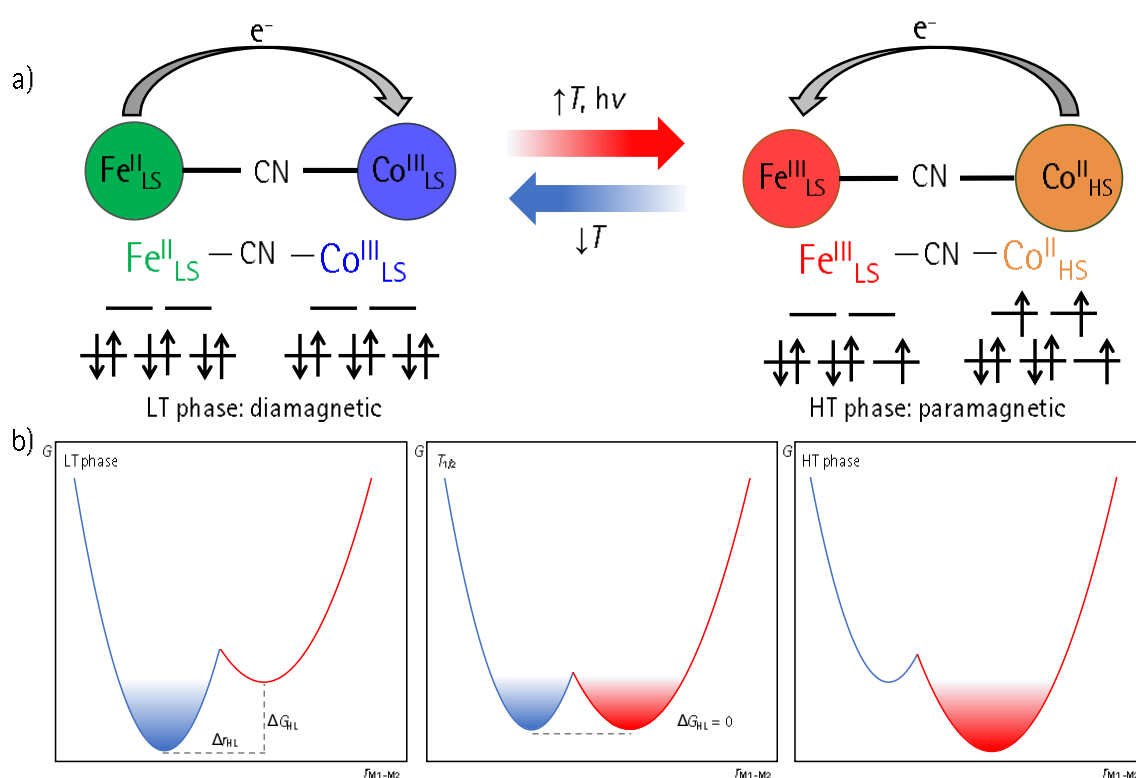


Figure 7: a) ETCST example of a [CoFe] pair. b) Standard potential well model of a cyanide-bridged redox couple. Left: Only the LT phase (blue) is occupied. Middle: Both phases are occupied for an ETCST complex at $T_{1/2}$. Right: Only the HT phase (red) is occupied. G is the Gibbs free energy and $\Delta r_{\text{M1-M2}}$ is the metal-metal distance. Adapted from Ref. ^[15]

The thermally induced ETCST, including the Gibbs free energy, can be described in analogy to the SCO (Chapter 2.1.1) by the potential well model (Figure 7b).^[15,84] However, in contrast to the SCO, the thermally induced ETCST is based on an intramolecular electron transfer and can therefore be described for molecular PBAs as $\Delta G^0 = F\Delta E_{DA} - w$, where $\Delta E_{DA} = E_D - E_A$; E_D and E_A are the redox potentials of the electron donor (D) and electron acceptor (A) moiety; F is the Faraday constant; w corresponds to the D^+ and A^- Coulomb interactions. The LT phase corresponds to the $[DA]$ and the HT phase to the $[D^+A^-]$ species. Hence, a molecular ETCST cannot be controlled by the ligand field splitting but by the redox potentials of the single building blocks. On the other hand, the redox potential can be controlled by the used metal ions and coordinated ligands.^[15] A detailed analysis of how to predict redox potentials of transition metal complexes was proposed by A. B. P. Lever et al. using an increment system.^[85-87] The relationship $\Delta G_{HL} \sim \Delta E_{FeCo}$ was investigated in detail for $[CoFe]$ systems. To obtain an ETCST complex, the difference of the redox potentials ΔE_{FeCo} needs to be in the estimated range of -0.4 V to -0.46 V, which was empirically determined (Figure 8) from previous publications and summarized by M. Nihei.^[15] Furthermore, this estimation can be used as well for building blocks before the reaction (giving a comparable picture to Figure 8), which is a powerful tool for the synthesis of new ETCST compounds. To obtain an ETCST complex, ΔE_{FeCo} (building block) must roughly be between -0.6 V and -1.0 V. However, there might be some exceptions caused by intermolecular interaction within the crystal lattice.^[17,35] In solution, even $T_{1/2}$ can roughly be estimated from ΔE_{FeCo} (building block), which is discussed in Chapter 2.2.3.^[15,35]

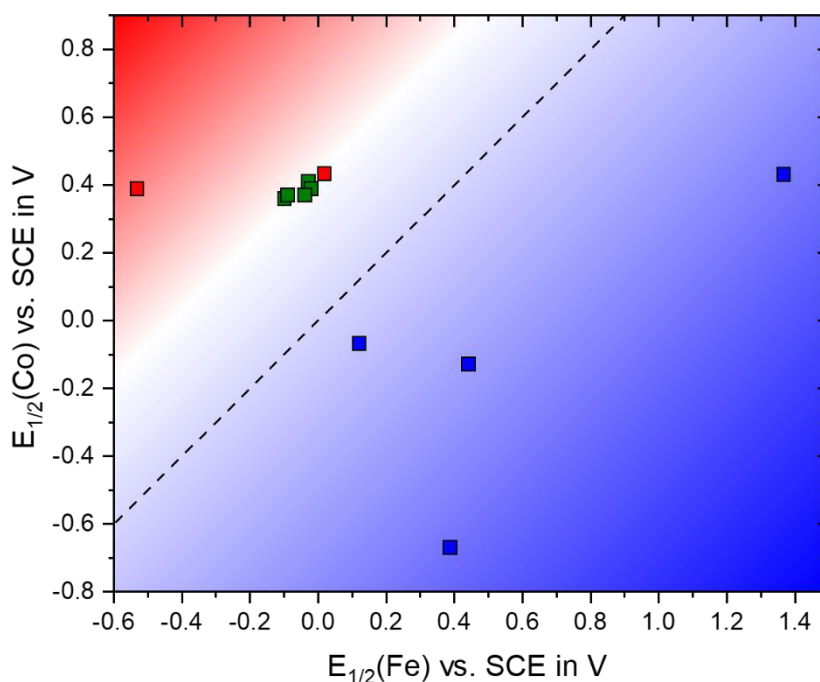


Figure 8: $E_{1/2}(Fe)$ vs. $E_{1/2}(Co)$ of previously reported cyanide-bridged mixed-valence $[CoFe]_X$ ($X = 1$ or 2) complexes.^[15,18,24,35,76,88] Dotted line: $E_{1/2}(Fe) = E_{1/2}(Co)$; blue: $[Co^{II}LSFe^{II}LS]$; red: $[Co^{II}HSFe^{III}LS]$; green: ETCST-active $[Co^{II}HSFe^{III}LS]$ complexes; data are summarized in Table 27 (Appendix Chapter 8, page 127). Adapted from Ref.^[15].

2. Current State of Research

While [CoFe] is the most common redox couple for ETCST complexes, further combinations are possible. In contrast to the SCO phenomenon, which is mostly limited to 3d elements due to the increasing ligand field splitting, one metal ion, mostly the cyanometalate, in ETCST complexes can be exchanged to osmium, tungsten, or molybdenum. Following an ETCST is known for [CoOs], [CoW], and [CoMo] (dehydration) compounds. The physical properties of ETCST complexes change in a similar manner as for SCO complexes. In addition, metal to metal electron transfer (MMET) of similar couples is known without showing a coupled SCO.^[16]

Below a few examples are discussed with regard to the number of nuclei and building blocks. Besides the 3D and 0D ETCST compounds, a 1D [CoFe] chain complex was reported by H. Oshio et al. in 2012. The chiral compound showed light and thermally induced ETCST and was synthesized from the tricyanometalate [Fe(tp)(CN)₃]⁻ (tp: hydrotris(pyrazol-1-yl)borate) and a chiral cobalt(II) building block. Noteworthy is that through the transition, the electric conductivity also switched between the insulating and semiconducting state, which makes it relevant for many electronic applications. Furthermore, the compound showed switchable single-chain magnetic properties.^[22]

A decanuclear [Co₆Fe₄] complex synthesized from a one-pot approach with [Fe(CN)₆]³⁻ and a chiral cobalt(II) building block resulted in a cage-like structure showing a gradual temperature induced ETCST.^[89] Mathoniere and Holmes et al. found an octanuclear [Co₄Fe₄] cube complex in 2008. It was the first soluble molecular PBA exhibiting thermally and light induced ETCST of all four [CoFe] redox couples. It was synthesized from [Fe(pztp)(CN)₃]⁻ (pztp: tetrakis(pyrazolyl)borate) and a cobalt(II) complex with a tridentate ligand.^[90] F. Breher and R. Lescouezec et al. published a similar ETCST [Co₄Fe₄] cubic complex with [Fe(tp)(CN)₃]⁻ and [Co(pztp)]⁺ moieties. However, within the cube a potassium cation was located. Therefore, one metal ion was non-reversibly reduced, due to the charge balance, during the reaction resulting in the [Fe^{II}₄Co^{III}₃Co^I] state at low temperatures. The compound shows high stability in solution with six accessible redox states shown by cyclic voltammetry (CV).^[91] By reducing the number of nuclei further, a hexanuclear [Co₂Fe₄] complex was reported by Oshio et al. in 2012. The building blocks were [Fe(pztp)(CN)₃]⁻ and [Co(bizimpy)]²⁺ (bizimpy: 2,6-bis(benzimidazol-2'-yl)pyridine). Noteworthy is that the light induced HT phase showed slow magnetic relaxation, which is typical for superparamagnetism and which had not been reported before for discrete molecules.^[92] As previously mentioned, the first molecular ETCST complex was a pentanuclear one and was reported in 2004.^{[93][83]} One year later, the same group published a second pentanuclear ETCST complex, which was sensitive to solvent loss within the crystal lattice.^[94] This behavior was subsequently observed for further compounds.^[25,95,96] Two trinuclear ETCST complexes were synthesized by T. Liu et al. and reported in 2012 and 2017. Both complexes showed a similar linear molecular structure consisting of two [Fe(tp)(CN)₃]⁻ building blocks as capping complexes and a centered cobalt(II) with 1-methylimidazole

and a methylimidazole derivative, respectively. These compounds exhibit an electron transfer induced nonpolar–polar conversion on a molecular scale. However, no bulk polarity can be measured because the electron transfer occurs randomly to both iron sites. Nonetheless, these results might lead to an electric field induced ETCST.^[23,97]

The research presented in this thesis is strongly based on dinuclear and tetranuclear square ETCST complexes, which are therefore highlighted in the separate Chapter 2.2.3. Noticeably, similar cyanometalates are used repeatedly, while the solvated metal ion building blocks (mostly containing cobalt(II)) change frequently. Further reviews about [CoFe] ETCST complexes were published by D. Aguila, C. Morthoniere and R. Clerac et al., discussing a rational molecular building block approach^[98] and by C. Mathoniere, highlighting general features for selected examples.^[99]

Below, a few examples of different redox couples are presented. S. Kang and O. Sato et al. published for the first time a homometallic PBA exhibiting a temperature induced MMET (without any spin transition). The [Fe^{II}Fe^{III}] coordination polymer was synthesized from [Fe(tp)(CN)₃]⁻ and Fe(ClO₂)₂ · 6H₂O with 1,2-bis(4-pyridyl)ethane.^[100] The groups of S. Ohkoshi and B. Sieklucka extensively investigated [CoW] ETCST coordination networks. In this case, the LT phase corresponds to the [Co^{II}₁₅W^{IV}] state and the HT phase to the [Co^I₁₅W] state. Typical building blocks are [W^{IV}(CN)₈]⁴⁻ and cobalt(II) with two monodentate ligands. These compounds show effects such as thermally and light induced ETCST and room temperature magnetic ordering.^[101–104] R. Podgajny and B. Sieklucka et al. published the trimetallic [Fe₆Co₃W₆] compound exhibiting an MMET between tungsten and iron and an ETCST between tungsten and cobalt. It is the first example of a trimetallic complex showing electron transitions between two different redox couples within the same compound.^[105] An [Mn^{II}₃Mn^{III}Fe^I₂Fe^{II}₂] octanuclear cube was synthesized by R. Lescouezec et al. showing an MMET switching between the two states [Mn^{III}Fe^I] and [Mn^{II}Fe^{II}]. It was synthesized from the [Fe^{III}(tp)(CN)₃]⁻ and [Mn^{II}(pztp)]⁺ building blocks and includes a cesium cation in its center. The thermally induced MMET is gradual and takes place above 300 K.^[106]

The presented compounds give a short overview of the synthesis strategy using different building blocks and the achievable properties applied in the field of multifunctional and multistable materials.

2.2.3 Dinuclear and Tetranuclear ETCST Complexes

Within the group of PBAs, the tetranuclear square complexes were described as the simplest model of the infinite Prussian blue structure by Oshio et al.,^[74] while C. Mathoniere and R. Clerac et al. published the smallest cyanide-bridged ETCST [CoFe] complex,^[25] which might be described as a PBA as well. However, in contrast to the large number of different switchable and non-switchable tetranuclear square complexes that were reported, only a small number of dinuclear ETCST complexes are known yet. Below, selected examples are presented.

In 2013, a dinuclear [CoFe] complex was reported by Mathoniere and Clerac et al. consisting of a bizimpy-tricyanometalate and the $[\text{Co}^{\text{II}}(\text{PY5Me}_2)^{2+}$ (PY5Me₂: 2,6-bis(1,1-di(pyridin-2-yl)ethyl)pyridine) building block, which has one accessible coordination site. The temperature induced change of magnetic susceptibility was explained by a cobalt(II) SCO, while an ETCST was observed through protonation of the dissolved sample. Redox data, measured by cyclic voltammetry during the addition of tetra trifluoroacetic acid showed that the iron site is protonated, shifting its redox potential to higher values and eventually inducing an ETCST. In this specific case, the bizimpy ligand was protonated twice.^[24] One year later, the same group published the first dinuclear ETCST PBA, entitled "The Ultimate Miniaturization." This [CoFe] complex was synthesized from $[\text{Fe}(\text{tp})(\text{CN})_3]^-$ and $[\text{Co}^{\text{II}}(\text{PY5Me}_2)^{2+}$. Its ETCST behavior can not only be triggered by light and temperature but also depends on the amount of solvent within the crystal structure.^[25] It is noteworthy that the small number of dinuclear ETCST complexes come from the lack of cobalt(II) building blocks with only one accessible coordination site and suitable redox potentials, whereas cobalt(II) building blocks with two accessible coordination sites are very common.^[15,24,25,88]

First non-switching tetranuclear square PBAs such as $[\text{Ti}_4]$,^[107] $[\text{Fe}^{\text{II}}_2\text{Cu}^{\text{II}}_2]$, $[\text{Fe}^{\text{III}}_2\text{Cu}^{\text{II}}_2]$,^[75] $[\text{Fe}^{\text{II}}_4]$, $[\text{Fe}^{\text{II}}_2\text{Co}^{\text{II}}_2]$ or $[\text{Fe}^{\text{II}}_2\text{Co}^{\text{III}}_2]$ ^[76] with cyclopentadiene or bipyridine capping ligands were reported in the 1990s and early 2000s. In the following years, the work was extended using further homo and heterometallic building blocks with bidentate, tridentate and tetradentate ligands.^[74,108] One example is a chiral $[\text{Fe}^{\text{II}}_2\text{Ni}_2]$ complex synthesized from an asymmetric iron(III)-tetracyanometalate and a chiral nickel building block. This complex showed an unusual sharp cyanide-nickel angle because of its bidentate iron ligand, which also coordinates the nickel.^[109] From 2010 investigations for $[\text{Co}_2\text{Fe}_2]$ ETCST complexes were increased. Clerac, Mathoniere, and Holmes et al. reported one of the first examples, which could be switched thermally and photo-induced in solid-state.^[110] One year later, Mathoniere and Clerac et al. published a similar complex that showed ETCST only in solution.^[111] A photo-switch was reported by B. L. Cointe and R. Lescouezec et al. A reversible ETCST could be induced by irradiation with 808 nm (HT phase) and 532 nm (LT phase) light, comparably to the LIESST and reverse-LIESST phenomenon.^[112,113] T. Liu et al. presented, through a series of square complexes the importance of counter-anions for this system. The π - π interactions between the cobalt ligands, which can be changed by the anions, controls the ETCST behavior or induces an HT phase. Therefore, it is an additional tool to tune the switching behavior, besides the building blocks themselves.^[17] Y. Li and R. Lescouezec et al. showed that pressure can induce an ETCST in $[\text{Co}_2\text{Fe}_2]$ complexes as well. While the square is in the HT phase from 100 K to 400 K at ambient pressure, it regains its switching behavior, which it had in solution, by applying pressure. Increasing the pressure led to an appearance and an increase of a hysteresis because of stronger intermolecular interactions. Additional examples were published, which had in common that the used building blocks (and capping ligands) were similar, and their redox

potentials were adjusted by functional groups (Figure 9). Furthermore, some showed crystal-solvent depending ETCST.^[95,96]

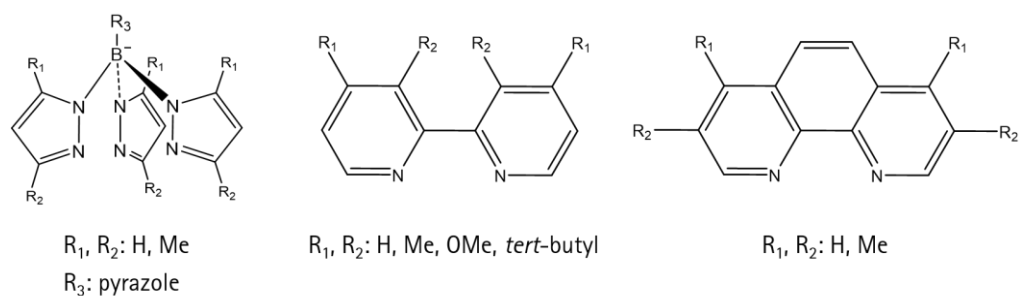


Figure 9: Frequently used capping ligands for square $[\text{Co}_2\text{Fe}_2]$ ETCST complexes.

Exceptional tetranuclear squares were published by Oshio et al. using a rational building block approach. They reported the first $[\text{Co}_2\text{Fe}_2]$ complex showing a two-step ETCST transition and demonstrated that the redox potentials and resulting spin states can be controlled by the capping ligands. Furthermore, they observed that the addition of acid to the dissolved sample can shift the redox potential of the iron ion, because a terminal cyanide ion is protonated. This process stabilizes the diamagnetic LT phase because the iron ion's d-electron density is withdrawn, which results in a shift of $T_{1/2}$ to higher temperatures.^[18,114] The possibility of controlling $T_{1/2}$ in solution by adjusting ΔE_{FeCo} (building block) was proposed by M. Nihei and H. Oshio et al. in 2019.^[35] However, the control of $T_{1/2}$ in solid-state is more difficult to predict due to the previously described interactions. Therefore, it can only be estimated whether an ETCST will occur or not by considering ΔE_{FeCo} (building block). In addition, the intermolecular interactions and the following switching behavior can be fine-tuned by anions, ligand shape, and even pressure. A new approach to control the intermolecular interactions was demonstrated by M. Nihei et al. A square complex was co-crystallized with 4-cyanophenol resulting in an ETCST behavior showing a three-step transition. The OH of the 4-cyanophenol built up hydrogen-bonding interactions to a terminal cyanide ion of the square complex, while the aromatic systems interacted with the cobalt ligand through π - π interactions. Its ETCST is accompanied by hydrogen-bonding interaction alterations between the 4-cyanophenol and the terminal cyanide.^[19] Furthermore, the aggregation of the complexes was controlled by co-crystallizing *p*-hydroquinone and phloroglucine giving directional hydrogen bonds. The two OH-groups of the *p*-hydroquinone led to a 1D linear hydrogen bonding controlled chain. Phloroglucine with three OH-groups led to a 2D sheet structure. Both compounds exhibited thermally and photoinduced ETCST.^[115] The use of this approach is further described in Chapter 5.

2.3 Potential Applications for Spin State Switching Materials

The fundamental features of SCO and ETCST materials are multistability and multiresponsiveness. Material properties such as magnetism, optics, conductivity, and mechanics that can be switched by light, temperature, and pressure, made these materials already in 1998 promising candidates for designing display devices and high-density data storages. Crucial requirements for these applications are a thermal hysteresis around RT, low thermal addressing power, short addressing time, a very small bit size (for data storage) and easy deposition e.g. by printing on any type of substrate.^[14] Further applications such as sensors or the use in micromechanics, switchable photonic devices, and spintronics are investigated, some in combination with porous frameworks or as composite materials. The great advantage of these materials and the key for commercial applications are being small while being efficient in terms of power and performance. More precisely, being smaller and more efficient than it is possible with currently used technologies based on semiconducting inorganic materials. As described in the previous chapters, the flexible and tunable nature of SCO and ETCST coordination compounds fulfill these requirements.^[6,10,13]

Miniaturization can be achieved by different approaches. Langmuir-Blodgett techniques can be used to produce thin films and SCO complex-polymer composites. However, for high quality SCO films in the range of nano- to micrometers, layer-by-layer assembly, vacuum sublimation, spin-coating, drop-casting, photo- and e-beam lithography, or soft lithography techniques are required.^[6,11,116] SCO nanoparticles are commonly synthesized by the reverse micelle method with particle sizes in the range of a few to several hundred nanometers. Subsequently, the nanoparticles can be redispersed in solvents to produce films, surface patterns, and composite materials.^[11,56,117] Even though the hysteresis and spin transition can be preserved in very small objects down to 5 nm, the SCO behavior differs from that in the bulk material and changes especially for mono- and few-layer films due to the electronic coupling between molecules and surface states creating an interfacial electronic structure.^[6,12] Kumar and Ruben et al.^[6] proposed the direct vacuum sublimation of charge-neutral SCO complexes as method of choice to create ultraclean mono- and multilayer films. Furthermore, the behavior of single molecules can be investigated with samples prepared by this method.^[6,12] Despite significant progress, it remains difficult to address single molecules for applications such as single-molecule electronic devices.^[10,12] Lately, the hysteresis loop of a single iron(II) triazole-derivative nanoparticle was measured using a newly developed surface plasmon resonance microscope.^[118] Further attempts to construct nano-devices in which a single SCO nanoparticle is electrically contacted were also successful. Coronado and van der Zant et al. showed that the nanoparticle had a spin state dependent conductivity, corresponding to the SCO and hysteresis.^[119] Besides the use of nanoparticles, the fabrication of crystalline SCO nanostripes and logical patterns on technological relevant surfaces was also demonstrated.^[120] Further approaches

might be to combine switchable materials with functional substrates or other functional materials to create symbiotic properties. M. Cavallini suggests in particular the combination with organic semiconductors to investigate the effect of the charge transport.^[121]

Commercial applications are rare but might be used by the company *Olikrom* in their multi responsive *Smart Pigments*.^[122] More common are concepts and prototypes. The mentioned nano-device of Coronado and van der Zant et al. can already be interpreted as prototype-memory-element based on SCO nanoparticles.^[119] A concept of how to design magnetic coordination complexes for quantum computing was presented by G. Aromi et al. Even though, they only described the use of paramagnetic metal aggregates and dinuclear complexes without specifically mentioning SCO and ETCST compounds,^[123] it seems reasonable that multistable magnetic compounds could be used as well. The concept is based on using electronic spins within metalorganic molecules to realize quantum logic operations. However, it will be a great challenge to use these molecules as hardware for quantum computing. A few issues that need to be solved are the molecular organization within a device, the tunable and switchable interactions between different molecular qubits, as well as the addressing and reading-out process.^[123] The use of SCO induced mechanical changes was demonstrated in microscopic and macroscopic actuator devices. These devices were produced by spray-coating of an iron(II) nanoparticle-polymer composite onto a silicon microcantilever and on macroscopic actuators. The resulting devices led to reproducible large actuation amplitudes and high associated work densities. Macroscopic soft actuators might be used as biomimetic artificial muscles.^[11] Garcia et al. presented a novel pressure and temperature sensor, which consists of two different SCO compounds showing a gradual transition. Simple temperature and pressure induced color changes detected by a reflected laser beam are sufficient for the measurement.^[124] F. Renz et al. showed that the spin state of an iron(II) complex is sensitive to water vapor and could therefore be used as a moisture sensor.^[125] A different kind of sensor was published by Salmon and Bousseksou et al. Quantitative gas sensing was possible, even with only a few hundred ppm of the analyte, by micropatterned SCO metal-organic frameworks. The guest-molecule induced SCO is associated with a change of the refractive index, which can even be detected at RT. Its selectivity is caused by the framework's structure and the SCO behavior, which is not triggered by any gas molecule.^[126]

3. Dinuclear Cyanide-Bridged Complexes

In Chapter 3, five novel dinuclear complexes are presented. It is divided into Chapter 3.1 with the Communication *Co(II) and Fe(II) Schiff Complexes in Dinuclear Prussian Blue Analogs*, soon to be submitted to Chemistry Open, and Chapter 3.2 in which, two modified compounds are presented.

Although many molecular ETCST PBAs are known, only one dinuclear complex which can thermally be switched was reported so far.^[25] If such an ETCST compound would show a molecular orientation along one crystallographic axis, the compound might show a temperature induced electron-transfer coupled polarization. Therefore, dinuclear cyanide-bridged compounds with chiral Schiff base ligands were investigated.

The four [FeCo] mixed-valence complexes $[\text{Co}(\text{L}^1)\text{-CN-Fe}(\text{tp})(\text{CN})_2](\text{BF}_4) \cdot \text{H}_2\text{O}$ (**1**), $[\text{Co}(\text{L}^1)\text{-CN-Fe}(\text{pztp})(\text{CN})_2](\text{BF}_4) \cdot \text{C}_2\text{H}_3\text{N}$ (**2**) (Chapter 3.1), $[\text{Co}(\text{L}^1)\text{-CN-Fe}(\text{tp})(\text{CN})_2](\text{ClO}_4) \cdot \text{H}_2\text{O}$ (**D1**), and $[\text{Co}(\text{L}^1)\text{-CN-Fe}(\text{tp}^*)(\text{CN})_2](\text{ClO}_4) \cdot 2(\text{C}_2\text{H}_3\text{N})$ (**D2**) (Chapter 3.2) (L^1 : symmetric pentadentate Schiff base ligand shown in Figure 10, tp: tris(pyrazolyl)borate, pztp: tetrakis(pyrazolyl)borate, tp*: potassium hydrotris(3,5-dimethylpyrazol-1-yl)borate) were prepared from a mononuclear Co(II) Schiff base and a Fe(III) tricyano precursor complex. The dinuclear compound $[\text{Fe}(\text{L}^2)\text{-CN-Fe}(\text{L}^2)](\text{PF}_6)_3 \cdot 3 \text{C}_2\text{H}_3\text{N}$ (**3**) (L^2 : asymmetric pentadentate Schiff base ligand shown in Figure 10) was synthesized through connecting two similar Fe(II) Schiff base complexes by cyanide.

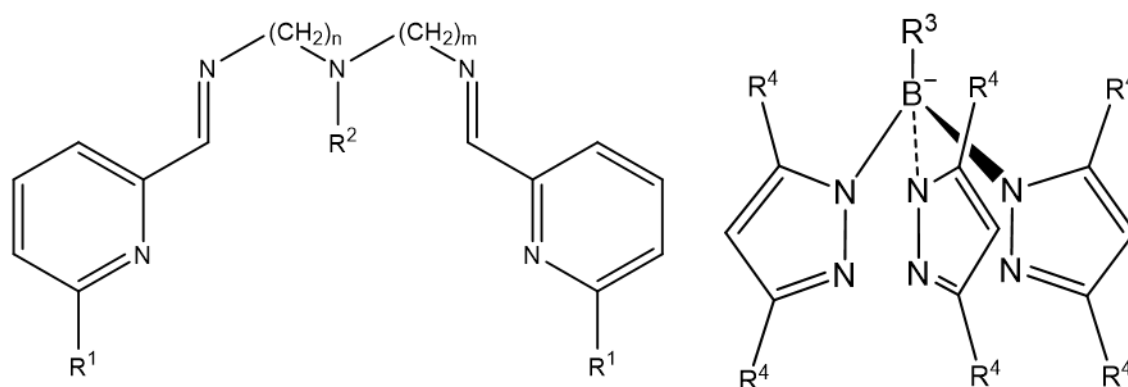


Figure 10: Ligands of the building blocks. For **1**: $\text{R}^1 = \text{Me}$, $\text{R}^2 = \text{Me}$, $\text{R}^3 = \text{H}$, $\text{R}^4 = \text{H}$, $n = 3$, $m = 3$; for **2**: $\text{R}^1 = \text{Me}$, $\text{R}^2 = \text{Me}$, $\text{R}^3 = \text{pyrazole}$, $\text{R}^4 = \text{H}$, $n = 3$, $m = 3$; for **3**: $\text{R}^1 = \text{H}$, $\text{R}^2 = \text{H}$, $\text{R}^3 = \text{not applicable}$, $\text{R}^4 = \text{H}$, $n = 3$, $m = 2$, for **D1**: $\text{R}^1 = \text{Me}$, $\text{R}^2 = \text{Me}$, $\text{R}^3 = \text{H}$, $\text{R}^4 = \text{H}$, $n = 3$, $m = 3$; **D2**: $\text{R}^1 = \text{Me}$, $\text{R}^2 = \text{Me}$, $\text{R}^3 = \text{H}$, $\text{R}^4 = \text{Me}$, $n = 3$, $m = 3$.

All the experiments and analysis for compound **1**, **2**, **D1**, and **D2** were performed and the initial manuscript for the publication was written by the author of this thesis. Compound **3** was synthesized and analyzed by Taishi Enomoto. Haruka Yoshino supported the magnetic measurements for **D1**. Dr. Takuya Shiga helped with the synthesis and measurements. Dr. Roman Boca fitted the magnetic data

of 1. Prof. Dr. Masaaki Ohba, Prof. Dr. Hiroki Oshio, and Prof. Dr. Franz Renz helped through discussions with the analysis and refined the manuscript.

The formatting of the following publication, soon to be submitted, was adjusted to the formatting of this dissertation. The wording and content might differ from the resulting publication due to revisions asked by the reviewers during the peer review process. To the references, the letter D or DI were added for the paper and the Supporting Information, respectively. Supporting information for this article are given in the Appendix Chapter 8.1 (page 128). The abbreviations, references as well as the labelling of figures and tables for the following publication and the corresponding supporting information are treated separately from the other chapters.

3.1 Co(II) and Fe(II) Schiff Base Complexes in Dinuclear Prussian Blue Analogs

Co(II) and Fe(II) Schiff Base Complexes in Dinuclear Prussian Blue Analogs

Dominik Natke,^{*[a]} Taishi Enomoto,^[b] Roman Boca,^[c,d] Takuya Shiga,^[b] Masaaki Ohba,^[e] Hiroki Oshio,^[b,f] Franz Renz^{*[a]}

[a] D. Natke, Prof. F. Renz
Institute of Inorganic Chemistry
Leibniz University Hannover
Callinstraße 9, 30167 Hannover, Germany
E-mail: dominik.natke@acd.uni-hannover.de, franz.renz@acd.uni-hannover.de

[b] T. Enomoto, Dr. T. Shiga, Prof. H. Oshio
Graduate School of Pure and Applied Sciences
University of Tsukuba
Tennodai, Tsukuba, Ibaraki 305-8577, Japan

[c] Prof. Dr. R. Boca
Institute of Inorganic Chemistry
Slovak University of Technology
Bratislava SK-81237, Slovakia

[d] Prof. Dr. R. Boca
Department of Chemistry (FPV)
University of SS Cyril and Methodius
91701 Trnava, Slovakia

[e] Prof. M. Ohba
Department of Chemistry
Faculty of Science, Kyushu University
744 Motooka, Nishi-ku, Fukuoka 819-0395, Japan

[f] Prof. H. Oshio
State Key Laboratory of Fine Chemicals
Dalian University of Technology
2 Linggong Rd., 116024 Dalian, China

Soon to be submitted to Chemistry Open

Abstract: The three novel cyanide-bridged dinuclear complexes $[\text{Co}(\text{L}^1)\text{-CN-Fe}(\text{tp})(\text{CN})_2](\text{BF}_4) \cdot \text{H}_2\text{O}$ (**1**), $[\text{Co}(\text{L}^1)\text{-CN-Fe}(\text{pztp})(\text{CN})_2](\text{BF}_4) \cdot \text{C}_2\text{H}_3\text{N}$ (**2**) and $[\text{Fe}(\text{L}^2)\text{-CN-Fe}(\text{L}^2)](\text{PF}_6)_3 \cdot 3 \text{C}_2\text{H}_3\text{N}$ (**3**) (L^1 and L^2 : symmetric and asymmetric pentadentate Schiff base ligand, respectively; tp: tris(pyrazolyl)borate, pztp: tetrakis(pyrazolyl)borate) were synthesized and their single crystal structure, magnetic susceptibility, and redox properties were analyzed. These results are suggesting that in both heterometallic complexes the Co(II) and Fe(III) ions are in the high spin and in the low spin states, respectively, for the temperature range between 5 K and 300 K. Furthermore, the $[\text{Fe}^{\text{II}}]$ complex was investigated to determine its potential as building block in mixed valance complexes.

Introduction

The photoinduced magnetization of $\text{K}_{0.2}\text{Co}_{1.4}[\text{Fe}(\text{CN})_6] \cdot 6.9 \text{H}_2\text{O}$ discovered by K. Hashimoto *et al.* in 1996^[D1] led to a new class of switchable materials. Several three dimensional (3D) Prussian blue analogs with tunable properties were reported to show tunable electronic and spin states by external stimuli such as heat and light.^[D2-D4] The magnetization changes are an electron transfer between Co and Fe ions, which is accompanied by a spin transition of the cobalt ions. Subsequently, two stable states exist, the diamagnetic $[\text{LS Co(III)} - \text{LS Fe(II)}]$ (LS: low spin) and the paramagnetic $[\text{HS Co(II)} - \text{LS Fe(III)}]$ (HS: high spin) state. Since the $[\text{Fe}(\text{CN})\text{Co}]$ redox couple is the essential moiety for this phenomenon, the 3D structure can be broken down into 1D^[D5] and 0D molecular complexes.^[D6-D8] For molecular species we refer to this phenomenon as electron transfer-coupled spin transition (ETCST).^[D9] Especially, the spin states of the 0D Prussian blue analogs can be controlled by their tunable structures, e.g. derivatization of their capping ligands. An ETCST in molecular $[\text{FeCo}]$ compounds was observed for decanuclear,^[D10] octanuclear,^[D11,D12] hexanuclear,^[D13,D14] pentanuclear,^[D15,D16] tetranuclear square,^[D17-D24] trinuclear^[D25,D26] and dinuclear^[D27] complexes. However, a metal to metal electron transfer is also possible for other cyanide-bridged redox couples^[D6] such as $[\text{Fe}^{\text{II}}\text{Fe}^{\text{III}}]/[\text{Fe}^{\text{III}}\text{Fe}^{\text{II}}]$,^[D28] $[\text{Co}^{\text{II}}\text{W}^{\text{V}}]/[\text{Co}^{\text{III}}\text{W}^{\text{IV}}]$ ^[D29] or $[\text{Co}^{\text{II}}\text{W}^{\text{V}}_2\text{Fe}^{\text{II}}]/[\text{Co}^{\text{III}}\text{W}^{\text{IV}}_2\text{Fe}^{\text{III}}]$.^[D30] The occurrence of an ETCST in mixed valence $[\text{CoFe}]$ complexes depends on the redox potential difference ($\Delta E_{1/2}$) between the components metal ions.^[D8,D27] It was shown that the transition temperatures in cyanide-bridged molecular squares of $[\text{Fe}_2\text{Co}_2]$ correlates with the redox potential difference ($\Delta E_{1/2}$) in solution.^[D18,D23] Furthermore, solution experiments revealed that the ETCST phenomena in dinuclear $[\text{FeCo}]$ ^[D31] and tetranuclear $[\text{Fe}_2\text{Co}_2]$ complexes^[D18,D23] were affected by protonation and deprotonation. The (de-)protonation occurred at the irons tridentate ligand in the dinuclear compound^[D31] and at the irons terminal (non-bridging) CN group in the tetranuclear complexes,^[D18,D23] leading to changing redox potentials of metal ions.^[D18,D23,D31] Protonation of the terminal cyanide can be mimicked through hydrogen bonding interactions by co-crystallization in solid-state.^[D32]

Beside the redox potential, the influence of the intra- and intermolecular interactions are also crucial for the ETCST behavior.^[D24] The previous researches on pentadentate Fe(III) Schiff base complexes showed that electronic properties such as spin state and/or spin crossover behavior can be easily changed through small modifications of the ligands.^[D33-D36] Therefore, we chose two modified Schiff base ligands to stabilize Co(II) and Fe(II) building blocks for the synthesis of cyanide-bridged dinuclear complexes. The ligands were prepared through the condensation of two pyridine-2-carbaldehyde derivatives with symmetric and asymmetric diamines (Figure 1).^[D37, D38]

Herein we report the three cyanide-bridged dinuclear complexes $[\text{Co}(\text{L}^1)\text{-CN-Fe}(\text{tp})(\text{CN})_2](\text{BF}_4) \cdot \text{H}_2\text{O}$ (**1**), $[\text{Co}(\text{L}^1)\text{-CN-Fe}(\text{pztp})(\text{CN})_2](\text{BF}_4) \cdot \text{C}_2\text{H}_3\text{N}$ (**2**) and $[\text{Fe}(\text{L}^2)\text{-CN-Fe}(\text{L}^2)](\text{PF}_6)_3 \cdot 3 \text{C}_2\text{H}_3\text{N}$ (**3**) (L¹/L²: symmetric/asymmetric pentadentate Schiff base ligand tp: tris(pyrazolyl)borate, pztp: tetrakis(pyrazolyl)borate) (Figure 1).

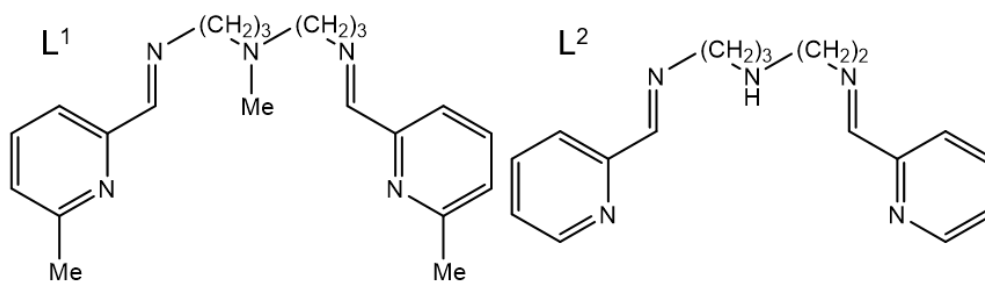


Figure 1: Scheme of L¹ and L².

Results and Discussion

Structural Data

Single crystal X-ray structures of **1**, **2**, **3** and the mononuclear precursor $[\text{Co}(\text{L}^1)(\text{H}_2\text{O})](\text{BF}_4)_2$ were determined at 100 K. The molecular structures are shown in Figure 2, the crystallographic data are summarized in Table S1 and the coordination bond length are listed in Table S2- S4. Note that the mononuclear complex is isostructural to the previously reported complex with perchlorate anions $[\text{Co}(\text{L}^1)(\text{H}_2\text{O})](\text{ClO}_4)_2$.^[D37]

The reaction of the mononuclear Co(II) complex with $[\text{Fe}(\text{tp})(\text{CN})_3]^-$ resulted in the cyanide-bridged dinuclear $[\text{Co}^{\text{II}}\text{Fe}^{\text{III}}]$ complex **1**. **1** crystallizes in the monoclinic space group Cc with one complex molecule, one BF_4^- anion and one water molecule. The iron ion has a slightly distorted octahedrally coordination geometry with three nitrogen atoms from the tp ligand and three carbon atoms from the three cyanide ions, of which one is bridged to the cobalt ion. The remaining coordination sites of the cobalt ion are occupied by five nitrogen atoms from the Schiff base ligand. The coordination bond length are indicating a Co(II) in the HS state (2.08 – 2.28 Å) and a Fe(III) in the LS state (1.93 – 1.98 Å).

Note that one non-bridging cyanide group is hydrogen bonded to a solvent water molecule with a N...O distance of 3.00(1) Å.

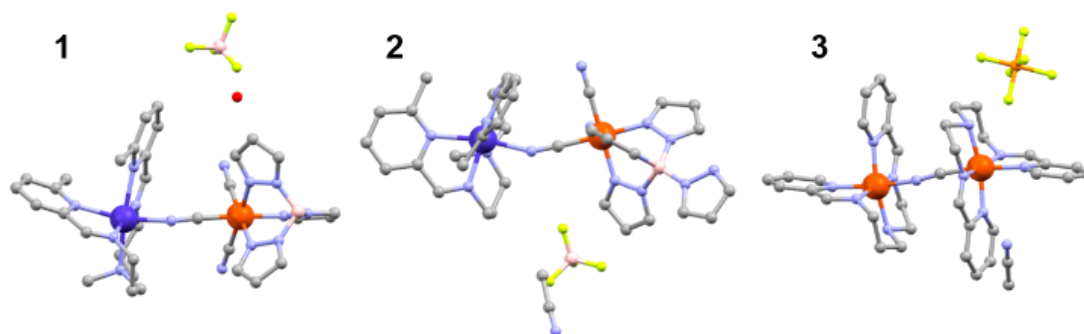


Figure 2: Molecular structure of **1**, **2** and **3**. Hydrogen atoms have been omitted for clarity. Color code: C, gray; N, light blue; O, red; Co, dark blue; Fe, orange; B, pink; F, light green; P, light orange.

Compound **2** crystallizes in the triclinic space group $P\bar{1}$ with both enantiomers inside the asymmetric unit (Figure S2). In addition, the asymmetric unit includes two BF_4^- and two acetonitrile solvent molecules. Despite the additional pyrazole, the coordination environment of **2** is similar to **1** (Figure S3) and the coordination bond lengths are corresponding to Co(II) in the HS states (2.06 – 2.29 Å) and Fe(III) in the LS states (1.90 – 2.00 Å) as well.

3 was prepared in situ by bridging two $[\text{Fe}^{\text{II}}(\text{L}^2)]^{2+}$ complexes through the addition of tetraethylammonium cyanide. It crystallizes in the monoclinic space group $C2/c$. Each Fe(II) ion is coordinated by five nitrogen atoms from L^2 and one carbon or nitrogen atom from the bridging cyanide ion. There exist three PF_6^- anions and three acetonitrile molecules in the crystal lattice per dinuclear complex. The bridging cyanide ion is located at the center of inversion, which implies that the carbon and nitrogen atoms are positionally disordered. The coordination bond lengths of the iron ions are in the range of 1.92 Å – 2.02 Å and therefore characteristic for Fe(II) in the LS state.

Magnetic Data

The magnetic properties of **1** and **2** were measured in the temperature range of 5 – 300 K (Figure 3). The magnetic data of **1** showed temperature-independent magnetism, which was corrected, and the data fitted (Figure S5). Details can be found in the SI.

1 and **2** show nearly constant $\chi_m T$ values from 300 K to 80 K of about 2.8 $\text{emu mol}^{-1} \text{K}$ and 3.0 $\text{emu mol}^{-1} \text{K}$, respectively. Below 80 K the values decrease strongly due to the thermal depopulation of the zero-field split (ZFS) multiplets. The $\chi_m T$ values of **1** and **2** correspond to a Fe(III) in the LS state and a Co(II) in the HS state, which match with the observed bond lengths.

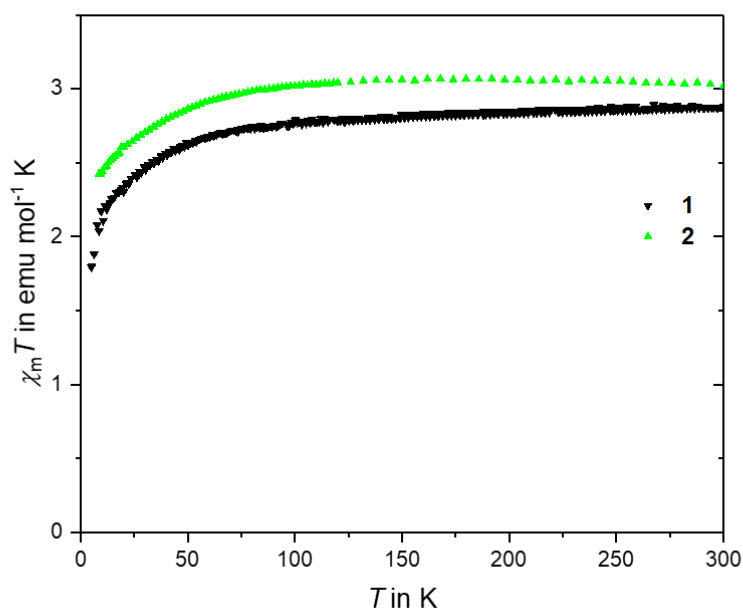


Figure 3: $\chi_m T - T$ plots of 1 and 2.

Redox and Optical Properties

Electrochemical properties of $[\text{Co}(\text{L}^1)(\text{H}_2\text{O})](\text{BF}_4)_2$, 1, 2 and 3 were investigated by cyclic voltammetry (Figure 4a, Table 1). The measurements were performed vs. SCE in a solution of tetrabutylammonium hexafluorophosphate in acetonitrile. The literature compound $[\text{Co}(\text{L}^1)(\text{H}_2\text{O})](\text{ClO}_4)_2$ was reported to show one quasi-reversible redox wave in methanol.^[D37] However, the mononuclear precursor $[\text{Co}(\text{L}^1)(\text{H}_2\text{O})](\text{BF}_4)_2$, which is expected to show a similar redox behavior, exhibited a two-step quasi-reversible redox process at -0.84 V and -1.08 V. To clarify the influence of the anion, the experiment was repeated with the perchlorate compound confirming our results. This excludes an effect of the anion. The reduction waves were observed first, which might be explained by the reduction of the ligand's pyridines including cis-trans-isomerization that is only possible for the mononuclear compound in solution (dimerization sterically favors the cis-isomer).^[D36] No $[\text{Co}^{\text{II}}/\text{Co}^{\text{III}}]$ oxidation was observed. For the ligand L^1 no redox wave could be observed, which might be due to the missing positive charge of the Co ion resulting in a large shift of the redox potential outside the possible measurement range. Furthermore, the redox wave at -0.835 V disappears for 1 and 2, while the second redox wave assigned to the ligand at -1.075 V is slightly shifted to -1.14 V, which might be due to reasons of charge balance as well.

The $[\text{Fe}^{\text{III}}\text{Co}^{\text{II}}]/[\text{Fe}^{\text{II}}\text{Co}^{\text{II}}]$ redox processes of the Fe(III) moieties are similar to previously reported di- and tetranuclear complexes at -0.295 V and -0.265 V for 1 and 2, respectively.^[D18,D23,D27] In addition, new redox processes appeared at 0.86 V (1) and 0.82 V (2), which can be assigned to the $[\text{Fe}^{\text{III}}\text{Co}^{\text{II}}]/[\text{Fe}^{\text{III}}\text{Co}^{\text{III}}]$ processes in comparison to other complexes (Figure 5). The minor redox process between the $[\text{Fe}^{\text{III}}\text{Co}^{\text{II}}]/[\text{Fe}^{\text{III}}\text{Co}^{\text{III}}]$ and $[\text{Fe}^{\text{III}}\text{Co}^{\text{II}}]/[\text{Fe}^{\text{II}}\text{Co}^{\text{II}}]$ redox processes might be caused by trinuclear complexes

3. Dinuclear Cyanide-Bridged Complexes

where two $[\text{Co}(\text{L}^1)]^{2+}$ complexes are connected to the $[\text{Fe}(\text{tp})(\text{CN})_3]^-/[\text{Fe}(\rho\text{ztp})(\text{CN})_3]^-$, which might form in solution. M. Nihei summarized the redox potentials of several ETCST complexes and showed a trend in which the spin state and a possible ETCST behavior is depending on the redox potentials of the Fe and Co ions.^[D8] According to this data, the $\Delta E_{1/2}(E_{1/2}(\text{Fe})-E_{1/2}(\text{Co}))$ value for 1 and 2 (-1.155 V and -1.085 V) needs to increase for an ETCST (Figure 5).

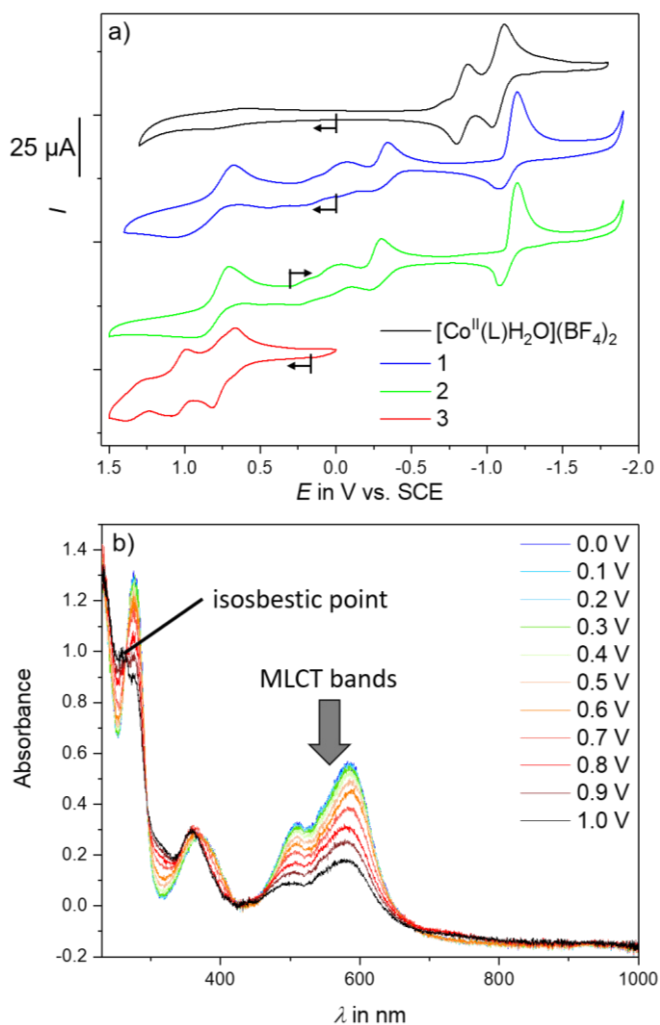


Figure 4: a) Cyclic voltammogram of $[\text{Co}^{\text{II}}(\text{H}_2\text{O})](\text{BF}_4)_2$, 1, 2 and 3. b) UV-Vis spectral changes for 3 with an applied potential from 0.0 V to 1.0 V.

The cyclic voltammogram of 3 shows quasi-reversible waves at 0.75 V and 1.04 V, which can be assigned to a two-step Fe(II)/Fe(III) redox processes. The separation of the redox waves is probably caused by the orientation of the cyanide.

UV-Vis spectra were measured for 3 at different applied potentials up to 1.0 V (Figure 4b). In the range of the first Fe(II) oxidation step (0.6 V), the absorption bands at 584 nm and 508 nm, which can be assigned to metal-to-ligand charge transfer (MLCT) bands,^[D31,D39] are decreasing as the potential increases. Furthermore, several isosbestic points are observed such as at 264 nm (Figure S5)^[D8] with two surrounding absorption bands that can be assigned to an intra-ligand $\pi \rightarrow \pi^*$ transition.^[D38,D41]

Additionally, tetraethylammonium cyanide was added to a solution of **3**, which was observed by UV-Vis spectroscopy and cyclic voltammetry (Figure S7). The appearance of isosbestic points in the UV-Vis spectra and the disappearance of one redox wave, while the second wave increase, in the cyclic voltammogram indicate a dissociation of **3** and a stabilization of the mononuclear cyanide complex.

Table 1: Redoxpotentials vs. SCE of $[\text{Co}(\text{L}^1)(\text{H}_2\text{O})](\text{BF}_4)_2$, **1**, **2** and **3**

	E_{red}	E_{ox}	$E_{1/2}$
$[\text{Co}(\text{L}^1)(\text{H}_2\text{O})](\text{BF}_4)_2$	-0.87 V	-0.80 V	-0.835 V
	-1.12 V	-1.03 V	-1.075 V
1	0.68 V	1.04 V	0.86 V
	-0.35 V	-0.24 V	-0.295 V
	-1.20 V	-1.08 V	-1.14 V
2	0.70 V	0.94 V	0.82 V
	-0.30 V	-0.23 V	-0.265 V
	-1.20	-1.08 V	-1.14 V
3	0.99 V	1.09 V	1.04 V
	0.67	0.82 V	0.745 V

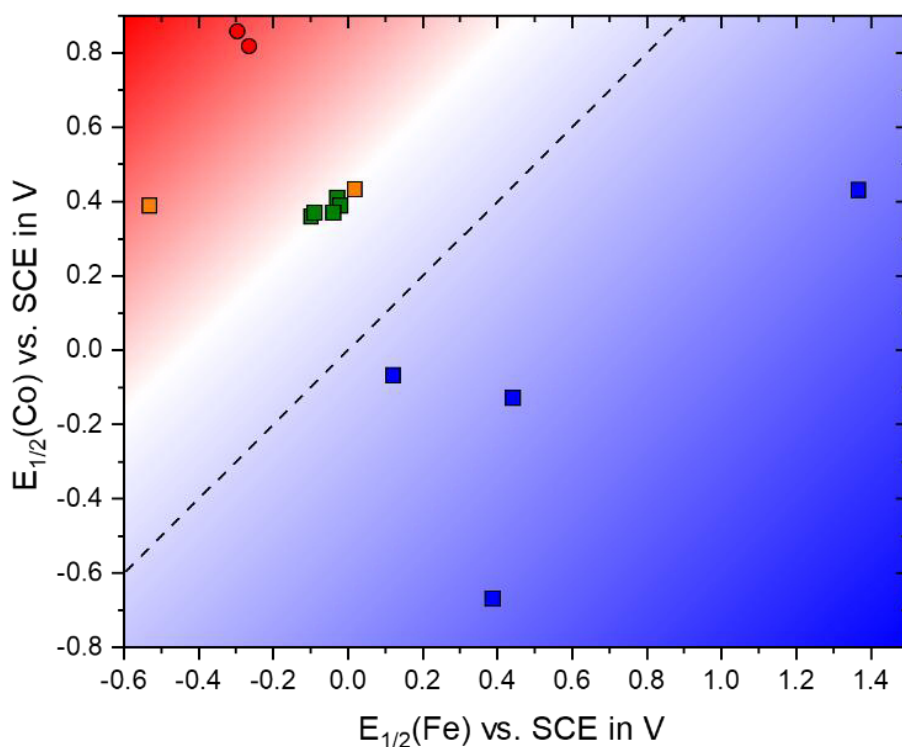


Figure 5: $E_{1/2}(\text{Fe})$ vs. $E_{1/2}(\text{Co})$ of previously reported cyanide-bridged mixed-valence $[\text{CoFe}]_x$ ($X = 1$ or 2) complexes^[D8,D18,D23,D31,D39,D40] and **1** and **2**. Dotted line: $E_{1/2}(\text{Fe}) = E_{1/2}(\text{Co})$; blue: $[\text{Co}^{\text{III}}(\text{LS})\text{Fe}^{\text{II}}(\text{LS})]$; orange: $[\text{Co}^{\text{II}}(\text{HS})\text{Fe}^{\text{III}}(\text{LS})]$; green: ETCST-active $[\text{Co}^{\text{II}}(\text{HS})\text{Fe}^{\text{III}}(\text{LS})]$ complexes; red: **1** and **2** (Table S5).

Conclusion

In summary three new dinuclear cyanide-bridged complexes were synthesized. The two [Fe^{III}Co^{II}] complexes **1** and **2** differ by their Fe(III) building blocks. Both compounds show paramagnetic behavior expected for Fe(III) in the LS state and Co(II) in the HS state. The redox potentials show a $\Delta E_{1/2}(E_{1/2}(\text{Fe})-E_{1/2}(\text{Co}))$ of -1.16 V for **1** and -1.09 V for **2**. The dinuclear [Fe^{II}]₂ complex **3** is in the LS state at 100 K and shows two distinct redox waves, which are depending on the cyanide's binding side. This compound can be dissociated into two mononuclear complexes by the addition of further cyanide ions and is therefore interesting as additional Schiff base building block.

Previous results suggest the possibility of creating ETCST compounds by a rational design relying on $\Delta E_{1/2}$ between the Co and Fe ions.^[D8,D18,D23,D27] Subsequently the chance of obtaining ETCST compounds from this class of Schiff base complexes can be increased by increasing $\Delta E_{1/2}$ of the [FeCo] centers.

Acknowledgements

This work was supported by the Hannover School for Nanotechnology (HSN) and the German Academic Exchange Service (DAAD).

Keywords: iron complex, cobalt complex, Schiff base complexes, cyclic voltammetry, magnetic susceptibility, mixed-valence

- [D1] O. Sato, T. Iyoda, A. Fujishima, K. Hashimoto, *Science* **1996**, *272*, 704–705.
- [D2] O. Sato, Y. Einaga, A. Fujishima, K. Hashimoto, *Inorg. Chem.* **1999**, *38*, 4405–4412.
- [D3] V. Escax, A. Bleuzen, C. Cartier dit Moulin, F. Villain, A. Goujon, F. Varret, M. Verdagner, *J. Am. Chem. Soc.* **2001**, *123*, 12536–12543.
- [D4] N. Shimamoto, S. Ohkoshi, O. Sato, K. Hashimoto, *Inorg. Chem.* **2002**, *41*, 678–684.
- [D5] N. Hoshino, F. Iijima, G. N. Newton, N. Yoshida, T. Shiga, H. Nojiri, A. Nakao, R. Kumai, Y. Murakami, H. Oshio, *Nat. Chem.* **2012**, *4*, 921–926.
- [D6] Y. S. Meng, O. Sato, T. Liu, *Angew. Chemie - Int. Ed.* **2018**, *57*, 12216–12226.
- [D7] C. Mathonière, *Eur. J. Inorg. Chem.* **2018**, 248–258.
- [D8] M. Nihei, *Chem. Lett.* **2020**, *49*, 1206–1215.
- [D9] G. N. Newton, M. Nihei, H. Oshio, *Eur. J. Inorg. Chem.* **2011**, 3031–3042.

- [D10] T. Shiga, T. Tetsuka, K. Sakai, Y. Sekine, M. Nihei, G. N. Newton, H. Oshio, *Inorg. Chem.* **2014**, *53*, 5899–5901.
- [D11] D. Li, R. Clérac, O. Roubeau, E. Harté, C. Mathonière, R. Le Bris, S. M. Holmes, *J. Am. Chem. Soc.* **2008**, *130*, 252–258.
- [D12] D. Garnier, J. R. Jiménez, Y. Li, J. Von Bardeleben, Y. Journaux, T. Augenstein, E. M. B. Moos, M. T. Gamer, F. Breher, R. Lescouëzec, *Chem. Sci.* **2016**, *7*, 4825–4831.
- [D13] M. Nihei, Y. Okamoto, Y. Sekine, N. Hoshino, T. Shiga, I. P. C. Liu, H. Oshio, *Angew. Chemie - Int. Ed.* **2012**, *51*, 6361–6364.
- [D14] J.-L. Wang, H.-L. Zhu, L. Zhao, L.-X. Ren, C.-Y. Duan, T. Liu, *Inorg. Chem. Commun.* **2017**, *76*, 55–58.
- [D15] C. P. Berlinguette, A. Dragulescu-Andrasi, A. Sieber, J. R. Galán-Mascarós, H. U. Güdel, C. Achim, K. R. Dunbar, *J. Am. Chem. Soc.* **2004**, *126*, 6222–6223.
- [D16] C. P. Berlinguette, A. Dragulescu-Andrasi, A. Sieber, H.-U. Güdel, C. Achim, K. R. Dunbar, *J. Am. Chem. Soc.* **2005**, *127*, 6766–6779.
- [D17] Y. Zhang, D. Li, R. Clérac, M. Kalisz, C. Mathonière, S. M. Holmes, *Angew. Chemie Int. Ed.* **2010**, *49*, 3752–3756.
- [D18] M. Nihei, Y. Sekine, N. Suganami, K. Nakazawa, A. Nakao, H. Nakao, Y. Murakami, H. Oshio, *J. Am. Chem. Soc.* **2011**, *133*, 3592–3600.
- [D19] D. Siretanu, D. Li, L. Buisson, D. M. Bassani, S. M. Holmes, C. Mathonière, R. Clérac, *Chem. - A Eur. J.* **2011**, *17*, 11704–11708.
- [D20] A. Mondal, Y. Li, M. Seuleiman, M. Julve, L. Toupet, M. Buron-Le Cointe, R. Lescouëzec, *J. Am. Chem. Soc.* **2013**, *135*, 1653–1656.
- [D21] Y. Z. Zhang, P. Ferko, D. Siretanu, R. Ababei, N. P. Rath, M. J. Shaw, R. Clérac, C. Mathonière, S. M. Holmes, *J. Am. Chem. Soc.* **2014**, *136*, 16854–16864.
- [D22] Y. Sekine, M. Nihei, H. Oshio, *Chem. Lett.* **2014**, *43*, 1029–1030.
- [D23] M. Nihei, K. Shiroyanagi, M. Kato, R. Takayama, H. Murakami, Y. Kera, Y. Sekine, H. Oshio, *Inorg. Chem.* **2019**, *58*, 11912–11919.
- [D24] C. Q. Jiao, Y. S. Meng, Y. Yu, W. J. Jiang, W. Wen, H. Oshio, Y. Luo, C. Y. Duan, T. Liu, *Angew. Chemie - Int. Ed.* **2019**, *58*, 17009–17015.

- [D25] T. Liu, D.-P. Dong, S. Kanegawa, S. Kang, O. Sato, Y. Shiota, K. Yoshizawa, S. Hayami, S. Wu, C. He, C. He, C. Y. Duan, *Angew. Chemie Int. Ed.* **2012**, *51*, 4367–4370.
- [D26] J. X. Hu, L. Luo, X. J. Lv, L. Liu, Q. Liu, Y. K. Yang, C. Y. Duan, Y. Luo, T. Liu, *Angew. Chemie - Int. Ed.* **2017**, *56*, 7663–7668.
- [D27] E. S. Koumouji, I. R. Jeon, Q. Gao, P. Dechambenoit, D. N. Woodruff, P. Merzeau, L. Buisson, X. Jia, D. Li, F. Volatron, et al., *J. Am. Chem. Soc.* **2014**, *136*, 15461–15464.
- [D28] K. Zhang, S. Kang, Z. S. Yao, K. Nakamura, T. Yamamoto, Y. Einaga, N. Azuma, Y. Miyazaki, M. Nakano, S. Kanegawa, O. Sato, *Angew. Chemie - Int. Ed.* **2016**, *55*, 6047–6050.
- [D29] Y. Miyamoto, T. Nasu, N. Ozaki, Y. Umetsu, H. Tokoro, K. Nakabayashi, S. Ohkoshi, *Dalt. Trans.* **2016**, *45*, 19249–19256.
- [D30] R. Podgajny, S. Chorazy, W. Nitek, M. Rams, A. M. Majcher, B. Marszałek, J. Żukrowski, C. Kapusta, B. Sieklucka, *Angew. Chemie* **2013**, *125*, 930–934.
- [31] I.-R. Jeon, S. Calancea, A. Panja, D. M. Piñero Cruz, E. S. Koumouji, P. Dechambenoit, C. Coulon, A. Wattiaux, P. Rosa, C. Mathonière, R. Clerac, *Chem. Sci.* **2013**, *4*, 2463.
- [D32] M. Nihei, Y. Yanai, D. Natke, R. Takayama, M. Kato, Y. Sekine, F. Renz, H. Oshio, *Chem. – A Eur. J.* **2019**, *25*, 7449–7452.
- [D33] I. Šalitraš, R. Boča, L. Dlhán, M. Gembický, J. Kozíšek, J. Linares, J. Moncol', I. Nemeč, L. Perašínová, F. Renz, I. Svoboda, H. Fuess, *Eur. J. Inorg. Chem.* **2009**, 3141–3154.
- [D34] C. Krüger, P. Augustin, I. Nemeč, Z. Travnicek, H. Oshio, R. Boca, F. Renz, *Eur. J. Inorg. Chem.* **2013**, 902–915.
- [D35] C. Krüger, P. Augustin, L. Dlhán, J. Pavlík, J. Moncol', I. Nemeč, R. Boca, F. Renz, *Polyhedron* **2015**, *87*, 194–201.
- [D36] P. Masárová, P. Zoufalý, J. Moncol, I. Nemeč, J. Pavlík, M. Gembický, Z. Trávníček, R. Boča, I. Šalitraš, *New J. Chem.* **2015**, *39*, 508–519.
- [D37] A. Panja, *Dalt. Trans.* **2014**, *43*, 7760.
- [D38] D. D. Narulkar, A. K. Srivastava, R. J. Butcher, K. M. Ansy, S. N. Dhuri, *Inorganica Chim. Acta* **2017**, *467*, 405–414.
- [D39] H. Oshio, H. Onodera, O. Tamada, H. Mizutani, T. Hikichi, T. Ito, *Chem. – A Eur. J.* **2000**, *6*, 2523–2530.

- [D40] P. V. Bernhardt, B. P. Macpherson, M. Martinez, *J. Chem. Soc. Dalton Trans.* 2002, 1435.
- [D41] L. Pogány, J. Moncol, M. Gál, I. Šalitraš, R. Boča, *Inorganica Chim. Acta* 2017, 462, 23–29.

3.2 Derivatives of [FeCo]-Complexes

In addition to the reported [Co^{II}Fe^{III}] dinuclear complexes in 3.1, the results of two further compounds are discussed below. For compound **D1**, which is similar to **1**, the anion was exchanged by ClO₄⁻. The second complex **D2** differs from **1** by modifications to the ligand of its Fe(III) building block. The single crystal X-ray structure, magnetic properties, and redox potential of the two complexes were investigated.

3.2.1 Experimentals

All chemicals were purchased from commercial suppliers and used without further purification. The Fe(III) complexes Bu₄N[Fe(tp)(CN)₃]^[127] and Bu₄N[Fe(tp*)(CN)₃]^[128] (Bu₄N: tetrabutylammonium) as well as the mononuclear compounds [Co(L¹)(H₂O)](ClO₄)₂ and [Co(L¹)(H₂O)](BF₄)₂ were synthesized as previously described.^[72] For the second cobalt complex Co(BF₄)₂ · 6H₂O was used instead of Co(ClO₄)₂ · 6H₂O. All syntheses were performed under aerobic conditions.

[Co(L¹)-CN-Fe(tp)(CN)₂](ClO₄) · H₂O (**D1**):

Bu₄N[Fe(tp)(CN)₃] (0.05 mmol) was added to a solution of [Co(L¹)(H₂O)](ClO₄)₂ (0.05 mmol) in 10 ml acetonitrile resulting in an orange solution. After 2 h of stirring at RT, the solution was filtrated, and orange single crystals could be obtained by vapor diffusion of diethyl ether. C₃₃H₄₃BClCoFeN₁₄O₆, [CoL-CN-Fe(tp)(CN)₂](ClO₄) · 2 H₂O: found % (calcd. %): C 43.83 (44.39), H 4.67 (4.39), N 21.87 (21.96); IR (KBr; cm⁻¹): 1093 (ClO₄⁻), 2075 (cyanide).

[Co(L¹)-CN-Fe(tp*)(CN)₂](BF₄) · 2C₂H₃N (**D2**):

Bu₄N[Fe(tp*)(CN)₃] (0.05 mmol) was added to a solution of [Co(L¹)(H₂O)](BF₄)₂ (0.05 mmol) in 10 ml acetonitrile resulting in an orange solution. After 20 min of stirring at RT, the solution was filtrated, and orange single crystals could be obtained by vapor diffusion of diethyl ether. C₃₉H₅₁B₂CoF₄FeN₁₄, [Co(L¹)-CN-Fe(tp*)(CN)₂](BF₄): found % (calcd. %): C 48.44 (50.46), H 5.49 (5.54), N 19.24 (21.12); IR (KBr; cm⁻¹): 1065 (BF₄⁻), 2054 (cyanide), 2097 (cyanide), 2124 (cyanide).

Crystal structure analysis: The diffraction data were collected with a Bruker SMART APEX II diffractometer with a CCD area detector and graphite-monochromated Mo-K α radiation ($\lambda = 0.71073$ Å). The data frames were integrated using the SAINT program and merged to give a unique data set for the determination of the structure. An absorption correction was performed using SADABS.^[129] The structure was solved by direct methods and refined on F² by the full-matrix least-squares methods using the SHELXTL package (Bruker Analytical X-ray systems, Olex2).^[130,131] Non-hydrogen atoms were refined with anisotropic thermal parameters. Hydrogen atoms were included in calculated positions

and refined with isotropic thermal parameters riding on those of the parent atoms. Electron densities of disordered solvent molecules for **D2** were flattened using Olex 2 solvent mask^[131] (BYPASS^[132]).

Physical measurements: Magnetic susceptibility data were collected using a Quantum Design MPMS-5S SQUID magnetometer. The measurements were performed with an applied magnetic field of 1000 Oe in the temperature range of 5 - 300 K. Magnetic data were corrected for the diamagnetism of the sample holder, and for the diamagnetism of the sample using Pascal's constants. **D1** was measured with a scan rate of 2 K/min in sweep mode. **D2** was measured with 5.0 K increments in the settle mode with a fixed scan rate of 3.0 K/min and 30 seconds after the temperature had stabilized. The samples were measured during the cooling and heating process. Infrared absorption spectra were measured with ATR for **D1** with a PerkinElmer FT-IR Spectrometer Spectrum Two and in KBr pellet samples for **D2** using a SHIMADZU IR Affinity-1 spectrometer. Cyclic voltammetry (CV) measurements were carried out in a standard one-compartment cell under N₂ at RT equipped with a platinum-wire counter electrode, an SCE reference electrode, and a glassy carbon (GC) working electrode using a BAS 620A electrochemical analyzer. The measurements were performed in MeCN with Bu₄NPF₆ (0.1 M) as the supporting electrolyte and a scan rate of 0.1 V/s.

3.2.2 Results and Discussion

Structural Data

The crystal structures of the complexes **D1** and **D2** were determined by single crystal X-ray diffraction (Table 1, Figure 11) at 100 K. **D1** crystallizes in the monoclinic *Cc* space group and is isostructural with the previously reported compound **1**, while **D2** crystallized in the monoclinic *P2₁/c* space group. Since the reaction of the two times positively charged cobalt(II) ion with the one time negatively charged iron(III) precursor results in a single positively charged complex, the asymmetric unit of **D1** and **D2** contain one ClO₄⁻ and BF₄⁻ anion for charge balance, respectively. Note that one terminal (non-bridging) cyanide ion of **D1** is hydrogen bonded to a solvent water molecule with a N-O distance of 2.997(6) Å. **D2** has two disordered acetonitrile per asymmetric unit which have been calculated from the removed electron densities through Olex 2 solvent mask^[131] (BYPASS^[132]). The coordination bond lengths of **D1** and **D2** (Table 28, page 139) are between 1.89 Å and 1.98 Å for the iron ions and 2.00 Å and 2.28 Å for the cobalt ions corresponding to [Fe^{III}₅Co^{II}₅] states. In comparison, both structures (Figure 58, page 139) show nearly no distortion of the Fe(III) part induced through the additional methyl groups. Whereas the Co site cannot be directly compared due to the different enantiomers. However, the molecular packing, especially the molecular orientation within the unit cell is different (Figure 12). While **D2** shows a unit cell with molecules in opposing directions, the unit cell of **D1** shows a predominant direction on the a-axis.

3. Dinuclear Cyanide-Bridged Complexes

Table 1: Crystallographic and structural data of D1 and D2.

	D1	D2
	$C_{33}H_{41}BClCoFeN_{14}O_5$	$C_{43}H_{56}B_2CoF_4FeN_{16}$
<i>T</i> in K	100	100
crystal System	monoclinic	monoclinic
space group	<i>Cc</i>	<i>P2₁/c</i>
<i>a</i> in Å	22.700(3)	11.928(9)
<i>b</i> in Å	11.2169(16)	19.307(15)
<i>c</i> in Å	16.331(2)	20.510(16)
α in °	90	90
β in °	109.921(2)	106.431(7)
γ in °	90	90
<i>V</i> in Å ³	3909.4(10)	4530(6)
<i>Z</i>	4	4
<i>R</i> ₁ / <i>wR</i> ₂ (<i>I</i> > 2σ <i>I</i>)	0.0361/0.0781	0.0880/0.2593

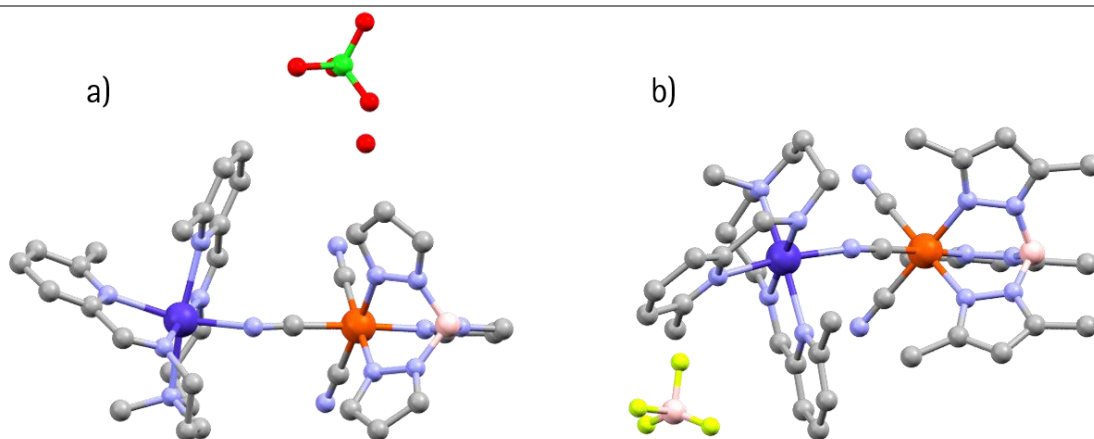


Figure 11: Molecular structure of a): D1 and b): D2. Hydrogen atoms have been omitted for clarity. Color code: C, gray; N, light blue; O, red; Co, dark blue; Fe, orange; B, pink; F, light green; Cl, dark green.

Magnetic Data

The temperature-depending magnetic susceptibility was measured in the range from 5 to 300 K for D1 and D2 (Figure 13). D1 shows a nearly constant $\chi_m T$ value from 300 to 80 K of about 3.1 emu mol⁻¹ K before it drops to $\chi_m T = 2$ emu mol⁻¹ K at 5 K due to the zero-field splitting (ZFS). In comparison to 1, D1 doesn't show any temperature-independent susceptibility. However, D2 shows a temperature-independent susceptibility (TIS) as well with a decrease from $\chi_m T = 3.9$ emu mol⁻¹ K at 300 K to 3.2 emu mol⁻¹ K at 80 K followed by a drop to 2.2 emu mol⁻¹ K at 5 K. The magnetic data of D2 were not fitted and therefore the TIS was not determined, but it is expected to be comparable to 1. Both values

of **D1** and **D2** are corresponding to the $[\text{Fe}^{\text{III}}\text{Co}^{\text{I}}\text{HS}]$ state^[25] agreeing with the coordination bond lengths from the crystal structures.

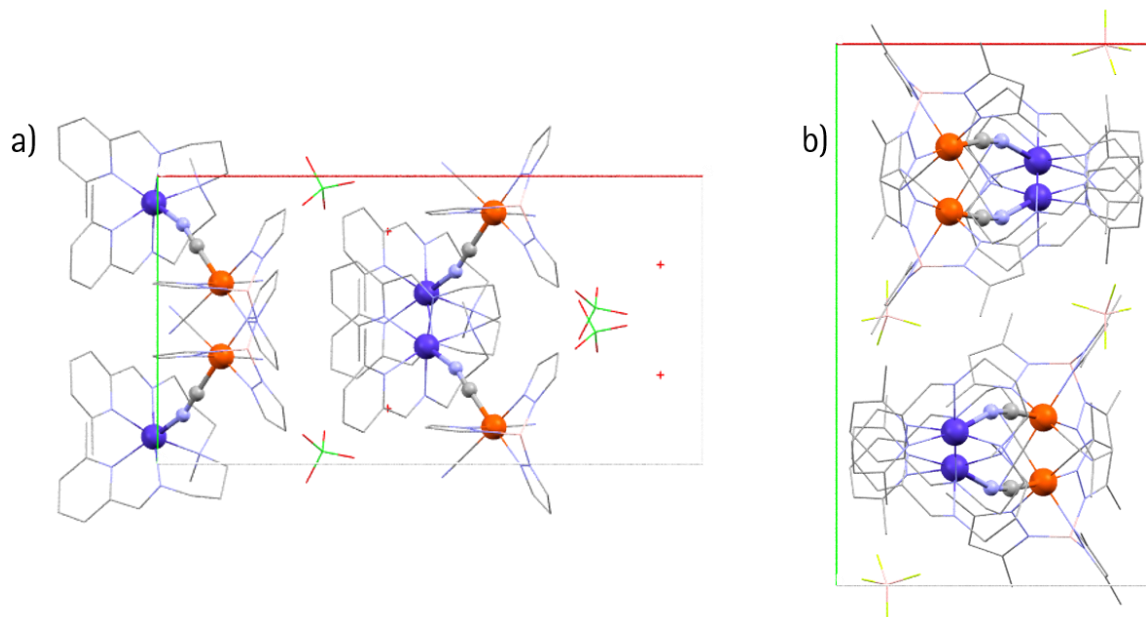


Figure 12: Unit cell of a) **D1** and b) **D2**, views along the c -axis. Hydrogen atoms have been omitted for clarity. Color code: C, gray; N, light blue; O, red; Co, dark blue; Fe, orange; B, pink; Cl, dark green; F, light green; a -axis, red line; b -axis, green line.

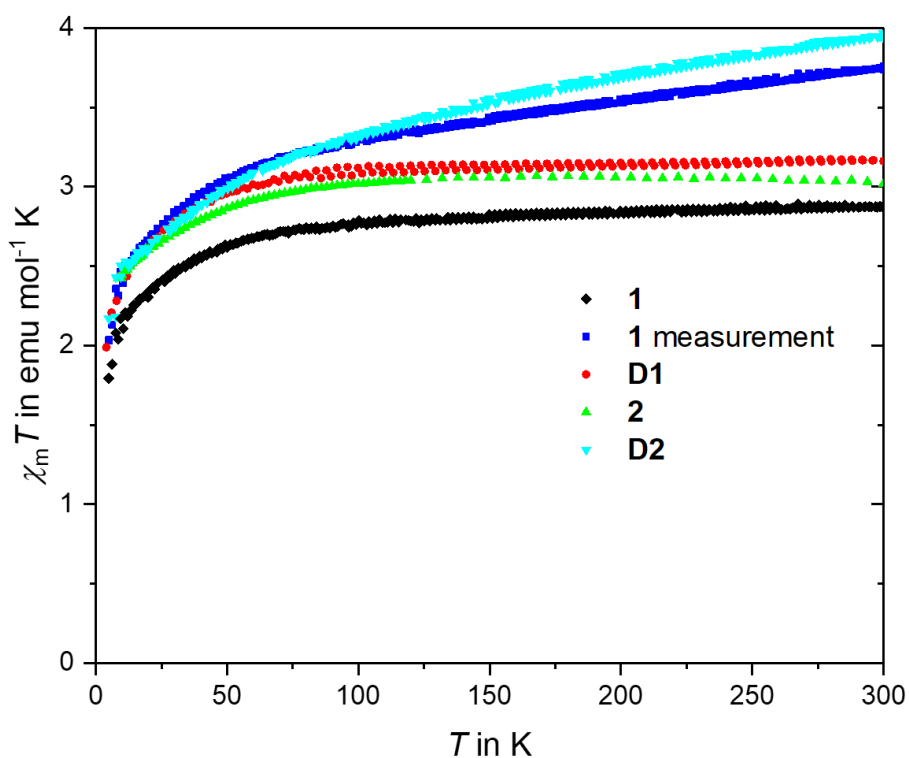


Figure 13: $\chi_m T - T$ plots of **1**, **D1**, **2** and **D2**. The blue dots (**1** measurement) are the $\chi_m T - T$ plot without the TIS.

Redox Potentials

The redox potential of **D2** was measured by cyclic voltammetry (Figure 14, Table 2). In comparison to the other cyclic voltammograms (CV) the redox waves are weaker due to a smaller concentration in the measurement solution. Four redox processes can be observed for **D2** that are comparable to **1** and **2**. The first redox process appears at -1.25 V, which can be assigned to the cobalt ligand as following described. For the two times positively charged precursor complex, two distinct reduction waves appear (-0.87 V and -1.12 V) before the oxidation waves and can therefore be assigned to the cobalt ligand instead of the Co(II) ion. This result stands in contrast to the publication of A. Panja who found only one quasi-reversible redox wave at higher potentials in methanol.^[72] Through the reaction to **D2**, the resulting complex carries only one positive charge and shows therefore only one redox process that can be assigned to the ligand. Due to the low concentration of **D2**, the redox process at 0.81 V, which is assigned to the $[\text{Fe}^{\text{III}}\text{Co}^{\text{II}}]/[\text{Fe}^{\text{III}}\text{Co}^{\text{III}}]$ redox pair, can hardly be recognized. The two redox processes at -0.17 V and -0.51 V are assigned to the $[\text{Fe}^{\text{III}}\text{Co}^{\text{II}}]/[\text{Fe}^{\text{II}}\text{Co}^{\text{II}}]$ redox couple and are shifted to the more negative region, compared to **1** and **2**, due to the electron pushing methyl groups at the iron ligand. While the wave at -0.51 V is assigned to **D2** according to **1** and **2**, the wave at -0.17 V might be caused by $[\text{FeCo}_2]$ or $[\text{FeCo}_3]$ complexes which might form in solution.

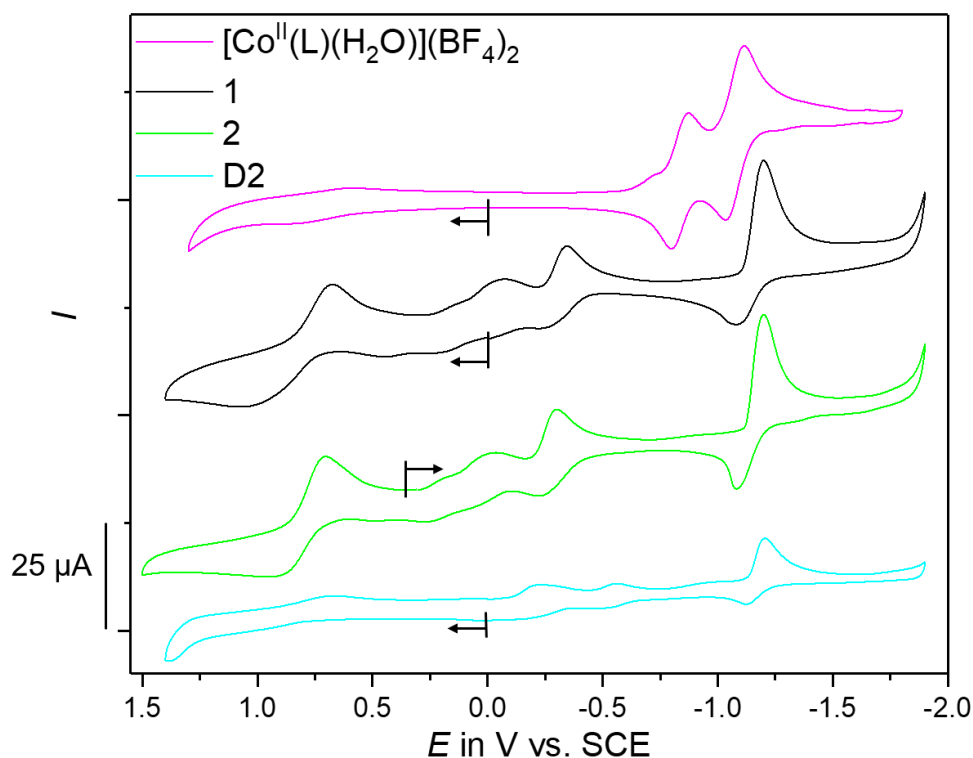


Figure 14: CV of $[\text{Co}(\text{L})(\text{H}_2\text{O})](\text{BF}_4)_2$, **1**, **2** and **D2**.

Table 2: Redox potentials of [Co(L)(H₂O)](BF₄)₂, 1, 2 and D2.

	E _{red}	E _{ox}	E _{1/2}
[CoL(H ₂ O)](BF ₄) ₂	-0.87 V	-0.80 V	-0.835 V
	-1.12 V	-1.03 V	-1.075 V
1	0.68 V	1.04 V	0.86 V
	-0.35 V	-0.24 V	-0.295 V
	-1.20 V	-1.08 V	-1.14 V
2	0.70 V	0.94 V	0.82 V
	-0.30 V	-0.23 V	-0.265 V
	-1.20	-1.08 V	-1.14 V
D2	0.66 V	~0.96 V	0.81 V
	-0.23 V	~ -0.11 V	-0.17 V
	-0.56 V	-0.46 V	-0.51 V
	-0.12 V	-0.13 V	-1.25 V

3.2.3 Conclusion and Outlook

Four new mixed-valence [Fe^{III}Co^{II}] complexes and one new [Fe^{II}₂] complex were synthesized and analyzed. 1, 2, D1, and D2 show a similar molecular structure with different packings. Noteworthy is the molecular orientation of the isostructural compounds 1 and D1 showing a predominant direction along the crystallographic a-axis. For ETCST compounds, this orientation is likely to result in an external stimuli induced electron transfer coupled polarization and is therefore highly interesting. Furthermore, the magnetic data for 1, 2, D1, and D2 suggest the paramagnetic [Fe^{III}_{1.5}Co^{II}_{1.5}] state for all four compounds in the temperature range of 300 K to 5 K, which is in agreement with the coordination bond lengths at 100 K. The differences of the [Fe^{III}Co^{II}]/[Fe^{III}Co^{III}] and [Fe^{III}Co^{II}]/[Fe^{II}Co^{II}] redox potentials are in the range of 1.085 V to 1.32 V and are therefore stabilizing the [Fe^{III}_{1.5}Co^{II}_{1.5}] state. To increase the chance for a dinuclear ETCST compound the redox potential gap must be reduced.^[15] This can be achieved by additional modifications of the ligands. The redox potential of the cobalt(II) ions can be shifted to smaller values by increasing its electron density through functional groups with +I and +M effects. On the other hand, the redox potential of the iron(III) ions need to be shifted to higher values through introducing functional groups with -I and -M effects or a completely new ligand design with remaining cyanides. Compound 3 is interesting as an ETCST building block for stabilizing Fe(II) at aerobic conditions. UV-Vis and CV measurements suggest that a mononuclear version of the dinuclear complex can exist in solution and therefore be used for further synthesis. To obtain a dinuclear ETCST compound the redox potential gap between Co and Fe before the reaction is supposed to be between 0.7 V and 0.9 V.^[15,25] Therefore, the Co(III)s or possibly Fe(III)s redox potential should be about 0 V.

4. Spin Crossover Building Blocks and its Derivatives

Chapter 4 is about mononuclear complexes with penta- N_3O_2 -dentate Schiff base ligands of which cyanide-bridged multinuclear complexes can be synthesized. In the first part, Chapter 4.1, the Full Paper *Structural, Magnetic and Electrochemical Characterization of Iron(III) and Cobalt Complexes with Penta- N_3O_2 -dentate Ligands* is presented, which was published with open access in 2021 in *European Journal of Inorganic Chemistry*. In Chapter 4.2 an angled trinuclear $[Co^{III}_2Co^{II}]$ complex and in the Chapters 4.3 two switchable pentanuclear complexes, $[Mo^VFe^{III}_4]$ and $[WCo_4]$, are presented.

During the last decade many mono- and multinuclear iron(III) and cobalt(III) complexes based on derivatives of the pentadentate Schiff base ligand N,N' -bis(2'-hydroxybenzylidene)-1,6-diamino-3-azahexane ($H_2salpet$, Figure 15) have been investigated. For the mononuclear compounds especially the influence of the substituents at the phenyl rings and of the monodentate ligands have been investigated. The aim was to gain a better understanding of how to control the spin state and SCO behavior of this complex system. However, the redox properties and the possibility of an ETCST have hardly been investigated.^[26–28,31–33,69–71,78,133–137] Therefore, in the following chapter the properties and especially the redox potentials of a series of mononuclear complexes with the general formula $[M(salpet_{R^1,R^2})X]$ (M : Fe^{III} or Co^{III} ; R^1 : H, Br; R^2 : H, Cl, Br, NO_2 ; X : Cl^- or pseudohalides) have been investigated. Furthermore, two trinuclear and two pentanuclear mixed-valence complexes have been synthesized and analyzed.

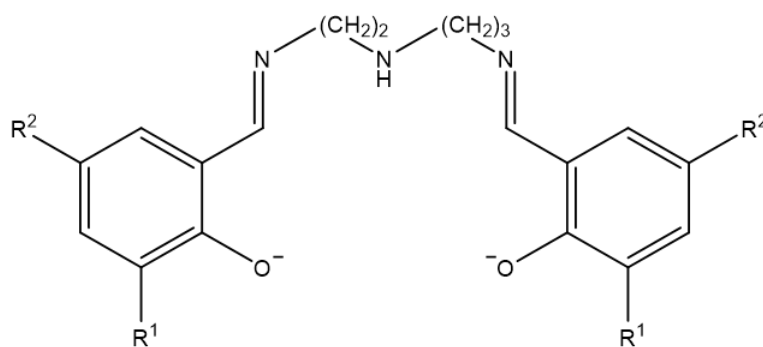


Figure 15: Pentadentate N_3O_2 Schiff base ligand ($salpet_{R^1,R^2}$) of the $Fe(III)$ and $Co(III)$ complexes. R^1 : H, Br; R^2 : H, Cl, Br, NO_2 .

All the experiments and analysis for the multinuclear compounds were performed by the author of this thesis. Furthermore, the author of this thesis synthesized most of the mononuclear complexes, performed the electrochemical analysis and wrote the initial manuscript for the publication. The mononuclear series $[Fe^{III}(salpet_{Br,Cl})X]$ presented in the publication in Chapter 4.1 was synthesized and analyzed by Annika Preiss. Haruka Yoshino supported the magnetic measurements for both trinuclear complexes. Prof. Roman Boca helped with the evaluation of the magnetic measurement of the

trinuclear compound in Chapter 4.1. Annika Preiss, Stephen Klimke, Dr. Takuya Shiga, Prof. Dr. Masaaki Ohba, Prof. Dr. Hiroki Oshio, and Prof. Dr. Franz Renz helped through discussions with the analysis and refined the manuscript.

The formatting of the following publication was adjusted to the formatting of this dissertation and the abbreviation of the ligand L was changed to salpet to avoid confusion with the compounds in Chapter 3. To the references, the letter T was added. However, the wording and content remained the same. Supporting information for this article are given in the Appendix Chapter 8.2 (page 140). The abbreviations, references as well as the labelling of figures and tables for the following publication and the corresponding supporting information are treated separately from the other chapters.

4.1 Structural, Magnetic and Electrochemical Characterization of Iron(III) and Cobalt(III) Complexes with Penta- N_3O_2 -dentate Ligands

Structural, Magnetic and Electrochemical Characterization of Iron(III) and Cobalt Complexes with Penta- N_3O_2 -dentate Ligands

Dominik Natke,^{*,[a],+} Annika Preiss,^{[a],+} Stephen Klimke,^[a] Takuya Shiga,^[b] Roman Boca,^[c,d] Masaaki Ohba,^[e] Hiroki Oshio,^[b,f] Franz Renz^{*,[a]}

[a] Mr. D. Natke, Mrs. A. Preiss, Mr. S. Klimke, Prof. Dr. F. Renz
Institute of Inorganic Chemistry
Leibniz University Hannover
Callinstraße 9, 30167 Hannover, Germany

* E-mail: dominik.natke@acd.uni-hannover.de, franz.renz@acd.uni-hannover.de

[b] Dr. T. Shiga, Prof. Dr. H. Oshio
Graduate School of Pure and Applied Sciences
University of Tsukuba
Tennodai, Tsukuba, Ibaraki 305-8577, Japan

[c] Prof. Dr. R. Boca
Institute of Inorganic Chemistry
Slovak University of Technology
Bratislava SK-81237, Slovakia

[d] Prof. Dr. R. Boca
Department of Chemistry (FPV)
University of SS Cyril and Methodius
91701 Trnava, Slovakia

[e] Prof. Dr. M. Ohba
Department of Chemistry
Faculty of Science, Kyushu University
744 Motoooka, Nishi-ku, Fukuoka 819-0395, Japan

[f] Prof. Dr. H. Oshio
State Key Laboratory of Fine Chemicals
Dalian University of Technology
2 Linggong Rd., 116024 Dalian, China

+ Authors contributed equally
European Journal of Inorganic Chemistry, 2021, 15, 1498-1504

Abstract: Six new mononuclear $[\text{Fe}^{\text{III}}(\text{salpet}_{\text{Br,Cl}})\text{X}]$ -complexes ($\text{salpet}_{\text{Br,Cl}}$ is the dianionic penta- N_3O_2 -dentate Schiff base ligand *N,N*-bis(2'-hydroxy-3-bromo-5-chlorobenzylidene)-1,6-diamino-3-azahexane; X: Cl^- , N_3^- , NCO^- , NCS^- , NCSe^- , CN^-) were synthesized and their structures, magnetic and electrochemical properties studied. Structure analysis and magnetic measurements showed that $[\text{Fe}^{\text{III}}(\text{salpet}_{\text{Br,Cl}})\text{CN}]$ is in the low spin state and the other five complexes are in high spin states. Furthermore, the trinuclear mixed valent cobalt complex $\{[\text{Co}^{\text{III}}(\text{salpet}_{\text{H,H}})\text{CN}]_2[\text{Co}^{\text{II}}(1\text{-methylimidazole})_3(\text{H}_2\text{O})]\}$ was prepared and its magnetic behavior studied.

Introduction

The trend of reducing the size of electronic components in technological applications lead to recent developments in the field of intelligent molecular devices. Coordination compounds, showing switching behavior, are promising candidates to be used in applications such as quantum devices, high density data storages and sensors.^[T1-T5] Bistable complexes with at least two thermodynamically stable electronic states or phases are therefore of increasing interest because of their reversible changes of optical, magnetic and electronic properties by external stimuli such as light, temperature, pressure, X-rays or guest absorption/desorption.^[T6-T11] These properties can be adjusted by proper molecular design and controlled assemblies of supramolecular networks.^[T12-T15]

Complexes with Schiff base ligands have the advantages of mostly simple syntheses and chemical modifications are easily possible.^[T16-T20] One example is the series of $[\text{M}^{\text{III}}(\text{salpet}_{\text{R}_1,\text{R}_2})\text{X}]$ complexes (M: Co or Fe; salpet : *N,N*-bis(2'-hydroxybenzylidene)-1,6-diamino-3-azahexane; X: pseudo halide or organic molecule) which was studied extensively in the past (Figure 1).^[T21-T27] The Co(III) complexes are in low spin (LS) states,^[T27] whereas some Fe(III) complexes showed temperature induced reversible conversions between LS and high spin (HS) states, called spin crossover (SCO).^[T21-T26,T28,T29] The spin state and SCO properties of these iron(III) complexes can be changed by introducing substituents to the Schiff base ligand and by exchanging the monodentate ligand. Especially the complexes $[\text{Fe}^{\text{III}}(\text{salpet}_{\text{H,Cl}})\text{X}]$,^[T22] $[\text{Fe}^{\text{III}}(\text{salpet}_{\text{H,Br}})\text{X}]$ ^[T24] and $[\text{Fe}^{\text{III}}(\text{salpet}_{\text{Cl,Cl}})\text{X}]$ ^[T29] (X = N_3^- , NCS^- , NCSe^-) should be mentioned, which show a temperature induced SCO, whereas the compounds $[\text{Fe}^{\text{III}}(\text{salpet}_{\text{Br,Br}})\text{X}]$ ^[T29] are only in the HS state. Complexes with X = CN^- are always in the LS state,^[T21,T22,T30] but some cyanide-bridged multinuclear complexes such as $[\text{Fe}^{\text{II}}(\text{CN})_6\{\text{Fe}(\text{salpet}_{\text{H,H}})\}_6]\text{Cl}_2$ were reported to show SCO.^[T30-T33] Moreover, these compounds belong to the class of PBAs and are not only interesting because of their SCO properties but they may show an electron transfer-coupled spin transition (ETCST).^[T34-T36] The electron transfer occurs between two metal sites within a cyanide-bridged redox pair such as $[\text{Co}^{\text{II}}\text{HSFe}^{\text{III}}\text{LS}]$ and $[\text{Co}^{\text{III}}\text{LSFe}^{\text{II}}\text{LS}]$.^[T35,T37-T40] Occurrence of the ETCST needs proper matching of the redox properties, which can be controlled by modifying the precursors, such as substituents of the capping

ligands,^[T39-T41] which is described in detail by M. Nihei for known building blocks.^[T42] However, so far no complex with a $[M(\text{salpet}_{R_1R_2})]^+$ -building block have been proven to show the ETCST behavior. Furthermore, the redox properties of only a few complexes with $\text{salpet}_{R_1R_2}$ have been reported yet.^[T27,T30-T33,T43,T44]

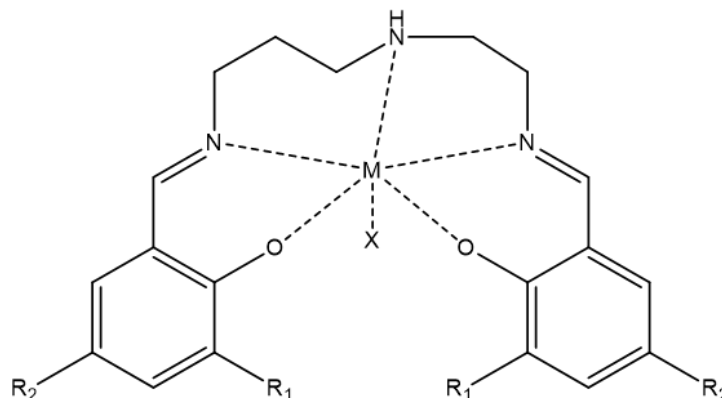


Figure 1: Mononuclear complex $[M(\text{salpet}_{R_1,R_2})X]$ with M for Co(III) or Fe(III), R_1 , R_2 for different substituents (e.g. R_1 : Br, R_2 : Cl) and X for pseudo halides or organic molecules.

Herein we report a series of six new $[\text{Fe}(\text{salpet}_{Br,Cl})X]$ (X : Cl^- , N_3^- , NCO^- , NCS^- , $\text{NCS}e^-$, NC^-) complexes. In extension to the previously reported complexes $[\text{Fe}^{\text{III}}(\text{salpet}_{Cl,Cl})X]$ and $[\text{Fe}^{\text{III}}(\text{salpet}_{Br,Br})X]$,^[T29] which show SCO and HS behavior, respectively, the temperature-depending magnetic behavior of the six new complexes was analyzed. In order to use $[M^{\text{III}}(\text{salpet}_{R_1,R_2})X]$ building blocks for designing ETCST complexes, we analyzed the redox properties of the $[\text{Fe}(\text{salpet}_{Br,Cl})X]$ complexes and of different derivatives.^[T22,T24,T25,T30] Thereby we determined a range of redox potentials that can be accessed by exchanging the substituents R_1 and R_2 with hydrogen and NO_2 . The hydrogen is neutral, while NO_2 is expected to show strong $-M$ (mesomeric) and $-I$ (inductive) effects resulting in a decreased electron density at the Fe ion. Furthermore, we prepared the trinuclear mixed valence compound $[\text{Co}^{\text{III}}(\text{salpet}_{H,H})\text{CN}]_2[\text{Co}^{\text{II}}(1\text{-methylimidazole})_3] \cdot 1.5 \text{ H}_2\text{O}$ ($[\text{Co}_2\text{Co}]$) from the mononuclear precursor complex $[\text{Co}(\text{salpet}_{H,H})\text{CN}]$ and analyzed its structure and magnetic behavior.

Results and Discussion

Structural Data

The crystallographic and structural data are summarized in Table 1. Metal ions in the six $[\text{Fe}(\text{salpet}_{Br,Cl})X]$ (Figure 2) and the $[\text{Co}(\text{salpet}_{H,H})\text{CN}]$ (Figure 3) complexes are octahedrally coordinated and the compounds $[\text{Fe}(\text{salpet}_{Br,Cl})\text{NCS}]$ and $[\text{Fe}(\text{salpet}_{Br,Cl})\text{NCS}e]$ are isostructural to each other. This six coordination sites of the Fe(III)/Co(III) ions are occupied by three nitrogen and two oxygen atoms and a monodentate halogen or pseudo halogen ligand. The three nitrogen atoms are coordinated in *fac* and the two oxygen in *cis* position. The mononuclear complex is overall neutral due to the two deprotonated

hydroxyl groups at $\text{salpet}_{R1,R2}$ and the negatively charged monodentate ligand. While the complexes can exist in two different enantiomers, all the samples crystallized as racemic mixture in the monoclinic non chiral space group $P2_1/c$. Furthermore, the six structures are showing slightly offset π - π stacking with centroid-centroid distances between 3.58 Å and 4.43 Å of the phenyl rings (Table S1). Most distances are comparable to those described for similar complexes,^[T22,T24] except for $[\text{Fe}(\text{salpet}_{Br,Cl})\text{NCO}]$ whose stacking distance is unusual small with 3.58 Å. The structure of $[\text{Co}(\text{salpet}_{H,H})\text{CN}]$ is similar to its precursor $[\text{Co}(\text{salpet}_{H,H})\text{Cl}]$ ^[T27] and both form a chain structure with hydrogen bonded water molecules (Figure 3). Crystals of the trinuclear complex $[\text{Co}_2\text{Co}]$ (Figure 4 a) grow in the $P2_1/n$ space group. In the trinuclear complex the two $[\text{Co}(\text{salpet}_{H,H})\text{CN}]$ and the central $[\text{Co}^{\text{II}}(1\text{-methylimidazole})_3]^{2+}$ form a cyanide-bridged linear structure. Note that three coordination sites of the centered Co(II) are coordinated by 1-methylimidazole. The fourth ligand is considered to be a strongly disordered water molecule which could not be modeled correctly. Therefore, its electron density was treated by the Olex 2 solvent mask^[T45] (BYPASS^[T46]). The void (Figure 4 b) is considered to be filled with 1.5 water molecules per asymmetric unit which correspond to 15 electrons with 14 found and is supported by the elemental analysis. Therefore, three water molecules are located between two neighboring complexes with a Co(II)-Co(II) distance of 9.191(2) Å, which suits the distance for a Co-H₂O-H₂O-H₂O-Co bridge (Figure S3). The angles between the Co(II) ligands match with a distorted octahedral coordination sphere (Table S2) as expected by the VSEPR concept.^[T47,T48] Additionally, the two charge balancing $[\text{BF}_4]^-$ anions do not occupy this coordination site (Figure S4).

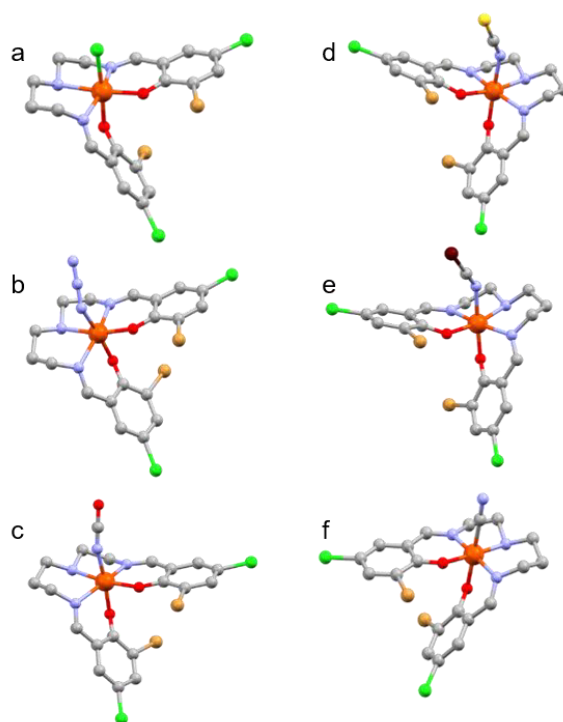


Figure 2: Molecular structure of a: $[\text{Fe}(\text{salpet}_{Br,Cl})\text{Cl}]$; b: $[\text{Fe}(\text{salpet}_{Br,Cl})\text{N}_3]$; c: $[\text{Fe}(\text{salpet}_{Br,Cl})\text{NCO}]$; d: $[\text{Fe}(\text{salpet}_{Br,Cl})\text{NCS}]$; e: $[\text{Fe}(\text{salpet}_{Br,Cl})\text{NCS}]$; f: $[\text{Fe}(\text{salpet}_{Br,Cl})\text{CN}]$. Hydrogen atoms have been omitted for clarity. Color code: C, gray; N, light blue; O, red; Fe, orange; Cl, green; Br, light brown; S, yellow; Se, brown red.

Bond length (Table S3) of $[\text{Fe}(\text{salpet}_{\text{Br,Cl}})\text{CN}]$ are characteristic for a Fe(III) in the LS state, while the bond length of the other five Fe(III) complexes are indicating a HS state.^[T22,T24,T30] The Co(III) ions bond lengths in $[\text{Co}(\text{salpet}_{\text{H,H}})\text{CN}]$ and $[\text{Co}_2\text{Co}]$ are typically for the LS state. Moreover, the bond lengths of the Co(II) ion are typically for a octahedral coordinated Co(II) in the HS state.^[T37,T40]

Table1: Crystallographic and structural data.

	$[\text{Fe}(\text{salpet}_{\text{Br,Cl}})\text{Cl}]$	$[\text{Fe}(\text{salpet}_{\text{Br,Cl}})\text{N}_3]$
	$\text{C}_{19}\text{H}_{17}\text{Br}_2\text{Cl}_3\text{FeN}_3\text{O}_2$	$\text{C}_{19}\text{H}_{17}\text{Br}_2\text{Cl}_2\text{FeN}_6\text{O}_2$
<i>T</i> in K	100	100
Crystal System	monoclinic	monoclinic
Space group	$P2_1/c$	$P2_1/c$
<i>a</i> in Å	9.410(2)	12.1339(12)
<i>b</i> in Å	9.496(2)	12.4927(13)
<i>c</i> in Å	25.951(5)	15.2751(16)
α, γ in °	90	90
β in °	93.51(3)	104.735(1)
<i>V</i> in Å ³	2314.7(8)	2239.3(4)
<i>Z</i>	4	4
R_1/wR_2 ($I > 2\sigma$)	0.0416/0.1175	0.0210/0.0529
	$[\text{Fe}(\text{salpet}_{\text{Br,Cl}})\text{NCO}]$	$[\text{Fe}(\text{salpet}_{\text{Br,Cl}})\text{NCS}]$
	$\text{C}_{20}\text{H}_{17}\text{Br}_2\text{Cl}_2\text{FeN}_4\text{O}_3$	$\text{C}_{20}\text{H}_{17}\text{Br}_2\text{Cl}_2\text{FeN}_4\text{O}_2\text{S}$
<i>T</i> in K	233	233
Crystal System	monoclinic	monoclinic
Space group	$P2_1/c$	$P2_1/c$
<i>a</i> in Å	9.5265(1)	8.4762(1)
<i>b</i> in Å	15.0275(1)	24.0299(2)
<i>c</i> in Å	16.5494(1)	12.2342(1)
α, γ in °	90	90
β in °	106.15	106.26
<i>V</i> in Å ³	2275.71(3)	2392.25(4)
<i>Z</i>	4	4
R_1/wR_2 ($I > 2\sigma$)	0.0373/0.0988	0.0346/0.0946

4. Derivatives of Spin Crossover Complexes as Building Blocks

Table 1: Crystallographic and structural data (continued).

	[Fe(salpet _{Br,Cl})NCSe]	[Fe(salpet _{Br,Cl})CN]
	C ₂₀ H ₁₇ Br ₂ Cl ₂ FeN ₄ O ₂ Se	C ₂₀ H ₁₇ Br ₂ Cl ₂ FeN ₄ O ₂
<i>T</i> in K	100	100
Crystal System	monoclinic	monoclinic
Space group	<i>P</i> ₂ ₁ / <i>c</i>	<i>P</i> ₂ ₁ / <i>c</i>
<i>A</i> in Å	8.3923(5)	8.1885(11)
<i>b</i> in Å	24.2183(16)	11.1909(15)
<i>c</i> in Å	12.2306(8)	24.353(3)
α, γ in °	90	90
β in °	106.571(1)	95.835(2)
<i>V</i> in Å ³	2382.6(3)	2220.1(5)
<i>Z</i>	4	4
<i>R</i> ₁ / <i>wR</i> ₂ (<i>I</i> > 2σ <i>I</i>)	0.0289/0.0742	0.0485/0.1089
	[Co(salpet _{H,H})CN]	[Co ₂ Co]
	C ₂₀ H ₂₃ CoN ₄ O ₃	C ₅₂ H ₆₃ Co ₃ N ₁₄ O _{5.5} B ₂ F ₈
<i>T</i> in K	100	100
Crystal System	monoclinic	monoclinic
Space group	<i>P</i> ₂ ₁ / <i>c</i>	<i>P</i> ₂ ₁ / <i>n</i>
<i>a</i> in Å	9.2557(11)	17.701(3)
<i>b</i> in Å	12.2576(15)	13.489(2)
<i>c</i> in Å	17.361(2)	24.558(4)
α, γ in °	90	90
β in °	101.523(2)	101.564(2)
<i>V</i> in Å ³	1929.9(4)	5744.7(17)
<i>Z</i>	4	4
<i>R</i> ₁ / <i>wR</i> ₂ (<i>I</i> > 2σ <i>I</i>)	0.0331/0.0824	0.0806/0.2228

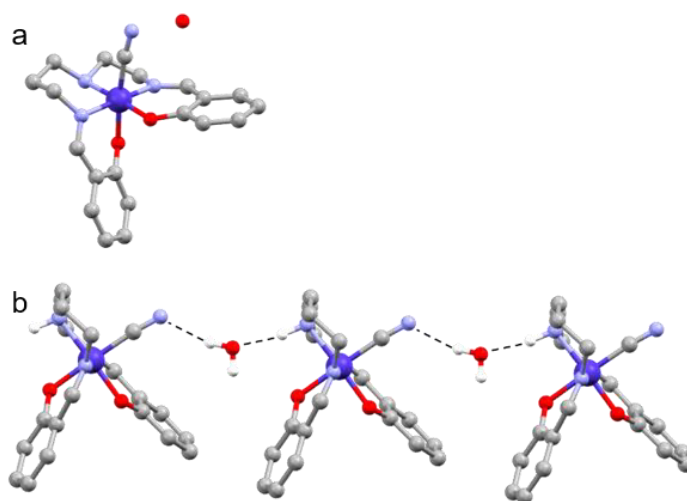


Figure 3: a: Molecular structure of $[\text{Co}(\text{salpet}_{\text{H,H}})\text{CN}]$. b: Hydrogen bonding network of $[\text{Co}(\text{salpet}_{\text{H,H}})\text{CN}]$. Most hydrogen atoms have been omitted for clarity. Color code: C, gray; N, light blue; O, red; Co, dark blue.

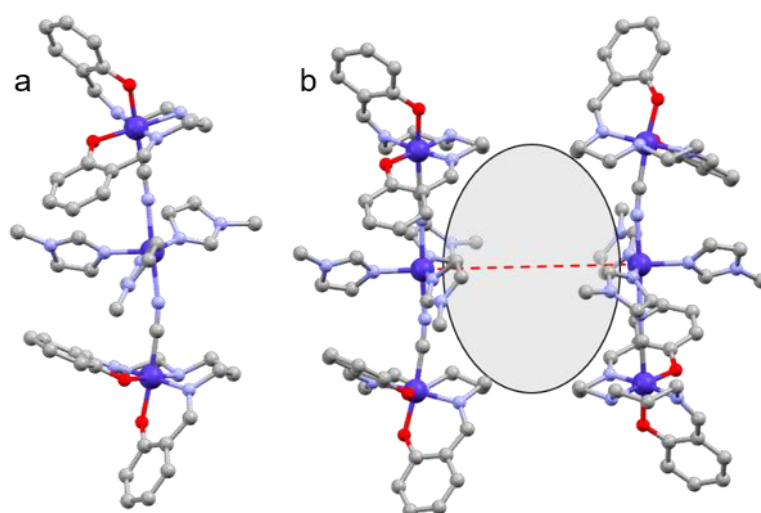


Figure 4: a: Molecular structure of $[\text{Co}_2\text{Co}]$. b: Void between two $[\text{Co}_2\text{Co}]$. Hydrogen atoms and counter anions have been omitted for clarity. Color code: C, gray; N, light blue; O, red; Co, dark blue.

Magnetic Data

Temperature dependences of magnetic data were measured for all compounds except $[\text{Co}(\text{salpet}_{\text{H,H}})\text{CN}]$ in the range of 5 – 300 K (Figure 5 a). The $\chi_m T$ values for the six Fe(III) show similar behavior as expected for HS and LS states. For the low temperature range magnetic anisotropy might be the origin, as expected for zero-field splitting (ZFS). $[\text{Fe}(\text{salpet}_{\text{Br,C}})\text{CN}]$ shows a $\chi_m T$ value of 0.28 $\text{emu mol}^{-1} \text{K}$ which is typically for a Fe(III) in the LS state^[T22,T30] with a slightly reduced g factor. The other five Fe(III) complexes showed $\chi_m T$ values of 4.0 – 4.4 $\text{emu mol}^{-1} \text{K}$ which are characteristic for Fe(III) complexes in HS state^[T21,T22,T24,T25,T30] and the results agree with the coordination bond length. Moreover, $[\text{Fe}(\text{salpet}_{\text{Br,C}})\text{NCO}]$ showed weak intermolecular ferromagnetic interactions below 20 K which might be caused through a stronger π - π stacking compared to the other five complexes. Unlike the compound $[\text{Fe}^{\text{III}}(\text{salpet}_{\text{Cl,C}})\text{NCSe}]$, which shows SCO with a broad thermal hysteresis, this series of complexes only

4. Derivatives of Spin Crossover Complexes as Building Blocks

shows one spin state. The $\chi_m T$ value for $[\text{Co}_2\text{Co}]$ is at 300 K 2.81 $\text{emu mol}^{-1} \text{K}$ which is consistent with an insulated $S = 3/2$ spin system with enlarged $g_{\text{av}} > g_e$ of the two LS-Co(III) and HS-Co(II).^[T49-T52] These values are slightly decreasing as the temperature lowers until ~ 100 K, followed by a gradual decrease of $\chi_m T$ which is typical for Co(II) systems with large ZFS. Details of the fitted magnetic data of $[\text{Co}_2\text{Co}]$ (Figure 5 b) are summarized in the supporting information (Table S4).

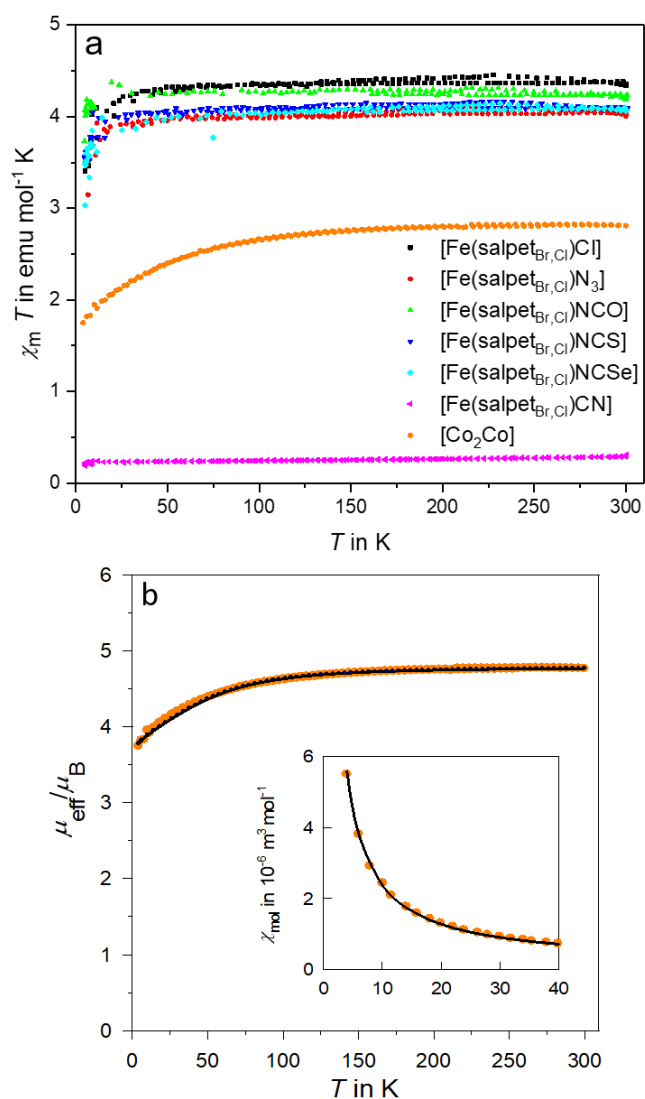


Figure 5: a: $\chi_m T - T$ plots of $[\text{Fe}(\text{salpet}_{\text{Br,Ci}})\text{X}]$ and $[\text{Co}_2\text{Co}]$. b: $\mu_{\text{eff}}/\mu_B - T$ and $\chi_m - T$ plot and fit of $[\text{Co}_2\text{Co}]$.

Electrochemical Data

The cyclic voltametric (CV) measurements of the six $[\text{Fe}(\text{salpet}_{\text{Br,Ci}})\text{X}]$ complexes and previously reported five $[\text{Fe}(\text{salpet}_{\text{H,R2}})\text{Cl/CN}]$ complexes showed quasi-reversible redox waves of $[\text{Fe}^{\text{III}}/\text{Fe}^{\text{II}}]$ processes. The redox potentials are summarized in Table 2. Note that no redox wave was observed for $[\text{Co}_2\text{Co}]$. Moreover, the second reduction wave of $[\text{Fe}(\text{salpet}_{\text{Br,Ci}})\text{NCSe}]$ might be caused by a partial solvent exchange of the monodentate ligand.

The redox potentials of the $[\text{Fe}(\text{salpet}_{\text{R1,R2}})\text{Cl}/\text{CN}]$ systems (Figure 6) show a clear trend for varying the phenyl substituents (R1,R2). By introducing electron withdrawing groups, $-\text{NO}_2$ (- I, - M), $-\text{Cl}$ and $-\text{Br}$ (- I), $E_{1/2}$ is shifted to higher values. The redox potential shift for the chloride compounds $\Delta E_{1/2}(E_{1/2}[\text{Fe}(\text{salpet}_{\text{H,H}})\text{Cl}] - E_{1/2}[\text{Fe}(\text{salpet}_{\text{R1,R2}})\text{Cl}])$ is -0.105 V for $[\text{Fe}(\text{salpet}_{\text{H,NO}_2})\text{Cl}]$ and -0.075 V for $[\text{Fe}(\text{salpet}_{\text{Br,Cl}})\text{Cl}]$. For the cyanide complexes the $\Delta E_{1/2}$ value of $E_{1/2}[\text{Fe}(\text{salpet}_{\text{H,H}})\text{CN}] - E_{1/2}[\text{Fe}(\text{salpet}_{\text{R1,R2}})\text{CN}]$ is about -0.05 V for $[\text{Fe}(\text{salpet}_{\text{H,Cl/Br}})\text{CN}]$, but for $[\text{Fe}(\text{salpet}_{\text{Br,Cl}})\text{CN}]$ with -0.145 V nearly twice of the shifts expected from Chloride complexes. Therefore, the redox potential of complexes with the general formula $[\text{Fe}(\text{salpet}_{\text{R1,R2}})\text{X}]$ cannot simply be calculated by increments suggested by Lever et al. for other coordination compounds.^[T53-T55] Furthermore, these redox potentials are in the range of typical Fe(III) precursors for $[\text{FeCo}]$ ETCST complexes which are between -0.45 V and -1.00 V vs. SCE.^[T39-T42]

Table 2: Redox potentials vs SCE of the mononuclear $[\text{Fe}(\text{salpet}_{\text{R1,R2}})\text{X}]$ compounds.

	E_{red}	E_{ox}	$E_{1/2}$
$[\text{Fe}(\text{salpet}_{\text{H,H}})\text{Cl}]$	-0.41 V	-0.32 V	-0.365 V
$[\text{Fe}(\text{salpet}_{\text{H,NO}_2})\text{Cl}]$	-0.31 V	-0.21 V	-0.26 V
$[\text{Fe}(\text{salpet}_{\text{Br,Cl}})\text{Cl}]$	-0.36 V	-0.22 V	-0.29 V
$[\text{Fe}(\text{salpet}_{\text{Br,Cl}})\text{NCS}]$	-0.22 V	-0.14 V	-0.18 V
$[\text{Fe}(\text{salpet}_{\text{Br,Cl}})\text{NCSe}]$	$-0.25/-0.35$ V	-0.17 V	-0.21 V/ -0.26 V
$[\text{Fe}(\text{salpet}_{\text{Br,Cl}})\text{N}_3]$	-0.4 V	-0.24 V	-0.32 V
$[\text{Fe}(\text{salpet}_{\text{Br,Cl}})\text{NCO}]$	-0.48 V	-0.28 V	-0.38 V
$[\text{Fe}(\text{salpet}_{\text{Br,Cl}})\text{CN}]$	-0.59 V	-0.52 V	-0.555 V
$[\text{Fe}(\text{salpet}_{\text{H,H}})\text{CN}]$	-0.75 V	-0.65 V	-0.70 V
$[\text{Fe}(\text{salpet}_{\text{H,Cl}})\text{CN}]$	-0.69 V	-0.61 V	-0.65 V
$[\text{Fe}(\text{salpet}_{\text{H,Br}})\text{CN}]$	-0.70 V	-0.61 V	-0.655 V

The $[\text{Fe}(\text{salpet}_{\text{Br,Cl}})\text{X}]$ complexes show the following trend, depending on their monodentate ligands in the order of decreasing redox potentials: $\text{NCS} \rightarrow \text{NCSe} \rightarrow \text{Cl} \rightarrow \text{N}_3 \rightarrow \text{NCO} \rightarrow \text{NC}^-$. The found order differs from the expected order found in the literature which depends on the π -backbonding abilities of the monodentate ligand: $\text{N}_3 \rightarrow \text{NCO} \rightarrow \text{Cl} \rightarrow \text{NCSe} \rightarrow \text{NCS} \rightarrow \text{NC}^-$, by the increment method of Lever et al.^[T53-T55] These results suggest that Lever's model is inapplicable for $[\text{Fe}(\text{salpet}_{\text{R1,R2}})\text{X}]$ complexes, likely because of its high generality,^[T55] ignoring the structural distortions and other inter- and intramolecular interactions. This needs to be further investigated and serves as a hint for an extension of Lever's model.

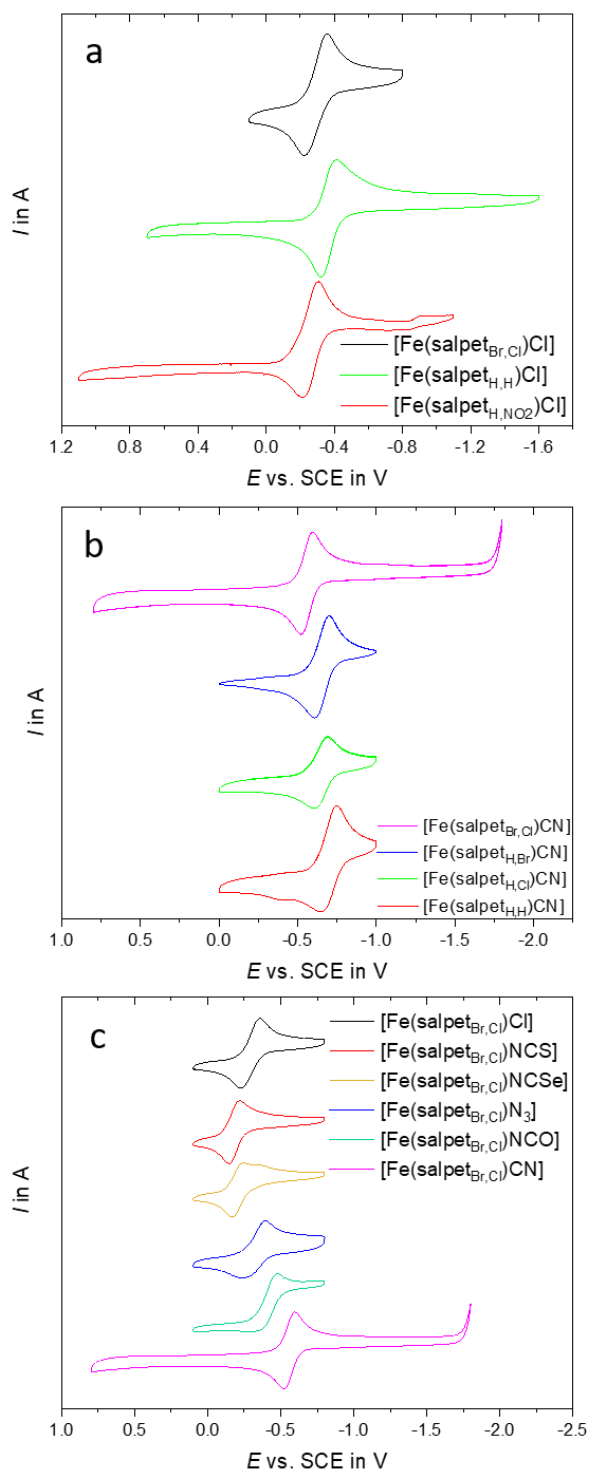


Figure 6: Cyclic voltammogram of different $[\text{Fe}(\text{salpet}_{R1,R2})\text{X}]$ complexes. a: Three $[\text{Fe}(\text{salpet}_{R1,R2})\text{Cl}]$ complexes. b: Four $[\text{Fe}(\text{salpet}_{R1,R2})\text{CN}]$ complexes. c: All six $[\text{Fe}(\text{salpet}_{Br,C})\text{X}]$ complexes.

Conclusion

A series of six new Fe(III) complexes $[\text{Fe}(\text{salpet}_{Br,C})\text{X}]$ (X: Cl^- , N_3^- , NCO^- , NCS^- , NCSe^- , NC^-) was studied. All mononuclear complexes crystallized in the $P2_1/c$ space group. Magnetic measurements agreed with the structural data that the monodentate cyanide ligand leads to the LS state while the other five

complexes are in the HS state. The electrochemical investigation indicates a one electron redox process with $E_{1/2}$ values between -0.18 V and -0.555 V. Additionally, the redox properties of previously reported [Fe(salpet_{R1,R2})Cl/CN] complexes have been investigated as well. The $E_{1/2}$ values of our reported complexes are in the range of typical ETCST precursors. However, all our attempts to synthesize mixed valance multinuclear complexes, starting from [Fe(salpet_{R1,R2})CN], did not succeed, nor to the best of our knowledge, such a compound is reported yet. Instead we yielded previously {[Fe^{III}(salpet_{H,H})]₂CN}.^[T30-T33,T43,T44] However, bridging cyanide containing compound e.g. [Fe^{II}(CN)₆]⁴⁻ to [Fe(salpet_{R1,R2})Cl] or using [Co(salpet_{R1,R2})CN] can result in multinuclear cyanide-bridged complexes^[T31-T33] and are promising for tunable switching compounds. Therefore, [Co(salpet_{H,H})CN] instead of [Fe(salpet_{R1,R2})CN] was used with Co(II) and 1-methylimidazole to synthesize the trinuclear mixed valence complex [Co₂Co]. The crystal structure and magnetic data of [Co₂Co] correspond to two LS-Co(III) species and one HS-Co(II) as only paramagnetic metal ion in this complex.

Previous results showed the tunability of spin states and SCO properties using the [M^{III}(salpet_{R1,R2})X] system.^[T22,T24,T25,T30,T31] This results reveal that also the redox potentials are tunable upon substitution of the Schiff base ligands and that the tuneability might be useful to design switchable molecules.

Experimental Section

All chemicals were purchased from commercial suppliers and used without further purification. The mononuclear complexes for CV were synthesized according to literature methods.^[T22,T24,T25,T27,T30] The synthesis of the other mononuclear complexes was slightly modified.

[Fe^{II}(salpet_{Br,Cl})Cl]:

A solution of 3-bromo-5-chlorosalicylaldehyde (10.6 mmol) in 60 ml methanol was combined with N-(2-aminoethyl)-1,3-propanediamine (5.3 mmol). The yellow solution was refluxed for 30 min. The precursor complex was synthesized in situ by the addition of FeCl₃·6H₂O (5.3 mmol) dissolved in 10 mL methanol and triethylamine (10.6 mmol) resulting in a dark red solution. After stirring the solution for 60 min at their boiling temperature, it was cooled to -37 °C for 24 h. The resulting black crystals were filtered off and washed with cold methanol. Single crystals were obtained by slow evaporation of the solvent. C₁₉H₁₇Br₂Cl₃FeN₃O₂: $M = 641.37 \text{ g mol}^{-1}$; found % (calcd. %) C 35.73 (35.58), H 2.54 (2.67), N 6.46 (6.55); ESI-MS m/z calc. for C₁₉H₁₇Br₂Cl₂N₃O₂Fe⁺: 602.8409, found 602.8420; IR (KBr; cm⁻¹): 3260 (N-H); 3048 (C-H_{arom}); 2935 (C-H_{alif}); 1637, 1612 (C=N).

General synthesis of [Fe^{III}(salpet_{Br,Cl})X] (X: N₃⁻, NCO⁻, NCS⁻, NCSe⁻, NC⁻):

The mononuclear complex [Fe^{III}(salpet_{Br,Cl})Cl] (0.3 mmol) was dissolved in 150 ml methanol. The solution was combined with a solution of NaN₃, KOCN, KSCN, KSeCN or KCN (0.3 mmol) in 2 ml methanol, respectively. After filtration, single crystals were obtained by slow evaporation of the solvent.

[Fe^{III}(salpet_{Br,Cl})N₃]:

C₁₉H₁₇Br₂Cl₂FeN₆O₂: *M* = 647.94 g mol⁻¹; found % (calcd. %): C 34.96 (35.22), H 2.46 (2.64), N 12.58 (12.97); ESI-MS *m/z* calc. for C₁₉H₁₇Br₂Cl₂N₃O₂Fe⁺: 602.8414, found 602.8414; IR (KBr; cm⁻¹): 3244 (N-H); 3057 (C-H_{arom}); 2932 (C-H_{alif}); 2083, 2066 (N=N); 1632, 1612 (C=N).

[Fe^{III}(salpet_{Br,Cl})NCO]:

C₂₀H₁₇Br₂Cl₂FeN₄O₃: *M* = 647.93 g mol⁻¹; found % (calcd. %): C 37.12 (37.07), H 2.35 (2.64), N 8.57 (8.65). ESI-MS *m/z* calc. for C₁₉H₁₇Br₂Cl₂N₃O₂Fe⁺: 602.8414, found 602.8414; IR (KBr; cm⁻¹): 3271 (N-H); 3069 (C-H_{arom}); 2934 (C-H_{alif}); 2207 (C≡N); 1637, 1612 (C=N).

[Fe^{III}(salpet_{Br,Cl})NCS]:

C₂₀H₁₇Br₂Cl₂FeN₄O₂S: *M* = 664.00 g mol⁻¹; found % (calcd. %): C 36.10 (36.18), H 2.35 (2.58), N 8.40 (8.44); ESI-MS *m/z* calc. for C₁₉H₁₇Br₂Cl₂N₃O₂Fe⁺: 602.8414, found 602.8403; IR (KBr; cm⁻¹): 3264 (N-H); 3053 (C-H_{arom}); 2934 (C-H_{alif}); 2039 (C≡N); 1638, 1619 (C=N).

[Fe^{III}(salpet_{Br,Cl})NCSe]:

C₂₀H₁₇Br₂Cl₂FeN₄O₂Se: *M* = 711.00 g mol⁻¹; found % (calcd. %): C 33.94 (33.79), H 2.20 (2.41), N 7.81 (7.88); ESI-MS *m/z* calc. for C₁₉H₁₇Br₂Cl₂N₃O₂Fe⁺: 602.8414, found 602.8422. IR (KBr; cm⁻¹): 3264 (N-H); 3049 (C-H_{arom}); 2934 (C-H_{alif}); 2043 (C≡N); 1638, 1618 (C=N).

[Fe^{III}(salpet_{Br,Cl})CN]:

C₂₀H₁₇Br₂Cl₂FeN₄O₂: *M* = 631.94 g mol⁻¹; found % (calcd. %): C 37.18 (38.01), H 2.50 (2.71), N 8.56 (8.87). ESI-MS *m/z* calc. for C₁₉H₁₇Br₂Cl₂N₃O₂Fe⁺: 602.8414, found 602.8420; IR (KBr; cm⁻¹): 3154 (N-H); 3063 (C-H_{arom}); 2932 (C-H_{alif}); 2127, 2114 (C≡N); 1626, 1618 (C=N).

[Co(salpet_{H,H})CN]:

[Co(L_{H,H})Cl] was synthesized according to a modified literature method.^[33] [Co(L_H)Cl] (2.3 mmol) was dissolved in 70 ml methanol. Remaining undissolved crystals were filtered off and the solution was added dropwise to a solution of KCN (4.15 mmol) in 30 ml methanol and stirred over night at RT. About

half of the solvent was removed and the solution stored over night at 4 °C. A dark red-black powder was filtered off and used for the following synthesis without further purification.

{[Co^{III}(salpet_{H,H})CN]₂[Co^{II}(1-methylimidazole)₃(BF₄)₂ · 1.5 (H₂O)]}: 1-Methylimidazole (0.4 mmol) was added to a solution of Co^{II}(BF₄)₂·6H₂O (0.1 mmol) in 10 ml Acetonitrile. Then a second solution containing [Co(salpet_{H,H})Cl] (0.2 mmol) in 5 ml Acetonitrile was dropwise added to the first solution. The mixture was stirred for 4 h at RT and filtrated. While slow evaporation of the solvent results in single crystals of [Co(salpet_{H,H})CN], single crystals of the trinuclear compound could be obtained by ether diffusion. C₅₂H₆₃Co₃N₁₄O_{5.5}B₂F₈: found % (calcd. %): C 47.55 (47.32), H 4.76 (4.48), N 14.93 (15.02); IR (KBr; cm⁻¹): 3213 (N-H), 3127 (C-H_{arom}), 2936 (C-H_{alif}), 2149 (C≡N), 1626 (C=N).

Crystal structure analysis: Most of the diffraction data were collected with a Bruker SMART APEX II diffractometer with a CCD area detector and graphite-monochromated Mo-K α radiation ($\lambda = 0.71073 \text{ \AA}$) at 100 K. The compounds [Fe^{III}(salpet_{Br,Ci})NCO] and [Fe^{III}(salpet_{Br,Ci})NCS] were collected with a KAPPA APEX II diffractometer with a CCD area detector and graphite-monochromated Cu-K α radiation ($\lambda = 1.54178 \text{ \AA}$) at 233 K. The data frames were integrated using the SAINT program and merged to give a unique data set for structure determination. An absorption correction was performed using SADABS.^[T56] The structure was solved by direct methods and refined on F^2 by the full-matrix least-squares methods using SHELXL package (Bruker Analytical X-ray systems, Olex2).^[T45,T57] Non hydrogen atoms were refined with anisotropic thermal parameters. Hydrogen atoms were included in calculated positions and refined with isotropic thermal parameters riding on those of the parent atoms. Electron densities of the disordered solvent molecules were flattened using Olex 2 solvent mask^[T45] (BYPASS^[T46]). The supplementary crystallographic data can be accessed free of charge from The Cambridge Crystallographic Data Centre with the Codes CCDC 2059672 for [Fe^{III}(salpet_{Br,Ci})Cl], 2059673 for [Fe^{III}(salpet_{Br,Ci})NCS], 2059674 for [Co^{III}(salpet_{Br,Ci})CN], 2059675 for [Fe^{III}(salpet_{Br,Ci})CN], 2059676 for [Fe^{III}(salpet_{Br,Ci})NCO], 2059677 for [Fe^{III}(salpet_{Br,Ci})N₃], 2059678 for [Fe^{III}(salpet_{Br,Ci})NCS_e], 2059679 for [CoCo₂].

Physical measurements: Magnetic susceptibility data were collected using a Quantum Design MPMS-5S SQUID magnetometer. The measurements were performed with an applied magnetic field of 1000 Oe in the temperature range of 5 - 300 K. Magnetic data were corrected for the diamagnetism of the sample holder, and for the diamagnetism of the sample using Pascal's constants. The six [Fe(salpet_{Br,Ci})X] compounds were measured at 5.0 K increments in the settle mode with a fixed scan rate of 3.0 K/min and 30 seconds after the temperature had stabilized. [Co₂Co] was measured with a scan rate of 2 K/min in sweep mode. Infrared absorption spectra were measured on KBr pellet samples using a SHIMADZU IR Affinity-1 spectrometer or a Bruker Tensor 27. Cyclic voltammetry measurements were carried out in a standard one-compartment cell under N₂ at RT equipped with a platinum-wire counter electrode,

an SCE reference electrode, and a glassy carbon (GC) working electrode using a BAS 620A electrochemical analyzer. The measurements were performed in MeCN or DMF with 0.1 M tetra-*n*-butylammonium hexafluorophosphate (Bu₄NPF₆) as the supporting electrolyte and a scan rate of 0.1 V/s.

Acknowledgements

This work was supported by the Hannover School for Nanotechnology (HSN) and the German Academic Exchange Service (DAAD).

Keywords: Iron(III) complex, Cobalt(III) complex, Schiff Base complexes, cyclic voltammetry, magnetic susceptibility, mixed valance

- [T1] O. Kahn, *Science*, **1998**, 279, 44–48.
- [T2] C.-M. Jureschi, J. Linares, A. Boulmaali, P. Dahoo, A. Rotaru, Y. Garcia, *Sensors* **2016**, 16, 1–9.
- [T3] G. Aromí, D. Aguilà, P. Gamez, F. Luis, O. Roubeau, *Chem. Soc. Rev.* **2012**, 41, 537–546.
- [T4] F. Prins, M. Monrabal-Capilla, E. A. Osorio, E. Coronado, H. S. J. Van Der Zant, *Adv. Mater.* **2011**, 23, 1545–1549.
- [T5] T. Matsumoto, G. N. Newton, T. Shiga, S. Hayami, Y. Matsui, H. Okamoto, R. Kumai, Y. Murakami, H. Oshio, *Nat. Commun.* **2014**, 5, 3865.
- [T6] G. Vankó, F. Renz, G. Molnár, T. Neisius, S. Kárpáti, *Angew. Chemie – Int. Ed.* **2007**, 46, 5306–5309.
- [T7] M. Ohba, K. Yoneda, G. Agusti, M. C. Muñoz, A. B. Gaspar, J. A. Real, M. Yamasaki, H. Ando, Y. Nakao, S. Sakaki, S. Kitagawa, *Angew. Chemie – Int. Ed.* **2009**, 48, 4767–4771.
- [T8] F. Renz, *J. Phys. Conf. Ser.* **2010**, 217, 012022.
- [T9] N. Hoshino, F. Iijima, G. N. Newton, N. Yoshida, T. Shiga, H. Nojiri, A. Nakao, R. Kumai, Y. Murakami, H. Oshio, *Nat. Chem.* **2012**, 4, 921–926.
- [T10] D. Unruh, P. Homenya, M. Kumar, R. Sindelar, Y. Garcia, F. Renz, *Dalt. Trans.* **2016**, 45, 14008–14018.
- [T11] T. Shiga, R. Saiki, L. Akiyama, R. Kumai, D. Natke, F. Renz, J. M. Cameron, G. N. Newton, H. Oshio, *Angew. Chemie – Int. Ed.* **2019**, 58, 5658–5662.
- [T12] M. Seredyuk, K. O. Znovjyak, J. Kusz, M. Nowak, M. C. Muñoz, J. A. Real, *Dalt. Trans.* **2014**, 43, 16387–16394.

- [T13] D. Müller, C. Knoll, M. Seifried, J. M. Welch, G. Giester, M. Reissner, P. Weinberger, *Chem. – A Eur. J.* **2018**, *24*, 5271–5280.
- [T14] I. Nemeč, R. Herchel, Z. Trávníček, *Dalt. Trans.* **2015**, *44*, 4474–4484.
- [T15] M. Nihei, Y. Yanai, D. Natke, R. Takayama, M. Kato, Y. Sekine, F. Renz, H. Oshio, *Chem. – A Eur. J.* **2019**, *25*, 7449–7452.
- [T16] P. N. Martinho, B. Gildea, M. M. Harris, T. Lemma, A. D. Naik, H. Müller-Bunz, T. E. Keyes, Y. Garcia, G. G. Morgan, *Angew. Chemie – Int. Ed.* **2012**, *51*, 12597–12601.
- [T17] I. Nemeč, R. Herchel, Z. Trávníček, *Molecules* **2016**, *21*, 1681.
- [T18] A. Preiss, L. Heyer, S. Klimke, G. Klingelhöfer, F. Renz, *Hyperfine Interact.* **2017**, *238*, 1–8.
- [T19] D. Natke, D. Unruh, B. Dreyer, S. Klimke, M. Jahns, A. Preiss, R. Sindelar, G. Klingelhöfer, F. Renz, *Hyperfine Interact.* **2018**, *239*, 1–9.
- [T20] O. A. Turanova, M. Y. Volkov, E. N. Frolova, L. Bazan, G. G. Garifzianova, L. G. Gafiyatullin, I. V. Ovchinnikov, A. N. Turanov, *J. Chem. Phys.* **2020**, *152*, 014306.
- [T21] I. Nemeč, R. Herchel, R. Boča, Z. Trávníček, I. Svoboda, H. Fuess, W. Linert, *Dalt. Trans.* **2011**, *40*, 10090.
- [T22] C. Krüger, P. Augustin, I. Nemeč, Z. Travnicek, H. Oshio, R. Boca, F. Renz, *Eur. J. Inorg. Chem.* **2013**, 902–915.
- [T23] R. Herchel, Z. Trávníček, *Dalt. Trans.* **2013**, *42*, 16279–16288.
- [T24] C. Krüger, P. Augustin, L. Dihan, J. Pavlik, J. Moncol', I. Nemeč, R. Boca, F. Renz, *Polyhedron* **2015**, *87*, 194–201.
- [T25] P. Masárová, P. Zoufalý, J. Moncol, I. Nemeč, J. Pavlik, M. Gembický, Z. Trávníček, R. Boča, I. Šalitraš, *New J. Chem.* **2015**, *39*, 508–519.
- [T26] P. Augustín, R. Boča, *Nov. Biotechnol. Chim.* **2015**, *14*, 96–103.
- [T27] L. Pogány, J. Moncol, M. Gál, I. Šalitraš, R. Boča, *Inorganica Chim. Acta* **2017**, *462*, 23–29.
- [T28] P. Gütlich, A. B. Gaspar, Y. Garcia, *Beilstein J. Org. Chem.* **2013**, *9*, 342–391.
- [T29] C. Rajnák, R. Mičová, J. Moncol, L. Dlháň, C. Krüger, F. Renz, R. Boča, *Dalt. Trans.* **2021**, *50*, 472–475.

- [T30] I. Šalitraš, R. Boča, L. Dlháň, M. Gembický, J. Kožíšek, J. Linares, J. Moncol', I. Nemeč, L. Perašínová, F. Renz, I. Svoboda, H. Fuess, *Eur. J. Inorg. Chem.* **2009**, 3141–3154.
- [T31] R. Boča, I. Šalitraš, J. Kožíšek, J. Linares, J. Moncol', F. Renz, *Dalt. Trans.* **2010**, 39, 2198.
- [T32] I. Šalitraš, R. Boča, R. Herchel, J. Moncol, I. Nemeč, M. Ruben, F. Renz, *Inorg. Chem.* **2012**, 51, 12755–12767.
- [T33] J. Pavlik, P. Masárová, I. Nemeč, O. Fuhr, M. Ruben, I. Šalitraš, *Inorg. Chem.* **2020**, 59, 2747–2757.
- [T34] O. Sato, T. Iyoda, A. Fujishima, K. Hashimoto, *Science*, **1996**, 272, 704–705.
- [T35] Y. S. Meng, O. Sato, T. Liu, *Angew. Chemie – Int. Ed.* **2018**, 57, 12216–12226.
- [T36] G. N. Newton, M. Nihei, H. Oshio, *Eur. J. Inorg. Chem.* **2011**, 3031–3042.
- [T37] T. Liu, D.-P. Dong, S. Kanegawa, S. Kang, O. Sato, Y. Shiota, K. Yoshizawa, S. Hayami, S. Wu, C. He, C. Y. Duan, *Angew. Chemie Int. Ed.* **2012**, 51, 4367–4370.
- [T38] C. Mathonière, *Eur. J. Inorg. Chem.* **2018**, 248–258.
- [T39] M. Nihei, Y. Sekine, N. Suganami, K. Nakazawa, A. Nakao, H. Nakao, Y. Murakami, H. Oshio, *J. Am. Chem. Soc.* **2011**, 133, 3592–3600.
- [T40] M. Nihei, K. Shiroyanagi, M. Kato, R. Takayama, H. Murakami, Y. Kera, Y. Sekine, H. Oshio, *Inorg. Chem.* **2019**, 58, 11912–11919.
- [T41] E. S. Koumoussi, I. R. Jeon, Q. Gao, P. Dechambenoit, D. N. Woodruff, P. Merzeau, L. Buisson, X. Jia, D. Li, F. Volatron, C. Mathoniere, R. Clerac, *J. Am. Chem. Soc.* **2014**, 136, 15461–15464.
- [T42] M. Nihei, *Chem. Lett.* **2020**, 49, 1206–1215.
- [T43] I. Nemeč, P. Zoufalý, R. Herchel, Z. Trávníček, *Inorg. Chem. Commun.* **2013**, 35, 50–53.
- [T44] I. Nemeč, R. Herchel, Z. Trávníček, T. Šilha, *RSC Adv.* **2016**, 6, 3074–3083.
- [T45] O. V. Dolomanov, L. J. Bourhis, R. J. Gildea, J. A. K. Howard, H. Puschmann, *J. Appl. Crystallogr.* **2009**, 42, 339–341.
- [T46] P. Van Der Sluis, A. L. Spek, *Acta Crystallogr. Sect. A*, **1990**, 46, 194–201.
- [T47] R. J. Gillespie, R. S. Nyholm, *Q. Rev. Chem. Soc.* **1957**, 11, 339.
- [T48] R. J. Gillespie, *Coord. Chem. Rev.* **2008**, 252, 1315–1327.

- [T49] I. Krivokapic, M. Zerara, M. L. Daku, A. Vargas, C. Enachescu, C. Ambrus, P. Tregenna-Piggott, N. Amstutz, E. Krausz, A. Hauser, *Coord. Chem. Rev.* **2007**, *251*, 364–378.
- [T50] A. Mondal, L. M. Chamoreau, Y. Li, Y. Journaux, M. Seuleiman, R. Lescouëzec, *Chem. – A Eur. J.* **2013**, *19*, 7682–7685.
- [T51] R. Ohtani, K. Shimayama, A. Mishima, M. Ohba, R. Ishikawa, S. Kawata, M. Nakamura, L. F. Lindoy, S. Hayami, *J. Mater. Chem. C*, **2015**, *3*, 7865–7869.
- [T52] F. Shen, W. Huang, D. Wu, Z. Zheng, X. C. Huang, O. Sato, *Inorg. Chem.* **2016**, *55*, 902–908.
- [T53] A. B. P. Lever, *Inorg. Chem.* **1990**, *29*, 1271–1285.
- [T54] S. S. Fielder, M. C. Osborne, A. B. P. Lever, W. J. Pietro, *J. Am. Chem. Soc.* **1995**, *117*, 6990–6993.
- [T55] A. J. L. Pombeiro, *Eur. J. Inorg. Chem.* **2007**, 1473–1482.
- [T56] G. M. Sheldrick, *SADABS: An Empirical Absorption Correction Program*, Bruker Analytica X-ray Systems, Madison, WI, **1996**.
- [T57] G. M. Sheldrick, *Acta Crystallogr. Sect. C Struct. Chem.* **2015**, *71*, 3–8.

4.2 Angled Trinuclear Cobalt Complex

Herein the trinuclear cobalt complex $\{[\text{Co}(\text{salpet}_{\text{H,H}})\text{CN}]_2[\text{Co}(\text{phen})_2]\}[\text{BF}_4]_2 \cdot \text{solvent}$ (**T1**, phen: 1,10-phenanthroline) is reported. In comparison to $[\text{Co}^{\text{III}}(\text{salpet}_{\text{H,H}})\text{CN}]_2[\text{Co}^{\text{II}}(1\text{-methylimidazole})_3] \cdot 1.5 \text{H}_2\text{O}$ ($[\text{Co}_2\text{Co}]$) the monodentate ligand was changed to the bidentate ligand phenanthroline. Therefore, the molecule changed from a linear to an angled geometry. The synthesis of **T1** was done to check whether it is possible to synthesize angled complexes with $[\text{Co}(\text{salpet}_{\text{H,H}})\text{CN}]$ capping complexes. Therefore, only the crystal structure and magnetic properties were determined.

4.2.1 Experimentals

All chemicals were purchased from commercial suppliers and used without further purification. All syntheses were performed under aerobic conditions.

$[\text{Co}(\text{salpet}_{\text{H,H}})\text{CN}]$:

$[\text{Co}(\text{salpet}_{\text{H,H}})\text{Cl}]$ was synthesized according to a modified literature method.^[33] $[\text{Co}(\text{salpet}_{\text{H,H}})\text{Cl}]$ (2.3 mmol) was dissolved in 70 ml methanol. Remaining undissolved crystals were filtered off and the solution was added dropwise to a solution of KCN (4.15 mmol) in 30 ml methanol and stirred over night at RT. About half of the solvent was removed and the solution stored over night at 4 °C. A dark red-black powder was obtained after filtration and was used for the following synthesis without further purification.

$\{[\text{Co}(\text{salpet}_{\text{H,H}})\text{CN}]_2[\text{Co}(\text{phen})_2]\}[\text{BF}_4]_2 \cdot \text{solvent}$ (**T1**):

A solution of $\text{Co}(\text{BF}_4)_2 \cdot 6 \text{H}_2\text{O}$ (0.1 mmol) and phen (0.2 mmol) in 10 ml acetonitrile was stirred for 5 min. $[\text{Co}(\text{salpet}_{\text{H,H}})\text{CN}]$ (0.2 mmol) was added, stirred for 2 h and filtrated afterwards. From the red solution single crystals could be obtained by vapor diffusion of diethyl ether after several days.

Crystal structure analysis: The diffraction data were collected with a Bruker SMART APEX II diffractometer with a CCD area detector and graphite-monochromated Mo-K α radiation ($\lambda = 0.71073 \text{ \AA}$). The data frames were integrated using the SAINT program and merged to give a unique data set for the determination of the structure. An absorption correction was performed using SADABS.^[129] The structure was solved by direct methods and refined on F2 by the full-matrix least-squares methods using the SHELXTL package (Bruker Analytical X-ray systems, Olex2).^[130,131] Non-hydrogen atoms were refined with anisotropic thermal parameters. Hydrogen atoms were included in calculated positions and refined with isotropic thermal parameters riding on those of the parent atoms. Electron densities of solvent molecules and anions were flattened using Olex 2 solvent mask^[131] (BYPASS^[132]).

Physical measurements: Magnetic susceptibility data were collected using a Quantum Design MPMS-5S SQUID magnetometer. The measurement was performed with an applied magnetic field of 1000 Oe in the temperature range of 5 - 300 K. Magnetic data were corrected for the diamagnetism of the sample holder, and for the diamagnetism of the sample using Pascal's constants. T1 was measured with a scan rate of 2 K/min in sweep mode. The sample was measured during the cooling and heating processes.

4.2.2 Results and Discussion

Structural Data

The single crystal structure of T1 was measured at 100 K. However, the quality of the diffraction data of all measured crystals was relatively low with at least $R_1 = 15.05\%$. This was due to a rapid loss of crystallinity which could be observed after mounting the crystal from the solution. Therefore, the following crystallographic and structural data (Table 3, Figure 16) should be seen as a rough model with certain inaccuracies compared to usual single crystal structures that were published. For this reason, the solvent molecules, BF_4^- anions, hydrogen atoms and minor parts of the ligands could not be modeled correctly. Therefore, the solvent molecules and anions have been removed by Olex 2 solvent mask^[131] (BYPASS^[132]).

Table 3: Crystallographic and structural data of T1. The moiety formula is an assumed one and not taken from the structural data.

	T1
	$\{[\text{Co}(\text{salpet}_{\text{H,H}})\text{CN}]_2[\text{Co}(\text{phen})_2]\}\text{[BF}_4\text{]}_2 \cdot \text{solvent}$
T in K	100
crystal System	monoclinic
space group	$P2_1/n$
a in Å	32.410(5)
b in Å	29.271(4)
c in Å	32.915(5)
α in °	90
β in °	90.731(2)
γ in °	90
V in Å ³	31223(8)
Z	28
R_1/wR_2 ($I > 2\sigma I$)	0.1505/0.2918

4. Derivatives of Spin Crossover Complexes as Building Blocks

The trinuclear compound **T1** consists, similar to $[\text{Co}_2\text{Co}]$, of two $[\text{Co}(\text{salpet}_{\text{H,H}})\text{CN}]$ building blocks connected through a $\text{CN-Co}^{\text{II}}-\text{NC}$ bridge. However, due to the bidentate character of the two phen capping ligands a linear arrangement of the trinuclear complex is prevented and the complex is forced into an angled geometry with a CN-Co-NC angle of $94 - 98.5^\circ$. The cobalt(III) ion in $[\text{Co}(\text{salpet}_{\text{H,H}})\text{CN}]$ is octahedrally coordinated by O_2N_4 donor atoms. Accordingly, the cyanides N atom is assumedly coordinate to the centered cobalt(II) ion.

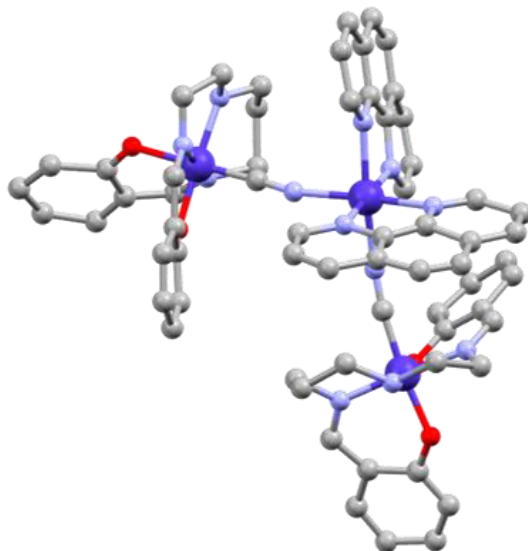


Figure 16: Molecular structure of **T1**. Hydrogen atoms and other molecules and ions within the asymmetric unit have been omitted for clarity. Color code: C, gray; N, light blue; O, red; Co, dark blue.

The average bond lengths (Table 4) for the $[\text{Co}(\text{salpet}_{\text{H,H}})\text{CN}]$ parts of **T1** are corresponding to cobalt(III) in the LS state. The centered cobalt ion shows significant higher bond lengths, which correspond to a cobalt(II) in the HS state. In total is the charge of one complex assumed to be $2+$. Since the BF_4^- anions could not be modeled correctly, the formula was manually adjusted. In addition, the trinuclear complexes build up 2D layers (Figure 17) which are probably interconnected by different types of interactions between the complexes, solvent molecules, and anions. The unit cell (Figure 59, page 147) contains for each complex a second one which is oriented in the opposite direction. In contrast to **D1** no orientation within the unit cell could be determined.

Table 4: Coordination bond lengths of **T1**.

bond	max. and min. coordination bond length
$[\text{Co}(\text{salpet}_{\text{H,H}})\text{CN}]$, Co-O	1.85 – 1.94 Å
$[\text{Co}(\text{salpet}_{\text{H,H}})\text{CN}]$, Co-N	1.83 – 2.08 Å
$[\text{Co}(\text{salpet}_{\text{H,H}})\text{CN}]$, Co-C	1.73 – 1.97 Å
$[\text{Co}(\text{phen})_2(\text{NC})_2]$, Co-N(cyanide)	1.98 – 2.15 Å
$[\text{Co}(\text{phen})_2(\text{NC})_2]$, Co-N(phen)	2.03 – 2.20 Å

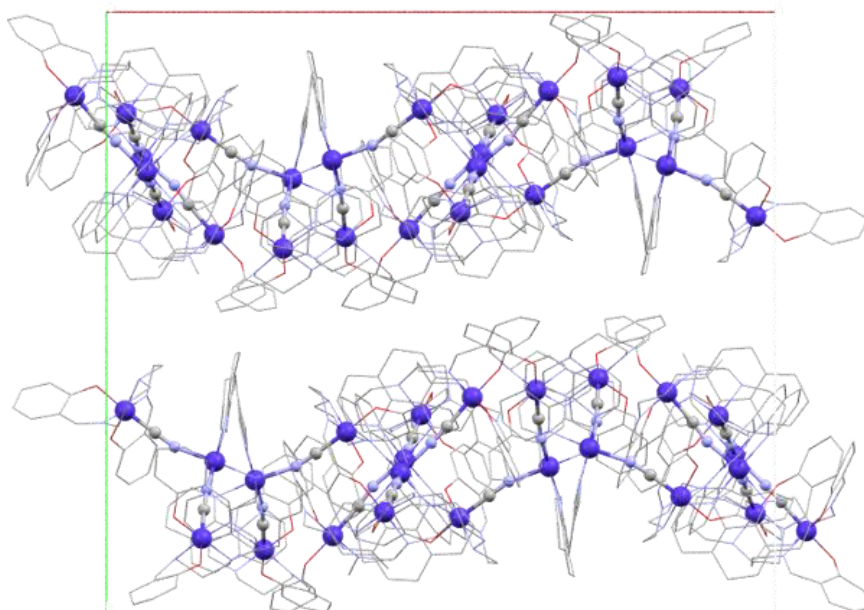


Figure 17: Unit cell of T1, views along the c -axis. Hydrogen atoms have been omitted for clarity. Color code: C, gray; N, light blue; O, red; Co, dark blue; a -axis, red line; b -axis, green line.

Magnetic Data

The temperature-depending molar magnetic susceptibility of T1 in the range of 5 – 300 K was measured (Figure 18). T1 shows a nearly constant $\chi_m T$ value of about 2.65 $\text{emu mol}^{-1} \text{K}$ from 300 K to 120 K with a decrease to 1.77 $\text{emu mol}^{-1} \text{K}$ at 5 K afterwards due to the ZFS with no observable magnetic interactions. The $\chi_m T$ value corresponds to two cobalt(III) in the LS and one cobalt(II) in the HS state which matches the observed bond lengths and the assumed charges.

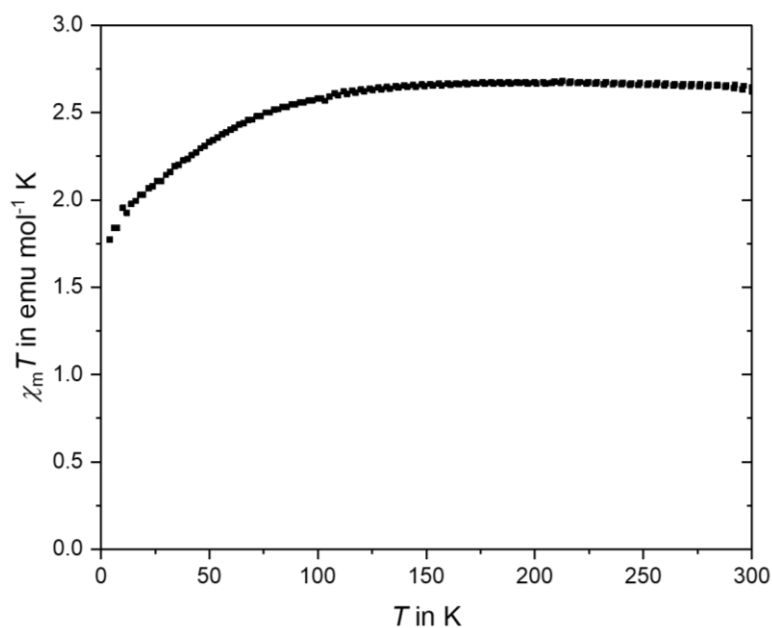


Figure 18: $\chi_m T - T$ plot of T1.

4.2.3 Conclusion and Outlook

The mixed-valence cyanide-bridged complex T1 shows an angled structure which builds up 2D layers. The coordination bond lengths and magnetic data are suggesting that the two capping complexes $[\text{Co}^{\text{III}}(\text{salpet}_{\text{H,H}})\text{CN}]$ are in the LS and the centered cobalt(II) is in the HS state. No switching behavior or magnetic interactions could be observed. This approach is the first evidence for a trinuclear angled complex with a salpet ligand. This molecular design might lead to new possibilities of introducing anisotropies into switchable compounds.

4.3 Switchable Pentanuclear Complexes

In the following chapter, the two novel pentanuclear complexes $\{[\text{Mo}(\text{CN})_8][\text{Fe}(\text{salpet}_{\text{H},\text{NO}_2})_4] \cdot 9(\text{C}_7\text{H}_5\text{N}) \cdot 8(\text{H}_2\text{O})$ (**P1**) and $\{[\text{W}(\text{CN})_8][\text{Co}(\text{salpet}_{\text{H},\text{NO}_2})_4] \cdot 15(\text{C}_7\text{H}_5\text{N}) \cdot 10(\text{H}_2\text{O})$ (**P2**) are presented. The two compounds are synthesized from mononuclear Schiff base complexes with iron or cobalt and octacyanometalate molybdenum or tungsten complexes respectively (Figure 19).

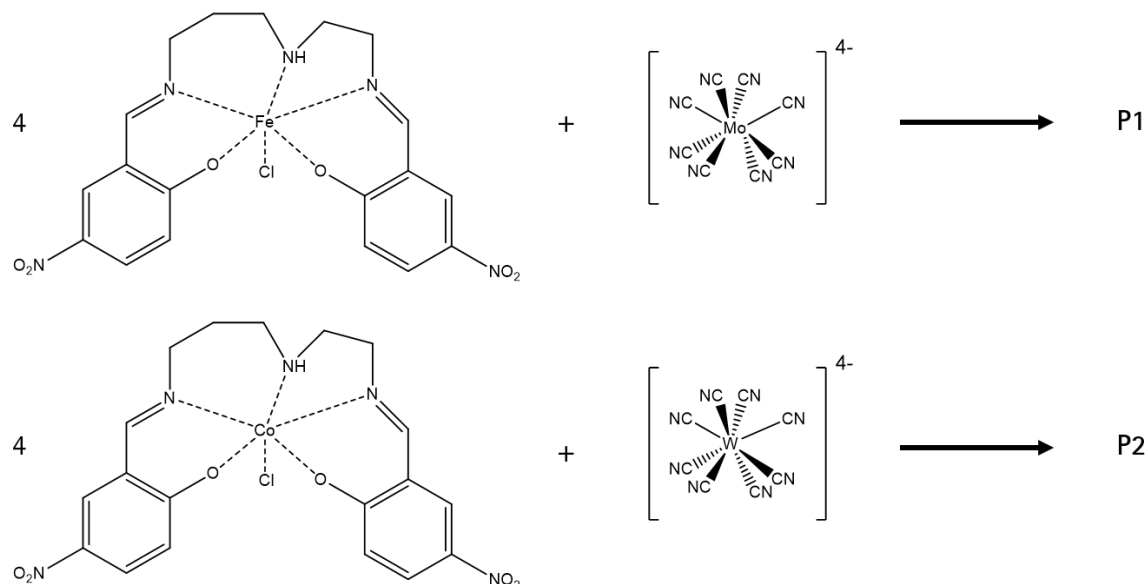


Figure 19: Reaction scheme for P1 and P2.

Two different compounds (**P1**(acetone) and **P1**) could be obtained by different synthesis for the pentanuclear molybdenum-iron complex. Further analyses were performed for **P1** since its synthesis provided more reproducible results.

4.3.1 Experimentals

All chemicals were purchased from commercial suppliers and used without further purification. The mononuclear compounds $\text{K}_4[\text{Mo}(\text{CN})_8]$ and $\text{K}_4[\text{W}(\text{CN})_8]$ ^[138–140] and the complexes $[\text{Fe}(\text{salpet}_{\text{H},\text{NO}_2})\text{Cl}]$ and $[\text{Co}(\text{salpet}_{\text{H},\text{NO}_2})\text{Cl}]$ ^[26,31,33] were synthesized according to modified literature methods. All syntheses were performed under aerobic conditions.

 $\{[\text{Mo}(\text{CN})_8][\text{Fe}(\text{salpet}_{\text{H},\text{NO}_2})_4] \cdot 8(\text{C}_3\text{H}_6\text{O}) \cdot 9(\text{H}_2\text{O})$ (P1**(acetone)):**

A solution of $\text{K}_4[\text{Mo}(\text{CN})_8]$ (0.00625 mmol) in 3 ml water was mixed with a solution of $[\text{Fe}(\text{salpet}_{\text{H},\text{NO}_2})\text{Cl}]$ (0.1 mmol) in 25 ml acetone. Bu_4NPF_6 (0.1 mmol) was added to the solution and stirred for 1 h. The solution was filtrated, and single crystals could be obtained through vapor diffusion of methyl *tert*-butyl ether. IR (KBr; cm^{-1}): 1306 (nitro), 1607 and 1628 (nitro and imine), 2116 (cyanide).

$\{[\text{Mo}(\text{CN})_8][\text{Fe}(\text{salpet}_{\text{H},\text{NO}_2)}]_4\} \cdot 9(\text{C}_7\text{H}_5\text{N}) \cdot 8(\text{H}_2\text{O})$ (P1):

A solution of $\text{K}_4[\text{Mo}(\text{CN})_8]$ (0.15 mmol) in 20 ml water was mixed with a solution of $[\text{Fe}(\text{salpet}_{\text{H},\text{NO}_2})\text{Cl}]$ (0.6 mmol) in 30 ml benzonitrile. AgPF_6 (0.6 mmol) in 10 ml water was added to the solution and stirred for 1 h. The water phase was removed, and the silver-black precipitation was filtered off. Acetone was added to the solution and single crystals could be obtained by slow evaporation of the solvent mixture. $\text{C}_{84}\text{H}_{92}\text{Fe}_4\text{N}_{28}\text{MoO}_{32}$, $\{[\text{Mo}(\text{CN})_8][\text{Fe}(\text{salpet}_{\text{H},\text{NO}_2)}]_4\} \cdot 8(\text{H}_2\text{O})$: found % (calcd. %): C 42.70 (43.39), H 3.61 (3.99), N 15.94 (16.87).

$\{[\text{W}(\text{CN})_8][\text{Co}(\text{salpet}_{\text{H},\text{NO}_2)}]_4\} \cdot 15(\text{C}_7\text{H}_5\text{N}) \cdot 10(\text{H}_2\text{O})$ (P2):

A solution of $\text{K}_4[\text{W}(\text{CN})_8]$ (0.0125 mmol) in 8 ml water was mixed with a solution of $[\text{Co}(\text{salpet}_{\text{H},\text{NO}_2})\text{Cl}]$ (0.05 mmol) in 20 ml methanol and 10 ml benzonitrile and stirred for 20 min. The black precipitation was filtered off. Afterwards, the solution separated into a white turbid aqueous phase and a dark organic phase. The two phases stood together over night. The water phase was removed and about 30 ml methanol was added. Single crystals could be obtained after one day through slow evaporation of the solvent mixture. $\text{C}_{168}\text{H}_{172}\text{Co}_8\text{N}_{56}\text{O}_{58}\text{W}_2$, $\{[\text{W}(\text{CN})_8][\text{Co}(\text{salpet}_{\text{H},\text{NO}_2)}]_4\} \cdot 10(\text{H}_2\text{O})$: found % (calcd. %): C 41.80 (42.55), H 3.65 (3.66), N 15.75 (16.54); IR (KBr; cm^{-1}): 1300 (nitro), 1605 and 1630 (nitro and imine), 2110 (cyanide).

Crystal structure analysis: The diffraction data were collected with a Bruker SMART APEX II diffractometer with a CCD area detector and graphite-monochromated Mo-K α radiation ($\lambda = 0.71073$ Å). The data frames were integrated using the SAINT program and merged to give a unique data set for the determination of the structure. An absorption correction was performed using SADABS.^[129] The structure was solved by direct methods and refined on F² by the full-matrix least-squares methods using the SHELXTL package (Bruker Analytical X-ray systems, Olex2).^[130,131] Non-hydrogen atoms were refined with anisotropic thermal parameters. Hydrogen atoms were included in calculated positions and refined with isotropic thermal parameters riding on those of the parent atoms. Electron densities of disordered solvent molecules for all three structures were flattened using Olex 2 solvent mask^[131] (BYPASS^[132]). Additional restraints were applied to a small part of the salpet ligand of P1 (acetone) and to one benzonitrile molecule of P1.

Physical measurements: Magnetic susceptibility data were collected using a Quantum Design MPMS-5S SQUID magnetometer. The measurements were performed with an applied magnetic field of 10000 Oe in the temperature range of 5 - 300 K. Magnetic data were corrected for the diamagnetism of the sample holder, and for the diamagnetism of the sample using Pascal's constants. The samples were measured during the cooling and heating process with 5.0 K increments in the settle mode with a fixed scan rate of 3.0 K/min and 30 seconds after the temperature had stabilized. Infrared absorption spectra

were measured using KBr pellet samples with a SHIMADZU IR Affinity-1 spectrometer. The temperature dependence of infrared absorption spectra was measured using KBr pellet samples and a UNISOKU USP-203-A cryostat. CV measurements were carried out in a standard one-compartment cell under N_2 at RT equipped with a platinum-wire counter electrode, an SCE reference electrode, and a glassy carbon (GC) working electrode using a BAS 620A electrochemical analyzer. The measurements were performed in MeCN with Bu_4NPF_6 (0.1 M) as the supporting electrolyte and a scan rate of 0.1 V/s. UV-Vis spectra were recorded with a SHIMADZU UV-3150 spectrometer equipped with a UNISOKU USP-203-A cryostat for temperature-depending measurements. The Mössbauer Spectrum was measured with a WissEl Mössbauer spectrometer using a $^{57}Co(Rh)$ source and the isomer shift is given relative to α -iron at RT.

4.3.2 Results and Discussion

Structural Data

The single crystal X-ray structures of **P1**(acetone), **P1**, and **P2** were determined at 100 K (Figure 20, Table 5). At 0 °C no structure could be determined because the crystallinity decreased too fast near RT outside the solution. In contrast to what was proposed without a single crystal structure in the literature for similar compounds,^[141] **P1**(acetone), **P1**, and **P2** are pentanuclear complexes. Even though the molecular structure of all three complexes is similar, **P1**(acetone) and **P1** are crystallizing in the monoclinic space group $P2_1/c$ and $C2/c$, respectively, and **P2** crystallizes in the triclinic space group $P-1$. For the three compounds, the centered molybdenum or tungsten ion is bridged by cyanide to the iron or cobalt complex. The cyanides C is oriented to the centered ion while the cyanides N is bonded to the iron or cobalt (Figure 21), offering in addition the possibility of an iron(III) SCO.^[26,69]

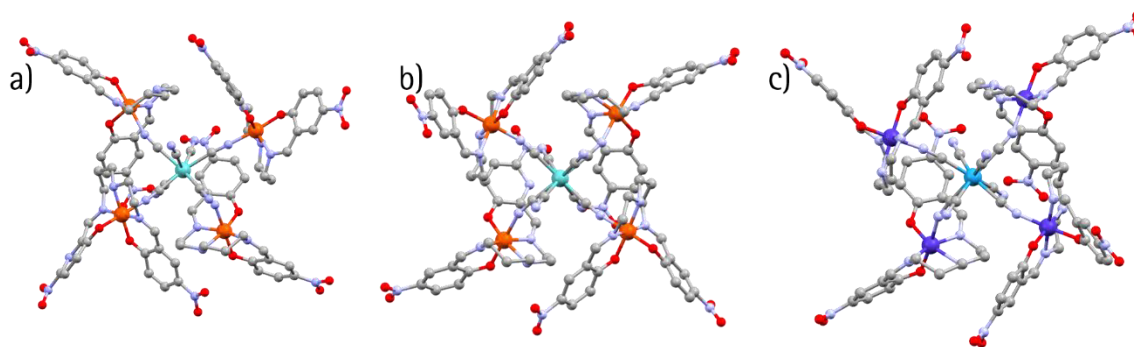


Figure 20: Molecular structure within the asymmetric unit of a) **P1**(acetone), b) **P1** and c) **P2**. Hydrogen atoms, solvent molecules and one pentanuclear complex for **P2** were omitted for clarity. Color code: C, gray; N, light blue; O, red; Fe, orange; Mo, light turquoise; Co, dark blue; W, dark turquoise.

The molybdenum and tungsten are coordinated by eight cyanides in a slightly distorted square antiprismatic coordination sphere (Figure 22). Four of these cyanides are bonded to an iron or cobalt ion resulting in a neutral complex. Besides the cyanides nitrogen, the iron and cobalt are octahedrally

4. Derivatives of Spin Crossover Complexes as Building Blocks

coordinated by three nitrogen and two oxygen atoms from the Schiff base ligand. Each structure shows a 3D network through weak salpet-salpet interactions, which build up cavities between the complexes (Figure 60, page 148). The disordered solvent molecules, which were removed by Olex 2 solvent mask^[131] (BYPASS^[132]), are probably located in these cavities.

Table 5: Crystallographic and structural data of P1(acetone), P1 and P2.

	P1(acetone)	P1	P2
	$C_{107}H_{138}Fe_4N_{29}O_{41}Mo$	$C_{140}H_{140}Fe_4N_{37}O_{36}Mo$	$C_{273}H_{247}Co_8N_{71}O_{58}W_2$
<i>T</i> in K	100	100	100
crystal System	monoclinic	monoclinic	triclinic
space group	<i>P</i> ₂ / <i>c</i>	<i>C</i> ₂ / <i>c</i>	<i>P</i> -1
<i>a</i> in Å	18.016(4)	42.317(13)	19.980(4)
<i>b</i> in Å	34.418(7)	19.987(4)	23.427(5)
<i>c</i> in Å	20.455(4)	38.090(11)	35.439(9)
α in °	90	90	77.485(2)
β in °	102.10(3)	117.461(2)	73.63
γ in °	90	90	64.76
<i>V</i> in Å ³	12402(5)	28586(13)	14306(6)
<i>Z</i>	4	8	2
<i>R</i> ₁ / <i>wR</i> ₂ (<i>I</i> > 2σ <i>I</i>)	0.0905/0.2458	0.0864/0.1672	0.0934/0.1950

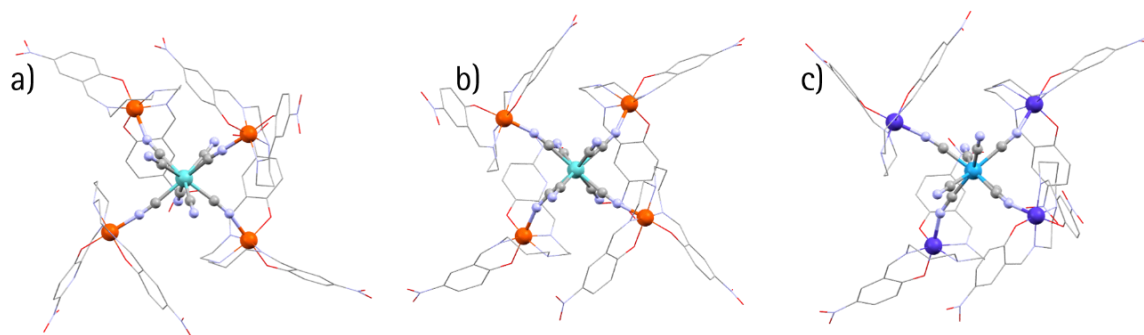


Figure 21: Molecular structure within the asymmetric unit of a) P1(acetone), b) P1, and c) P2. The mixed valenced bonds are highlighted. Hydrogen atoms, solvent molecules, and one pentanuclear complex for P2 have been omitted for clarity. Color code: C, gray; N, light blue; O, red; Fe, orange; Mo, light turquoise; Co, dark blue; W, dark turquoise.

Noteworthy is, that even though the compounds P1 and P2 are crystallizing in different crystal systems, the packings look remarkably similar. The powder XRD patterns have been calculated from the single crystal structures to compare the packings of P1 and P2 more easily (Figure 61, page 149). The patterns for the most intense reflexes are similar and therefore, the structures seem to be isostructural. The different crystal systems are probably caused by different asymmetric units. While the asymmetric unit

of **P1** only contains one pentanuclear complex, the asymmetric unit of **P2** contains two distinguishable complexes. Hence, the solvent used for the synthesis seems to have a larger impact on the crystal structure than the used metal ions, which show similar chemical behavior regarding the coordination and crystallization in these complexes.

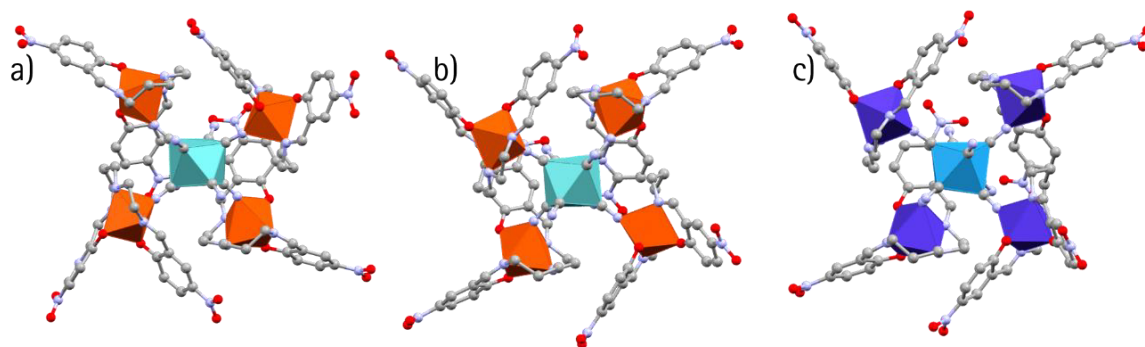


Figure 22: Molecular structure within the asymmetric unit of a) **P1**(acetone), b) **P1**, and c) **P2**. The coordination polyhedrons have been highlighted. Hydrogen atoms, solvent molecules, and one pentanuclear complex for **P2** have been omitted for clarity. Color code: C, gray; N, light blue; O, red; Fe, orange; Mo, light turquoise; Co, dark blue; W, dark turquoise.

Furthermore, the iron coordination bond lengths (Table 6) of **P1**(acetone) and **P1** are showing shorter bonds for two ions corresponding to an iron(III) in the LS state. The bonds of the other two ions are significantly increased and correspond to iron(III) in HS state (Chapter 4.1).^[26,27] Following, **P1**(acetone) and **P1** have mixed spin states with a possible SCO. The structure of **P2** shows four cobalt ions with shorter coordination bond lengths corresponding to cobalt(III) in the LS state and four ions with larger bond lengths. The larger bond lengths in **P2** could be explained by an ETCST between $[\text{Co}^{\text{II}}\text{W}^{\text{V}}]/[\text{Co}^{\text{III}}\text{W}^{\text{IV}}]$, which is described in the literature^[23,101,142] or by an SCO of cobalt(III). However, due to the very weak ligand field necessary to stabilize a cobalt(III) in the HS state,^[8,143,144] an ETCST is more likely. Typically cobalt(II) HS bond lengths are $\sim 2.1 \text{ \AA}$.^[18,25] Therefore, the observed intermediate bond lengths resulted from the distribution of the two HS states on two different cobalt ions per tungsten. Hence, enlarged bond lengths can be observed within all three structures indicating mixed electronic states or switchable behavior located on preferred ions.

The salpet ligand of the $[\text{M}(\text{salpet}_{\text{H},\text{NO}_2})\text{NC}]$ part in **P1**(acetone), **P1**, and **P2** with longer bond lengths shows a notable distortion compared with $[\text{Fe}(\text{salpet}_{\text{B},\text{Cl}})\text{NCS}]$ (Figure 23). Ideally, the first atom of the monodentate ligand is coordinated perpendicular to the plane built by the ligand around the three coordinating Nitrogen atoms in *mer* position, which expresses the distortion through the A-M-C angle (Figure 23). This angle is significantly decreased for the cobalt and iron ions with longer bond lengths in **P1**(acetone), **P1**, and **P2** and may therefore be coupled with the spin state (Table 7). If this angle is compared with literature examples from iron(III) and cobalt(III) mono- and multinuclear complexes

4. Derivatives of Spin Crossover Complexes as Building Blocks

with salpet ligands (Table 29 and Figure 62, page 150), no direct trend can be observed. While the angle of most LS complexes is between 70 ° and 90 °, with some exceptions at 101.7 °, the HS complexes are distributed between 65 ° and 110 °. Consequently, these distortions are significant for P1(acetone), P1, and P2 but are not a general trend observable for many complexes with salpet ligands.

Table 6: Coordination bond lengths of iron and cobalt in P1(acetone), P1, and P2. For clarity, the numbering of the eight distinguishable cobalt ions is Co1 - Co4 with an assignment to the two different tungsten ions (W1, W2).

bond	max. and min. coordination bond lengths in Å	
	P1(acetone)	P1
Fe1-O	1.883(5), 1884(5)	1.883(6), 1.893(5)
Fe1-N	1.921(5) – 1.996(6)	1.908(7) – 1.996(5)
Fe1-cyanide	1.943(6)	1.931(7)
Fe2-O	1.865(5), 1.903(4)	1.921(6), 1.932(4)
Fe2-N	1.881(7) – 1.999(6)	2.067(7) – 2.178(6)
Fe2-cyanide	1.930(6)	2.068(8)
Fe3-O	1.920(7), 1.937(5)	1.891(5), 1.892(5)
Fe3-N	2.049(6) – 2.132(7)	1.944(9) – 2.042(7)
Fe3-cyanide	2.058(6)	1.943(6)
Fe4-O	1.927(5), 1.936(6)	1.916(5), 1.930(7)
Fe4-N	2.038 – 2.167(6)	2.029(7) – 2.131(9)
Fe4-cyanide	2.075(7)	2.043(6)
	P2 (W1)	P2 (W2)
Co1-O	1.914(9), 1.936(7)	1.884(7), 1.885(7)
Co1-N	2.04(1) – 2.17(1)	1.92(1) – 1.991(6)
Co1-cyanide	2.075(9)	1.930(7)
Co2-O	1.873(8), 1.880(8)	1.926(8), 1.942(8)
Co2-N	1.929(9) – 2.005(9)	2.09(1) – 2.19(1)
Co2-cyanide	1.920(9)	2.07(1)
Co3-O	1.886(9), 1.899(8)	1.895(8), 1.896(7)
Co3-N	1.92(1) – 2.04(1)	1.91(1) – 2.038(7)
Co3-cyanide	1.96(1)	1.97(1)
Co4-O	1.924(6), 1.935(8)	1.918(7), 1.929(7)
Co4-N	2.08(1) – 2.20(1)	2.04(1) – 2.129(9)
Co4-cyanide	2.047(8)	2.085(9)

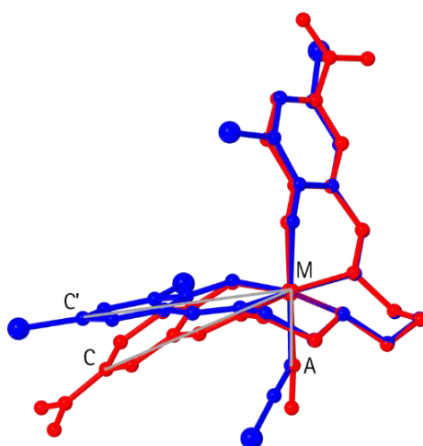


Figure 23: Comparison of the salpet structure of P1 (red) and [Fe(salpet_{Br,Ci})NCS] (blue). Only one [Fe(salpet_{H,NO2})NC] unit of P1 is shown. This unit is corresponding to Fe2 (Table 6). Hydrogen atoms have been omitted for clarity.

Table 7: Shortest angle between the binding atom (A) of the monodentate ligand (X) and the outer carbon atom (C) of the phenyl ring inside [M(salpet)X] for P1(acetone), P1 and P2 (Figure 23). The numbering of the metal ions is corresponding to the metal ions in Table 6.

metal ion or compound	shortest angle A-M-C in degree			
	P1(acetone)	P1	P2 (W1)	P2 (W2)
M1	83.2(2)	80.7(2)	69.2(3)	81.3(3)
M2	86.0(2)	66.7(2)	81.6(3)	66.3(3)
M3	67.1(2)	85.7(2)	86.1(3)	96.2(3)
M4	64.0(2)	70.2(2)	66.2(3)	68.9(3)

Magnetic Data and Mössbauer Spectroscopy

The temperature-depending magnetic susceptibility was measured in the range from 5 to 300 K for P1 and P2 (Figure 24). All $\chi_m T$ values were calculated for the formula approximated by the elemental analysis, which suggests a hygroscopic behavior for both compounds. P1 shows a gradual decrease from $\chi_m T = 8.6 \text{ emu mol}^{-1} \text{ K}$ at 300 K to $\chi_m T = 4.9 \text{ emu mol}^{-1} \text{ K}$ at 30 K with a subsequent drop to $3.7 \text{ emu mol}^{-1} \text{ K}$ at 5 K caused by the ZFS. At 300 K, the $\chi_m T$ value is relatively close to the theoretically calculated value of $9.5 \text{ emu mol}^{-1} \text{ K}$ for one diamagnetic molybdenum(IV) ion in the LS state, 2 iron(III) ions in the LS state and 2 iron(III) ions in the HS state. With regard to the stronger rising $\chi_m T$ values above 200 K, it is likely that the SCO will continue above 300 K. Furthermore, the low temperature $\chi_m T$ value corresponds roughly to a spin transition from one iron(III) in the HS to the LS state, which has the theoretically calculated value of $5.5 \text{ emu mol}^{-1} \text{ K}$ and which matches the single crystal structure at 100 K. Therefore, P1 is likely to undergo an SCO from [Mo^{IV}(LS)Fe^{III}(LS)₃Fe^{III}(HS)] at low temperatures to [Mo^{IV}(LS)Fe^{III}(LS)₂Fe^{III}(HS)₂] slightly above RT. The SCO might even continue resulting in more than two iron(III) ions in the HS state per molecule. Light irradiation experiments at 5 K did not show any change

of the $\chi_m T$ value. A second sample was synthesized according to the procedure of P1 (P1MB). P1MB was analyzed by Mössbauer spectroscopy at RT and 77 K to confirm its spin states (Figure 25). At RT, one doublet can be observed with an isomer shift of 0.37 mm s⁻¹ and a quadrupole splitting of 0.7 mm s⁻¹ corresponding to an iron(III) HS state. At 77 K, two doublets can be observed. The first one with an isomer shift of 0.44 mm s⁻¹ and a quadrupole splitting of 0.80 mm s⁻¹ corresponding to an iron(III) HS state and with a ratio of 54 %. The second doublet shows an isomer shift of 0.21 mm s⁻¹ and a quadrupole splitting of 2.86 mm s⁻¹ corresponding to an iron(III) LS state and with a ratio of 46 %. These data suggest an SCO between 77 K and RT from two iron(III) in the LS state and two iron(III) in the HS state to four iron(III) in the HS state. While the magnetic data and Mössbauer spectra agree that an SCO occurred, both measurements disagree about the number of iron(III) ions per molecule that showed an SCO. Partial solvent loss might be an explanation, which can be easier prevented for Mössbauer measurements. Another reason is probably the reproducibility of the synthesis, which is discussed in Chapter 4.3.3.

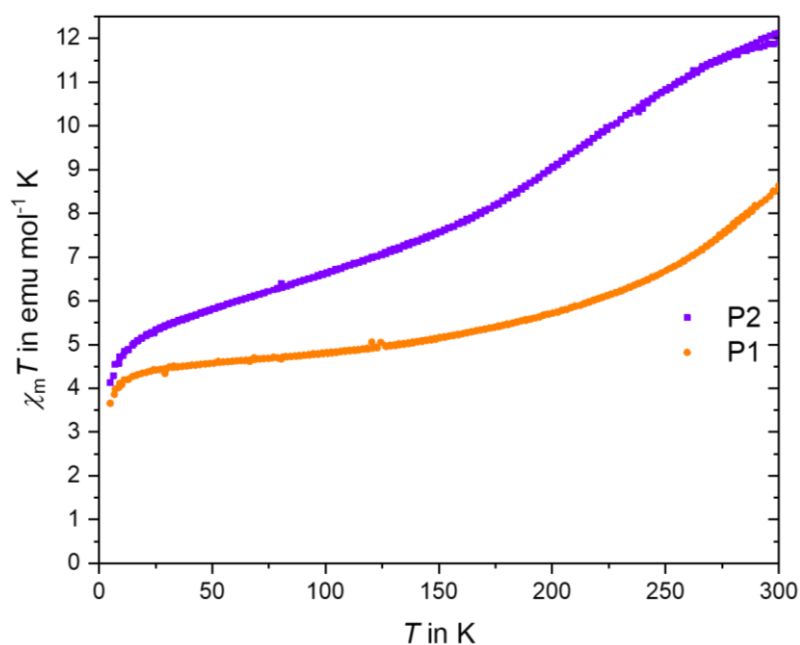


Figure 24: $\chi_m T$ – T plot of P1 and P2.

P2 shows a gradual decrease from $\chi_m T = 12.1$ emu mol⁻¹ K at 300 K to $\chi_m T = 5.4$ emu mol⁻¹ K at 30 K which can be roughly divided into two parts. While the $\chi_m T$ value decreases stronger from 12.1 emu mol⁻¹ K to 7.9 emu mol⁻¹ K at 165 K, at lower temperatures it decreases linear to 5.5 emu mol⁻¹ K at 30 K. At temperatures below 30 K the $\chi_m T$ value drops to 4.1 emu mol⁻¹ K at 5 K due to the ZFS. The observed change of the $\chi_m T$ value is about 6.7 emu mol⁻¹ K, which is comparable to an ETCST of two [WCo] (7 emu mol⁻¹ K). However, while a diamagnetic spin state with $\chi_m T = 0$ is expected for a typical [W^{IV}(LS)Co^{III}(LS)] redox couple at low temperatures,^[103,142,145] the value of P2 at 30 K is 5.4 emu mol⁻¹ K and therefore is already closer to two [W^{IV}Co^{II}(HS)] states. Subsequently, the $\chi_m T$ value

at 300 K is too high for an $[W^{IV}(LS)Co^{III}(LS)]/[W^{VI}Co^{II}(HS)]$ ETCST described previously.^[16,103,142,145] Two possible explanations could be: a cobalt(III) SCO, which is unlikely due to the weak ligand field needed,^[8,143,144] or a not yet observed second ETCST with the $[W^{VI}Co^{II}(HS)Co^{III}(LS)]/[W^{VI}Co^{II}(HS)Co^{II}(HS)]$ redox couple.

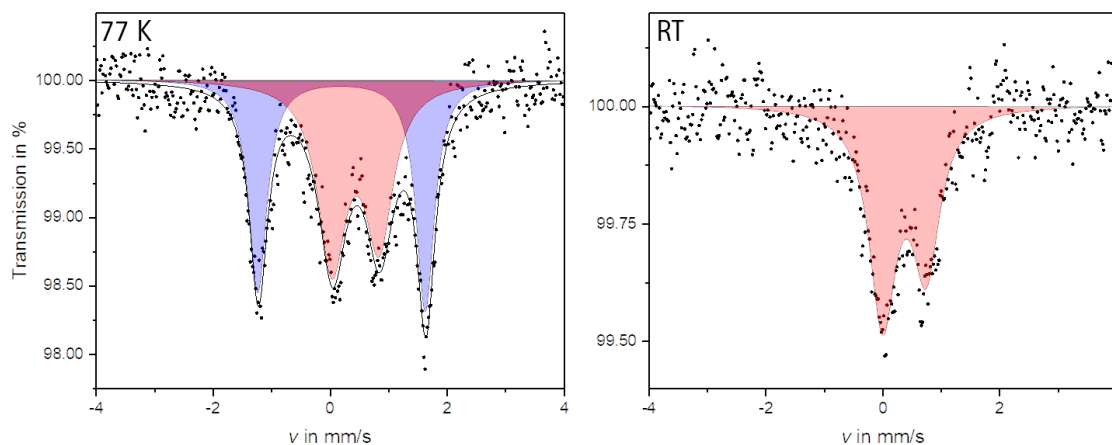


Figure 25: Mössbauer Spectra of P1MB at RT and 77 K. The dots visualize the measurement, the black line, the fits, red area the iron(III) HS state absorption and the blue are the iron(III) LS state absorption.

UV-Vis Spectroscopical Measurements

UV-Vis spectra for P1 and its precursor $[Fe(salpet_{H,NO_2})Cl]$ were measured in benzonitrile at RT (Figure 26) to determine possible metal-metal charge transfer bands. Furthermore, temperature-depending UV-Vis spectra have been measured for P2 in butyronitrile (Figure 27) to determine a possible temperature induced spin change in solution.

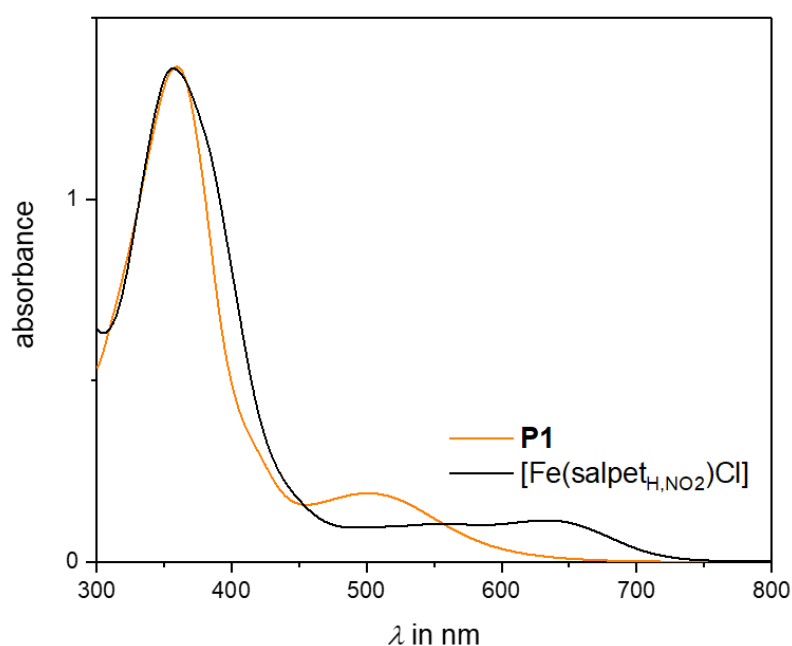


Figure 26: UV-Vis spectra at RT of P1 and its precursor complex $[Fe(salpet_{H,NO_2})Cl]$.

4. Derivatives of Spin Crossover Complexes as Building Blocks

Both spectra for **P1** and $[\text{Fe}(\text{salpet}_{\text{H},\text{NO}_2})\text{Cl}]$ show an intense absorption band at 359 nm and 357 nm, respectively, resulting from a $\pi \rightarrow \pi^*$ transitions of the ligands phenyl rings.^[31,146,147] While two further absorption bands at 557 nm and 633 nm were observed for $[\text{Fe}(\text{salpet}_{\text{H},\text{NO}_2})\text{Cl}]$, only one additional absorption band at 502 nm was observed for **P1**. The two bands of $[\text{Fe}(\text{salpet}_{\text{H},\text{NO}_2})\text{Cl}]$ might be caused by ligand-metal charge transfer (LMCT) of the phenolate^[31] and a chloride LMCT, respectively. Note that the band at 633 nm disappears after the reaction to **P1** and the band at 557 nm is not only shifted to 502 nm but also significantly increased. Therefore, it is suggested that the band at 502 nm of **P1** is caused by the LMCTs of the phenolate and cyanide ligands.^[31]

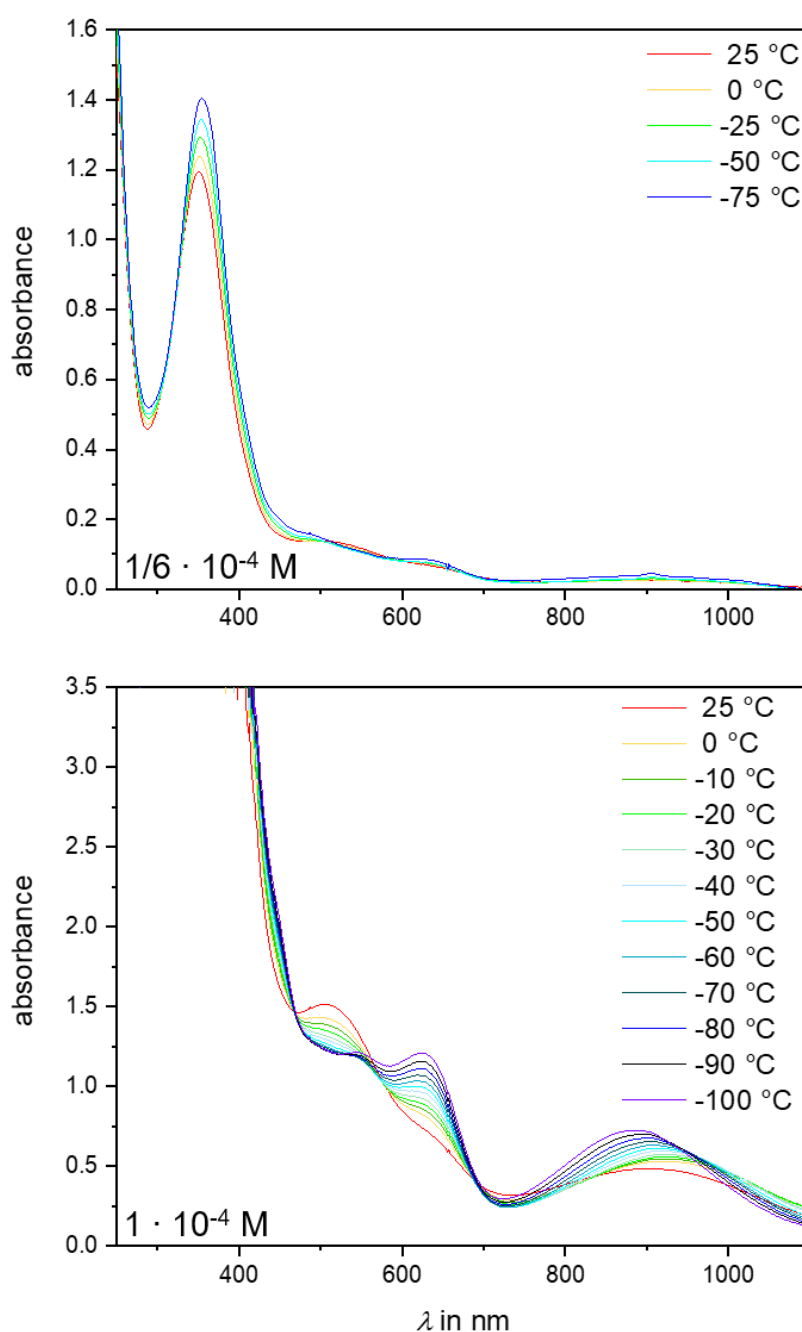


Figure 27: Temperature-depending UV-Vis spectra of **P2** with a concentration of $c = 6^{-1} \cdot 10^{-4} \text{ M}$ and 10^{-4} M .

Cooling a solution of **P2** in butyronitrile with liquid nitrogen results in a color change from red to green (Figure 28). To visualize all four main absorption bands clearly, two different concentrations were used for measuring the UV-Vis spectra of **P2**. The temperature was varied between 25 °C and -100 °C. All absorption bands of **P2** are influenced by the temperature changes resulting in an isosbestic point at 562 nm. This is probably caused by an equilibrium of two states, possibly through an ETCST between $[W^{IV}(LS)Co^{III}(LS)]/[W^{VI}Co^{II}(HS)]$ or $[W^{VI}Co^{II}(HS)Co^{III}(LS)]/[W^{IV}Co^{II}(HS)Co^{II}(HS)]$. O. Sato et al. measured the UV-Vis spectra of three different tetranuclear cobalt grid complexes. These complexes contained only cobalt(II) or cobalt(III) ions. In contrast to the absorption band around 475 nm, which can be observed for cobalt(II) and cobalt(III) complexes, the cobalt(III) complex shows a band at 375 nm and an intense broad band around 800 nm.^[148] Both bands are comparable with the absorption band of **P2** at 355 nm and 884 nm, which indicate an increasing amount of cobalt(III) with decreasing temperature. This confirms the assumption of an electron transfer.

Similar complexes showing this kind of ETCST behavior were analyzed by temperature-depending UV-Vis spectroscopy in solid-state by Ohkoshi et al.^[102,104] Due to the similar structure of **P1** and **P2** an intense $\pi \rightarrow \pi^*$ absorption band at 355 nm can be observed which is caused by the ligands phenyl rings.^[31,146,147] Probably, this band is overlapping with a d-d band of tungsten(IV)^[102] explaining the increase of intensity with decreasing temperature through a $[W^{VI}Co^{II}(HS)] \rightarrow [W^{IV}(LS)Co^{III}(LS)]$ transition. On the other hand the band might overlap with a W^{VI} -CN LMCT band.^[102] This band would decrease with a typical $[W^{VI}Co^{II}(HS)] \rightarrow [W^{IV}(LS)Co^{III}(LS)]$ transition but increase with a $[W^{VI}Co^{II}(HS)Co^{II}(HS)] \rightarrow [W^{VI}Co^{II}(HS)Co^{III}(LS)]$ transition, which is suggested by the magnetic data. The two bands next to the isosbestic point (562 nm) at 520 nm and at 625 nm decrease and increase, respectively, with a sinking temperature. Therefore, both can be assigned to metal-metal charge transfer (MMCT) bands and might overlap with the LMCT band of the phenolate as for **P1**. At 520 nm the transition is proposed to be a $Co^{II} \rightarrow W^{VI}$ MMCT and at 625 nm to be a $W^{IV} \rightarrow Co^{III}$ MMCT,^[102,104] which supports the known $[W^{VI}Co^{II}(HS)] \rightarrow [W^{IV}(LS)Co^{III}(LS)]$ ETCST behavior for different W-Co compounds.

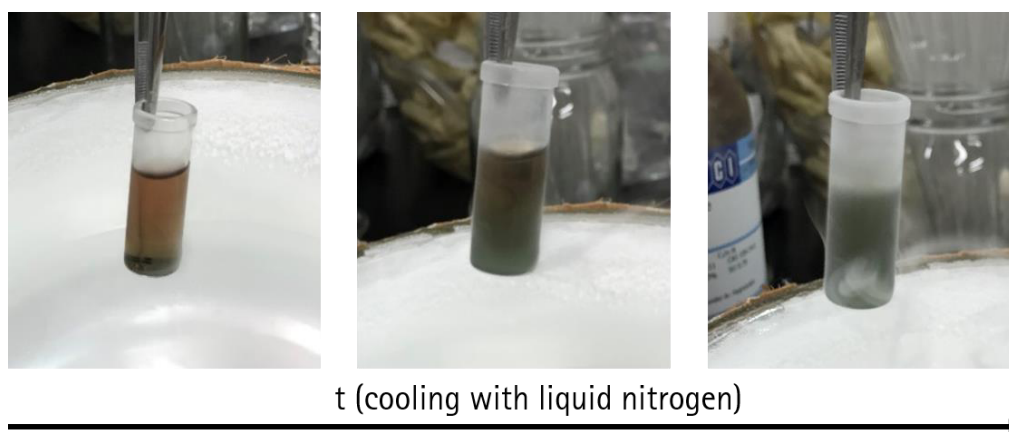


Figure 28: Color change of **P2** in butyronitrile while cooling with liquid nitrogen.

Electrochemical Measurements

A CV was measured for P1 (Figure 29) and P2 (Figure 30) to analyze the possibilities of an MMCT between Mo-Fe and W-Co, respectively.

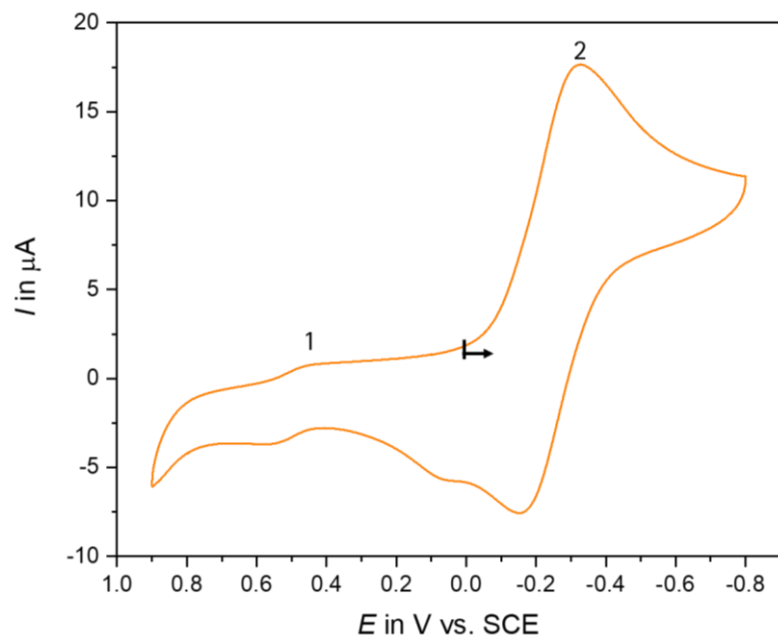


Figure 29: CV of P1.

P1 shows two quasi-reversible redox waves. Its first redox wave at $E_{1/2} = 0.5$ V corresponds to the $[\text{Mo}^{\text{IV}}\text{Fe}^{\text{III}}_4]/[\text{Mo}^{\text{V}}\text{Fe}^{\text{III}}_4]$ redox couple and the second one at -0.09 V to the $[\text{Mo}^{\text{IV}}\text{Fe}^{\text{III}}_4]/[\text{Mo}^{\text{IV}}\text{Fe}^{\text{II}}_4]$ redox couple (Table 8) resulting in a $\Delta E_{1/2}(\text{Mo-Fe})$ value of 0.59 V. Note that the redox potentials of P1s iron ions have higher values than the redox potential of the mononuclear precursor complex $[\text{Fe}(\text{salpet}_{\text{H,N02}})\text{Cl}]$ which is at $E_{1/2} = -0.26$ V (Chapter 4.1), while mononuclear complexes of the general formula $[\text{Fe}(\text{salpet}_{\text{R1,R2}})\text{CN}]$ usually show smaller values than $[\text{Fe}(\text{salpet}_{\text{R1,R2}})\text{Cl}]$ (as shown in Chapter 4.1). Furthermore, the ratio of $i_{\text{red}}(2)/i_{\text{ox}}(1) = -4.83$ can be calculated from the measured current which depends on the ion concentration. The value of 4.83 is larger than the expected ratio of 4 which might be caused by impurities of $[\text{Fe}(\text{salpet}_{\text{H,N02}})\text{Cl}]$.

Table 8: Redox potentials of P1 and P2.

		E_{red}	E_{ox}	$E_{1/2}$
P1	1	0.45 V	0.55 V	0.50 V
	2	-0.33 V	0.15 V	-0.09 V
P2	1	-0.28 V	-0.18 V	-0.23 V
	2	-1.40 V	-	-
	3	-1.71 V	-1.46 V	-1.585 V

To the best of our (mentioned researcher from Chapter 4) knowledge, there is no Mo-Fe ETCST complex.^[16] However, if the concept of Nihei et al.^[15] can be applied not only to [FeCo] ETCST complexes, but also to other species, the [Mo^{IV}Fe^{III}]₄ state is comparable with the diamagnetic [Fe^{II}Co^{III}] state. Therefore, the redox potentials must be adjusted to $\Delta E_{1/2}(\text{Mo-Fe}) > 0.59 \text{ V}$ in order to increase the possibility for a [MoFe] ETCST complex.

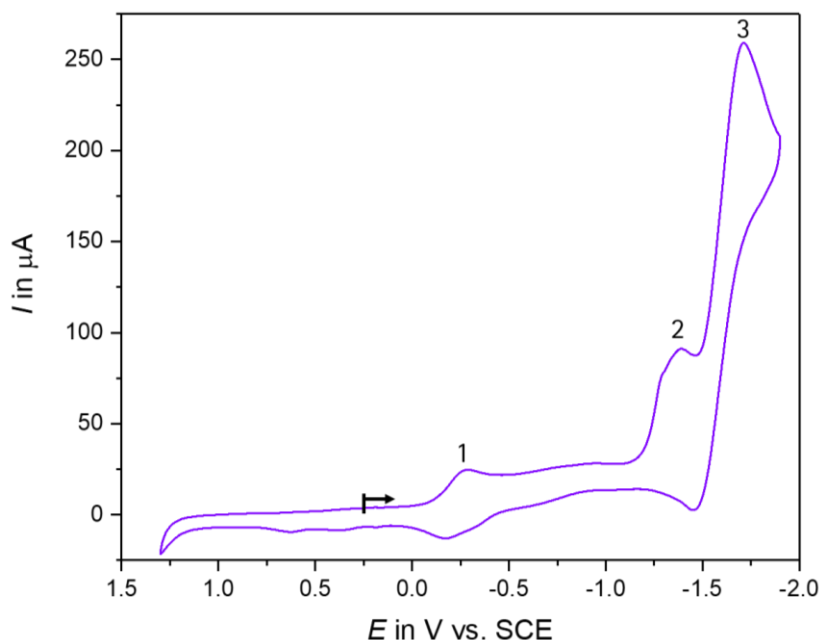


Figure 30: CV of P2.

P2 shows two redox waves and one irreversible reduction. The quasi-reversible redox wave (1) at -0.23 V can be assigned to the reduction and oxidation of tungsten(V) through the comparison with the CV of $(\text{Bu}_4\text{N})_3[\text{W}(\text{CN})_8]$ (Figure 63, page 151). In addition, the irreversible reduction peak (2) at -1.4 V can be assigned to the cobalt(III) reduction and the redox wave (3) at -1.585 V to the NO_2 group. Note that the NO_2 redox potential is known to show a strong reduction peak.^[149] This is supported by the current ratios $I_{\text{red}}(2)/I_{\text{red}}(1) = 3.7$ (expected for $[\text{W}^{\text{V}}\text{Co}^{\text{III}}_3\text{Co}^{\text{II}}]$: 3) and $I_{\text{red}}(3)/I_{\text{red}}(1) = 10.5$ (expected for $[\text{W}^{\text{V}}\text{Co}^{\text{III}}_3\text{Co}^{\text{II}}]$: 8). The deviation from the expected values might be due to impurities of the cobalt precursor complex $[\text{Co}(\text{salpet}_{\text{H},\text{NO}_2})\text{Cl}]$. However, the cobalt oxidation cannot be observed, possibly due to an overlap with the NO_2 redox wave (3) or intramolecular electron transfer processes. Furthermore, the $\Delta E_{\text{red}}(\text{W-Co})$ value is with 1.12 V larger than the $\Delta E_{1/2}$ for [CoFe] ETCST compounds.^[15]

Temperature Dependent IR-Spectra

Temperature-dependending IR-spectra of P2 have been measured in KBr pellets in the temperature range of RT to $-150 \text{ }^\circ\text{C}$ (Figure 64, page 151). Previous examples of $[\text{W}^{\text{V}}\text{Co}^{\text{III}}]/[\text{W}^{\text{V}}\text{Co}^{\text{II}}]$ ETCST compounds showed a shift and a strong decrease of the W-CN band through the $[\text{W}^{\text{V}}\text{Co}^{\text{III}}] \rightarrow [\text{W}^{\text{V}}\text{Co}^{\text{II}}]$ transition.^[102]

However, **P2** (Figure 31) does not show a significant change of intensity and only a small shift of 4 cm^{-1} . In contrast to the magnetic data, the IR spectra do not indicate a phase transition. One explanation might be the previously mentioned $[\text{WCo}^{\text{II}}_{\text{HS}}\text{Co}^{\text{III}}_{\text{LS}}]/[\text{W}^{\text{VI}}\text{Co}^{\text{II}}_{\text{HS}}\text{Co}^{\text{II}}_{\text{HS}}]$ ETCST, which might show only small changes of the W-CN band in temperature-depending IR spectra. A second explanation might be the loss of crystal solvent in combination with the KBr-matrix, which might effect a possible ETCST behavior.

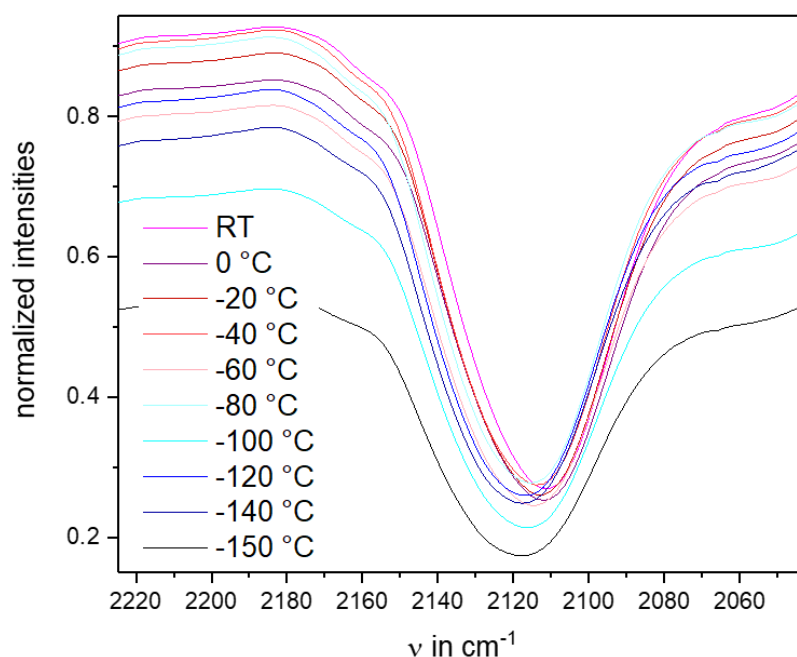


Figure 31: Temperature-depending IR spectra of **P2** showing the cyanide band.

4.3.3 Conclusion and Outlook

Two novel cyanide-bridged pentanuclear iron-molybdenum and cobalt-tungsten complexes have been presented. The two investigated compounds **P1** and **P2** are isostructural despite their different transition metal ions and each show different switching behavior. The first $[\text{MoFe}^{\text{III}}_4]$ complex can crystallize in two different solvent-depending structures, **P1** and **P1**(acetone) of which the sample **P1** was investigated further. **P1** shows a thermally induced gradual incomplete SCO of the iron(III) ions which is indicated by the coordination bond lengths at 100 K, the temperature-depending magnetic data, and Mössbauer spectra. No signs of a charge transfer could be observed by UV-Vis spectra and electrochemical measurement. In addition to these data, a crystal structure near RT, magnetic data up to 400 K and additional Mössbauer spectra for the confirmation of the spin states should be measured from the same sample.

P2 shows increased coordination bond lengths for half of the cobalt ions at 100 K indicating the cobalt(II) HS state, although cobalt(III) complexes were used for the reaction. Therefore, it seems that

during the reaction an ETCST occurred, which might not be reversible in solid-state. The magnetic data show a gradual change of 6.7 emu mol⁻¹ K which can hardly be explained by literature data but might arise from a not yet described [W^VCo^{II}(HS)Co^{III}(LS)]/[W^VCo^{II}(HS)Co^{II}(HS)] ETCST. Temperature-depending UV-Vis spectra show increasing and decreasing bands with isosbestic points suggesting an ETCST. However, these results cannot clearly infer whether a [W^VCo^{II}(HS)] → [W^{IV}(LS)Co^{III}(LS)] or [W^{VI}Co^{II}(HS)Co^{II}(HS)] → [W^VCo^{II}(HS)Co^{III}(LS)] ETCST occur, since the different interactions in solid-state and solution have a strong impact on the switching behavior.^[35] Also, for this compound, a crystal structure at RT should be measured, not only to observe the coordination bond lengths but also to gain new information about the correlation between the distortion of the salpet ligand and the spin state, as suggested by the crystal structures at 100 K for **P1** and **P2**. Temperature-depending NMR spectra in solid-state and solution might give additional information if **P2** is in a diamagnetic or paramagnetic spin state as demonstrated previously for other compounds.^[24] Furthermore, electron paramagnetic resonance (EPR) spectra and tungsten Mössbauer spectroscopy at different temperatures could be measured to obtain more information of the spin states. Beside additional measurements, new synthesis of complexes with similar redox potentials could be performed to compare the spin states and possible switching behavior.

It should be noted that the compounds **P1**, **P1**(acetone) and **P2** are sensitive to solvent loss and the samples might contain impurities of the mononuclear precursor. Some syntheses yielded acceptable results, as for the sample for **P1**, **P1**(acetone), **P1MB** and **P2**, while other syntheses just yielded the mononuclear precursor. Important factors might be the temperature and the amount of water inside the organic solution. Therefore, the magnetic data ($\chi_m T$ values) might show small deviations. For this reason, the syntheses need to be refined to obtain more reliable results of the bulk sample. However, the switching behavior of both samples is clearly demonstrated. Furthermore, a technique of measuring single crystal structures near RT without losing the crystal solvent should be applied for both compounds as well as additional measurements for determining the spin states at different temperatures. Similar techniques should be used for time-consuming measurements near RT such as Mössbauer spectroscopy, which is already difficult due to the molybdenum. Especially the switching mechanism of **P2** is not solved yet and needs to be investigated further, offering the possibility of identifying a yet unknown [W^VCo^{II}_{HS}Co^{III}_{LS}]/[W^{VI}Co^{II}_{HS}Co^{II}_{HS}] ETCST.

5. Co-Crystallization of Tetranuclear [Co₂Fe₂]-Complexes

In Chapter 5, the publication *Solid-State Hydrogen-Bond Alteration in a [Co₂Fe₂] Complex with Bifunctional Hydrogen-Bonding Donors* is presented. This Communication was published 2019 in *Chemistry - A European Journal*.^[150] The copyright is held by Wiley-VCH and it is reprinted with permission.

During the last 10 years, a large number of ETCST square [Co₂Fe₂] complexes have been developed through molecular design and the choice of suitable anions.^[17,18,35,95,96,110-114] It was shown that some of these complexes can be switched through temperature changes in solution and protonation of the terminal cyanides by the addition of tetrafluoro acetic acid at a constant temperature.^[18,35] The second effect was mimicked in solid-state through the co-crystallization of ETCST [Co₂Fe₂] complexes with hydrogen-bond donor molecules such as 4-cyanophenol,^[19] *p*-hydroquinone, and phloroglucine.^[115] This strategy provides further possibilities of changing the ETCST behavior through the hydrogen-bond controlled assemble of these compounds. In the following publication, this strategy was used to control the aggregation of [Co₂Fe₂] complexes with the bifunctional hydrogen-bond donor *p*-aminobenzoic acid. An irreversible alteration of the hydrogen interactions between the complex and organic molecule could be observed by removing the crystal solvent as well as a reversible alteration, which is coupled with the change of the electronic state.

All the experiments and analysis for this publication were performed by the author of this thesis and Yuta Yanai. Additionally, the author of this thesis added new ideas for characterizing the desolvation process and refined the manuscript. Ryo Takayama and Marina Kato refined some of the results. Dr. Yoshihiro Sekine helped with the initial idea. Prof. Dr. Masayuki Nihei started with the initial idea, wrote the manuscript and helped through discussions. Prof. Dr. Hiroki Oshio and Prof. Dr. Franz Renz helped through discussions with the analysis and refined the manuscript.

The formatting of the following publication was adjusted to the formatting of this dissertation and the abbreviation of the investigated compound [Co₂Fe₂(bpy*)₄(CN)₆(tp*)₂](PF₆)₂ · 2*p*-aminobenzoic acid · 4benzonitrile · 2diisopropyl ether (bpy*: 4,4'-dimethyl-2,2'-bipyridine) was changed from **1** (in the original publication) to **SQ1** to avoid confusion with the compounds in Chapter 3. To the references, the letter S or SI were added for the paper and the Supporting Information, respectively. However, the wording and content remained the same. Supporting information for this article are given in the Appendix Chapter 8.3 (page 152). The other abbreviations, references as well as the labelling of figures and tables for the following publication and the corresponding supporting information are treated separately from the other chapters.

Solid state hydrogen bond alterations in a [Co₂Fe₂] complex with bifunctional hydrogen bonding donors

Masayuki Nihei,^[a] Yuta Yanai,^[a] Dominik Natke,^[b] Ryo Takayama,^[a] Marina Kato,^[a] Yoshihiro Sekine,^[a] Franz Renz,^[b] and Hiroki Oshio^{*[a]}

[a] Dr. M. Nihei, Mr. Y. Yanai, Miss M. Kato, Dr. Y. Sekine, Prof. H. Oshio
Department of Chemistry, Faculty of Pure and Applied Sciences, University of Tsukuba
Tennodai 1-1-1, Tsukuba, Ibaraki, Japan
E-mail: nihei@chem.tsukuba.ac.jp

[b] Mr. D. Natke, Prof. F. Renz
Institut für Anorganische Chemie, Leibniz University Hannover
Callinstr. 9 D-30167 Hannover, Germany

[†] These authors contributed equally to this work.
Chemistry a European Journal, 2019, 25,7449–7452

Abstract: A hydrogen bonding donor-acceptor system, [Co₂Fe₂(bpy*)₄(CN)₆(tp*)₂](PF₆)₂·2ABA·4BN·2PE (SQ1_{solv}), was prepared by co-crystallization of an external stimuli-responsive cyanide-bridged tetranuclear [Co₂Fe₂] complex and bifunctional hydrogen-bonding donors, *p*-aminobenzoic acid (ABA). Compound 1_{solv} exhibited a gradual electron transfer-coupled spin transition (ETCST), and the removal of solvent molecules led to an abrupt thermal ETCST behavior with increased transition temperature. X-ray structural analysis revealed that the modification of ETCST was caused by a significant alteration of a hydrogen-bonding mode between the tetranuclear [Co₂Fe₂]²⁺ cations and ABA molecules. Variable temperature IR measurements indicated that the desolvated form, SQ1_{desolv}, showed dynamic alteration of hydrogen-bonding interactions coupled with thermal ETCST behavior. These results suggested that the tetranuclear [Co₂Fe₂] complex shows solid state modulations of hydrogen bond strengths by external stimuli.

Hydrogen bonding (HB)-directed redox reactions and external stimuli-induced HB alterations play an important role in biological functions in natural proteins. Flavoproteins, which are ubiquitous redox enzymes, participate wide range of biological process, and the redox processes of the flavin cofactors were directed by HB interactions with apo-enzyme.^[S1] Bacteriorhodopsin acts as a light-driven proton pump and this function originates from the pK_a modulations of the chromophores induced by photoisomerization.^[S2] The biological functions described above are based on combined two orthogonal equilibria, acid-base equilibria and redox/photoisomerization equilibria. In molecular systems, photochromic molecules with proton acceptor/donor sites have been reported to exhibit pH dependent photo-isomerization and reversible light-induced pK_a changes, where ΔpK_a is typically in the range of 1–3 pK_a units.^[S3] Such photochromic molecules were applied as a photo-responsive molecular switch in multi-component systems, such as light-gated catalytic reactions,^[S4a] light-controlled particle aggregations,^[S4b] and optical molecular logic system.^[S4c] On the other hand, redox-active molecules

with HB donor or acceptor sites have been reported as bio-inspired receptors and the redox potentials of the receptors were significantly altered by HB interactions with target molecules.^[S5] It should be noted that all functions described above are only operative in solution.

Hydrogen-bonded molecular crystals showed unique solid-state properties, such as HB-directed ferroelectricity and electric/proton conductivities. Such solid-state properties are based on the HB interactions between HB donor and acceptors, and are significantly influenced by the HB strengths.^[S6] Molecules exhibiting solid state alterations of HB interactions by external stimuli are, therefore, expected to be useful switching unit in multi-functional molecular solids. In the last decade, cyanide-bridged mixed-valent Co-Fe complexes were recognized as a family of external stimuli-responsive switching molecules, and their switching behaviour is based on intramolecular electron transfers between iron and cobalt ions, which is coupled with spin transition in the cobalt ions,^{[S7],[S8]} herein we refer to this phenomenon as an "electron transfer-coupled spin transition" (ETCST). Tetranuclear mixed-valent complexes with a general formula of [Co₂Fe₂(CN)₆(L1)₂(L2)₄](X)₂ ([Co₂Fe₂](X)₂, L1 and L2: tri- and bi-dentate ligands for Fe and Co ions, X: counter anions), have been reported to show thermal and light-induced ETCST behaviour between LS ($[(lS-Co^{II})_2(lS-Fe^{II})_2]$) and HS ($[(hS-Co^{II})_2(lS-Fe^{II})_2]$) states (*lS* and *hS* denote low-spin and high-spin states, respectively),^[S8] and the transition temperature ($T_{1/2}$) of the thermal ETCST in solution can be modulated by the addition of organic acids.^{[S8],[S9]} The pH dependent ETCST behaviour in solution is originating from the interplay of thermal intramolecular redox equilibrium (ETCST) and the acid-base equilibrium. The [Co₂Fe₂]²⁺ cations have two terminal cyanide groups coordinating to the iron ions, and non-coordinating nitrogen atoms act as Brønsted base. Protonation reactions of the terminal nitrogen atoms of [Co₂Fe₂] cause positively shifted redox potential of the iron ions, and affects intermetallic electron transfers in ETCST.^[S9] Recently, we have reported that the [Co₂Fe₂]²⁺ cations act as a HB acceptor, and co-crystallizations with organic HB donors give a variety of HB donor-acceptor systems.^[S10] With all in mind, it is expected that a donor-acceptor system composed of [Co₂Fe₂]²⁺ and suitable HB donor may show HB dependent ETCST and external stimuli-induced alterations of HB interactions in solid state. Herein, we employed 4-aminobenzoic acid (ABA) as an asymmetric bifunctional HB donor. ABA has been known to act as a bridging HB donor in a variety of HB donor-acceptor crystals, in which amino and carboxy groups showed weak and strong HB donor abilities, respectively.^[S11] We report herein a HB donor-acceptor system, [Co₂Fe₂(bpy*)₄(CN)₆(tp*)₂](PF₆)₂·2ABA·4BN·2PE (**SQ1**_{solv}) (bpy* = 4,4'-dimethyl-2,2'-bipyridine, tp* = hydrotris(3,5-dimethylpyrazol-1-yl)borate, BN = benzonitrile, PE = diisopropyl ether), exhibiting solid-state alterations of HB interactions. In **SQ1**_{solv}, significant alterations of the HB mode, associating with a change of ETCST behaviour, was found upon a single-crystal-to-single-crystal (SC-SC) transformation from **SQ1**_{solv} to a de-solvated form, **SQ1**_{desolv}, ([Co₂Fe₂(bpy*)₄(CN)₆(tp*)₂](PF₆)₂·2ABA). In addition, solid-

state modulations of HB interactions through thermal ETCST of $\text{SQ1}_{\text{desolv}}$ was investigated by variable temperature IR measurements.

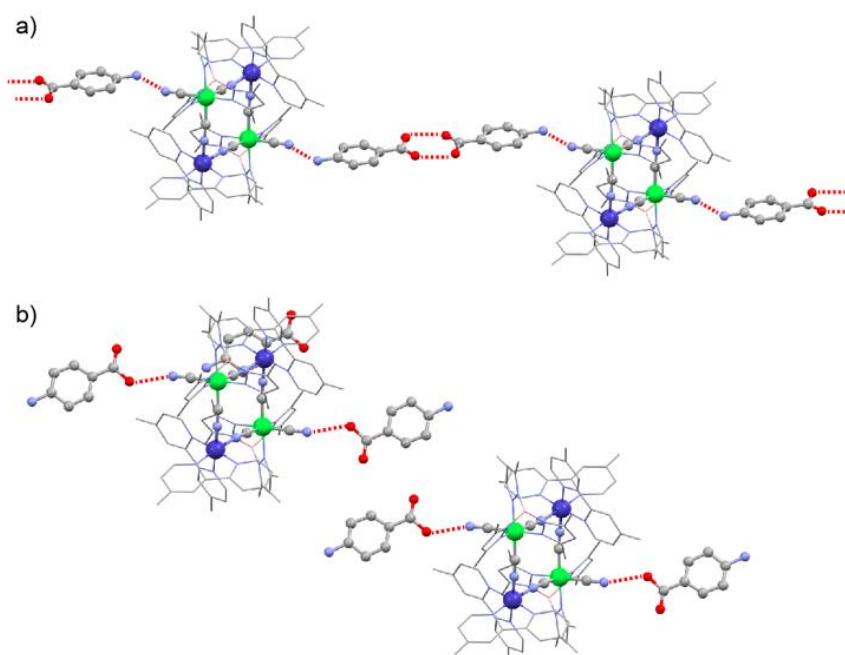


Figure 1. X-ray crystal structure of SQ1_{solv} (a) and $\text{SQ1}_{\text{desolv}}$ (b). Red dotted lines represent hydrogen-bonding interactions between terminal cyanide nitrogen (N_{CN}) and amino nitrogen (N_{ABA}) atoms (a) or carboxy oxygen atoms (b) in ABA molecules. Hydrogen atoms, counteranions, and solvent molecules have been omitted for clarity. Color code: C, gray; N, light blue; O, red; *ls* Co^{III} , blue; *ls* Fe^{II} , green.

Compound SQ1_{solv} was prepared by the reaction of $\text{Co}(\text{OTf})_2 \cdot 6\text{H}_2\text{O}$ with bpy^* , $\text{Bu}_4\text{N}[\text{Fe}(\text{CN})_3(\text{tp}^*)]$, $\text{Bu}_4\text{N}(\text{PF}_6)$, and ABA in benzonitrile. X-ray structural analysis was performed at 100 K (Figure 1a) and the crystallographic and structural parameters were summarized in Table S1 and S2. Compound SQ1_{solv} crystallized in a triclinic space group $P\bar{1}$ and the asymmetric unit contains a dinuclear $[(\text{bpy}^*)_2\text{Co}-(\mu\text{-CN})\text{-Fe}(\text{CN})_2(\text{tp}^*)]$ sub-unit of the $[\text{Co}_2\text{Fe}_2]^{2+}$ cation and two ABA molecules (Figure 1a). The $[\text{Co}_2\text{Fe}_2]^{2+}$ cation has a tetranuclear cyclic core composed of two iron and two cobalt ions bridged by cyanide ions, and resides on the centre of symmetry. The average coordination bond lengths of Co and Fe ions are 1.929(3) and 1.965(4) Å, which are characteristic of *ls*-Co(III) and *ls*-Fe(II) ions, respectively, suggesting the $[\text{Co}_2\text{Fe}_2]^{2+}$ cation being in the LS states ($[(\text{ls}\text{-Co}^{\text{III}})_2(\text{ls}\text{-Fe}^{\text{II}})_2]$) at 100 K.^[S7-S9] The ABA molecules formed HB dimers with the carboxy groups and the interatomic distance between carboxy oxygen atoms is 2.639(5) Å (red dotted lines in Figure 1a). The amino nitrogen atoms (N_{ABA}) of the ABA dimers show weak HB interactions with the terminal cyanide nitrogen atoms (N_{CN}) of the $[\text{Co}_2\text{Fe}_2]$ cations and interatomic distances between N_{CN} and N_{ABA} was 2.948(8) Å. As a result, the $[\text{Co}_2\text{Fe}_2]^{2+}$ cations and the ABA dimers formed hydrogen bonded one-dimensional chains (Figure 1a). Crystal solvent molecules of BN and PE are located in the void between the hydrogen bonded chains (Figure S1).

Temperature dependent magnetic susceptibility measurements on the crystalline sample of SQ1_{solv} revealed the occurrence of thermal ETCST behaviour depending on the release of crystal solvent molecules (Figure 2). In SQ1_{solv} , the $\chi_m T$ value (6.16 emu mol⁻¹ K at 300 K) agrees with the theoretical value (ca. 6.5 emu mol⁻¹ K) for a magnetically isolated system of two low-spin Fe(III) ($S = 1/2$) and two high-spin Co(II) ($S = 3/2$) ions,^[57-59] suggesting that the $[\text{Co}_2\text{Fe}_2]^{2+}$ cation is in the HS state ($[(hs\text{-Co}^{II})_2(ls\text{-Fe}^{III})_2]$). As the temperature was lowered, the $\chi_m T$ values showed a gradual decrease down to 1.21 emu mol⁻¹ K at 10 K, suggesting the occurrence of thermal ETCST from the paramagnetic HS state to the diamagnetic LS state with $T_{1/2} = 170$ K. The non-zero $\chi_m T$ values at lower temperature might be due to the partial release of solvent molecules in the sample, which was supported by the magnetic susceptibility measurements on the partially desolvated SQ1_{solv} (Figure S2 in the Supporting Information). After heating the sample at 400 K, the $\chi_m T$ - T profile significantly changed and an abrupt ETCST behaviour was observed at $T_{1/2} = 240$ K. Thermogravimetric (TG) measurements on 1_{solv} showed stepped weight loss upon heating up to 400 K (Figure S3 in the supporting information). The initial weight loss around 50 °C corresponds to the release of two PE molecules, and four BN molecules were released upon heating up to 100 °C. Further weight loss higher than 180 °C corresponds to the release of two ABA molecules. The TG measurements suggested that SQ1_{solv} shows stepwise release of solvent molecules and the significant change of the ETCST behaviour after heating up to 400 K is caused by the release of two PE and four BN molecules from the crystal lattice.

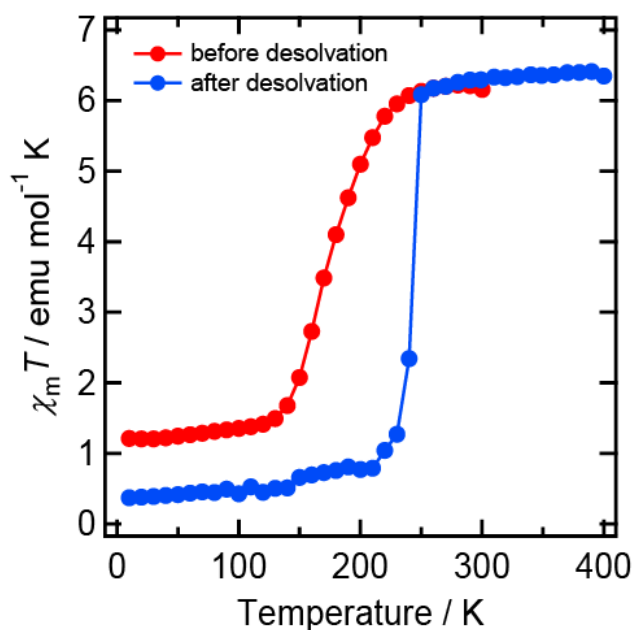


Figure 2. $\chi_m T$ - T plot for SQ1_{solv} before (red) and after (blue) desolvation.

Powder X-ray diffraction (PXRD) measurements on SQ1_{solv} were conducted to investigate the structural change upon release of solvent molecules (Figure S4 in the Supporting Information). The diffraction

peaks of **SQ1**_{solv} gradually diminished in intensity upon standing the crystalline sample of **SQ1**_{solv} at room temperature, and a new crystalline phase appeared after standing for 24 hours, suggesting the transformation of **SQ1**_{solv} to the desolvated form (**SQ1**_{desolv}) with retaining the crystallinity. Single crystals of **SQ1**_{desolv} were obtained by standing the single crystal of **SQ1**_{solv} for 24 hours at room temperature, and the structural analysis of **SQ1**_{desolv} was performed, in which the quality of diffraction data was relatively low due to the degradation of the crystal during the release of solvent molecules (Figure 1b, Table S1 and S2 in the Supporting Information). As a result, **SQ1**_{desolv} exhibited significant alteration of the HB mode between the [Co₂Fe₂]²⁺ cations and the ABA molecules upon SC-SC transformation from **SQ1**_{solv} induced by the solvent release. Compound **SQ1**_{desolv} adopts the same space group with **SQ1**_{solv}, while the unit-cell volume was reduced by 26%, which is due to the release of two PE and four BN molecules associating with the significant rearrangement of the [Co₂Fe₂]²⁺ cations and the ABA molecules (Figure S1 in the Supporting Information). Upon desolvation, the dimer structure of the ABA molecules in **1**_{solv} collapsed and new HBs were formed between the carboxy oxygen atoms (O_{ABA}) of ABA and the terminal nitrogen atoms (N_{CN}) of the [Co₂Fe₂] cations, resulting in a discrete HB donor-acceptor structure in **SQ1**_{desolv}. The interactions of N_{CN} with the stronger HB donor of carboxy groups led to the formation of stronger HB with $d_{\text{N(CN)}\cdots\text{O(ABA)}} = 2.79(3)$ Å at 100 K. The average coordination bond lengths of Co and Fe ions are 1.93(1) and 1.95(2) Å at 100 K and 2.07(2) and 1.93(2) Å at 270 K, respectively, indicating the occurrence of the thermal ETCST behaviour of **1**_{desolv} as seen in the magnetic data. The higher $T_{1/2}$ in **SQ1**_{desolv} (240 K) than **SQ1**_{solv} (170 K) could be ascribed to the formation of the stronger HB with ABA, which modulates the redox potential of iron ions to stabilize the LS state (Figure 2). In addition, the higher density of the crystal packing of **SQ1**_{desolv} led to the more abrupt and cooperative ETCST behaviour in comparison to that of **SQ1**_{solv}. Consequently, **SQ1**_{solv} exhibited solvent induced SC-SC transformation associating with the significant alteration of the HB mode, and the switching of the HB sites led to the modulation of transition temperature in solid state. Light-irradiation experiments were performed on a ground sample of **SQ1**_{desolv} at 5 K (Figure S5 in the Supporting Information). Upon irradiation at 808 nm at 5 K, a significant increase in $\chi_m T$ value was observed, suggesting an occurrence of light-induced ETCST of [Co₂Fe₂]²⁺ cations from the LS state to the metastable HS state. As the temperature was raised after turning off the laser light, the $\chi_m T$ values showed a sudden decrease at 100 K, which is ascribed to the thermal relaxation of the light-induced state to the ground state. This experiment demonstrated that [Co₂Fe₂]²⁺ cations in **SQ1**_{desolv} shows both thermal and light-induced ETCST behaviour.

In hydrogen-bonded benzoic acid derivatives, ν_{CO} frequencies are sensitive to the HB strengths with HB acceptors, and stronger HB interactions lead to lower frequencies in the ν_{CO} bands.^[S12] To obtain insights of the interplay between the ETCST and HB interactions in $\text{SQ1}_{\text{desolv}}$, variable temperature IR spectra were measured in the temperature range of 320 – 170 K (Figure 3). At 320 K, ν_{CN} absorption peaks were observed at 2147 and 2121 cm^{-1} , which are characteristic of the bridging and the terminal cyanide groups of the HS $[\text{Co}_2\text{Fe}_2]^{2+}$ cations (Figure 3a). When the temperature was lowered to 170 K, ν_{CN} intensity for the HS species decreased in intensity and new absorption peaks for the LS $[\text{Co}_2\text{Fe}_2]^{2+}$ cations appeared at 2095 and 2069 cm^{-1} .^[S7-S9]

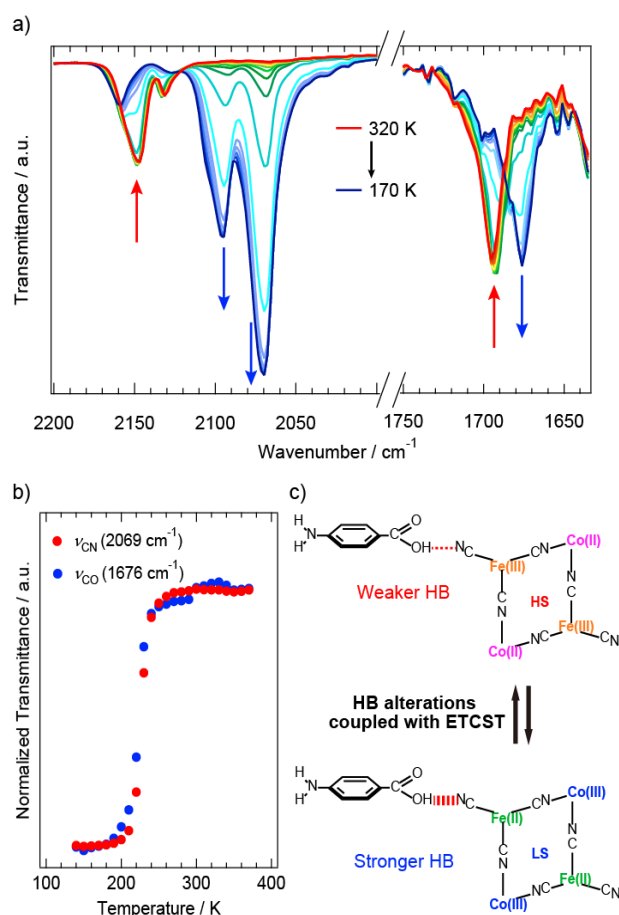


Figure 3. a) Variable temperature IR spectra of $\text{SQ1}_{\text{desolv}}$, b) temperature dependence of normalized transmittance of ν_{CN} and ν_{CO} peaks, c) Proposed scheme of HB alterations coupled with ETCST.

A ν_{CO} peak of ABA molecules in $\text{SQ1}_{\text{desolv}}$ was shifted from 1695 cm^{-1} at 320 K to 1676 cm^{-1} at 170 K associating with the thermal ETCST behaviour of the $[\text{Co}_2\text{Fe}_2]^{2+}$ cations. The -19 cm^{-1} shift of the ν_{CO} frequency suggests the formation of stronger HB bonds between ABA and LS $[\text{Co}_2\text{Fe}_2]^{2+}$ cations. Normalized transmittance of ν_{CN} and ν_{CO} peaks showed the same temperature dependence (Figure 3b). This result indicates that the electronic state change in $[\text{Co}_2\text{Fe}_2]^{2+}$ cations induced by the thermal ETCST is completely coupled with the alteration of HB interactions between the $[\text{Co}_2\text{Fe}_2]^{2+}$ cation and ABA (Figure 3c). In a series of hydrogen-bonded 1:1 pyridine-benzoic acid complexes, correlations

between ν_{CO} frequencies and pK_a values of the constituent molecules have been systematically studied.^[S12a] In $\text{SQ1}_{\text{desolv}}$, the change of the ν_{CO} frequencies (-19 cm^{-1}) between the hydrogen bonded ABA molecules with HS and LS [Co₂Fe₂]²⁺ cations suggested that the pK_a value of the LS [Co₂Fe₂]²⁺ cation is approximately one unit higher than that of the HS cation.

In summary, we presented solid-state alterations of HB interactions in a HB donor-acceptor system composed of ETCST-active [Co₂Fe₂]²⁺ cations and bifunctional HB donors. The HB donor-acceptor system showed HB-affected thermal ETCST behaviour and the ETCST temperature of the [Co₂Fe₂]²⁺ cations are changed by solid state alteration of HB modes. In addition, the [Co₂Fe₂]²⁺ cations exhibited dynamic HB alterations coupled with thermal ETCST behaviour. The present results suggested that the tetranuclear [Co₂Fe₂]²⁺ cation could act as a solid-state HB modulator, in which a certain pK_a change can be induced by external stimuli such as light irradiations. Such molecular unit can be useful for applications to multi-functional solids exhibiting switchable hydrogen-bond-based physical properties.

Acknowledgements

This work was supported by a JSPS KAKENHI Grant Number 26288021 and 16H06523. D. N. and F. R. would like to thank the German Academic Exchange Service (DAAD) and Hannover School for Nanotechnology (HSN) for funding.

Conflict of interest

The authors declare no conflict of interest.

Keywords: cobalt, cyanides, mixed-valent compounds, hydrogen bond, spin transition

- [S1] A. Niemz, V. M. Rotello, *Acc. Chem. Res.* **1999**, *32*, 44-52, and references therein.
- [S2] O. P. Ernst, D. T. Lodowski, M. Elstner, P. Hegemann, L. S. Brown, H. Kandori, *Chem. Rev.* **2014**, *114*, 126-163, and references therein.
- [S3] a) S. H. Kawai, S. L. Gilat, J. M. Lehn, *Eur. J. Org. Chem.* **1999**, 2359-2366; b) J. Vallet, J.-C. Micheau, C. Coudret, *Dyes Pigm.* **2016**, *125*, 179-184; c) J. Gurke, Š. Budzák, B. M. Schmidt, D. Jacquemin, S. Hecht, *Angew. Chem. Int. Ed.* **2018**, *57*, 4797.
- [S4] a) R. S. Stoll, S. Hecht, *Angew. Chem. Int. Ed.* **2010**, *49*, 5054-5075; b) P. K. Kundu, D. Samanta, R. Leizrowice, B. Margulis, H. Zhao, M. Börner, T. Udayabhaskararao, D. Manna, R. Klajn, *Nat. Chem.* **2015**, *7*, 646-652; c) S. Silvi, E. C. Constable, C. E. Housecroft, J. E. Beves, E. L. Dunphy, M. Tomasulo, F. M. Ryamo, A. Credi, *Chem. Eur. J.* **2009**, *15*, 178-185.

- [S5] a) G. Cooke, F. M. A. Duclairoir, P. John, N. Polwart, V. M. Rotello, *Chem. Commun.* **2003**, 2468–2469; b) J. Bu, D. Lilienthal, J. E. Woods, C. E. Nohrden, K. T. Hoang, D. Truong, D. K. Smith, *J. Am. Chem. Soc.* **2005**, *127*, 6423–6429; c) J. D. Carr, S. J. Coles, J. B. Hursthouse, M. E. Light, J. H. R. Tucker, J. Westwood, *Angew. Chem. Int. Ed.* **2000**, *39*, 3296–3299; G. Cooke, V. M. Rottelo, *Chem. Soc. Rev.* **2002**, *31*, 275–286.
- [S6] a) S. Horiuchi, F. Ishii, R. Kumai, Y. Okimoto, H. Tachibana, N. Nagaosa, Y. Tokura, *Nat. Mater.* **2005**, *4*, 163–166; b) S. Horiuchi, R. Kumai, Y. Tokura, *Angew. Chem. Int. Ed.* **2007**, *16*, 3497–3501; c) A. Ueda, S. Yamada, T. Isono, H. Kamo, A. Nakao, R. Kumai, H. Nakao, Y. Murakami, K. Yamamoto, Y. Nishio, H. Mori, *J. Am. Chem. Soc.* **2014**, *136*, 12184–12192; d) O. Sato, *Nat. Chem.* **2016**, *8*, 644–656; e) A.-L. Li, Q. Gao, J. Xu, X.-H. Bu, *Coord. Chem. Rev.* **2017**, *344*, 54–82.
- [S7] a) C. Mathonière, *Eur. J. Inorg. Chem.* **2018**, 248–258; b) D. Aguilà, Y. Prado, D. S. Koumoussi, C. Mathonière, R. Clérac, *Chem. Soc. Rev.* **2016**, *45*, 203–224, and references therein; c) C. P. Berlinguette, A. Dragulescu-Andrasi, A. Sieber, J. R. Galán-Mascarós, H.-U. Güdel, C. Achim, K. R. Dunbar, *J. Am. Chem. Soc.* **2004**, *126*, 6222–6223; d) D. Li, R. Clérac, O. Roubeau, E. Harté, C. Mathonière, R. Le Bris, S. M. Holmes, *J. Am. Chem. Soc.* **2008**, *130*, 252–258; e) T. Liu, Y.-J. Zhang, S. Kanegawa, O. Sato, *J. Am. Chem. Soc.* **2010**, *132*, 8250–8251; f) T. Liu, Y.-J. Zhang, S. Kanegawa, O. Sato, *Angew. Chem.* **2010**, *122*, 8827–8830; *Angew. Chem. Int. Ed.* **2010**, *49*, 8645–8648; g) K. Mitsumoto, E. Oshiro, H. Niashikawa, T. Shiga, Y. Yamamura, K. Saito, H. Oshio, *Chem. Eur. J.* **2011**, *17*, 9612–9618; h) M. Nihei, Y. Okamoto, Y. Sekine, N. Hoshino, T. Shiga, I. P. Liu, H. Oshio, *Angew. Chem.* **2012**, *124*, 6467–6470; *Angew. Chem. Int. Ed.* **2012**, *51*, 6361–6364; i) Y. Sekine, M. Nihei, H. Oshio, *Chem. Lett.* **2014**, *43*, 1029–1030; j) E. S. Koumoussi, I. R. Jeon, Q. Gao, P. Dechambenoit, D. N. Woodruff, P. Merzeau, L. Buisson, X. L. Jia, D. F. Li, F. Volatron, C. Mathonière, R. Clérac, *J. Am. Chem. Soc.* **2014**, *136*, 15461–15464; k) T. Shiga, T. Tetsuka, K. Sakai, Y. Sekine, M. Nihei, G. N. Newton, H. Oshio, *Inorg. Chem.* **2014**, *53*, 5899–5901; l) N. Hoshino, F. Iijima, G. N. Newton, N. Yoshida, T. Shiga, H. Nojiri, A. Nakao, R. Kumai, Y. Murakami, H. Oshio, *Nat. Chem.* **2012**, *4*, 921–926; m) R.-J. Wei, T. Shiga, G. N. Newton, D. Robinson, S. Takeda, H. Oshio, *Inorg. Chem.* **2016**, *55*, 12114–12117; n) R.-J. Wei, R. Nakahara, J. M. Cameron, G. N. Newton, T. Shiga, H. Sagayama, R. Kumai, Y. Murakami, H. Oshio, *Dalton Trans.* **2016**, *45*, 17104–17107.
- [S8] a) M. Nihei, Y. Sekine, N. Suganami, H. Oshio, *Chem. Lett.* **2010**, *39*, 978–979; b) Y. Zhang, D. Li, R. Clérac, M. Kalisz, C. Mathonière, S. M. Holmes, *Angew. Chem.* **2010**, *122*, 3840–3844; *Angew. Chem. Int. Ed.* **2010**, *49*, 3752–3756; c) J. Mercurol, Y. Li, E. Pardo, O. Risset, M.

- Seuleiman, H. Rousselière, R. Lescouëzec, M. Julve, *Chem. Commun.* **2010**, *46*, 8995; d) Y.-Z. Zhang, P. Ferko, D. Siretanu, R. Ababei, N. P. Rath, M. J. Shaw, R. Clérac, C. Mathonière, S. M. Holmes, *J. Am. Chem. Soc.* **2014**, *136*, 16854–16864; e) A. Mondal, Y. Li, M. Seuleiman, M. Julve, L. Toupet, M. Buron-Le Cointe, R. Lescouëzec, *J. Am. Chem. Soc.* **2013**, *135*, 1653; f) Y. Sekine, M. Nihei, R. Kumai, H. Nakao, Y. Murakami, H. Oshio, *Chem. Comm.* **2014**, *38*, 4050–4052; g) Y. Sekine, M. Nihei, R. Kumai, H. Nakao, Y. Murakami, H. Oshio, *Inorg. Chem. Front.* **2014**, *1*, 540–543; h) D. Siretanu, D. Li, L. Buisson, D. M. Bassani, S. M. Holmes, C. Mathonière, R. Clérac, *Chem. Eur. J.* **2011**, *17*, 11704–11708.
- [S9] M. Nihei, Y. Sekine, N. Suganami, K. Nakazawa, A. Nakao, H. Nakao, Y. Murakami, H. Oshio, *J. Am. Chem. Soc.* **2011**, *133*, 3592–3600.
- [S10] a) M. Nihei, T. Yanai, I.-J. Hsu, Y. Sekine, H. Oshio, *Angew. Chem. Int. Ed.* **2017**, *56*, 591–594; b) Y. Sekine, M. Nihei, H. Oshio, *Chem. Eur. J.* **2017**, *23*, 5193–5197.
- [S11] a) M. C. Etter, G. M. Frankenbach, *Chem. Mater.* **1989**, *1*, 10–12; b) J. R. Bowers, G. W. Hopkins, G. P. A. Yap, K. A. Wheeler, *Cryst. Growth Des.* **2004**, *5*, 727–736.
- [S12] a) S. L. Johnson, K. A. Rumon, *J. Phys. Chem.* **1965**, *69*, 74–86; b) F. Fillaux, H. H. Limage, F. Romain, *Chem. Phys.* **2002**, *276*, 181–210.

6. Framework Structures Emerged from Thiocyanate-Based Prussian Blue Analogs

The cyanide-bridged Prussian blue analogs are widely studied due to their properties such as porosity, photomagnetism, SCO, and electrochromaticity which are interesting for applications such as hydrogen storage, molecular sieves, electrode materials, nanoscopic sensors, and quantum devices.^[74,151-153] M. J. Cliffe et al.^[36] published the first example of a thiocyanate-based PBA $M[\text{Bi}(\text{SCN})_6]$ (M : Fe, Cr, Sc) in 2019. The compounds are isostructural to each other and did not crystallize in a cubic structure, which is typical for 3D Prussian blue, but in a distorted monoclinic one. $\text{Cr}^{\text{III}}[\text{Bi}(\text{SCN})_6]$ showed a reversible solvent uptake and release, which might be interesting for exchanging guest molecules and the optical properties of all three compounds might be used for photocatalysis.^[36] $\text{Fe}^{\text{II}}[\text{Bi}(\text{SCN})_6]$ is especially interesting because transition metal PBAs show potential SCO behavior. However, the coordination bond lengths of $\text{Fe}^{\text{II}}[\text{Bi}(\text{SCN})_6]$ remain the same at 180 K, 300 K and 375 K.^[36] Furthermore, M. J. Cliffe et al.^[37] reported in 2020 the structural analysis of six new $[\text{Bi}(\text{SCN})_6]^{3-}$ coordination frameworks with additional manganese(II), cobalt(II), nickel(II), and zinc(II) ions (two different structures with Co and Zn). The bond lengths of the cobalt compounds were only measured at a single temperature at 120 K or 180 K^[37] and show an HS state.

Coordination frameworks showing a SCO induced by host-guest interactions were presented by M. Ohba et al. in 2009.^[48,50] $\{\text{Fe}^{\text{II}}(\text{pyrazole})[\text{Pt}^{\text{II}}(\text{CN})_4]\}$ is a microporous coordination framework that shows bidirectional SCO with memory effect induced by the adsorption of CS_2 and benzene solvent vapor. The solvent-framework interactions occurred through open metal sites of the square planar coordinated platinum and through the aromatic pyrazine ligands.^[48,50] Y. Yamada et al. were able to stabilize the open metal sites in a thiocyanate-based platinum(IV) coordination polymer through the addition of a pyridine ligand.^[154]

With this previous research, Kevin Tran synthesized 2020 in his master thesis,^[38] supervised by the author of this thesis, two new thiocyanate-based Co-Bi coordination compounds $\{\text{Co}^{\text{II}}_2[\text{Bi}(\text{SCN})_6]_2[\text{Co}^{\text{II}}(\text{H}_2\text{O})_2]\} \cdot 2 \text{Et}_2\text{O}$ (**B1**) (Et_2O : diethyl ether) and $\text{K}\{[\text{Bi}(\text{SCN})_6][\text{Co}^{\text{II}}(3\text{-cyanopyridine})_2]\} \cdot 3 \text{acetone}$ (**B2**). The compounds **B1** and **B2** exhibited a temperature induced color change from blue to green and from orange/brown to green (Figure 32), respectively, which can indicate an SCO. Therefore, the author of this thesis reproduced the synthesis for further temperature-depending analysis and expanded it to other metal ions and ligands. The following chapter is about the combination of the transition metal ions cobalt(II), iron(II), and nickel(II) with different organic ligands and the $[\text{Bi}(\text{SCN})_6]^{3-}$

building block to investigate the possibilities of controlling structural and physical properties of the resulting framework structure.

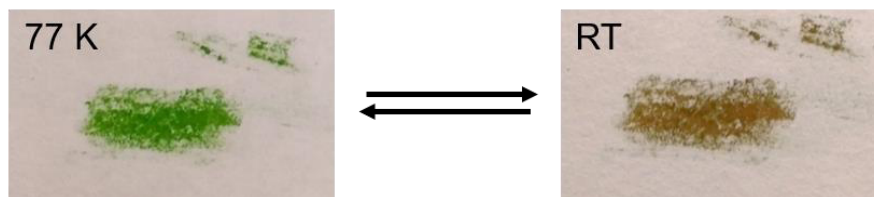


Figure 32: Temperature induced color change of B2.^[38]

All the experiments and analysis that are following presented were performed by the author of this thesis. Kevin Tran started the initial experiments. Dr. Yuta Ohtsubo performed the N₂ adsorption measurements. Haruka Yoshino helped with the magnetic measurements. Prof. Dr. Masaaki Ohba, Prof. Dr. Hiroki Oshio, and Prof. Dr. Franz Renz helped through discussions with the analysis and refined the manuscript.

6.1 Thiocyanate-Based Coordination Compounds with Co, Fe, and Ni

The cobalt(II) compounds **B1**, **B2**, [Bi₂(SCN)₁₂Co^{II}₃(3-cyanopyridine)₆] · 2 H₂O (**B3**), Na[Bi(SCN)₆Co^{II}(3-cyanopyridine)₂] · 2 acetone (**B4**), the iron(II) compound K[Bi(SCN)₆Fe^{II}(3-cyanopyridine)₂] · 3 acetone (**B5**), and the nickel(II) compound K[Bi(SCN)₆Ni^{II}(3-cyanopyridine)₂] · 3 acetone (**B6**) were synthesized and their structural and magnetic properties were analyzed. Notable is that the compounds **B2** and **B3** were obtained from the same synthesis, while the other synthesis only yielded one metal-bismuth compound.

6.1.1 Experimentals

All chemicals were purchased from commercial suppliers and used without further purification. All synthesis are modified versions of or build upon previously reported synthesis.^[36,38]

{Co^{II}₂[Bi(SCN)₆]₂[Co^{II}(H₂O)₂]} · 2 Et₂O (**B1**):

Bi(NO₃)₃ · 5 H₂O (1 mmol) was mixed together with KSCN (6 mmol) in 20 ml of acetone. Immediately, a white precipitation appeared in the yellow solution, which was stirred for 20 min. The precipitation was removed by filtration and Co(NO₃)₂ · 6 H₂O (1.76 mmol) was added. The blue solution was stirred for 3 h while a white precipitation appeared. After filtration, the solution was stirred for further 13 h before it was filtrated again to remove newly appeared white precipitation. Blue single crystals of **B1** could be obtained alongside white crystals through vapor diffusion of diethyl ether at 4 °C. After the crystals were taken out of the solution, their color changed to red-brown.

$K\{[Bi(SCN)_6][Co^{II}(3\text{-cyanopyridine})_2]\} \cdot 3 \text{ acetone (B2)}$ and $\{[Bi(SCN)_6]_2[Co^{II}(3\text{-cyanopyridine})_2]_3\} \cdot 2 H_2O$ (B3):

$Bi(NO_3)_3 \cdot 5 H_2O$ (1 mmol) was mixed together with KSCN (6 mmol) in 20 ml of acetone. Immediately, a white precipitation appeared in the yellow solution, which was stirred for 20 min. The precipitation was removed by filtration and a second solution of $Co(NO_3)_2 \cdot 6 H_2O$ (1.16 mmol) and 3-cyanopyridine (2 mmol) in 5 ml acetone was added. The blue solution was stirred for 3 h while a white precipitation appeared. After filtration, the solution was stirred for further 13 h before it was filtrated again to remove newly appeared white precipitation. Brown single crystals could be obtained alongside white crystals through vapor diffusion of diethyl ether at 4 °C. Single crystals of B2 and B3 could both be found within the same solution (B2 + B3 reverses to the mixed sample). $C_{75}H_{54}Bi_3Co_4N_{49}K_{16}O_{50}S_{18}$, $K[Bi(SCN)_6Co^{II}(3\text{-cyanopyridine})_2] \cdot 3 \text{ acetone} + [Bi_2(SCN)_{12}Co^{II}_3(3\text{-cyanopyridine})_6] \cdot 2 H_2O + 15 KNO_3$: found % (calcd. %): C 20.26 (19.99), H 1.06 (1.21), N 15.46 (15.23); IR (ATR; cm^{-1}): 1333, 1360, 1420, 1474, and 1599 (3-cyanopyridine), 2097, 2115 (SCN⁻), 2240 (3-cyanopyridine).

$Na\{[Bi(SCN)_6][Co^{II}(3\text{-cyanopyridine})_2]\} \cdot 2 \text{ acetone (B4)}$:

$Bi(NO_3)_3 \cdot 5 H_2O$ (0.5 mmol) was mixed together with NaSCN (3 mmol) in 10 ml of acetone. Immediately a white precipitation appeared in the yellow solution, which was stirred for 2 h. The precipitation was removed by filtration and a second solution of $Co(NO_3)_2 \cdot 6 H_2O$ (0.5 mmol) and 3-cyanopyridine (1 mmol) in 5 ml acetone was added. The blue solution was stirred overnight while a white precipitation appeared. After filtration, brown single crystals of B4 could be obtained alongside white crystals through vapor diffusion of diethyl ether at 4 °C. $C_{24}H_{20}BiCoN_{17}Na_8O_{23}S_6$, $Na[Bi(SCN)_6Co^{II}(3\text{-cyanopyridine})_2] \cdot 2 \text{ acetone} + 7 NaNO_3$: found % (calcd. %): C 18.1 (18.49), H 1.00 (1.29), N 15.59 (15.28); IR (ATR; cm^{-1}): 1347, 1418, 1475, 1596, and 1708 (3-cyanopyridine), 2098, 2115 (SCN⁻), 2241 (3-cyanopyridine).

$K\{[Bi(SCN)_6][Fe^{II}(3\text{-cyanopyridine})_2]\} \cdot 3 \text{ acetone (B5)}$:

$Bi(NO_3)_3 \cdot 5 H_2O$ (1 mmol) was mixed together with KSCN (6 mmol) in 10 ml of acetone. Immediately a white precipitation appeared in the yellow solution, which was stirred for 3 h. The precipitation was removed by filtration and the solution was degassed and put under a N_2 atmosphere. The first solution was added under anaerobic conditions to a second solution of $Fe(BF_4)_2 \cdot 6 H_2O$ (1 mmol) and 3-cyanopyridine (2 mmol) in 11 ml of degassed acetone. The red solution was stirred for 24 h under inert gas and then filtrated under a N_2 atmosphere to remove a white precipitation. Single crystals of B5 could be obtained alongside white crystals through vapor diffusion of diethyl ether at 4 °C under exclusion of O_2 . $C_{24}H_{20}BiFeN_{12}K_3O_8S_6$, $K[Bi(SCN)_6Fe^{II}(3\text{-cyanopyridine})_2] \cdot 2 \text{ acetone} + 2 KNO_3$: found %

(calcd. %): C 24.30 (24.45), H 1.11 (1.71), N 15.37 (14.26); IR (ATR; cm^{-1}): 1366, 1419, 1475, 1571, 1596, and 1705 (3-cyanopyridine), 2100 (SCN^-), 2241 (3-cyanopyridine).

$\text{K}\{\text{Bi}(\text{SCN})_6\}[\text{Ni}^{\text{II}}(\text{3-cyanopyridine})_2] \cdot 3 \text{ acetone (B6)}$:

$\text{Bi}(\text{NO}_3)_3 \cdot 5 \text{ H}_2\text{O}$ (0.5 mmol) was mixed together with KSCN (3 mmol) in 10 ml of acetone. Immediately, a white precipitation appeared in the yellow solution, which was stirred for 1 h. The precipitation was removed by filtration and a second solution of $\text{Ni}(\text{NO}_3)_2 \cdot 6 \text{ H}_2\text{O}$ (0.5 mmol) and 3-cyanopyridine (1 mmol) in 10 ml acetone was added. The orange solution was stirred overnight while a white precipitation appeared. The solution was filtrated to remove the newly appeared white precipitation. Green single crystals of **B6** could be obtained alongside white crystals through vapor diffusion of diethyl ether at 4 °C. $\text{C}_{27}\text{H}_{26}\text{BiNiK}_6\text{N}_{16}\text{O}_{18}\text{S}_6$, $\text{K}[\text{Bi}(\text{SCN})_6]\text{Ni}^{\text{II}}(\text{3-cyanopyridine})_2 \cdot 3 \text{ acetone} + 5 \text{ KNO}_3$: found % (calcd. %): C 21.71 (21.01), H 1.33 (1.70), N 14.44 (13.61); IR (ATR; cm^{-1}): 1367, 1411, 1423, 1474, 1573, 1598, 1698, and 1762 (3-cyanopyridine), 2107, 2132 (SCN^-), 2243 (3-cyanopyridine).

Crystal structure analysis: The diffraction data were collected with a Bruker SMART APEX II diffractometer with a CCD area detector and graphite-monochromated $\text{Mo-K}\alpha$ radiation ($\lambda = 0.71073 \text{ \AA}$). The data frames were integrated using the SAINT program and merged to give a unique data set for the determination of the structure. An absorption correction was performed using SADABS.^[129] The structure was solved by direct methods and refined on F2 by the full-matrix least-squares methods using the SHELXTL package (Bruker Analytical X-ray systems, Olex2).^[130,131] Non-hydrogen atoms were refined with anisotropic thermal parameters. Hydrogen-atoms were included in calculated positions and refined with isotropic thermal parameters riding on those of the parent atoms. Electron densities of disordered solvent molecules were flattened for some structures using Olex 2 solvent mask^[131] (BYPASS^[132]).

Physical measurements: Magnetic susceptibility data were collected using a Quantum Design MPMS-5S SQUID magnetometer. The measurements were performed with an applied magnetic field of 1000 Oe for **B1** – **B3** and **B5** and with 5000 Oe for **B4** and **B6** in the temperature range of 5 – 300 K. Magnetic data were corrected for the diamagnetism of the sample holder, and for the diamagnetism of the sample using Pascal's constants. More details are described in the section 4.3.2 Results and Discussion. The samples were measured with a scan rate of 2 K/min in sweep mode. Infrared absorption spectra were measured with the ATR method using a PerkinElmer FT-IR Spectrometer Spectrum Two. Powder XRD were measured with a microcrystalline sample using an Ultima IV X-Ray diffractometer from Rigaku at RT with $\text{Cu-K}\alpha$ radiation ($\lambda = 1.5406 \text{ \AA}$). The TG and DTA measurements for **B2 + B3**, **B4**, and **B6** were performed at nitrogen or air atmosphere with an Thermo plus TG 8120 from Rigaku in the temperature range of 22 °C to 500 °C. For **B5** the TG measurement was done with a Perkin Elmer STA6000 under N_2

atmosphere in the temperature range of 22 °C to 700 °C. The Mössbauer Spectrum was measured with a WissEl Mössbauer spectrometer using a $^{57}\text{Co}(\text{Rh})$ source and the isomer shift is given relative to α -iron at RT. The N_2 adsorption and desorption isotherm was acquired using a BELSORP-MAX volumetric adsorption equipment (MicrotracBEL Corp) at 77.36 K.

6.1.2 Results and Discussion

Structural Data

The crystal structures of the previously investigated^[38] compounds **B1** and **B2** were measured at 100 K and 273 K to determine the cause of their thermochromic behavior (Figure 32). Furthermore, the compounds **B3**, **B4**, **B5**, and **B6** were measured at 100 K and **B5** was additionally measured at 223 K and 273 K (Table 9 and Table 13).

B1 crystallized in the monoclinic $P2_1/c$ space group as a 3D framework with (Figure 33) two distinguishable cobalt(II) ions and one bismuth(III) ion. Co1 is octahedrally coordinated by four thiocyanate ions and two *cis* coordinated water molecules. Co2 is tetrahedrally coordinated by four thiocyanate ions and exists in a ratio of 2:1 compared to Co1. The cobalt ions are bonded to the N-side of the thiocyanate and interconnected via $[\text{NCS-Bi-SCN}]^+$ bridges. Subsequently, each bismuth ion, which is octahedrally coordinated by six thiocyanate ions, is bonded via thiocyanate ions to four Co2 and two Co1 (Figure 65, page 159). The resulting 3D framework consists of $\{\text{Co}^{II}_2[\text{Bi}(\text{SCN})_6]_2\}^{2-}$ layers of Co2 which are connected via thiocyanate bond $[\text{Co}(\text{H}_2\text{O})_2]^{2+}$ bridges of Co1. Through these bridges, cavities open up which are occupied by diethyl ether (Figure 34).

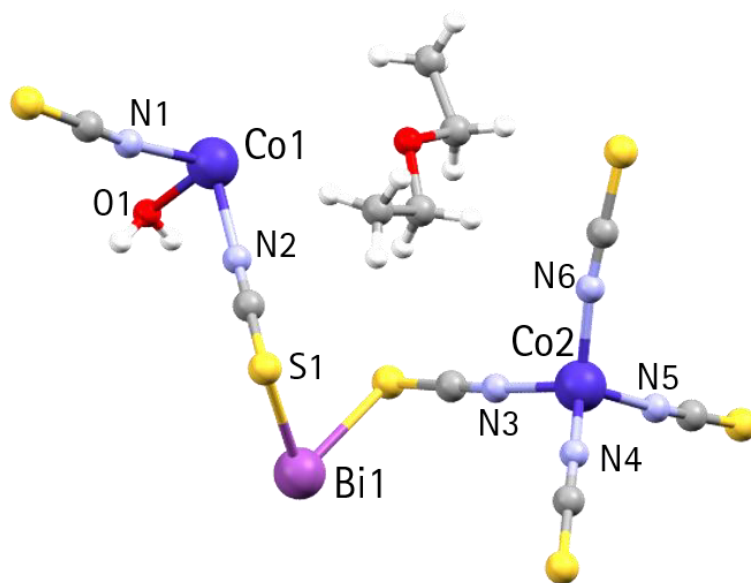


Figure 33: Asymmetric unit of **B1**. Color code: C, gray; N, light blue; O, red; Co, dark blue; Bi, magenta; S, yellow; H, white.

Table 9: Crystallographic and structural data of B1, B2, B3, and B4.

	B1	B2
	$C_{24}H_{40}Bi_2Co_3N_{12}O_4S_{12}$	$C_{27}H_{28}BiCoN_{10}KO_3S_6$
<i>T</i> in K	100	100
crystal System	monoclinic	triclinic
space group	<i>P</i> ₂ ₁ / <i>c</i>	<i>P</i> -1
<i>a</i> in Å	10.6391(9)	8.2320(11)
<i>b</i> in Å	8.5437(8)	13.5532(18)
<i>c</i> in Å	26.421(2)	17.984(2)
α in °	90	82.7880(10)
β in °	97.8120(10)	87.9980(10)
γ in °	90	89.4220(10)
<i>V</i> in Å ³	2379.3(4)	1989.3(5)
<i>Z</i>	2	2
<i>R</i> ₁ / <i>wR</i> ₂ (<i>I</i> > 2σ)	0.0342/0.0774	0.0365/0.1164
	B3	B4
	$C_{48}H_{28}Bi_2Co_3N_{24}O_2S_{12}$	$C_{24}H_{20}BiCoN_{10}NaO_2S_6$
<i>T</i> in K	100	100
crystal System	monoclinic	triclinic
space group	<i>P</i> ₂ ₁ / <i>c</i>	<i>P</i> -1
<i>a</i> in Å	8.1609(16)	8.2928(12)
<i>b</i> in Å	25.964(5)	8.9416(13)
<i>c</i> in Å	17.038(4)	13.354(2)
α in °	90	81.690(2)
β in °	92.555(2)	86.034(2)
γ in °	90	88.201(2)
<i>V</i> in Å ³	3606.7(13)	977.3(2)
<i>Z</i>	2	1
<i>R</i> ₁ / <i>wR</i> ₂ (<i>I</i> > 2σ)	0.0406/0.0885	0.0378/0.1117

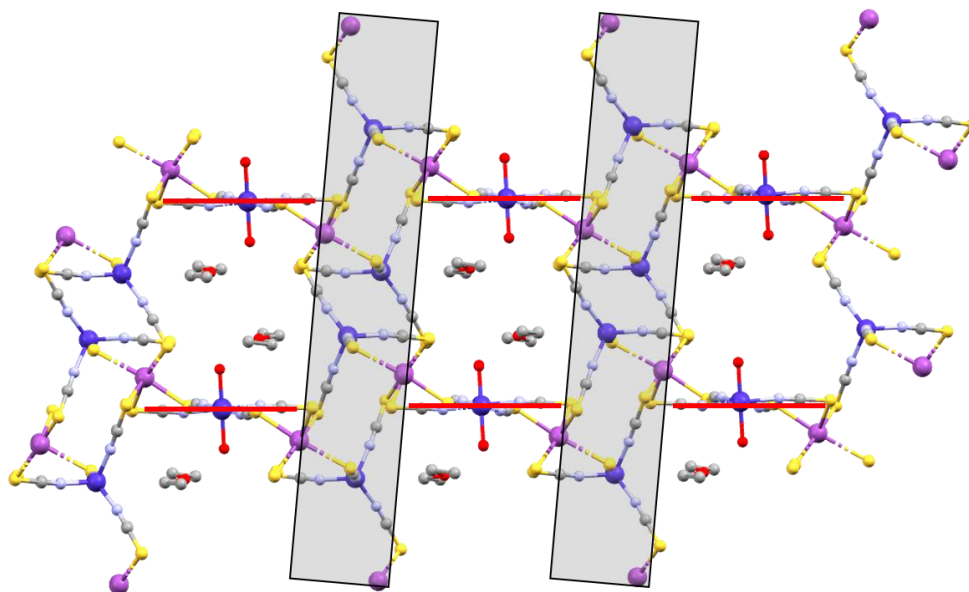


Figure 34: Crystal structure packing of **B1** along the *b* axis. Color code: C, gray; N, light blue; O, red; Co, dark blue; Bi, magenta; S, yellow; H, white; red line, *a* axis; blue line, *c* axis. Gray boxes visualize the layers of $\{\text{Co}^{II}_2[\text{Bi}(\text{SCN})_6]_2\}^{2-}$ connected through the $[\text{Co}(\text{H}_2\text{O})_2]^{2+}$ units visualized by the red lines.

The cobalt(II) coordination bond lengths at 100 K and 273 K (Table 10) are each indicating an HS state for the octahedrally coordinated Co1 at both temperatures. Therefore, the color change is not caused by an SCO. However, the NCS–Bi–SCN and SCN–Co–OH₂ bonding angles of Co1 (Table 11) change between the two temperatures by 11.63 ° and 3.67 °, respectively (Figure 35). Since the compound's color strongly depends on both cations,^[36] a small change of the coordination environment, such as changing angles, might be the cause for the thermochromic behavior. Previously conducted thermogravimetric (TG) analysis by Kevin Tran showed a solvent loss of the water until 225 °C and a loss of the diethyl ether until 410 °C.^[38] These results suggest a weak coordination bond of the water molecules. Subsequently, the water ligand was replaced by the organic ligand 3-cyanpyridine to modify the ligand field strength and obtain more information about the thermochromic behavior.

Table 10: Cobalt coordination bond lengths of **B1**.

bond	max. and min. coordination bond lengths in Å	
	B1 (100 K)	B1 (273 K)
Co1–N1	2.131	2.133
Co1–N2	2.089	2.102
Co1–O1	2.062	2.068
Co2–N3	1.959	1.978
Co2–N4	1.947	1.948
Co2–N5	1.957	1.962
Co2–N6	1.960	1.956

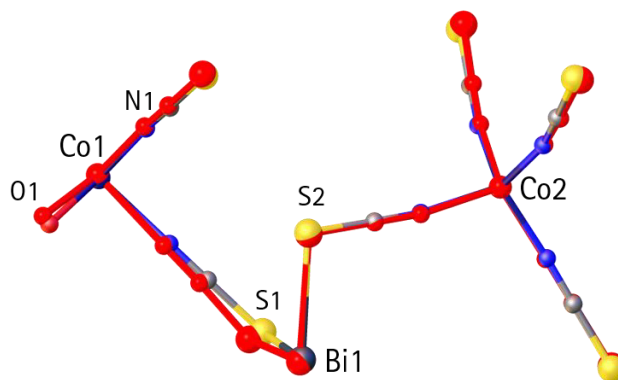


Figure 35: Comparison of the asymmetric unit of **B1** at 100 K (colored) and 273 K (red). Color code: C, gray; N, light blue; O, single red atoms; Co, dark blue; Bi, magenta; S, yellow. Hydrogen atoms have been omitted for clarity.

Table 11: Selected bonding angles of **B1**.

angle between	angle in ° at 100 K	angle in ° at 273 K
N1-Co1-O1	91.56	87.89
S2-Bi1-S1	89.34	100.97

B2 and **B4** crystalize both in the triclinic $P\bar{1}$ space group (Figure 36) and show a similar, but not isostructural, 2D layer structure. Both structures contain cobalt(II) that is octahedrally coordinated by four NCS⁻ ions and two 3-cyanopyridines. The bismuth(III) ions are octahedrally coordinated by the sulfur side of the thiocyanate anions. These interconnected cations build plains with an interplane distance of 13.398 Å for **B2** (Figure 37) and 13.186 Å for **B4** (Figure 39), respectively. Between the planes, potassium (for **B2**) or sodium (for **B4**) cations are located and coordinated by thiocyanate anions, 3-cyanopyridines and acetone solvent molecules. The thiocyanate anions and 3-cyanopyridines are coordinated to the bismuth and cobalt ions within the plains. In addition, the sodium and acetone in **B4** are slightly disordered. In contrast to the two layered structures of **B2** and **B4**, **B3** shows a 3D [Bi₂(SCN)₁₂Co^{II}₃] framework. The structure of **B3** contains two distinguishable cobalt(II) ions which are octahedrally coordinated by two 3-cyanopyridine and four thiocyanate ligands (Figure 36). Co2 builds up 2D [Bi(SCN)₂Co(3-cyanopyridine)₂]₂⁻² plains with a distance of 12.815 Å and which are connected via [Co(3-cyanopyridine)₂]²⁺ bridges (Figure 38). Note that Co1 is bonded via two thiocyanate ions to the same bismuth ion (in total it is bonded to two different Bi³⁺), while Co2 is connected to four different bismuth ions.

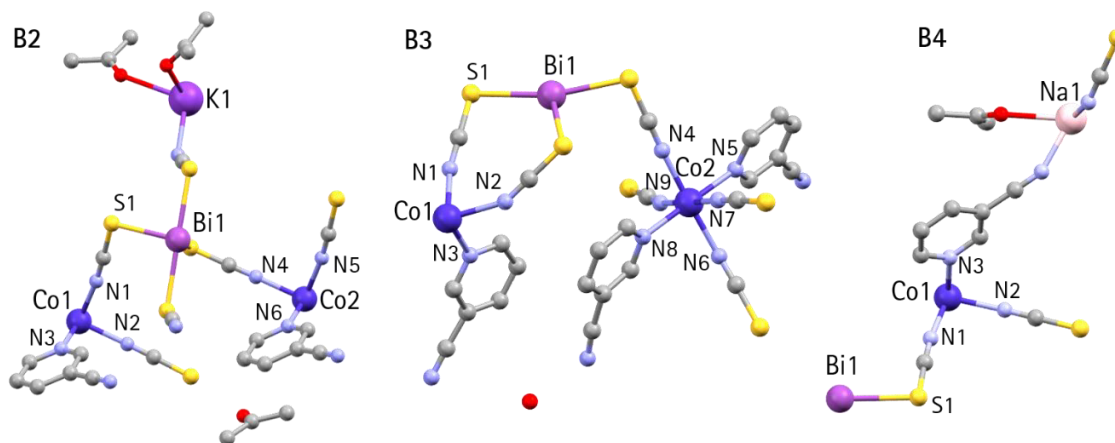


Figure 36: Asymmetric unit of **B2** and **B3**. Color code: C, gray; N, light blue; O, red; Co, dark blue; Bi, magenta; S, yellow.

To summarize, the insertion of potassium ions in **B2** sets the structure of **B2** and **B3** apart. Subsequently, **B2** builds a 2D structure which is loosely interconnected through coordinated potassium ions, indicated by the plain distance. In contrast, the plain-plain distance of **B3** is shorter because the plains are directly connected via a complex bridge. However, both compounds were obtained from the same sample and the crystals could not be distinguished under the microscope or separated in another way. Therefore, both were handled as combined sample **B2 + B3**. The cobalt(II) coordination bond lengths of **B2**, **B3**, and **B4** (Table 12) are all indicating the HS state at 100 K and for **B2** at 273 K as well. Therefore, these compounds do not show a temperature induced SCO behavior above 100 K. Furthermore, only a minor temperature induced change of the potassium-acetone bond can be observed for **B2** at 100 K and 273 K (Figure 66, page 159).

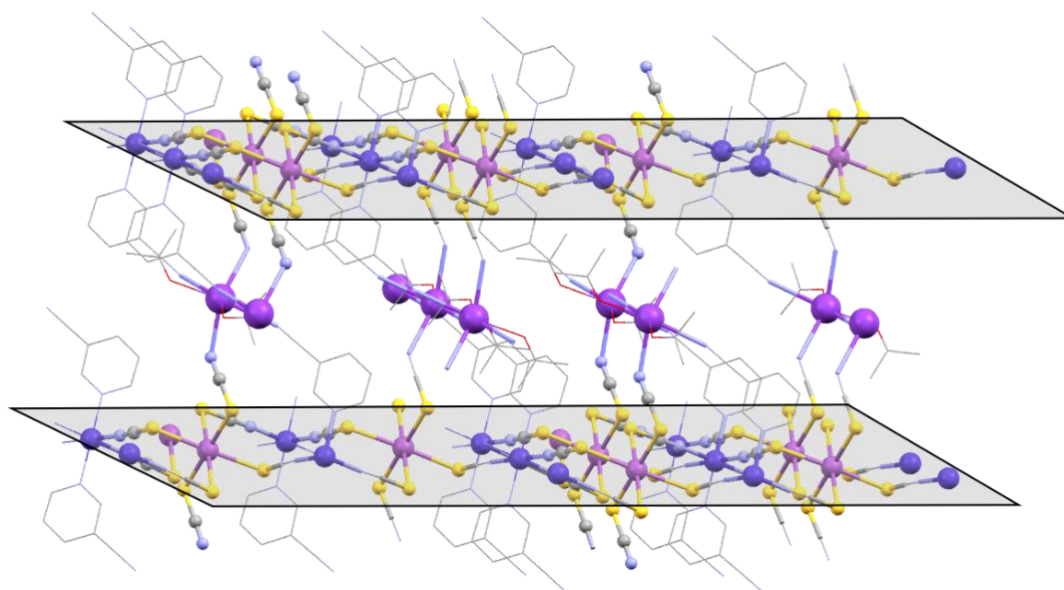


Figure 37: Crystal structure packing of **B2**. Color code: C, gray; N, light blue; O, red; Co, dark blue; Bi, magenta; K, violet; S, yellow. Gray boxes visualize the 2D planes build by the $[\text{Co}(\text{NCS})_4\text{Bi}]^+$ units.

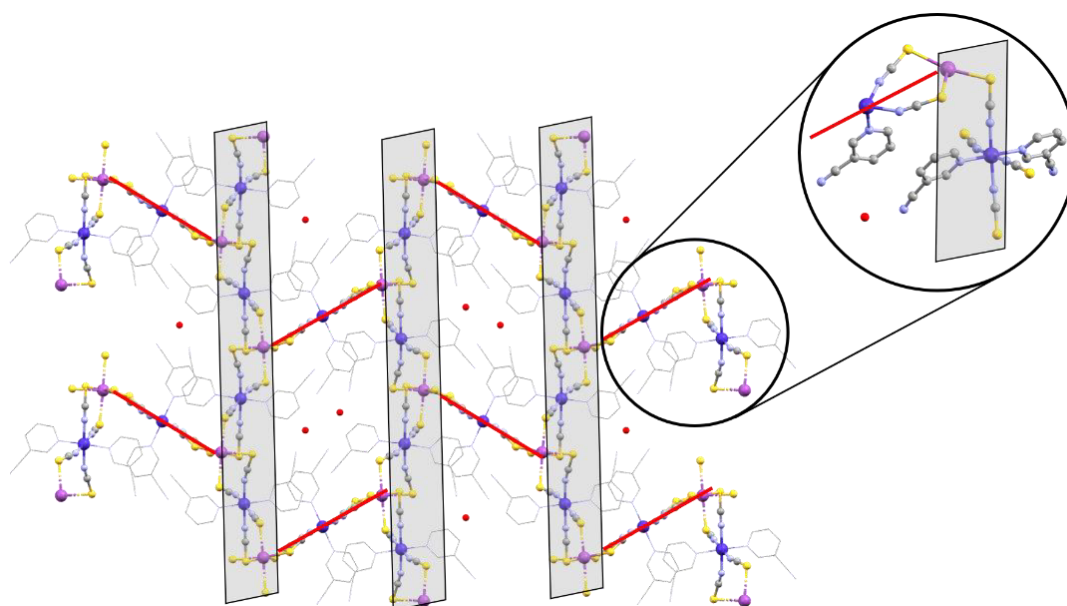


Figure 38: Crystal structure packing of **B3**. Color code: C, gray; N, light blue; O, red; Co, dark blue; Bi, magenta; S, yellow. Gray boxes visualize the 2D planes build by the $[\text{Co}(\text{NCS})_4\text{Bi}]^{+2}$ units which are interconnected by $[\text{Co}(\text{NCS})_4]^{2-}$ bridges.

Powder XRD was measured at RT for sample **B2** + **B3** and compared with the calculated powder XRDs from the single crystal structures of **B2** and **B3** at 100 K (Figure 40). The measured diffractogram shows reflexes of both structures which are slightly shifted, probably due to the different measurement temperatures. However, the estimation of the **B2** and **B3** ratio in this sample was done using the elemental analysis and the thermo gravimetric data. Possible impurities might be overlapped by the reflexes of **B2** and **B3**.

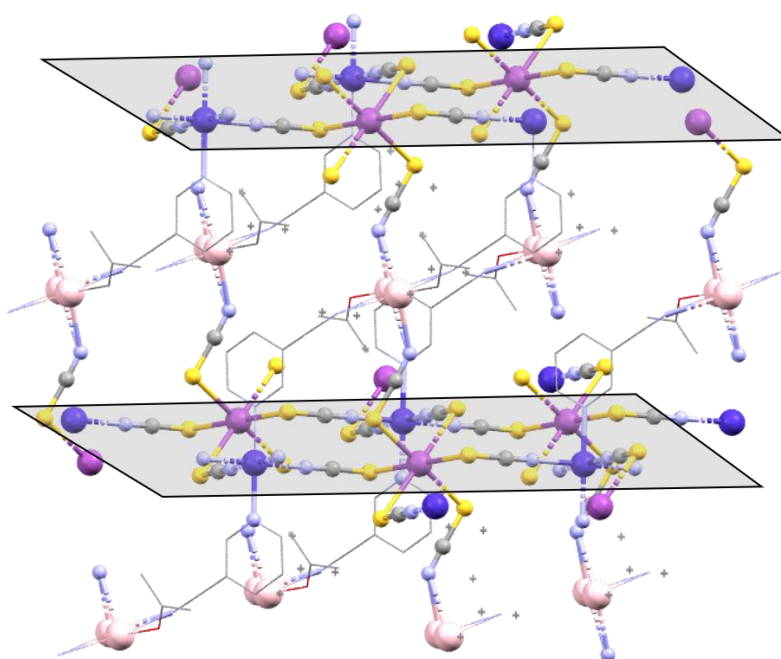


Figure 39: Crystal structure packing of **B4**. Color code: C, gray; N, light blue; O, red; Co, dark blue; Bi, magenta; Na, pink; S, yellow. Gray boxes visualize the 2D planes build by the $[\text{Co}(\text{NCS})_4\text{Bi}]^+$ units.

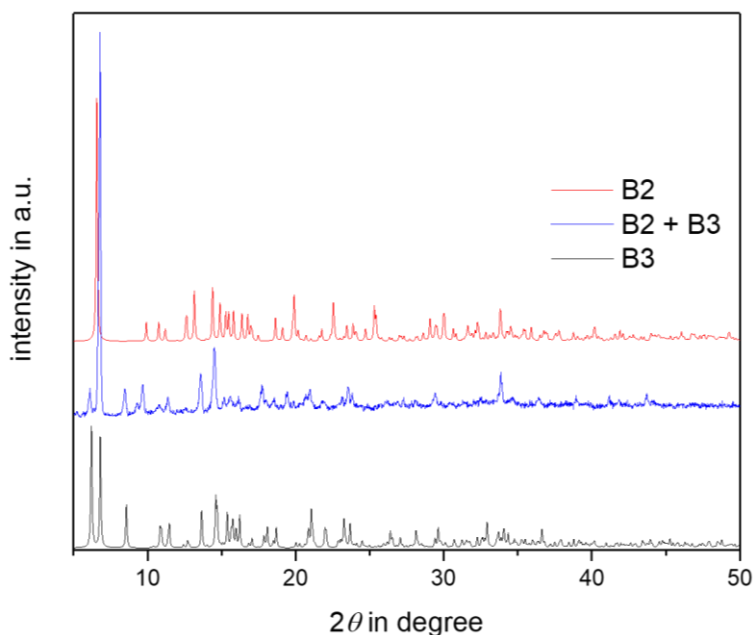


Figure 40: Powder XRD calculated from the single crystal structures of **B2**, **B3** and the powder XRD measurement of the mixed sample **B2 + B3**.

Table 12: Cobalt coordination bond lengths of **B2**, **B3**, and **B4**.

bond	max. and min. coordination bond length in Å			
	B2 (100 K)	B2 (273 K)	B3 (100 K)	B4 (100 K)
Co1-N1	2.103	2.101	2.118	2.093
Co1-N2	2.114	2.122	2.091	2.112
Co1-N3	2.158	2.153	2.182	2.151
Co2-N4	2.108	2.101	2.079	
Co2-N5	2.110	2.121	2.142	
Co2-N6	2.151	2.153	2.119	
Co2-N7			2.104	
Co2-N8			2.157	
Co2-N9			2.103	

In addition to the four cobalt(II) compounds, the iron(II) compound **B5** and the nickel(II) compound **B6** were synthesized analog to the sample **B2 + B3**. The crystal structure of **B5** was measured at 100 K, 223 K and 273 K and for **B6** at 100 K (Table 13). Both compounds are isostructural to **B2** at 100 K (Figure 41) which is confirmed by the simulated powder XRD of **B2**, **B5**, and **B6** (Figure 42). The inter-plain distances for **B5** and **B6** are 13.452 Å and 13.396 Å, respectively. The coordination bond lengths (Table 14) of iron(II) indicates the HS state at all three temperatures.

Table 13: Crystallographic and structural data of B5 and B6.

	B5	B5	B6
	$C_{27}H_{26}BiFeN_{10}KO_3S_6$	$C_{27}H_{26}BiFeN_{10}KO_3S_6$	$C_{27}H_{26}BiNiN_{10}O_3S_6$
<i>T</i> in K	100	273	100
crystal System	triclinic	triclinic	triclinic
space group	<i>P</i> -1	<i>P</i> -1	<i>P</i> -1
<i>a</i> in Å	8.2448(7)	8.3702(16)	8.2320(11)
<i>b</i> in Å	13.5651(12)	13.710(3)	13.5532(18)
<i>c</i> in Å	18.0452(16)	18.065(3)	17.984(2)
α in °	82.6200(10)	83.367(2)	82.7880(10)
β in °	88.0130(10)	88.478(2)	87.9980(10)
γ in °	89.3570(10)	87.954(2)	89.4220(10)
<i>V</i> in Å ³	2000.2(3)	2057.4(7)	1989.3(5)
<i>Z</i>	2	2	2
<i>R</i> ₁ / <i>wR</i> ₂ (<i>I</i> > 2σ)	0.0280/0.0815	0.0445/0.1211	0.0365/0.1164

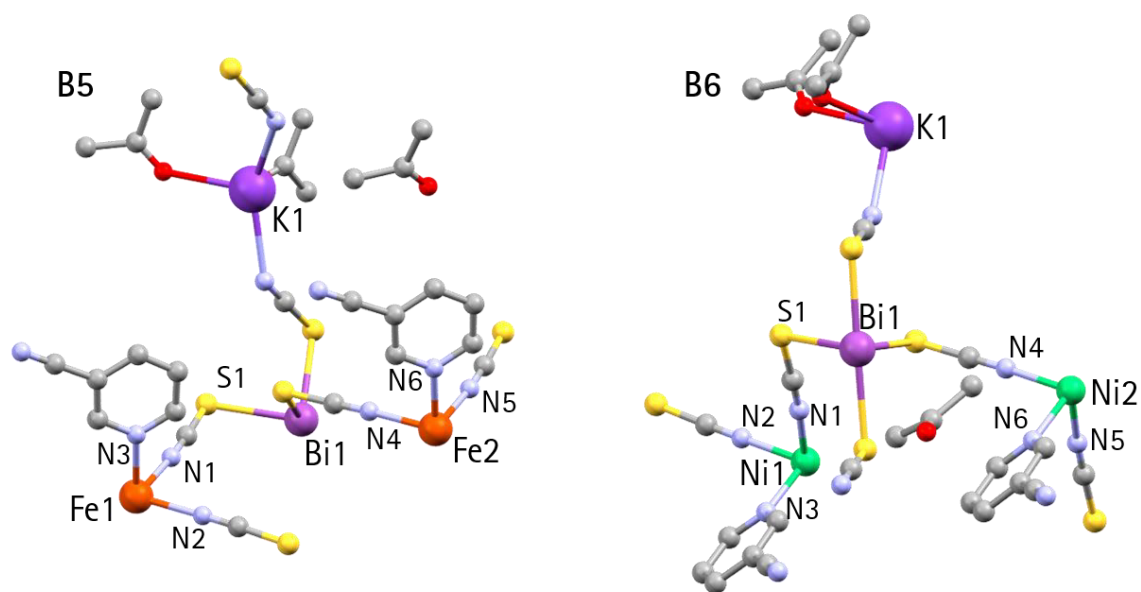


Figure 41: Asymmetric unit of B5 and B6. Color code: C, gray; N, light blue; O, red; Fe, orange; Ni, green; Bi, magenta; K, violet; S, yellow.

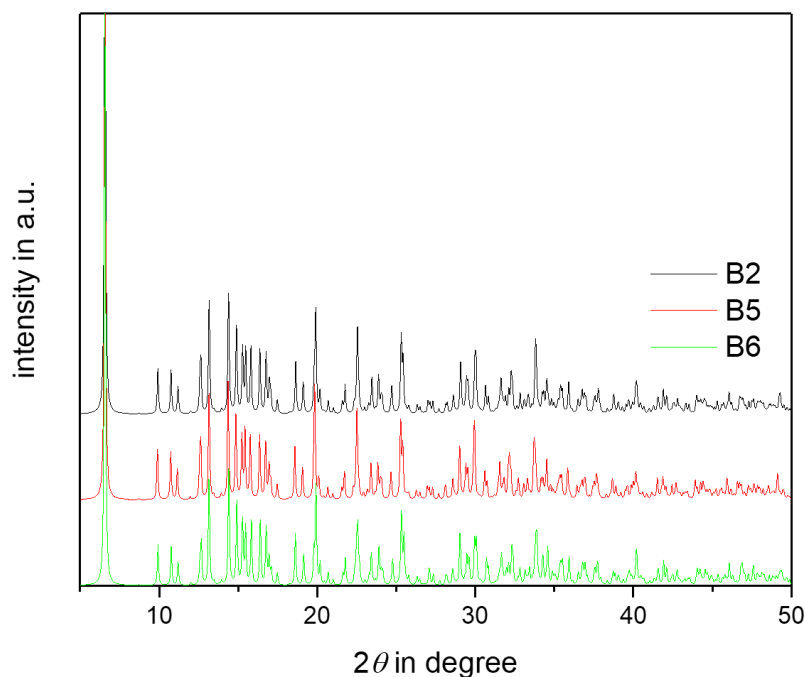


Figure 42: Powder XRD calculated from the single crystal structures of **B2**, **B5**, and **B6**.

It is noteworthy that **B5** exhibits a phase transition between 100 K and 273 K. This is shown in the comparison of the calculated powder XRDs (Figure 43). The overlaid structures at 100 K and 273 K (Figure 67, page 160) show a changing potassium coordination mode in which the position but not the coordination environment changes. In contrast to the calculated powder XRD at 232 K, which does not show a clear high temperature or low temperature phase, the overlaid structures at 100 K and 232 K are more similar than at 232 K and 273 K. These results might be explained by a gradual transition between the phases.

Table 14: iron(II) and nickel(II) (M) coordination bond lengths of **B5** und **B6**.

bond	max. and min. coordination bond lengths in Å			
	B5 (100 K)	B5 (223 K)	B5 (273 K)	B6 (100 K)
M1-N1	2.136	2.138	2.155	2.064
M1-N2	2.147	2.153	2.140	2.073
M1-N3	2.208	2.208	2.211	2.107
M2-N4	2.139	2.149	2.135	2.075
M2-N5	2.137	2.138	2.159	2.070
M2-N6	2.185	2.198	2.213	2.100

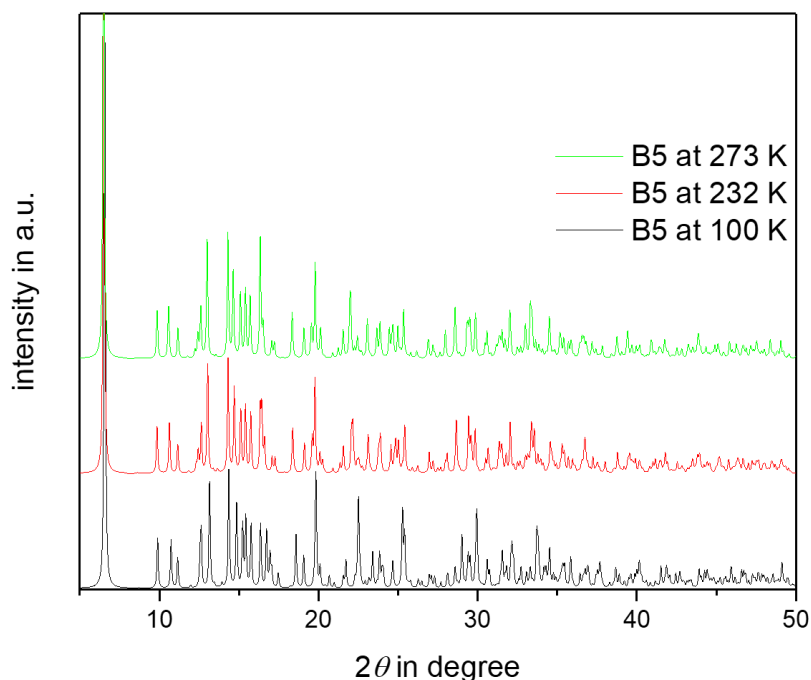


Figure 43: Powder XRD calculated from the single crystal structures of **B5** at 100 K and 273 K.

Thermogravimetric Analysis

The ratio of the white impurities to the samples **B2** – **B6** was analyzed by thermogravimetric (TG) measurements. In addition, a differential thermal analysis (DTA) was performed for **B2** + **B3**, **B4**, and **B6**. The TG of **B1** was already analyzed and discussed by Kevin Tran.^[38] All calculated steps and the assumed chemical formula are complementary to the elemental analysis (Chapter 6.1.1 Experimentals). The moiety formula was approximated by using one type of impurities, which is assumed to contain nitrate because of the exothermic reactions around 300 °C shown in the DTA measurements. However, the composition of the impurities might be more complex.

Table 15: Analyzed TG results under N₂ atmosphere of **B2** + **B3** divided into single steps and residue.

step	step in °C	mass in %	correlated weight loss	theoretical mass %
1	22 – 110	-3.7	3 acetone	-3.86
2	110 – 213	-20.4	2 3-cyanopyridine + 2 H ₂ O	-19.28
3	213 – 500	-22.2	18 SCN ⁻	-23.2
residue	-	53.7	3 Bi ³⁺ + 4 Co ²⁺ + 15 KNO ₃	53.66

For **B2** + **B3** the moiety formula $\text{K}[\text{Bi}(\text{SCN})_6\text{Co}^{\text{II}}(\text{3-cyanopyridine})_2] \cdot 3 \text{ acetone} + [\text{Bi}_2(\text{SCN})_{12}\text{Co}^{\text{II}}_3(\text{3-cyanopyridine})_6] \cdot 2 \text{ H}_2\text{O} + 15 \text{ KNO}_3$ was calculated from the elemental analysis and TG/DTA measurements (Figure 44). The mass loss of the single steps (Table 15) corresponds to the calculated solvent and ligand molecules. Up to 213 °C the process is endotherm and is, therefore, probably an evaporation of the solvents and the 3-cyanopyridine ligand. Afterwards, the process becomes

exothermic which might be caused by a reaction of the nitrate with the thiocyanate bridges and the remaining metal ions. Consequently, it is likely that the resulting product of a thiocyanate + nitrate reaction is removed, and that mass corresponds to all of the thiocyanate ligands. The measurement under an air atmosphere resulted in two additional peaks in the DTA and a higher remaining mass, probably caused by a greater amount of metal oxides.

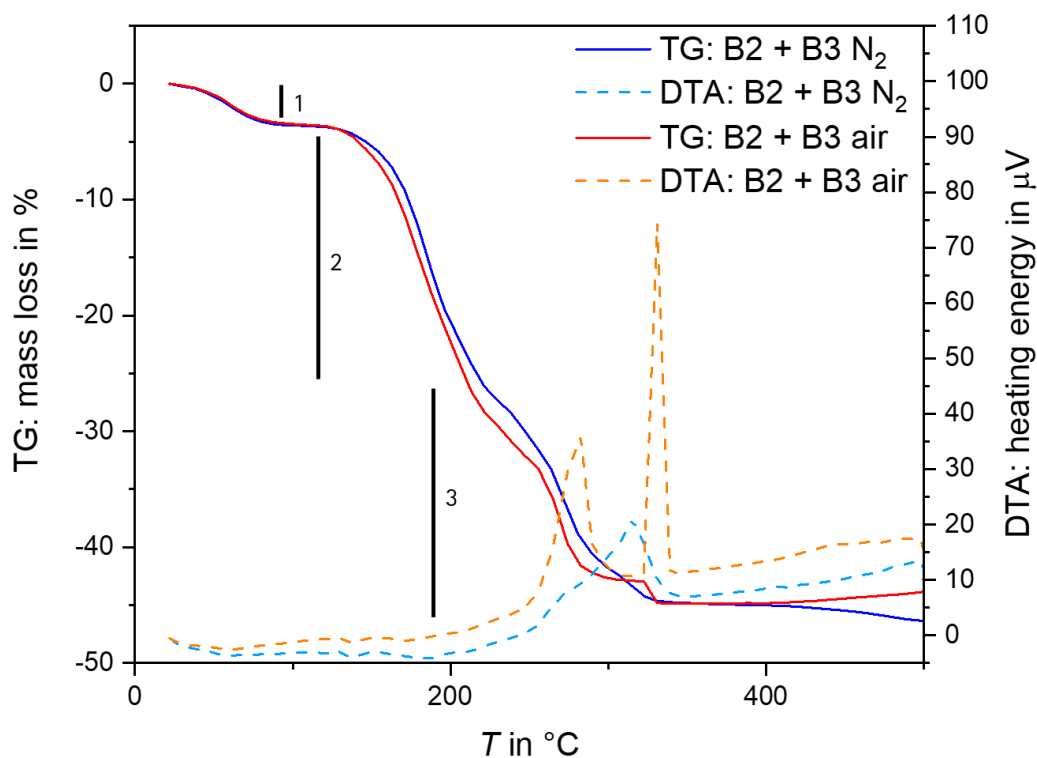
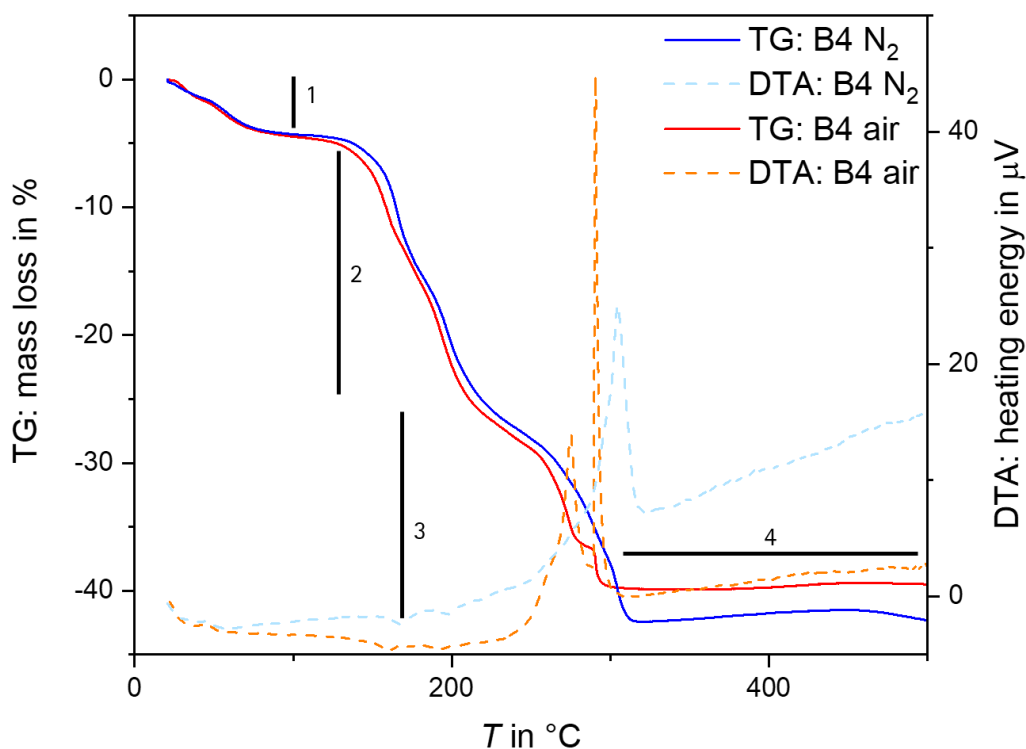


Figure 44: TG and DTA measurements of B2 + B3 under N₂ and air atmospheres.

The moiety formula of B4 was approximated to be Na[Bi(SCN)₆Co^{II}(3-cyanopyridine)₂] · 2 acetone + 7 NaNO₃ from the elemental analysis and TG/DTA measurement (Figure 45). The single steps (Table 16) correspond to the removed solvent molecules and ligands with remaining metal ions and NaNO₃. However, as for B2 + B3 it is likely that the residuals are a product left by the previously assumed nitrate-oxidation process caused. Both measurements are similar except for the exothermic processes around 300 °C measured under an air atmosphere and resulting in a higher remaining mass. Note that the split-up amount of removed acetone might be caused by different positions in the crystal lattice caused by disordered solvent molecules and can also be found in the moiety formula of the crystal structure cif file.

Table 16: Analyzed TG results under N₂ atmosphere of B4 divided into single steps and residue.

step	step in °C	mass in %	correlated weight loss	theoretical mass %
1	22 - 110	-4.4	1.2 acetone	-4.47
2	110 - 220	-15.7	2 3-cyanopyridine + 0.8 acetone	-16.36
3	220 - 320	-22.3	6 SCN ⁻	-22.36
4	320 - 500	0	oxidation processes	-
residue		57.6	1 Bi ³⁺ + 1 Co ²⁺ + 7 NaNO ₃	56.83

Figure 45: TG and DTA measurements of B4 under N₂ and air atmospheres.

B5 was calculated (Figure 46) to be approximately $K[\text{Bi}(\text{SCN})_6\text{Fe}^{\text{II}}(\text{3-cyanopyridine})_2] \cdot 2 \text{ acetone} + 2 \text{ KNO}_3$. Step 1 and 2 (Table 17) are comparable to the previous samples. However, steps 3 and 4 correspond less well to the mass of thiocyanate than for B2 + B3 and B4. This might be due to a comparably smaller amount of KNO₃ impurities and a subsequent smaller amount of volatile reaction products. The remaining mass is therefore higher than expected. Whereas for the other samples no mass loss step could be found that corresponds to the impurities, step 3 of B5 also corresponds to the amount of KNO₃.

6. Framework Structure Emerged from Thiocyanate-Based PBAs

Table 17: Analyzed TG results under N₂ atmosphere of B5 divided into single steps and residue.

step	step in °C	mass in %	correlated weight loss	theoretical mass %
1	22 – 157	-9.7	2 acetone	-9.85
2	157 – 195	-15.7	2 3-cyanopyridine	-17.66
3	195 – 400	-18.7	4 SCN ⁻ /2 KNO ₃	-19.7/17.15
4	400 – 700	-8.7	2 SCN ⁻	-9.85
residue		47.2	1 Bi ³⁺ + 1 Fe ²⁺ + 2 KNO ₃	42.94

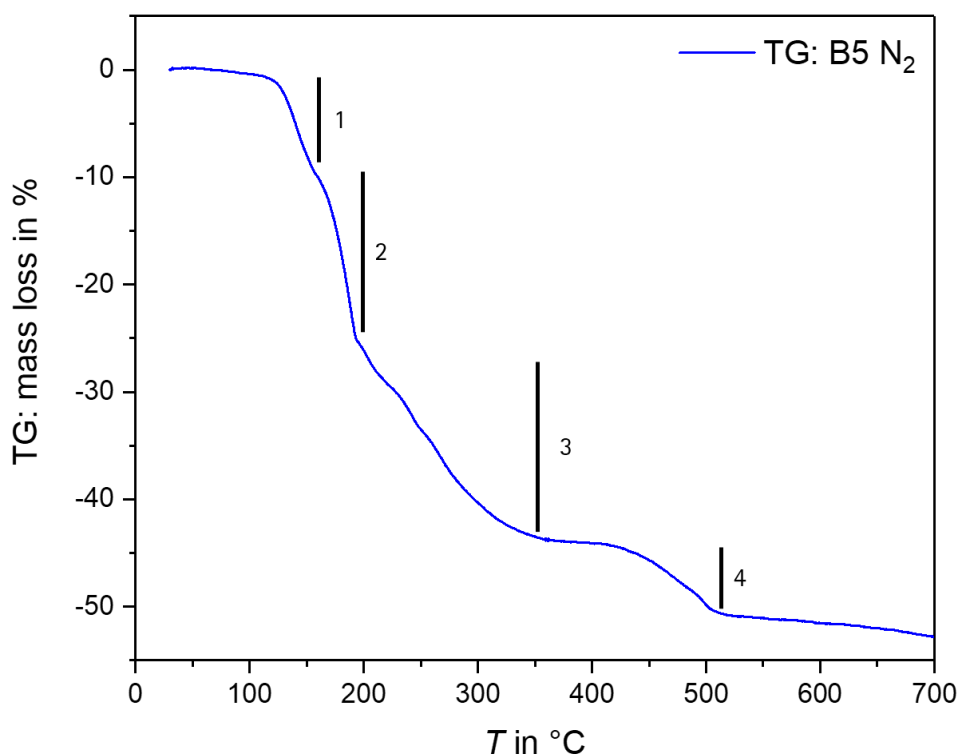
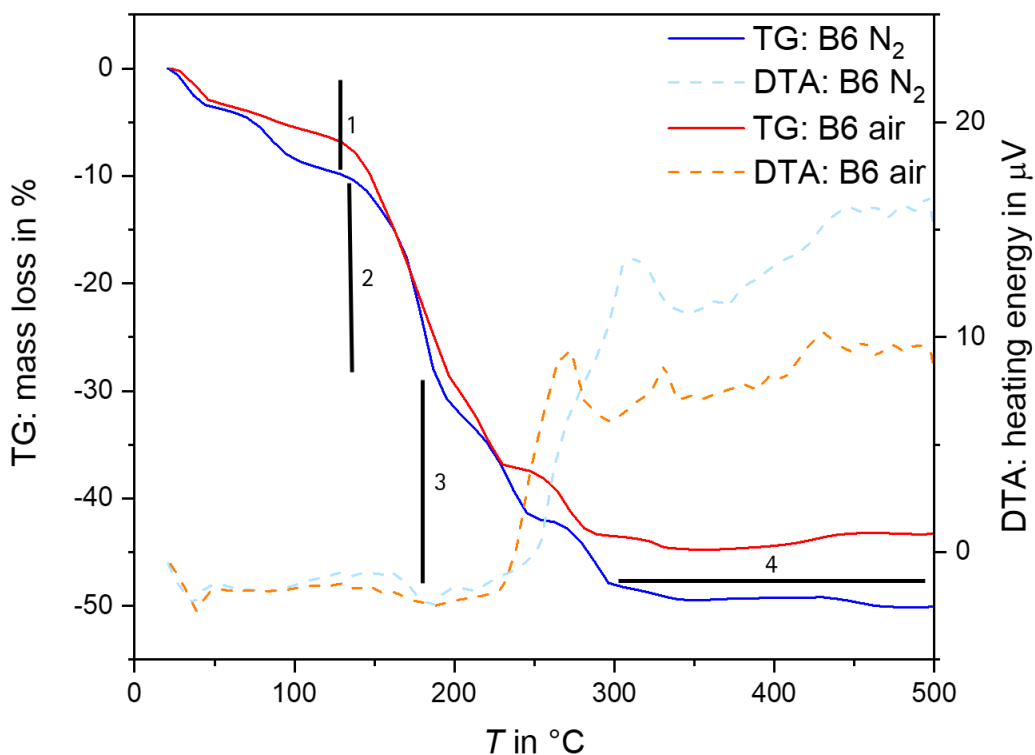


Figure 46: TG measurements of B5 under N₂ atmospheres.

The formula $K[Bi(SCN)_6Ni^{II}(3\text{-cyanopyridine})_2] \cdot 2 \text{ acetone} + 5 \text{ KNO}_3$ was determined for B6 from the elementary analysis and TG/DTA measurements (Figure 47). Even though the steps (Table 18) are overlapping, they match the measurement well and are comparable with the TG/DTA measurements for B2 + B3 and B4. Furthermore, the measurements under air and N₂ atmosphere differ more than expected which might be due to a hygroscopic sample behaviour or an inhomogeneous sample.

Table 18: Analyzed TG results under N₂ atmosphere of B6 divided into single steps and residue.

step	step in °C	mass in %	correlated weight loss	theoretical mass %
1	22 - 145	-11.4	2 acetone	-11.12
2	145 - 187	-16.6	2 3-cyanopyridine	-13.52
3	187 - 296	-19.9	6 SCN	-22.63
4	296 - 500	-2.2	oxidation processes	-
residue	-	49.9	1 Bi ³⁺ + 1 Ni ²⁺ + 7 KNO ₃	52.74

Figure 47: TG and DTA measurements of B6 under N₂ and air atmospheres.

All four samples showed similar steps for the decomposition process of the compounds. In the first step, the solvent molecules evaporate up to 120–150 °C. Secondly, the 3-cyanopyridine is removed up to approximately 220 °C: In the third step, a mass corresponding to the SCN⁻ ligands is removed up to approximately 350 °C. The remaining mass after heating to 500 °C corresponds to the metal ions and nitrate impurities. The temperatures vary for the different compounds. These results suggest that under anaerobic conditions, the decomposition of the thiocyanate depends on the nitrate impurities. Therefore, it is likely that a reaction product of thiocyanate and nitrate volatilizes instead of pure thiocyanate. For reasons of charge balance, it is likely that anionic residues and metal oxides result from this reaction as well.

Magnetic Properties, Mössbauer Spectrum and Adsorption Measurement

The temperature-depending magnetic susceptibility was measured for the samples **B2 + B3**, **B4**, **B5**, and **B6** in the range of 5 K – 300 K. As previously analyzed, the samples contained impurities, which made an exact calculation of the $\chi_m T$ values impossible. Therefore, three different calculations with different assumptions were made for each of the four samples (Figure 48). All calculations are based on the measured SQUID data with changing molar mass and diamagnetic correction. The calculated $\chi_m T$ values for the first approach (red) are based on the chemical formula from the single crystal structure and the approximation of the elemental analysis and TG measurements. In the second approach (yellow), the chemical formula, determined only by the single crystal structure was used to calculate the $\chi_m T$ values. In the third approach (blue), the $\chi_m T$ values correspond to the expected values for the cobalt(II), iron(II), and nickel(II) ions in HS state.

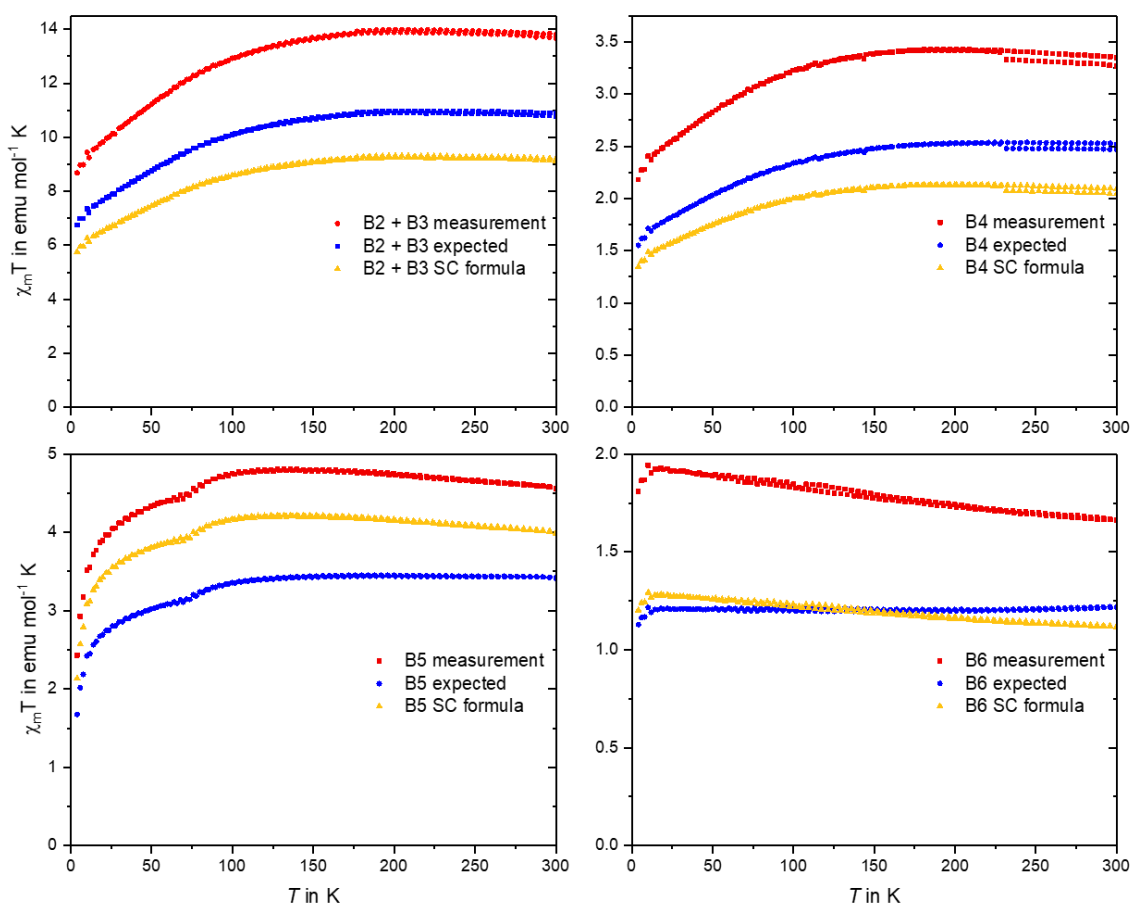


Figure 48: Temperature-depending magnetic measurements of **B2 + B3**, **B4**, **B5**, and **B6**. The red points represent the calculated $\chi_m T$ values according to the formula determined by the elemental analysis and TG measurements, the blue points represent the expected values based on the measurement data and the yellow points represent the calculated $\chi_m T$ values according to the formula determined by the crystal structure without impurities.

The crystal structure revealed the transition metal ions cobalt(II), iron(II), and nickel(II) as the only magnetic-active species in these compounds. However, all red-marked $\chi_m T$ values are significantly

larger than the expected values (blue), while the yellow-marked values correspond better to the blue ones. The $\chi_m T$ values for **B2 + B3** (Figure 68, page 160) are nearly constant up to 150 K at about 13.9 emu mol⁻¹ K for red, at about 10.9 emu mol⁻¹ K for blue, and at about 9.3 emu mol⁻¹ K for yellow. Below 150 K, the $\chi_m T$ values are strongly decreasing due to the ZFS. $\chi_m T = 10.9$ emu mol⁻¹ K corresponds to four magnetically isolated cobalt(II) in the HS state. **B4** (Figure 69, page 161) shows approximately constant $\chi_m T$ values up to 150 K as well with 3.4 emu mol⁻¹ K for red, 2.5 emu mol⁻¹ K for blue (corresponding to one cobalt(II) in the HS state) and 2.1 emu mol⁻¹ K for yellow. In contrast to **B5** and **B6**, both previous samples show similar behavior for all three approaches. The red and yellow $\chi_m T$ values for **B5** (Figure 70, page 161) are not only higher than the expected (blue) ones, but also unexpectedly increase from 300 K to 135 K from 4.6 emu mol⁻¹ K to 4.8 emu mol⁻¹ K and from 4.0 emu mol⁻¹ K to 4.2 emu mol⁻¹ K, respectively. The increase might be caused by magnetic interactions or by the diamagnetic impurities. Afterwards, at about 73 K, a sudden decrease can be observed to 4.4 emu mol⁻¹ K and 3.9 emu mol⁻¹ K, respectively, which might be caused by a phase transition. Since standard methods for crystal structure determination cannot be used below 100 K, a Mössbauer spectrum at 70 K was measured (Figure 49) showing an isomer shift of 1.03 mm s⁻¹, a quadrupole splitting of 1.51 mm s⁻¹ and a line width of 0.5 mm s⁻¹. These data correspond to an iron(II) in HS state^[52,155,156] with an expected $\chi_m T$ value of about 3.4 emu mol⁻¹ K and show that the spin state has not changed.

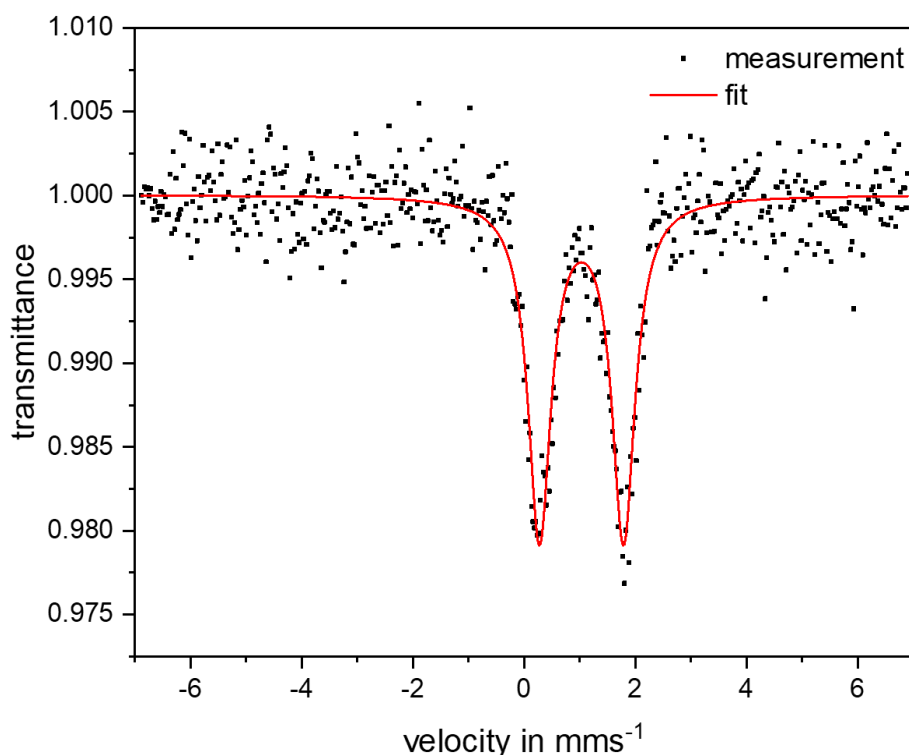


Figure 49: Mössbauer spectrum at 70 K of B5.

The magnetic properties of **B6** (Figure 71, page 162) also show $\chi_m T$ values that are higher than expected for the red-marked measurement. However, the yellow $\chi_m T$ values match the expected ones of 1.2 emu mol⁻¹ K with a g-factor of 2.2 for an octahedrally coordinated nickel(II) very well.^[157] Unexpectedly, the red and yellow-marked $\chi_m T$ values increase nearly linear in the temperature range from 300 K to 15 K from 1.7 emu mol⁻¹ K to 1.9 emu mol⁻¹ K and from 1.1 emu mol⁻¹ K to 1.3 emu mol⁻¹ K, respectively. As for **B5**, this might be caused by magnetic interactions or by the diamagnetic impurities.

In general, there are two possible explanations for the high $\chi_m T$ values (red) approximated from the elemental analysis and the TG measurements. The first is that magnetic interactions between the magnetic-active transition metal ions caused an increase of the $\chi_m T$ values. This is unlikely though, due to the magnetic inactive bridging. The second explanation might be that the approximation of the calculated species and the amount of impurities by the elemental analysis and TG measurement was not precise enough. $\chi_m T$ values, which were calculated too high, might indicate an overestimation of the impurity amount. Subsequently, the $\chi_m T$ values calculated from the single crystal formula are expected to be too small. For **B5**, removed solvent might cause the higher yellow-marked $\chi_m T$ values. To obtain reliable magnetic data, a synthesis route yielding pure compounds needs to be developed.

Absorption and desorption isotherms of **B2 + B3** and **B6** were measured before and after keeping the samples at 105 °C for one day (Figure 50). The activation temperature of 105 °C was chosen according to the TG measurements to remove the solvent molecules under modest conditions without damaging the organic ligand. The BET surface was calculated from this data by Dr. Yuta Ohtsubo for all four samples (Table 19). The results show no adsorption of the N₂ for all four samples which are, therefore, probably not porous with BET surface areas between 3 m² g⁻¹ and 13 m² g⁻¹. A trend can be observed showing a slight increase of the adsorption and the BET surface areas after the activation. This might be caused by smaller particle sizes or bigger interparticle caves.

Table 19: Calculated BET surface areas for **B2 + B3** and **B6** before (0) and after (a) heating the sample at 105 °C for one day.

sample	BET surface area
B2 + B3 0	3.0064 m ² g ⁻¹
B2 + B3 a	7.8061 m ² g ⁻¹
B6 0	7.6074 m ² g ⁻¹
B6 a	12.944 m ² g ⁻¹

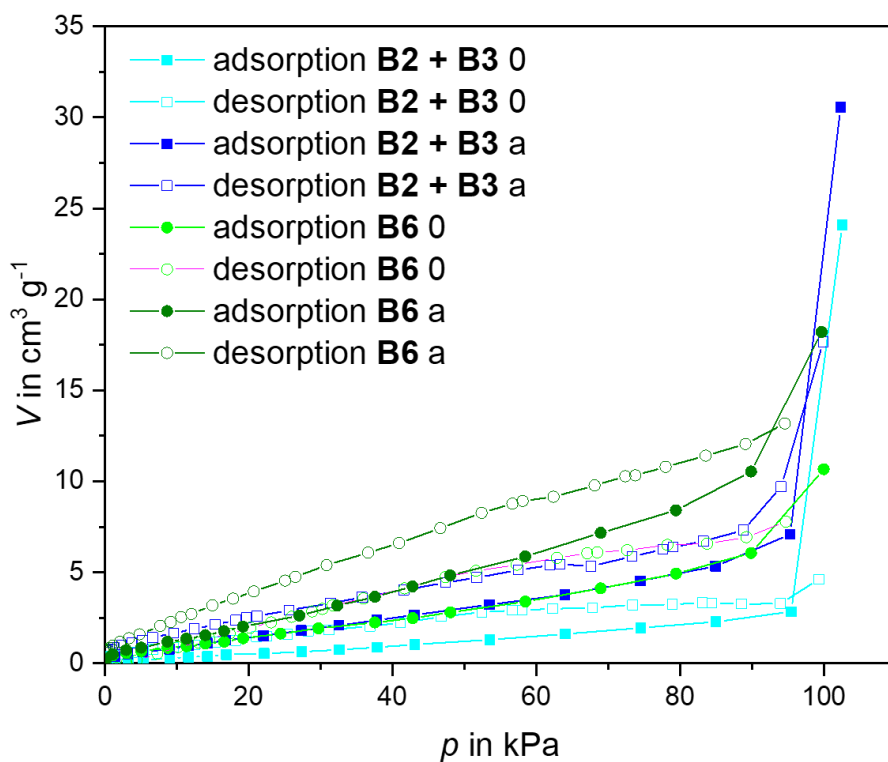


Figure 50: N_2 adsorption isotherm of the samples B2 + B3 and B6 before (0) and after heating at 105 °C (a) for one day.

6.2 How to Control the Aggregation of Bi–NCS Coordination Frameworks

In addition to the six presented compounds, the syntheses and crystal structures of six further bismuth(III) thiocyanate-based coordination polymers are discussed in the following chapter. These structures are the results of a larger synthesis series to gain a better understanding how the aggregation process of the $[\text{Bi}(\text{SCN})_6]^{3-}$, transition metal ions and ligands can be controlled, which is discussed as well.

6.2.1 Experimentals

All chemicals were purchased from commercial suppliers and used without further purification. All synthesis are modified versions of or build upon previously reported synthesis.^[36,38]

$\{\text{Co}^{\text{II}}[\text{Bi}(\text{SCN})_6][\text{Co}^{\text{II}}(\text{acetone})(\text{H}_2\text{O})_2]\} \cdot 2 \text{ acetone} \cdot 1 \text{ Et}_2\text{O}$ (SB1):

$\text{Bi}(\text{NO}_3)_3 \cdot 5 \text{ H}_2\text{O}$ (1/3 mmol) was mixed together with KSCN (2 mmol) in 7 ml of acetone. Immediately, a white precipitation appeared in the yellow solution, which was stirred for 20 min. The precipitation was removed by filtration. The solution was degassed and added to $\text{Co}(\text{BF}_4)_2 \cdot 6 \text{ H}_2\text{O}$ (1.5 mmol). The blue solution was stirred overnight before it was filtrated to remove the newly appeared white precipitation. Red single crystals of SB1 could be obtained alongside white crystals after the addition of 15 ml diethyl ether and storing the solution for a few days at about 4 °C.

$\text{K}[\text{Bi}(\text{SCN})_6\text{Co}^{\text{II}}]_2$ (SB2):

$\text{Bi}(\text{NO}_3)_3 \cdot 5 \text{ H}_2\text{O}$ (1 mmol) was mixed together with KSCN (6 mmol) in 10 ml of acetone. Immediately, a white precipitation appeared in the yellow solution, which was stirred for 30 min. The precipitation was removed by filtration and a second solution of $\text{Co}(\text{BF}_4)_2 \cdot 6 \text{ H}_2\text{O}$ (1 mmol) and imidazole (1 mmol) was added. The blue solution was stirred overnight before it was filtrated again to remove the newly appeared white precipitation. Red single crystals could be obtained alongside white crystals through vapor diffusion of diethyl ether after a few days.

$\{[\text{Bi}(\text{SCN})_6]_2[\text{Co}^{\text{II}}(\text{H}_2\text{O})_2]_3\}[\text{Co}(\text{NCS})_2(\text{H}_2\text{O})_4] \cdot 4 \text{ H}_2\text{O}$ (SB3):

$\text{Bi}(\text{NO}_3)_3 \cdot 5 \text{ H}_2\text{O}$ (1 mmol) was mixed together with KSCN (6 mmol) in 10 ml of acetone. Immediately, a white precipitation appeared in the yellow solution, which was stirred for 1 h. The precipitation was removed by filtration and a second solution of $\text{Co}(\text{BF}_4)_2 \cdot 6 \text{ H}_2\text{O}$ (1.5 mmol) in 20 ml methanol was added. The green solution was stirred for 23 h while a white precipitation appeared. After filtration, red single crystals of SB3 could be obtained alongside white crystals through vapor diffusion of diethyl ether after a few days.

{[Bi(SCN)₆]₂[Co^{II}(4-cyanopyridine)₂]₃} (SB4):

Bi(NO₃)₃ · 5 H₂O (0.5 mmol) was mixed together with KSCN (3 mmol) in 10 ml of acetone. Immediately, a white precipitation appeared in the yellow solution, which was stirred for 2 h. The precipitation was removed by filtration and a second solution of Co(BF₄)₂ · 6 H₂O (0.5 mmol) and 4-cyanopyridine (1 mmol) in 10 ml acetone was added. The green solution was stirred overnight while a white precipitation appeared. The solution was filtrated to remove the newly appeared white precipitation. Red single crystals of SB4 could be obtained alongside white crystals through vapor diffusion of diethyl ether after one day.

(*H*-isoquinoline)₃{[Bi(SCN)₆][Co^{II}(isoquinoline)₂]}[Co(NCS)₄] (SB5):

Bi(NO₃)₃ · 5 H₂O (0.5 mmol) was mixed together with KSCN (3 mmol) in 10 ml of acetone. Immediately, a white precipitation appeared in the yellow solution, which was stirred for 20 h. The precipitation was removed by filtration. A second solution of Co(BF₄)₂ · 6 H₂O (0.5 mmol) and isoquinoline (1 mmol) in 10 ml acetone was added. The greenish blue solution was stirred for 3 days. The yellow precipitation was removed by filtration from the blue solution. Green single crystals of SB5 could be obtained alongside white crystals through vapor diffusion of diethyl ether after a few days.

Na{[Bi(SCN)₆][Ni^{II}(3-cyanopyridine)₂]} · 2 acetone (SB6):

Bi(NO₃)₃ · 5 H₂O (0.5 mmol) was mixed together with NaSCN (3 mmol) in 10 ml of acetone. Immediately, a white precipitation appeared in the yellow solution, which was stirred for 30 min. The precipitation was removed by filtration and a second solution of Ni(NO₃)₂ · 6 H₂O (0.5 mmol) and 3-cyanopyridine (1 mmol) in 10 ml acetone was added. The solution was stirred overnight while a white precipitation appeared. The solution was filtrated to remove the newly appeared white precipitation. Green single crystals of SB6 could be obtained alongside white crystals through vapor diffusion of diethyl ether at 4 °C.

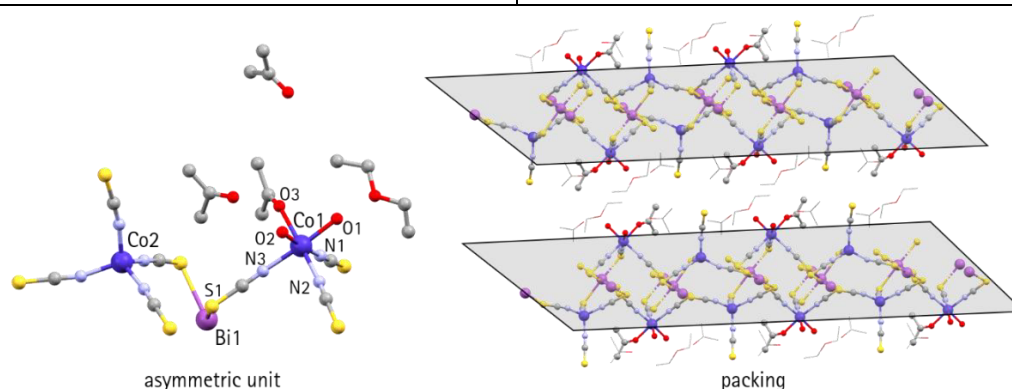
Crystal structure analysis: The diffraction data were collected with a Bruker SMART APEX II diffractometer with a CCD area detector and graphite-monochromated Mo-K α radiation ($\lambda = 0.71073 \text{ \AA}$). The data frames were integrated using the SAINT program and merged to give a unique data set for the determination of the structure. An absorption correction was performed using SADABS.^[129] The structure was solved by direct methods and refined on F² by the full-matrix least-squares methods using the SHELXTL package (Bruker Analytical X-ray systems, Olex2).^[130,131] Non-hydrogen atoms were refined with anisotropic thermal parameters. Hydrogen atoms were included in calculated positions and refined with isotropic thermal parameters riding on those of the parent atoms.

6.2.2 Crystal Structures

The compound **SB1** crystallizes in a 2D layer structure with two different cobalt sites (Table 20, Figure 51). Co1 is octahedrally coordinated by three thiocyanate ions, two water and one acetone molecule, while Co2 is tetrahedrally coordinated by four thiocyanate ions. Both cobalt sites are connected via $[\text{NCS-Bi-SCN}]^+$ bridges and build up a 2D plane. Two non-coordinating acetone and one diethyl ether molecule per asymmetric unit are located between these parallel planes. The inter plane distance of 16.165 Å is discussed at the end of this chapter (Table 26). The coordination bond lengths of Co1 correspond to cobalt(II) in the HS state, comparable to **B2**. One reason, a different structure was obtained than for **B2** and **B3**, might be the comparably less amount of potassium and thiocyanate during the reaction. The resulting formula shows 3.5 thiocyanate per cobalt while it is 4 for **B3** and 6 for **B2**. Possibly, the structure might be controlled by the amount of potassium ions in the solution.

Table 20: Crystallographic data and octahedral coordinated cobalt(II) coordination bond lengths of **SB1**.

	$\text{C}_{20}\text{H}_{32}\text{BiCo}_2\text{N}_7\text{O}_6\text{S}_7$	type of bond	bond lengths in Å
<i>T</i> in K	100	Co1-N1	2.07
crystal System	monoclinic	Co1-N2	2.12
space group	$P2_1/c$	Co1-N3	2.10
<i>a</i> in Å	13.820(5)	Co1-O1	2.05
<i>b</i> in Å	8.482(3)	Co1-O2	2.11
<i>c</i> in Å	33.181(13)	Co1-O3	2.16
α in °	90		
β in °	102.02		
γ in °	90		
<i>V</i> in Å ³	3875		
<i>Z</i>	4		
R_1/wR_2 ($I > 2\sigma I$)	0.0924/0.2259		

Figure 51: Asymmetric unit and packing of **SB1**. Color code: C, gray; N, light blue; O, red; Co, dark blue; Bi, magenta; S, yellow. The grey boxes visualize the 2D layer structure.

SB2 crystallizes in comparison to the other discussed compounds B1 – B6, SB1 and SB3 – SB6 in the high symmetric cubic $Pn-3$ space group (Table 21). Therefore, the compound can be described as PBA with the asymmetric unit (Figure 52) containing only a thiocyanate-bridged Co-Bi couple with a non-coordinated potassium ion. The Co-Bi unit builds up cubic cages with a potassium ion in its center comparable to 3D^[80,82,84,151] and molecular^[91] PBAs. However, the angled Bi-S-C bond reduces the size of ions and molecules that can be exchanged after the cages build up. The bond length indicates a cobalt(II) in the HS state. This structure results from the imidazole not coordinating and also refraining the water molecules from coordinating to the cobalt ions. Therefore, the formation of B1 is prevented and the thiocyanate bound to the bismuth ion remains as the only coordination option resulting in SB2. Further reactions with dry solvents and salts might lead to the same compound. Ohkoshi et al. demonstrated the absorption of terahertz light by caged cesium ions in manganese-iron PBAs.^[151] Similar properties might be found for this compound if the potassium ion is exchanged by cesium.

Table 21: Crystallographic data and cobalt(II) coordination bond length of SB2.

	$C_{12}Bi_2Co_2N_{12}S_{12}K$	type of bond	bond length in Å
T in K	100	Co1-N1	2.098
crystal System	cubic		
space group	$Pn-3$		
a, b, c in Å	12.195(2)		
α, β, γ in °	90		
V in Å ³	1813.8(9)		
Z	2		
R_1/wR_2 ($I > 2\sigma$)	0.0383/0.1125		

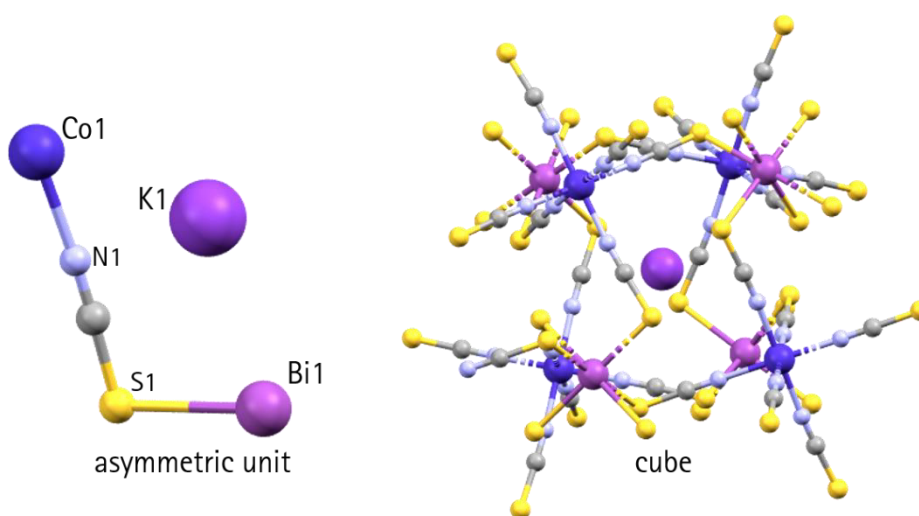


Figure 52: Asymmetric unit and cube structure of SB2. Color code: C, gray; N, light blue; Co, dark blue; Bi, magenta; S, yellow; K, violet.

Addition of methanol leads to **SB3** crystallizing in the monoclinic $P2_1/n$ space group (Table 22). It builds up a 3D framework structure with two cobalt sites which are octahedrally coordinated by four thiocyanate ions and two water molecules. The water molecules are in trans position for Co1 and in cis position for Co2. Similar to **B1**, the Co2 ions build up bridges between $\{[\text{Bi}(\text{SCN})_6]_2[\text{Co}^{\text{II}}(\text{H}_2\text{O})_2]_2\}^{2-}$ layers (Figure 53). However, instead of diethyl ether, molecules of $[\text{Co}(\text{NCS})_2(\text{H}_2\text{O})_4]$ are located within the pores. It might be possible to exchange these cobalt complexes within the pores with other molecules of a similar size to introduce different properties such as spin crossover of luminescence.

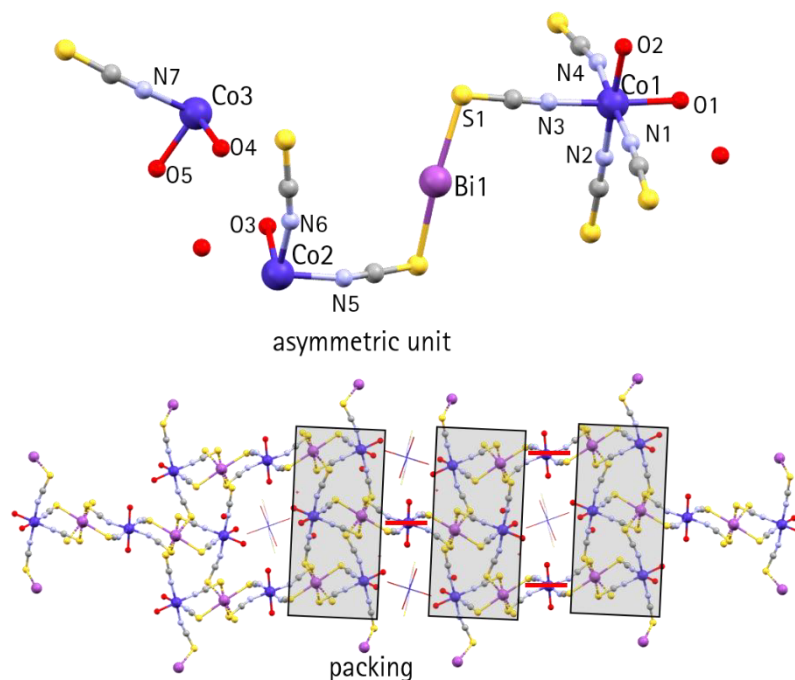


Figure 53: Asymmetric unit and packing of **SB3**. Color code: C, gray; N, light blue; O, red; Co, dark blue; Bi, magenta; S, yellow. Grey boxes visualize the layers of $\{[\text{Bi}(\text{SCN})_6]_2[\text{Co}^{\text{II}}(\text{H}_2\text{O})_2]_2\}^{2-}$ connected through the $[\text{Co}(\text{H}_2\text{O})_2]^{2+}$ units visualized by the red lines.

Exchanging the cobalt ligand from 3-cyanopyridine to 4-cyanopyridine results in **SB4** (Figure 54), whose structure is comparable but not isostructural to **B3**. In contrast to **B3**, **SB4** crystallizes in the triclinic space group $P-1$ (Table 23) and shows 3 distinguishable cobalt sites. However, this structure consists as well of 2D $[\text{Bi}(\text{SCN})_6\text{Co}(3\text{-cyanopyridine})_2]_2$ plane with a 2.8 % shorter distance of 12.455 Å (12.815 Å for **B3**) and which are connected via $[\text{Co}(3\text{-cyanopyridine})_2]^{2+}$ bridges. Also, Co3 is bonded to two thiocyanate ions to the same bismuth ion. Solvent molecules might not be found due to the slightly increased R value. The exchange of modified versions of the monodentate ligand 3-cyanopyridine is possible. This is an additional way of controlling the aggregation of the $[\text{Bi}(\text{SCN})_6]^{3-}$ and cobalt units.

Table 22: Crystallographic data and cobalt(II) coordination bond lengths of SB3.

	$C_{14}H_{28}Bi_2Co_4N_{14}O_{14}S_{14}$	type of bond	bond lengths in Å
<i>T</i> in K	100	Co1-N1	2.092
crystal System	monoclinic	Co1-N2	2.076
space group	$P2_1/n$	Co1-N3	2.079
<i>a</i> in Å	8.2429(7)	Co1-N4	2.084
<i>b</i> in Å	15.528(2)	Co1-O1	2.134
<i>c</i> in Å	12.0597(11)	Co1-O2	2.105
α in °	90	Co2-N5	2.075
β in °	90.8960(10)	Co2-N6	2.100
γ in °	90	Co2-O3	2.167
<i>V</i> in Å ³	2537.4(4)	Co3-N7	2.069
<i>Z</i>	2	Co3-O4	2.123
R_1/wR_2 ($I > 2\sigma$)	0.0260/0.0523	Co3-O5	2.120

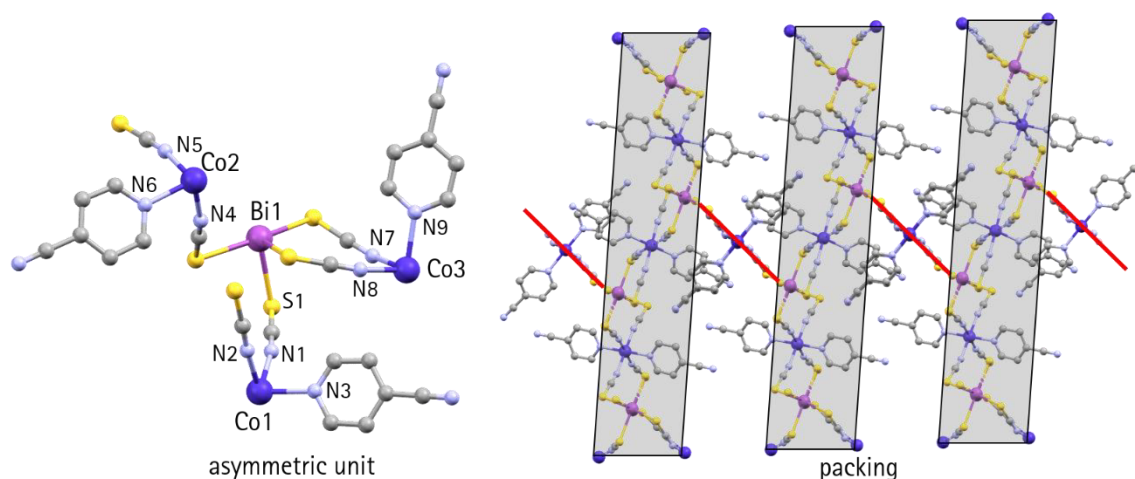


Figure 54: Asymmetric unit and packing of SB4. Color code: C, gray; N, light blue; Co, dark blue; Bi, magenta; S, yellow. The grey boxes and red lines visualize the 2D layer structure and its connecting bridges.

For SB5, the 3-cyanopyridine was exchanged by isoquinoline and it crystallizes in the monoclinic space group $P2_1/m$ (Table 24). The resulting compound shows a layer structure consisting of $\{[Bi(SCN)_6][Co^{II}(\text{isoquinoline})_2]\}^+$ planes which have an interplane distance of 39.114 Å (Figure 55). $[Co(NCS)_4]^{2-}$ complexes and protonated isoquinoline ions are located between these planes. Furthermore, these ions are necessary for the charge balance and are causing the notably large inter layer distance. Two planes are connected via hydrogen interactions of terminal thiocyanate ions and one (*H*-isoquinoline)⁺ with SCN-C distances of 3.045(9) Å and 3.299(1) Å (Figure 72, page 162). The coordination bond lengths of the octahedrally coordinated Co1 correspond to the cobalt(II) HS state. Introducing a larger ligand resulted in an unexpected large interplane distance, which might open up

6. Framework Structure Emerged from Thiocyanate-Based PBAs

the possibility of introducing certain molecules or ions between the layers and therefore control the compounds properties. Furthermore, the interplane distance is larger than most comparable compounds, such as MoS₂ (6.2 Å), and might therefore be used in batteries.^[158,159]

Table 23: Crystallographic data and cobalt(II) coordination bond lengths of SB4.

	C ₁₄ H ₂₈ Bi ₂ Co ₄ N ₁₄ O ₁₄ S ₁₄	type of bond	bond lengths in Å
<i>T</i> in K	100	Co1-N1	2.10
crystal System	triclinic	Co1-N2	2.11
space group	<i>P</i> -1	Co1-N3	2.15
<i>a</i> in Å	8.107(5)	Co2-N4	2.13
<i>b</i> in Å	13.917(9)	Co2-N5	2.10
<i>c</i> in Å	17.285(11)	Co2-N6	2.12
α in °	105.963(7)	Co3-N7	2.12
β in °	91.223(7)	Co3-N8	2.06
γ in °	101.506(7)	Co3-N9	2.19
<i>V</i> in Å ³	1831(2)		
<i>Z</i>	1		
<i>R</i> ₁ / <i>wR</i> ₂ (<i>I</i> > 2σ <i>I</i>)	0.1062/0.2926		

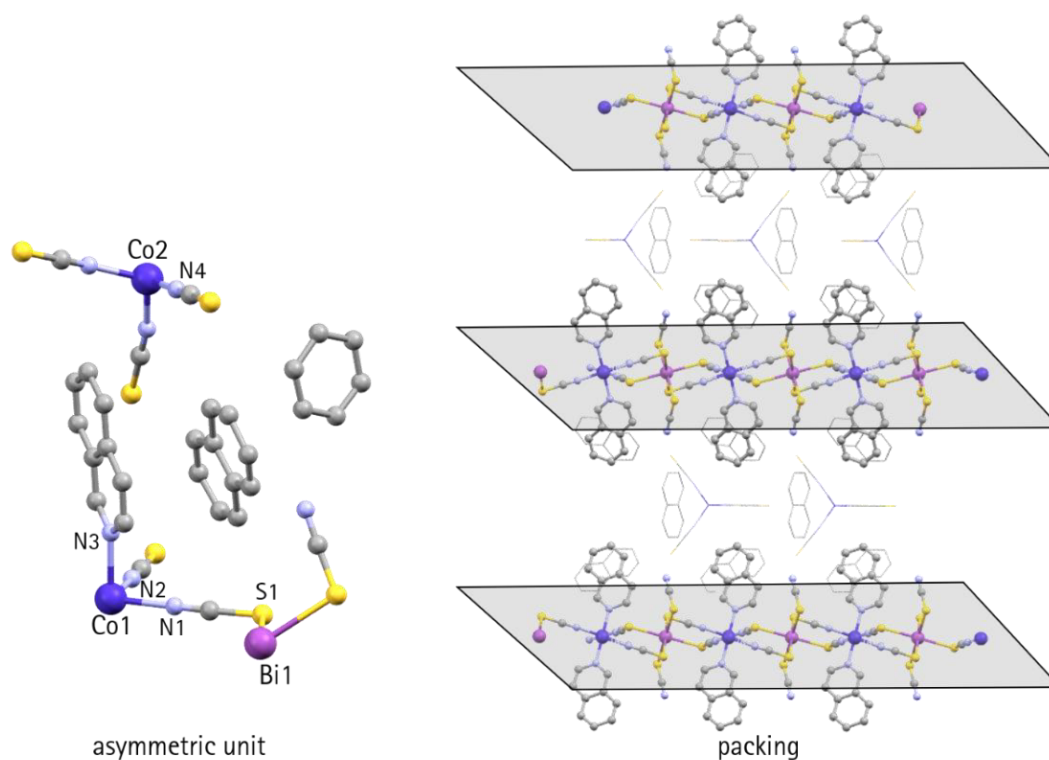


Figure 55: Asymmetric unit and packing of SB5. Color code: C, gray; N, light blue; Co, dark blue; Bi, magenta; S, yellow. The grey boxes visualize the 2D layer structure. The N atoms of the not bonded (*H*-isoquinoline)⁺ ions are not displayed and shown as grey C atoms.

Table 24: Crystallographic data and octahedral coordinated cobalt(II) coordination bond lengths of SB5.

	$C_{14}H_{28}Bi_2Co_4N_{14}O_{14}S_{14}$	type of bond	bond lengths in Å
T in K	100	Co1-N1	2.119
crystal System	monoclinic	Co1-N2	2.158
space group	$P2_1/m$	Co1-N3	2.140
a in Å	8.2612(13)		
b in Å	39.114(6)		
c in Å	9.3360(14)		
α in °	90		
β in °	91.768(2)		
γ in °	90		
V in Å ³	3015.3(8)		
Z	4		
R_1/wR_2 ($I > 2\sigma$)	0.0506/0.0982		

SB6 shows a similar layer structure to B4, which is not isostructural. It crystallizes in the triclinic $P-1$ space group (Table 25) with $[Bi(SCN)_4Ni]^+$ planes (Figure 56). The layers are connected through the coordination of acetone molecules and sodium cations by terminal thiocyanate ions and 3-cyanopyridine molecules. The interlayer distance is 13.173 Å.

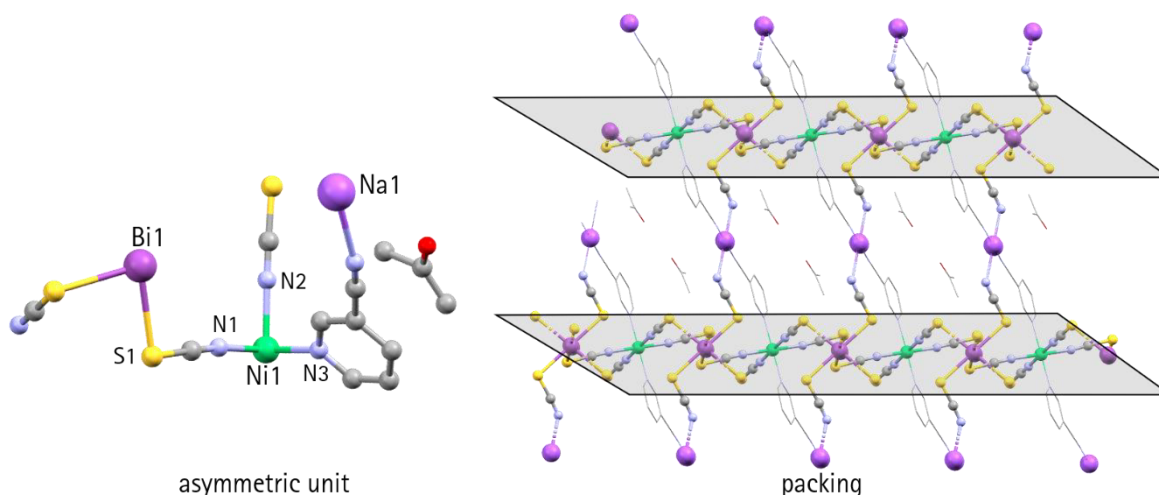


Figure 56: Asymmetric unit and packing of SB6. Color code: C, gray; N, light blue; Ni, green; Bi, magenta; S, yellow; Na, violet. The grey boxes visualize the 2D layer structure.

6. Framework Structure Emerged from Thiocyanate-Based PBAs

Table 25: Crystallographic data and octahedral coordinated cobalt(II) coordination bond lengths of **SB6**.

	$C_{24}H_{20}BiNiN_{10}O_2S_6$	type of bond	bond lengths in Å
T in K	100	Ni1-N1	2.07
crystal System	triclinic	Ni1-N2	2.08
space group	$P\bar{1}$	Ni1-N3	2.11
a in Å	8.198(6)		
b in Å	8.859(7)		
c in Å	13.389(10)		
α in °	85.513(8)		
β in °	80.655(7)		
γ in °	88.786(7)		
V in Å ³	956.5(13)		
Z	1		
R_1/wR_2 ($I > 2\sigma I$)	0.0713/0.1866		

The variation of the transition metal ions shows in comparison that the interplane distances of the 2D layer structures (Table 26) change less than 1 %. Exchanging potassium for sodium ions resulted in an interplane distance change of about 2 %. Larger variations of the interplane distances might be possible by introducing larger cations such as cesium or Bu_4N^+ . the use of unusual cations or the use of additional anions as for **SB1** and **SB5** had an even bigger impact, which resulted in an increased interplane distance of about 21 % and 194 %, respectively.

Table 26: Interplane distances of various 2D bismuth-thiocyanate-based coordination polymers.

	B2	B4	B5	B6	SB1	SB5	SB6
transition metal cation	Co	Co	Fe	Ni	Co	Co	Ni
(alkali) metal cation	K	Na	K	K	-	isoquinoline	Na
interplane distance in Å	13.398	13.186	13.452	13.396	16.165	39.114	13.173

6.3 Conclusion and Outlook

In this chapter, 12 new bismuth(III) thiocyanate coordination framework compounds including cobalt(II), nickel(II) and iron(II) were presented. The compounds were derived from the first reported bismuth thiocyanate-based PBA^[36], but, except for SB2, all compounds show 3D or 2D structures that are different from Prussian blue. Even though the samples could not be obtained without impurities, which are assumed to be mainly nitrate-salts, a detailed crystal structure analysis, magnetic measurements for B2 – B6 and N₂ adsorption and desorption measurements for B2 + B3 and B6 were performed. The structure analysis showed that the water ligand of B1 can be exchanged by monodentate ligands of different sizes such as 3-cyanopyridine and isoquinoline. It was not possible to obtain any crystal structure from multidentate or bridging monodentate ligands such as 2,2'-bipyridine, 4,4'-bipyridine, or pyrazine. Mostly, compounds with the monodentate ligand 3-cyanopyridine were investigated showing very similar 2D structures with alternating [Bi(SCN)₆M]⁻ (M: Co^{II}, Ni^{II}, and Fe^{II}) and (solvent-A)⁺ (A: K or Na) layers for B2, B4, B5, B6, and SB6. However, the same synthesis as for B2 yielded also B3 to which SB4 (4-cyanopyridine instead of 3-cyanopyridine) is very similar. Exceptional crystal structures were derived from varying the [Bi(SCN)₆]³⁻ and [Co(3-cyanopyridine)₂]²⁺ ratio (SB1), introducing compounds which are not coordinating themselves and also preventing the water from coordinating (SB2), exchanging the solvent (SB3), and introducing large ligands (SB5). The resulting compounds show enlarged interplane distances up to 39 Å for 2D structures, co-crystallized complexes, or are PBAs. The temperature-depending magnetic data are not very reliable but can be assumed to show cobalt(II) and iron(II) in the HS state and nickel(II), respectively. B5 shows a possible phase transition at about 73 K without changing its spin state which was confirmed by a Mössbauer spectrum. The N₂ adsorption and desorption measurements showed no porosity for B2 + B3 and B6 before and after activation at 105 °C. Furthermore, all samples could easily be redissolved, probably because of the weak Bi-SCN bond.

These results suggest that the structure of the bismuth(III) thiocyanate-based coordination frameworks can be controlled by the addition of organic monodentate ligands and non-coordinating organic compounds. While the exchange of potassium with sodium cations resulted in small changes for the properties and crystal structures, larger cations such as cesium and Bu₄N⁺ might have a bigger impact. The magnetic and optical properties can be controlled through the exchange of the transition metal ions. Co-crystallization of smaller molecules or ions might be possible between the [Bi(SCN)₆M]⁻ layers in 2D structures, especially in SB5, or in cavities occurring in SB3. This might be a possibility for introducing further properties such as luminescence or SCO while controlling the compounds surrounding. One approach might be to use the terminal thiocyanate ions in the 2D structures and coordinate SCO complexes such as [Fe^{III}(salpet_{R1,R2})₂]⁺ (Chapter 4.1) to it. Furthermore, the framework

6. Framework Structure Emerged from Thiocyanate-Based PBAs

might be used as new sensor material^[126] if SCO properties would be achieved, intrinsically through exchanging the transition metal ions and ligands or extrinsically through the previously described introduction of SCO complexes. **SB5** might also be used as battery material due to its large interlayer distances.^[158,159] Another interesting approach is the PBA **SB2** which might be used for similar reasons as other PBAs such as absorption of terahertz light,^[151] hydrogen storage, molecular sieves, electrode material, and nanoscale devices.^[74,153]

7. General Conclusion and Outlook

The topic of this dissertation is the characterization of novel cyanide and thiocyanate-bridged multinuclear complexes synthesized from mononuclear building blocks. The aim was to investigate how the switching behavior and crystal structure formation can be controlled by analyzing single building blocks and utilizing their properties in a rational building block approach. Important building blocks utilized in this thesis were a penta- N_5 -dentate Schiff base ligand stabilizing cobalt(II) ions at aerobic conditions (Chapter 3), a similar penta- N_3O_2 -dentate Schiff base ligand stabilizing iron(III) and cobalt(III) complexes (Chapter 4), a complete tetranuclear $[Co_2Fe_2]$ complex used as a building block to co-crystallize it with 4-aminobenzoic acid (Chapter 5), and the $[Bi^{III}(SCN)_6]^{3-}$ building block to build up new kinds of 2D and 3D frameworks (Chapter 6).

In Chapter 3, a series of four dinuclear complexes based, on a cobalt(II) complex with one accessible site, were investigated. The cobalt(II) complex was combined with $[Fe(tp)(CN)_3]^-$, $[Fe(tp^*)(CN)_3]^-$, and $[Fe(pztp)(CN)_3]^-$ obtaining three different compounds with a fourth one resulting from the exchange of BF_4^- with ClO_4^- for the tp compound. All four complexes show the $[Fe^{III}_5Co^{II}_{HS}]$ phase down to 5 K which is stabilized by the redox potential difference of the iron and cobalt ions between 1.085 V and 1.32 V. Literature data suggest^[15] that smaller redox potential differences could lead to an ETCST, which can be achieved by modifications of the ligands. Noteworthy is that both dinuclear complexes with the iron-tp building block show a molecular predominant direction within the crystal structure that could lead to a macroscopic electron transfer induced polarization, in the case of an ETCST.

A series of $[Fe(salpet_{R1,R2})X]$ ($X: Cl^-, N_3^-, NCO^-, NCS^-, NCS_2^-, NC^-$) building blocks was investigated in Chapter 4 with regard to their redox properties. The redox potentials for the chloride complexes are between -0.260 V and -0.365 V and for the cyanide complexes between -0.555 V and -0.700 V, which is comparable to already known building blocks for ETCST complexes.^[15] Therefore, $[Fe(salpet_{R1,R2})CN]$ building blocks could be attractive capping complexes for dinuclear and trinuclear ETCST complexes. However, no mixed-valence multinuclear compound could be synthesized starting from these cyanometalates nor has been reported yet. Instead, two new synthesis strategies were applied. First, the use of $[Co(salpet_{H,H})CN]$ building blocks, which resulted in two mixed-valence trinuclear $[Co^{III}_2Co^{II}]$ complexes. While both complexes showed the HS state for the cobalt(II) and the LS state the cobalt(III) ions, the molecular shape and resulting crystal structure could be controlled by the used monodentate (linear molecule) and bidentate (angled structure) ligands. The second synthesis strategy included the use of different cyanometalates in combination with $[M(salpet_{R1,R2})Cl]$ ($M: Fe^{III}, Co^{III}$). In contrast to $[M(salpet_{R1,R2})CN]$, the cyanide is differently orientated, which resulted in new multinuclear compounds

and switching behavior. Two pentanuclear complexes were obtained by combining $[\text{Mo}(\text{CN})_8]^{4-}$ and $[\text{W}(\text{CN})_8]^{4-}$ with $[\text{Fe}(\text{salpet}_{\text{H},\text{NO}_2})\text{CN}]$ and $[\text{Co}(\text{salpet}_{\text{H},\text{NO}_2})\text{CN}]$, respectively. The $[\text{Mo}^{\text{IV}}\text{Fe}^{\text{III}}_4]$ complex showed thermally induced SCO behavior in solid-state. Moreover, the $[\text{WCo}_4]$ complex showed typical MMCT UV-Vis bands in solution indicating an ETCST and possibly a new ETCST behavior in solid-state ($[\text{W}^{\text{V}}\text{Co}^{\text{II}}_{\text{HS}}\text{Co}^{\text{III}}_{\text{LS}}]/[\text{W}^{\text{VI}}\text{Co}^{\text{II}}_{\text{HS}}\text{Co}^{\text{III}}_{\text{HS}}]$), which needs to be investigated further. Based on the two presented synthesis strategies, new SCO and likely ETCST complexes can be synthesized, enlarging the variety of different capping complexes.

Chapter 5 is about solid-state alterations of hydrogen bonding interactions between an ETCST-active $[\text{Co}_2\text{Fe}_2]$ tetranuclear complex and 4-aminobenzoic acid (aba). The crystal structure changes dramatically through desolvation of the compound inducing a significant change of the thermal ETCST behavior. Furthermore, the hydrogen bonding interactions between the $[\text{Co}_2\text{Fe}_2]$ complex and the aba change together with the ETCST. These results suggest that the control of the ETCST transition in solution through protonation of terminal cyanide ions in tetranuclear square $[\text{Co}_2\text{Fe}_2]$ complexes^[18,35] can be mimicked by co-crystallization in solid-state and offer new possibilities of influencing the crystal structure and its switching behavior.

In the last chapter, the synthesis, structures, and properties of 12 new bismuth(III) thiocyanate-based frameworks derived from a PBA were discussed. The combination of $[\text{Bi}^{\text{III}}(\text{SCN})_6]^{3-}$ building blocks with cobalt(II), iron(II), or nickel(II) and monodentate ligands led to 2D and 3D framework structures. Previous results showed thermochromic behavior for two of the investigated compounds,^[38] which was not caused by a cobalt(II) SCO but likely by small structural changes. Magnetic and N_2 adsorption measurements were performed for some of the samples showing the HS state for the cobalt(II) and iron(II) ions and no porosity, respectively. It was investigated how the crystal structure can be altered through the used metal ions, by adjusting the synthesis, and through the addition of different ligands and additives. Especially the interplane distances for the 2D structures could be controlled through the reaction procedure and varied between 13 Å and 39 Å. To obtain an SCO framework, the ligand field splitting must be further increased by an appropriate choice of ligands. Furthermore, it might be possible to introduce additional functionalities through co-crystallization or exchangeable guest molecules within the framework.

To generally summarize the results, new and known building blocks were analyzed and used for the synthesis of multinuclear complexes. Switchable properties were demonstrated for two pentanuclear and one tetranuclear complex. The $[\text{WCo}_4]$ pentanuclear complex might show a new kind of ETCST behavior, which needs to be further investigated. In addition, the co-crystallization approach for the $[\text{Co}_2\text{Fe}_2]$ complex leads to new possibilities of controlling the aggregation and ETCST behavior of similar complexes. Furthermore, a large number of structural and physical characterizations were performed

and summarized. These results open the possibility of using the analyzed building blocks for further reactions to synthesize new outstanding compounds. Examples for desirable properties in compounds derived from these results are following described. The first example is an ETCST induced polarization based on the molecular orientation within the crystal structure of mixed-valence PBAs as described for two dinuclear complexes (Chapter 3). In addition, the iron(III) and cobalt(III) building blocks from Chapter 4 might be a suitable complement. An electron transfer towards one predominant crystallographic direction might also be achieved by co-crystallization (Chapter 5) of chiral molecules or ions. Continuous development of this approach might also lead to an ETCST induced by electric fields, which can be a big step towards applications in electronic devices.^[99] The co-crystallization approach can also be used to alter the SCO or luminescence behavior of complexes or molecules through ETCST modulated hydrogen bonding interactions. Furthermore, the large interplane distances achieved within the new bismuth-thiocyanate-based frameworks (Chapter 6) might be used as battery material.^[158,159] On the other hand, the introduction of SCO properties into these bismuth-thiocyanate-based frameworks might lead to new sensor materials as described for other SCO frameworks before.^[126] Further sensor applications might be derived from the acid-sensitive $[\text{Co}_2\text{Fe}_2]$ complex (Chapter 5) through producing complex-polymer composites. These examples show how this research can be continued and that the presented compounds can potentially lead to new chemical sensors and multi responsive molecular devices.

8. Appendix

Table 27: Redox potentials vs. SCE of previously reported cyanide-bridged mixed-valence $[\text{CoFe}]_x$ ($X = 1$ or 2) complexes. Data for Figure 8.

$E_{1/2}(\text{Fe})$ in V	$E_{1/2}(\text{Co})$ in V	$\Delta E_{1/2}(E_{1/2}(\text{Fe}) - E_{1/2}(\text{Co}))$ in V	Spin state	reference
-0.18, -0.02	0.39, 0.52	-0.41	ETCST-active $[\text{Co}^{\text{II}}(\text{HS})\text{Fe}^{\text{III}}(\text{LS})]$	[15,18]
-0.16, 0.02	0.43, 0.57	-0.41	$[\text{Co}^{\text{II}}(\text{HS})\text{Fe}^{\text{III}}(\text{LS})]$	[15,18]
0.6, 0.44	-0.13	+0.57	$[\text{Co}^{\text{III}}(\text{LS})\text{Fe}^{\text{II}}(\text{LS})]$	[15,18]
-0.18, -0.04	0.37, 0.52	-0.41	ETCST-active $[\text{Co}^{\text{II}}(\text{HS})\text{Fe}^{\text{III}}(\text{LS})]$	[15,35]
-0.25, -0.09	0.37, 0.52	-0.46	ETCST-active $[\text{Co}^{\text{II}}(\text{HS})\text{Fe}^{\text{III}}(\text{LS})]$	[15,35]
-0.17, -0.03	0.41, 0.59	-0.44	ETCST-active $[\text{Co}^{\text{II}}(\text{HS})\text{Fe}^{\text{III}}(\text{LS})]$	[15,35]
-0.25, -0.10	0.36, 0.55	-0.46	ETCST-active $[\text{Co}^{\text{II}}(\text{HS})\text{Fe}^{\text{III}}(\text{LS})]$	[15,35]
1.51, 1.37	0.43, 0.28	0.94	$\text{Co}^{\text{III}}(\text{LS})\text{Fe}^{\text{II}}(\text{LS})]$	[15,76]
-0.53	0.39	-0.92	$[\text{Co}^{\text{II}}(\text{HS})\text{Fe}^{\text{III}}(\text{LS})]$	[15,24]
0.12	-0.07	0.19	$\text{Co}^{\text{III}}(\text{LS})\text{Fe}^{\text{II}}(\text{LS})]$	[15,24]
0.39	-0.67	1.06	$\text{Co}^{\text{III}}(\text{LS})\text{Fe}^{\text{II}}(\text{LS})]$	[15,88]

8.1 Novel Dinuclear Cyanide-Bridged Complexes

Co(II) and Fe(II) Schiff Base Complexes in Dinuclear Prussia Blue Analogs

Supporting Information

Dominik Natke,* Taishi Enomoto, Roman Boca, Takuya Shiga, Masaaki Ohba, Hiroki Oshio, Franz Renz*

Contents

Experimental Section

Table S1: Crystallographic data of $[\text{Co}(\text{L}^1)(\text{H}_2\text{O})](\text{BF}_4)_2$, 1, 2 and 3

Figure S1: Molecular structure of 1

Table S2: Coordination bond length of 1

Figure S2: Molecular structure of 2

Table S3: Coordination bond length of 2

Figure S3: Comparison of the molecular structure of 1 and 2

Figure S4: Asymmetric unit of 3

Table S4: Coordination bond length of 3

Fitting of the Magnetic Data (Figure S5)

Table S5: Redoxpotentials previously reported cyanide-bridged mixed-valence complexes

Figure S6: UV-Vis spectra of 3 with applied potentials

Figure S7: Changes of the UV-Vis spectra a cyclic voltammograms for 3 through the addition of tetraethylammonium cyanide

Experimental Section

All chemicals were purchased from commercial suppliers and used without further purification. The mononuclear compound $[\text{Co}(\text{L}^1)(\text{H}_2\text{O})](\text{BF}_4)_2$ was synthesized as previously described^[D11] with $\text{Co}(\text{BF}_4)_2 \cdot 6\text{H}_2\text{O}$ instead of $\text{Co}(\text{ClO}_4)_2 \cdot 6\text{H}_2\text{O}$ and the Fe(III) complexes $\text{Bu}_4\text{N}[\text{Fe}(\text{tp})(\text{CN})_3]$ ^[D12] and $\text{Bu}_4\text{N}[\text{Fe}(\text{pztp})(\text{CN})_3]$ ^[D13] (Bu_4N = tetrabutylammonium) were synthesized according to literature methods. All syntheses were performed under aerobic conditions.

$[\text{Co}(\text{L}^1)\text{-CN-Fe}(\text{tp})(\text{CN})_2](\text{BF}_4) \cdot \text{H}_2\text{O}$ (1):

To a solution of $[\text{Co}(\text{L}^1)(\text{H}_2\text{O})](\text{BF}_4)_2$ (0.05 mmol) in 10 ml acetonitrile $\text{Bu}_4\text{N}[\text{Fe}(\text{tp})(\text{CN})_3]$ (0.05 mmol) was added together with Bu_4NPF_6 (0.075 mmol) resulting in an orange solution. After 2 h of stirring at RT, the solution was filtrated, and orange single crystals could be obtained by vapor diffusion of diethyl ether. $\text{C}_{33}\text{H}_{41}\text{F}_4\text{B}_2\text{CoFeN}_{14}\text{O}$, $[\text{Co}(\text{L}^1)\text{-CN-Fe}(\text{tp})(\text{CN})_2](\text{BF}_4) \cdot 2 \text{H}_2\text{O}$: found % (calcd. %): C 44.74 (45.03), H 4.71 (4.92), N 21.82 (22.28); IR (KBr; cm^{-1}): 1045 (BF_4^-), 2114 (cyanide).

$[\text{Co}(\text{L}^1)\text{-CN-Fe}(\text{pztp})(\text{CN})_2](\text{BF}_4) \cdot \text{C}_2\text{H}_3\text{N}$ (2):

To a solution of $[\text{Co}(\text{L}^1)(\text{H}_2\text{O})](\text{BF}_4)_2$ (0.05 mmol) in 10 ml acetonitrile $\text{Bu}_4\text{N}[\text{Fe}(\text{tp})(\text{CN})_3]$ (0.05 mmol) was added resulting in a orange solution. After 20 min of stirring at RT, the solution was filtrated, and orange single crystals could be obtained by vapor diffusion of diethyl ether. $\text{C}_{38}\text{H}_{44}\text{B}_2\text{CoF}_4\text{FeN}_{17}$, $[\text{Co}(\text{L}^1)\text{-CN-Fe}(\text{pztp})(\text{CN})_2](\text{BF}_4) \cdot \text{acetonitrile}$: found % (calcd. %): C 47.66 (47.98), H 4.58 (4.66), N 24.70 (25.03); IR (KBr; cm^{-1}): 1084 (BF_4^-), 2126 (cyanide).

$[\text{Fe}(\text{L}^2)\text{-CN-Fe}(\text{L}^2)](\text{PF}_6)_3 \cdot 3 \text{C}_2\text{H}_3\text{N}$ (3):

2-Pyridinecarboxaldehyde (2 mmol) and *N*-(2-aminoethyl)-1,3-propanediamine (1 mmol) were mixed in 5 ml methanol and stirred at 60 °C for 5 min. The solvent was removed, and the orange oil was used for the next step without further purification. The oil was added dropwise to a solution of $\text{Fe}(\text{BF}_4)_2 \cdot 6\text{H}_2\text{O}$ (1 mmol) in 5 ml acetonitrile resulting in violet solution which changed to blue after the addition of tetraethylammonium cyanide (1 mmol). The solution was filtrated after the addition of Bu_4NPF_6 (12 mmol) and single crystals of 3 could be obtained through vapor diffusion if tert-butylmethylether. $\text{C}_{38}\text{H}_{39}\text{F}_{18}\text{Fe}_2\text{N}_{11}\text{P}_3$, $[\text{Fe}(\text{L}^2)\text{-CN-Fe}(\text{L}^2)](\text{PF}_6)_3$: found % (calcd. %): C 36.14 (36.14), H 3.64 (3.23), N 13.24 (13.39); IR (KBr; cm^{-1}): 839 (PF_6^-), 2124 (cyanide).

Crystal structure analysis: The diffraction data were collected with a Bruker SMART APEX II diffractometer with a CCD area detector and graphite-monochromated Mo-K α radiation ($\lambda = 0.71073 \text{ \AA}$). The data frames were integrated using the SAINT program and merged to give a unique data set for structure determination. An absorption correction was performed using SADABS.^[D14] The structure was solved by direct methods and refined on F^2 by the full-matrix least-squares methods

using the SHELXTL package (Bruker Analytical X-ray systems, Olex2).^[D15,D16] Non-hydrogen atoms were refined with anisotropic thermal parameters. Hydrogen atoms were included in calculated positions and refined with isotropic thermal parameters riding on those of the parent atoms.

Physical measurements: Magnetic susceptibility data were collected using a Quantum Design MPMS-5S SQUID magnetometer. The measurements were performed with an applied magnetic field of 1000 Oe for **1** and 10000 Oe for **2** in the temperature range of 5 - 300 K. Magnetic data were corrected for the diamagnetism of the sample holder, and for the diamagnetism of the sample using Pascal's constants. The compounds **1** and **2** were measured at 5.0 K increments in the settle mode with a fixed scan rate of 3.0 K/min and 30 seconds after the temperature had stabilized. The samples **1** was measured during cooling and heating and sample **2** only during the cooling process. Infrared absorption spectra were measured on KBr pellet samples for **1**, **2** and **3** using a SHIMADZU IR Affinity-1 spectrometer. Cyclic voltammetry measurements were carried out in a standard one-compartment cell under N₂ at RT equipped with a platinum-wire counter electrode, an SCE reference electrode, and a glassy carbon (GC) working electrode using a BAS 620A electrochemical analyzer. The measurements were performed in MeCN with 0.1 M tetra-n-butylammonium hexafluorophosphate (Bu₄NPF₆) as the supporting electrolyte and a scan rate of 0.1 V/s. UV-Vis absorption spectra were recorded with a SHIMADZU UV-3150 spectrometer.

[D11] A. Panja, *Dalt. Trans.* 2014, 43, 7760.

[D12] J. Kim, S. Han, I.-K. Cho, K. Y. Choi, M. Heu, S. Yoon, B. J. Suh, *Polyhedron*, 2004, 23, 1333–1339.

[D13] C. Q. Jiao, Y. S. Meng, Y. Yu, W. J. Jiang, W. Wen, H. Oshio, Y. Luo, C. Y. Duan, T. Liu, *Angew. Chemie - Int. Ed.* 2019, 58, 17009–17015.

[D14] G. M. Sheldrick, *SADABS: An Empirical Absorption Correction Program*, Bruker Analytica X-ray Systems, Madison, WI, 1996.

[D15] G. M. Sheldrick, *Acta Crystallogr. Sect. C Struct. Chem.* 2015, 71, 3–8.

[D16] O. V. Dolomanov, L. J. Bourhis, R. J. Gildea, J. A. K. Howard, H. Puschmann, *J. Appl. Crystallogr.* 2009, 42, 339–341.

8. Appendix

Table S1: Crystallographic data of [Co(L¹)(H₂O)](BF₄)₂, 1, 2 and 3.

	[Co(L ¹)(H ₂ O)](BF ₄) ₂	1
	C ₂₁ H ₃₁ B ₂ CoF ₈ N ₅ O	C ₃₃ H ₄₁ B ₂ CoF ₄ FeN ₁₄ O
<i>T</i> in K	100	100
Crystal System	Monoclinic	monoclinic
Space group	<i>P</i> 2 ₁ / <i>c</i>	C <i>c</i>
<i>a</i> in Å	8.3557(9)	22.685(5)
<i>b</i> in Å	19.962(2)	11.222(2)
<i>c</i> in Å	15.4646(16)	16.315(3)
α in °	90	90
β in °	100.3680(10)	110.077(2)
γ in °	90	90
<i>V</i> in Å ³	2537.3(5)	3901.1(14)
<i>Z</i>	4	4
<i>R</i> ₁ / <i>wR</i> ₂ (<i>I</i> > 2σ <i>I</i>)	0.0346/0.0869	0.0563/0.1325
	2	3
	C ₃₈ H ₄₄ B ₂ CoF ₄ FeN ₁₇	C ₄₁ H ₄₈ F ₁₈ Fe ₂ N ₁₄ P ₃
<i>T</i> in K	100	100
Crystal System	triclinic	monoclinic
Space group	<i>P</i> -1	C2/ <i>c</i>
<i>a</i> in Å	12.7776(17)	24.273(2)
<i>b</i> in Å	18.211(3)	23.130(2)
<i>c</i> in Å	18.943(3)	10.1819(10)
α in °	83.358(2)	90
β in °	86.090(2)	107.7780(10)
γ in °	80.305(2)	90
<i>V</i> in Å ³	4310.4(10)	5443.3(9)
<i>Z</i>	4	4
<i>R</i> ₁ / <i>wR</i> ₂ (<i>I</i> > 2σ <i>I</i>)	0.0559/0.1444	0.0466/0.1285

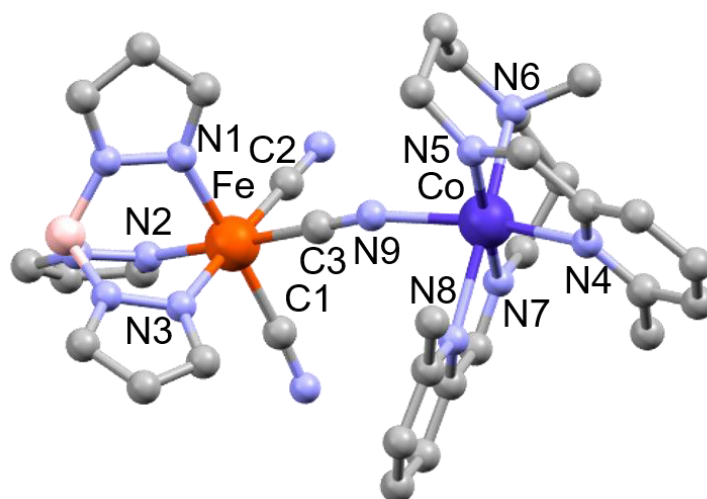


Figure S1: Molecular structure of 1. Hydrogen atoms, solvent and anions have been omitted for clarity. Color code: C, gray; N, light blue; Co, dark blue; Fe, orange; B, pink.

Table S2: Coordination bond length of 1.

Bond length in Å	1
Fe-N1	1.976(7)
Fe-N2	1.966(7)
Fe-N3	1.971(6)
Fe-C1	1.929(9)
Fe-C2	1.932(7)
Fe-C3	1.901(8)
Co-N4	2.203(7)
Co-N5	2.108(6)
Co-N6	2.262(5)
Co-N7	2.112(6)
Co-N8	2.284(6)
Co-N9	2.083(8)

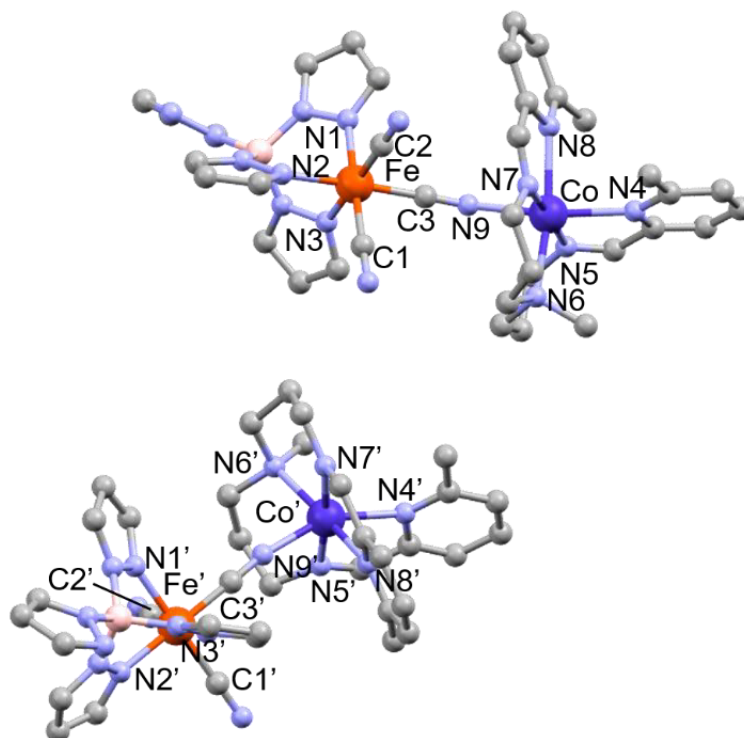


Figure S2: Molecular structure of 2. Hydrogen atoms, solvent and anions have been omitted for clarity. Color code: C, gray; N, light blue; Co, dark blue; Fe, orange; B, pink.

Table S3: Coordination bond length of 2.

Bond length in Å	2	Bond length in Å	2
Fe-N1	1.960(3)	Fe'-N1'	1.988(3)
Fe-N2	1.995(3)	Fe'-N2'	1.966(2)
Fe-N3	1.972(3)	Fe'-N3'	1.977(3)
Fe-C1	1.925(3)	Fe'-C1'	1.930(4)
Fe-C2	1.923(3)	Fe'-C2'	1.931(3)
Fe-C3	1.906(4)	Fe'-C3'	1.896(4)
Co-N4	2.218(3)	Co'-N4'	2.214(3)
Co-N5	2.084(3)	Co'-N5'	2.122(3)
Co-N6	2.224(3)	Co'-N6'	2.257(3)
Co-N7	2.084(3)	Co'-N7'	2.108(3)
Co-N8	2.281(3)	Co'-N8'	2.290(3)
Co-N9	2.127(3)	Co'-N9'	2.059(2)

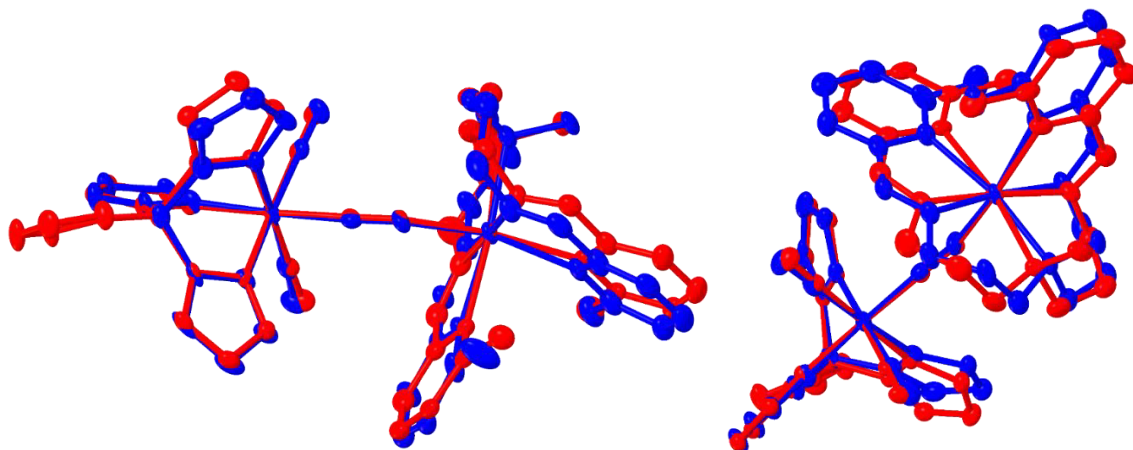


Figure S3: Comparison of the molecular structure of 1 and 2. Blue 1; red: 2.

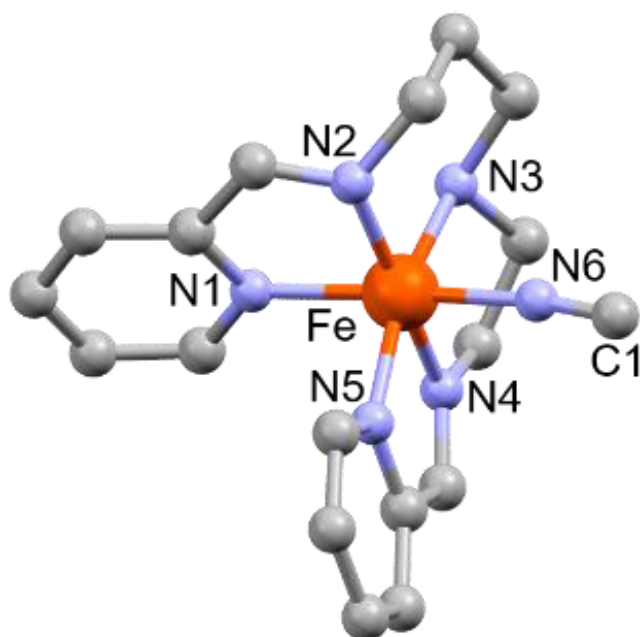


Figure S4: Asymmetric unit of 3. Hydrogen atoms, solvent and anions have been omitted for clarity. Color code: C, gray; N, light blue; Fe, orange.

Table S4: Coordination bond length of 3.

Bond length in Å	3
Fe-N1	1.981(2)
Fe-N2	1.922(2)
Fe-N3	2.016(2)
Fe-N4	1.885(2)
Fe-N5	1.975(2)
Fe-N6	1.918(2)
Fe-C1	1.918(2)

Fitting of the Magnetic Data

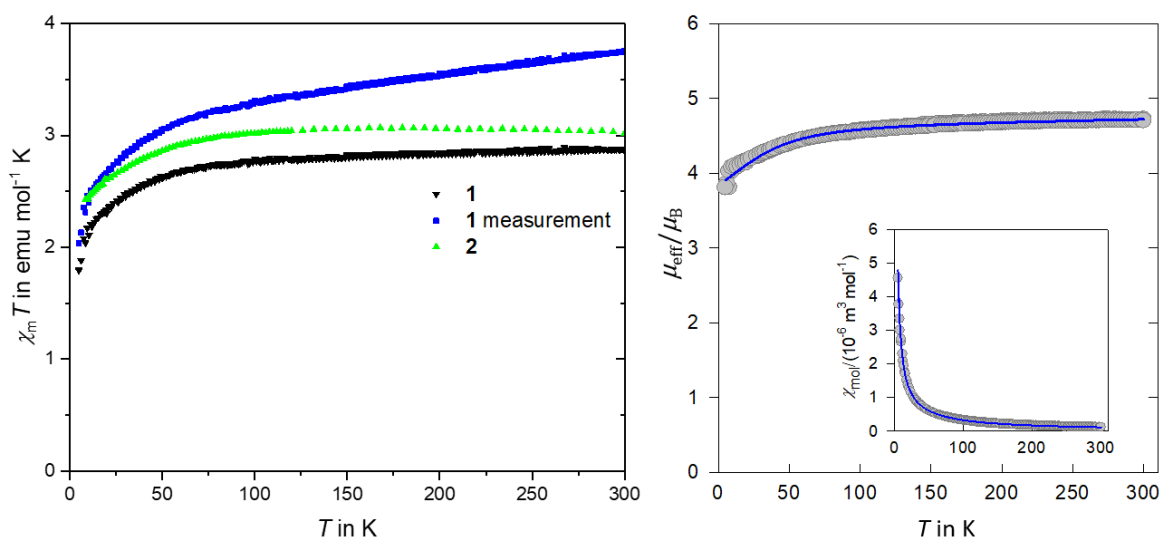


Figure S5: $\chi_m T - T$ plots (left) of 1, 2 and the calculated data of 1 without the correction of the temperature-independent susceptibility. Fitted magnetic data of 1 (right) and molar magnetic susceptibility (right-inset).

The magnetic data of 1 were fitted by using the spin Hamiltonian

$$\hat{H} = -J(\vec{S}_{\text{Co}} \cdot \vec{S}_{\text{Fe}})\hbar^{-2} + D_{\text{Co}}(\hat{S}_{\text{Co},z}^2 - \vec{S}_{\text{Co}}^2/3)\hbar^{-2} \\ + \mu_B B(g_{\text{Co}}\hat{S}_{\text{Co},z})\hbar^{-1} + \mu_B B(g_{\text{Fe}}\hat{S}_{\text{Fe},z})\hbar^{-1}$$

which contains the isotropic exchange interaction, the zero-field splitting at the Co(II) center, and isotropic spin Zeeman terms for Co(II) and Fe(III); $S_{\text{Co}} = 3/2$ and $S_{\text{Fe}} = 1/2$. The fitting procedure gave $J/hc = -0.014 \text{ cm}^{-1}$, $g_{\text{Co}} = 2.12(9)$, $g_{\text{Fe}} = 2.50(51)$, $D_{\text{Co}}/hc = 44(7)$ and the temperature-independent susceptibility $\chi_{\text{IM}} = 5(2) \times 10^{-9} \text{ m}^3 \text{ mol}^{-1}$ (SI units).

Table S5: Redoxpotentials vs. SCE of previously reported cyanide-bridged mixed-valence $[\text{CoFe}]_x$ ($X = 1$ or 2) complexes and 1 and 2.

$E_{1/2}(\text{Fe})$ in V	$E_{1/2}(\text{Co})$ in V	$\Delta E_{1/2}(E_{1/2}(\text{Fe})-E_{1/2}(\text{Co}))$ in V	Spin state	reference
-0.18, -0.02	0.39, 0.52	-0.41	ETCST-active $[\text{Co}^{\text{II}}(\text{HS})\text{Fe}^{\text{III}}(\text{LS})]$	7,8
-0.16, 0.02	0.43, 0.57	-0.41	$[\text{Co}^{\text{II}}(\text{HS})\text{Fe}^{\text{III}}(\text{LS})]$	7,8
0.6, 0.44	-0.13	+0.57	$[\text{Co}^{\text{III}}(\text{LS})\text{Fe}^{\text{II}}(\text{LS})]$	7,8
-0.18, -0.04	0.37, 0.52	-0.41	ETCST-active $[\text{Co}^{\text{II}}(\text{HS})\text{Fe}^{\text{III}}(\text{LS})]$	7,9
-0.25, -0.09	0.37, 0.52	-0.46	ETCST-active $[\text{Co}^{\text{II}}(\text{HS})\text{Fe}^{\text{III}}(\text{LS})]$	7,9
-0.17, -0.03	0.41, 0.59	-0.44	ETCST-active $[\text{Co}^{\text{II}}(\text{HS})\text{Fe}^{\text{III}}(\text{LS})]$	7,9
-0.25, -0.10	0.36, 0.55	-0.46	ETCST-active $[\text{Co}^{\text{II}}(\text{HS})\text{Fe}^{\text{III}}(\text{LS})]$	7,9
1.51, 1.37	0.43, 0.28	0.94	$\text{Co}^{\text{III}}(\text{LS})\text{Fe}^{\text{II}}(\text{LS})]$	7,10
-0.53	0.39	-0.92	$[\text{Co}^{\text{II}}(\text{HS})\text{Fe}^{\text{III}}(\text{LS})]$	7,11
0.12	-0.07	0.19	$\text{Co}^{\text{III}}(\text{LS})\text{Fe}^{\text{II}}(\text{LS})]$	7,11
0.39	-0.67	1.06	$\text{Co}^{\text{III}}(\text{LS})\text{Fe}^{\text{II}}(\text{LS})]$	7,12
-0.295	0.86	-1.155	$[\text{Co}^{\text{II}}(\text{HS})\text{Fe}^{\text{III}}(\text{LS})]$	
-0.265	0.82	-1.085	$[\text{Co}^{\text{II}}(\text{HS})\text{Fe}^{\text{III}}(\text{LS})]$	

[7] M. Nihei, Chem. Lett. 2020, 49, 1206–1215.

[8] M. Nihei, Y. Sekine, N. Suganami, K. Nakazawa, A. Nakao, H. Nakao, Y. Murakami, H. Oshio, J. Am. Chem. Soc. 2011, 133, 3592–3600.

[9] M. Nihei, K. Shiroyanagi, M. Kato, R. Takayama, H. Murakami, Y. Kera, Y. Sekine, H. Oshio, Inorg. Chem. 2019, 58, 11912–11919.

[10] H. Oshio, H. Onodera, O. Tamada, H. Mizutani, T. Hikichi, T. Ito, Chem. – A Eur. J. 2000, 6, 2523–2530.

[11] I.-R. Jeon, S. Calancea, A. Panja, D. M. Piñero Cruz, E. S. Koumoussi, P. Dechambenoit, C. Coulon, A. Wattiaux, P. Rosa, C. Mathonière, et al., Chem. Sci. 2013, 4, 2463.

[12] P. V. Bernhardt, B. P. Macpherson, M. Martinez, J. Chem. Soc. Dalt. Trans. 2002, 1435–1441.

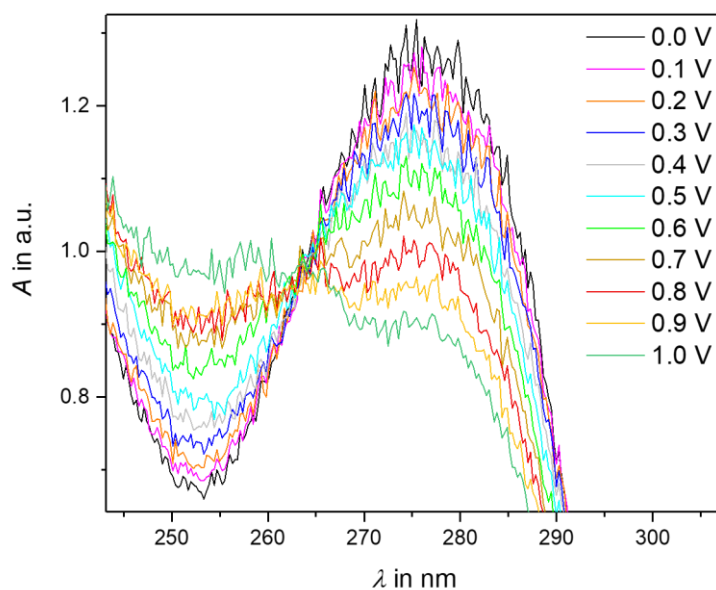


Figure S6: UV-Vis spectra of 3 with applied potentials from 0.0 V to 1.0 V in the range of 243 - 307 nm.

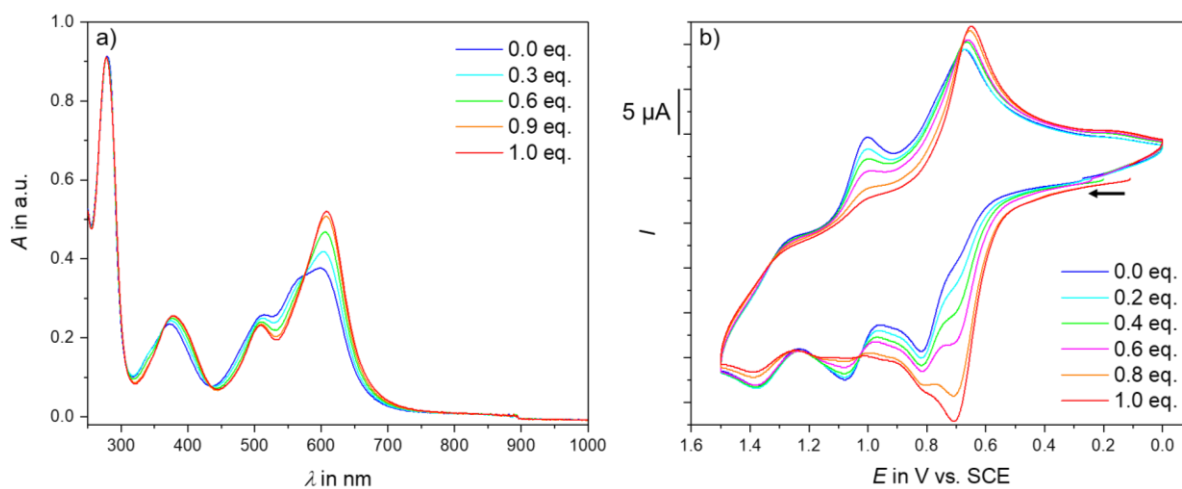


Figure S7: a) UV-Vis spectral changes for 3 through the addition of tetraethylammonium cyanide. b) Changes of the cyclic voltammograms of 3 through the addition of tetraethylammonium cyanide.

According to this cyclic voltammogram, the redox wave at 0.745 V can be assigned to the Fe(II) at the C-bonded cyanide side and the redox wave at 1.04 V to the Fe(II) at the N-bonded cyanide side.

Derivatives of [FeCo]-Complexes

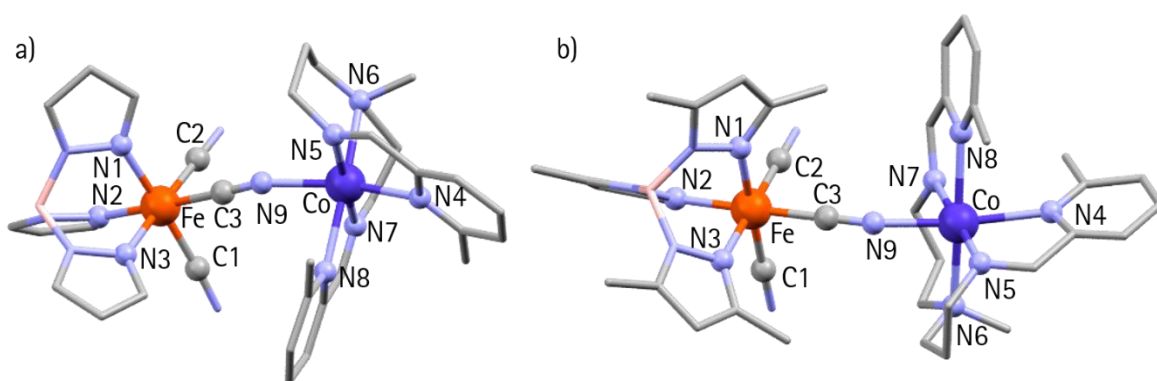


Figure 57: Molecular structure of a): D1 and b): D2. Hydrogen atoms, solvent and anions have been omitted for clarity. Color code: C, gray; N, light blue; Co, dark blue; Fe, orange; B, pink.

Table 28: Coordination bond lengths of D1 and D2.

Bond length in Å	D1	D2
Fe-N1	1.975(3)	1.964(5)
Fe-N2	1.971(4)	1.967(5)
Fe-N3	1.972(3)	1.981(6)
Fe-C1	1.931(4)	1.904(8)
Fe-C2	1.933(3)	1.893(8)
Fe-C3	1.910(4)	1.892(7)
Co-N4	2.201(3)	2.263(6)
Co-N5	2.097(3)	2.001(9)
Co-N6	2.260(3)	2.181(7)
Co-N7	2.115(3)	2.111(8)
Co-N8	2.279(3)	2.254(7)
Co-N9	2.087(4)	2.097(5)

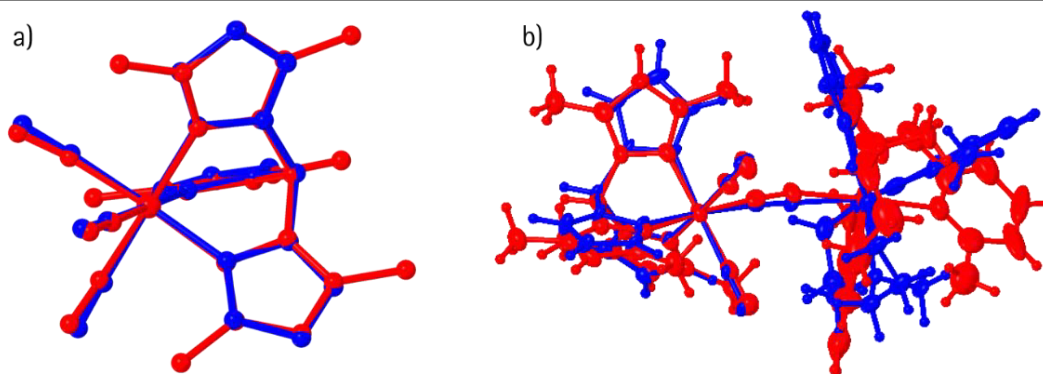


Figure 58: Comparison of the molecular structure of D1 (blue) and D2 (red). For a) the hydrogen atoms and Co(II) part of the complex have been omitted for clarity. b) shows a comparison of the whole molecules.

8.2 Derivatives of Spin Crossover Complexes as Building Blocks

Structural, Magnetic and Electrochemical Characterization of Iron(III) and Cobalt(III) Complexes with Schiff Base Ligands

Supporting Information

Dominik Natke,* Annika Preiss, Stephen Klimke, Takuya Shiga, Roman Boca, Masaaki Ohba, Hiroki Oshio, Franz Renz*

Contents:

Figure S1: Crystal structure showing π - π interactions

Table S1: Centroid-centroid distances of Fe(III) complexes

Table S2: Angles between ligands of Co(II) in [Co₂Co]

Figure S2: Coordination sphere of Co(II) in [Co₂Co]

Figure S3: Structure of [Co₂Co] to visualize the Co-H₂O-H₂O-H₂O-Co bridge

Figure S4: Structure of [Co₂Co] with BF₄⁻ anions

Table S3: Coordination bond length

Fitting of the Magnetic Data

Figure S3: $\mu_{\text{eff}}/\mu_B - T$ and $\chi_m - T$ plot and fit of [Co₂Co]

Table S4: Results of the magnetic data fitting.

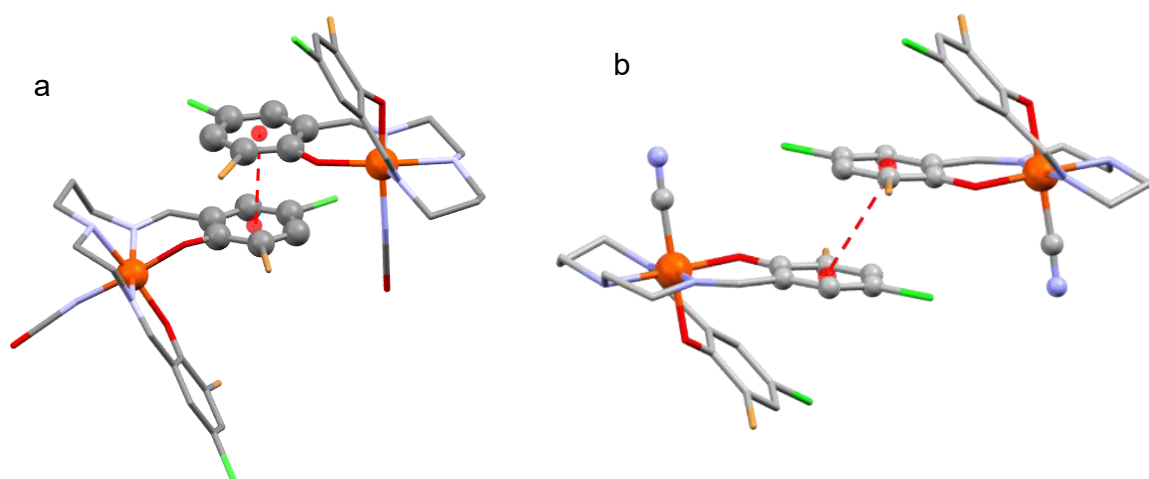


Figure S1: Crystal structure showing π - π interactions of a: [Fe(salpet_{Br,C})NCSe] and b: [Fe(salpet_{Br,C})CN]. Hydrogen atoms have been omitted for clarity. Color code: C, gray; N, light blue; O, red; Fe, orange; Cl, green; Br brown; transparent red, centroid.

Table S1: Centroid-centroid distances of Fe(III) complexes.

Compound	Distance in Å
[Fe(salpet _{Br,C})Cl]	4.432
[Fe(salpet _{Br,C})N ₃]	4.201
[Fe(salpet _{Br,C})NCO]	3.584
[Fe(salpet _{Br,C})NCS]	4.171
[Fe(salpet _{Br,C})NCSe]	4.062
[Fe(salpet _{Br,C})CN]	3.676

Table S2: Angles between ligands of Co(II) in $[\text{Co}_2\text{Co}]$.

	Angle in °
N4-N2	91.3(2)
N5-N2	90.8(2)
N1-N2	97.0(2)
N2-N3	102.7(2)
N4-N1	89.4(2)
N5-N1	89.9(2)
N4-N3	92.5(2)
N5-N3	87.4(2)

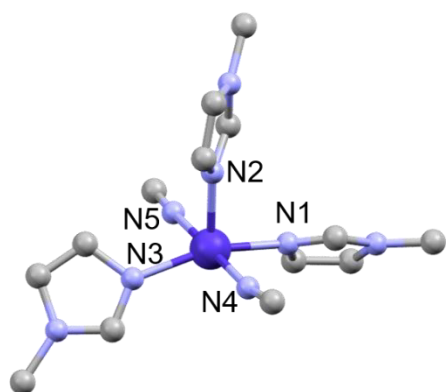


Figure S2: Coordination sphere of Co(II) in $[\text{Co}_2\text{Co}]$. Hydrogen atoms, counter anions and $[\text{Co}(\text{salpet}_{\text{H,H}})]^+$ building blocks have been omitted for clarity. Color code: C, gray; N, light blue; Co, dark blue.

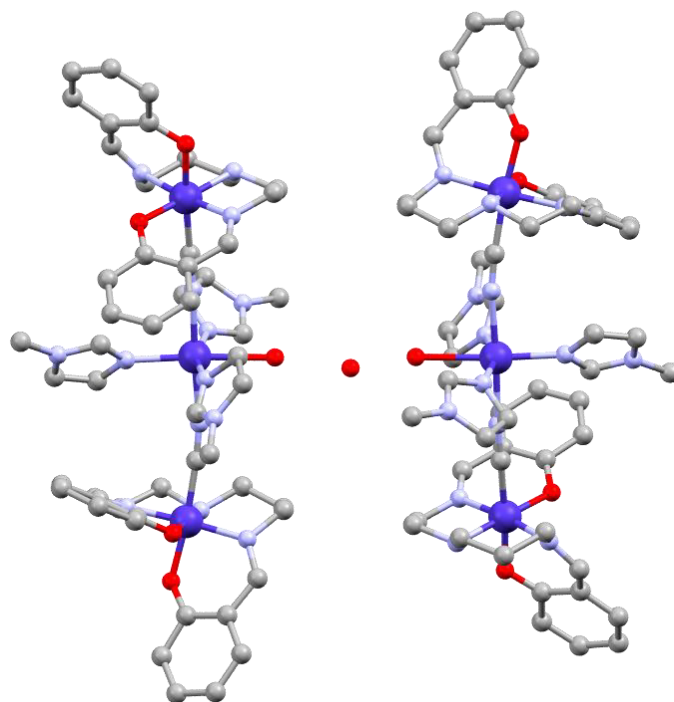


Figure S3: Structure of $[\text{Co}_2\text{Co}]$. To visualize the $\text{Co-H}_2\text{O-H}_2\text{O-H}_2\text{O-Co}$ bridge, possible positions for the disordered water molecules are suggested. Hydrogen atoms and counter anions have been omitted for clarity. Color code: C, gray; N, light blue; O, red; Co, dark blue.

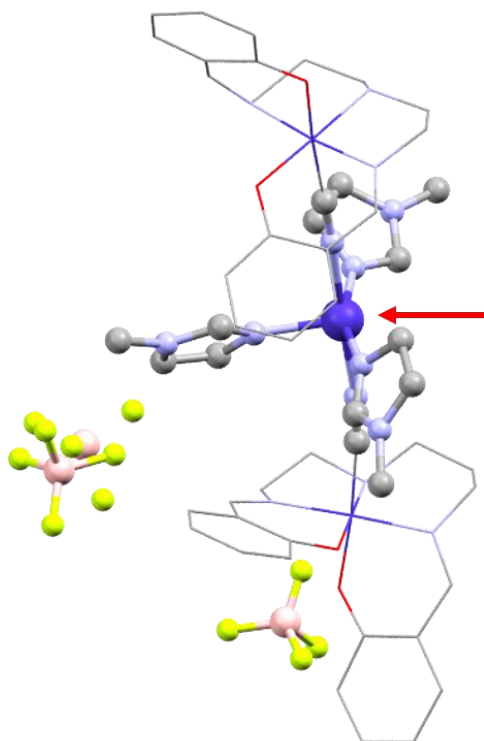


Figure S4: Structure of $[\text{Co}_2\text{Co}]$ with BF_4^- anions. The red arrow indicates the water coordination site. Hydrogen atoms have been omitted for clarity. Color code: C, gray; N, light blue; O, red; Co, dark blue.

Table S3: Coordination bond length.

Bond length of	[Fe(salpet _{Br,C})Cl]	[Fe(salpet _{Br,C})N ₃]
Fe-O in Å	1.983(2)/1.917(2)	1.979(1)/1.938(1)
Fe-N in Å	2.096(3)/2.188(3)/2.108(3)	2.120(2)/2.100(1)/2.216(2)
Fe-X in Å	2.356(1)	2.032(2)
	[Fe(salpet _{Br,C})NCO]	[Fe(salpet _{Br,C})NCS]
Fe-O in Å	1.937(2)/1.963(2)	1.919(2)/1.956(2)
Fe-N in Å	2.111(3)/2.111(3)/2.201(3)	2.103(3)/2.193(2)/2.111(3)
Fe-X in Å	2.016(3)	2.079(3)
	[Fe(salpet _{Br,C})NCSe]	[Fe(salpet _{Br,C})CN]
Fe-O in Å	1.917(2)/1.948(2)	1.907(3)/1.887(3)
Fe-N in Å	2.097(3)/2.187(2)/2.102(3)	1.999(4)/1.926(4)/1.907(3)
Fe-X in Å	2.110(3)	1.958(5)
	[Co(salpet _{H,H})CN]	
Co-O in Å	1.889(2)/1.924(1)	
Co-N in Å	1.885(2)/1.968(2)/1.920(2)	
Co-X in Å	1.892(2)	
	[Co ₂ Co]	
Co ^{III} -O in Å	1.906(3)/1.902(3)/1.911(3)/1.907(3)	
Co ^{III} -N in Å	1.923(4)/1.976(4)/1.890(4)/1.896(4)/1.920(4)/1.981(4)	
Co ^{III} -C (cyanide) in Å	1.899(4)/1.901(5)	
Co ^{II} -N (1-methylimidazole) in Å	2.068(6)/2.067(5)/2.065(5)	
Co ^{II} -N (cyanide) in Å	2.118(4)/2.134(4)	

Fitting of the Magnetic Data

The standard spin Hamiltonian with the axial ZFS parameter D and anisotropic g -factor has been used in the data fitting; the final magnetic parameters were $g_z = 2.0$, $g_{xy} = 2.60(1)$, and $D/hc = 70.4(26)$ cm⁻¹. The additional correction to the temperature-independent magnetism $\chi_{\text{TIM}} = 2.5 \times 10^{-9}$ m³ mol⁻¹ (SI units) and the molecular-field correction $j/hc = -0.019$ cm⁻¹ improve the data fitting yielding the discrepancy factor $R = 0.017$. There is no indication for a visible magnetic interaction between molecules.

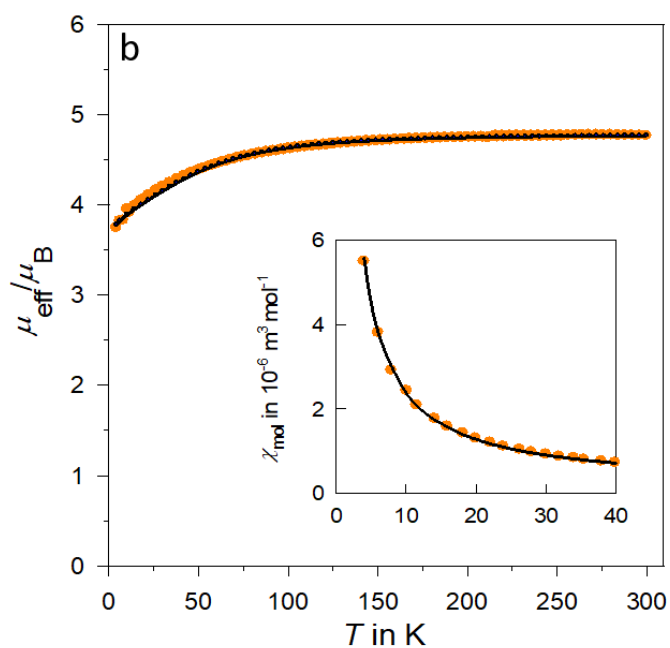


Figure S5: $\mu_{\text{eff}}/\mu_B - T$ and $\chi_m - T$ plot and fit of [Co₂Co].

Table S4: Results of the magnetic data fitting. R-factor(DataSet1 X : fitX.i)= 0.1688496E-01, error=0.00568.

Parameters	Var	Scale	Final	Initial	Min	Max	Alert
1 gz	0	0	2.00000	2.00000	2.00000	2.50000	*
2 gx	1	0	2.59971	2.59971	2.10000	3.00000	
3 D [cm ⁻¹]	1	0	70.36884	70.37787	2.00000	150.00000	
4 vV	1	-9	2.49989	2.49989	0.00000	10.00000	
5 zj	1	0	-0.01947	-0.01946	-0.50000	0.00000	
6 xPI	0	0	0.00000	0.00000	0.00000	0.00000	*
7 gPI	0	0	0.00000	0.00000	0.00000	0.00000	*
8 tPI	0	0	0.00000	0.00000	0.00000	0.00000	*
9 SPI	0	0	0.00000	0.00000	0.00000	0.00000	*
10 mPI	0	0	0.00000	0.00000	0.00000	0.00000	*
	Scale Parameter		(+-) SD				
2 gx	0	2.59971	0.01179				
3 D [cm ⁻¹]	0	70.36884	2.68130				
4 vV	-9	2.49989	1.07602				
5 zj	0	-0.01947	0.00762				

Angled Trinuclear Cobalt Complex

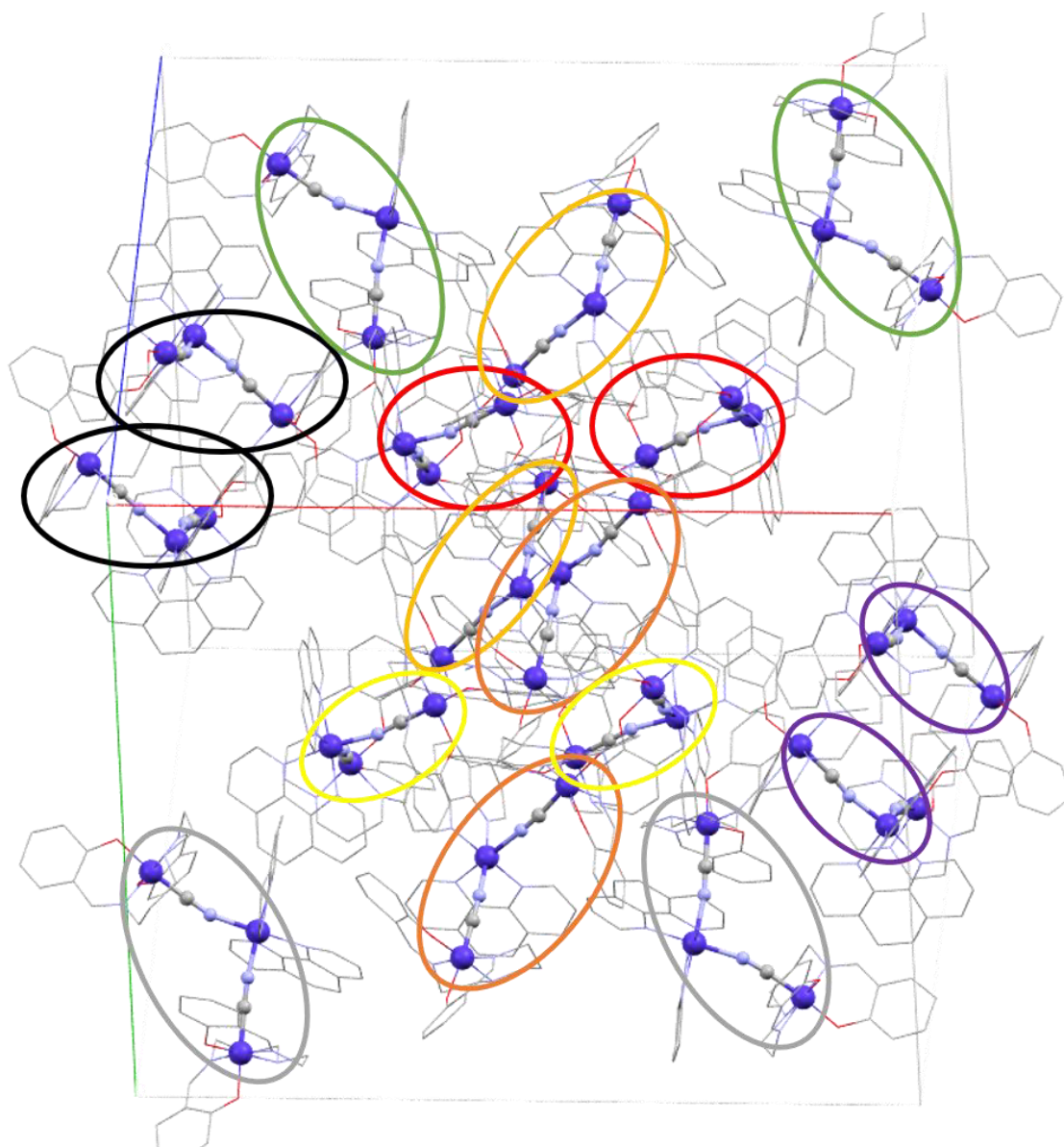


Figure 59: Unit cell of T1. Colored ovals mark corresponding molecules with opposite orientation. Hydrogen atoms have been omitted for clarity. Color code: C, gray; N, light blue; O, red; Co, dark blue; a-axis, red line; b-axis, green line; c-axis, blue line.

Switchable Pentanuclear Complexes

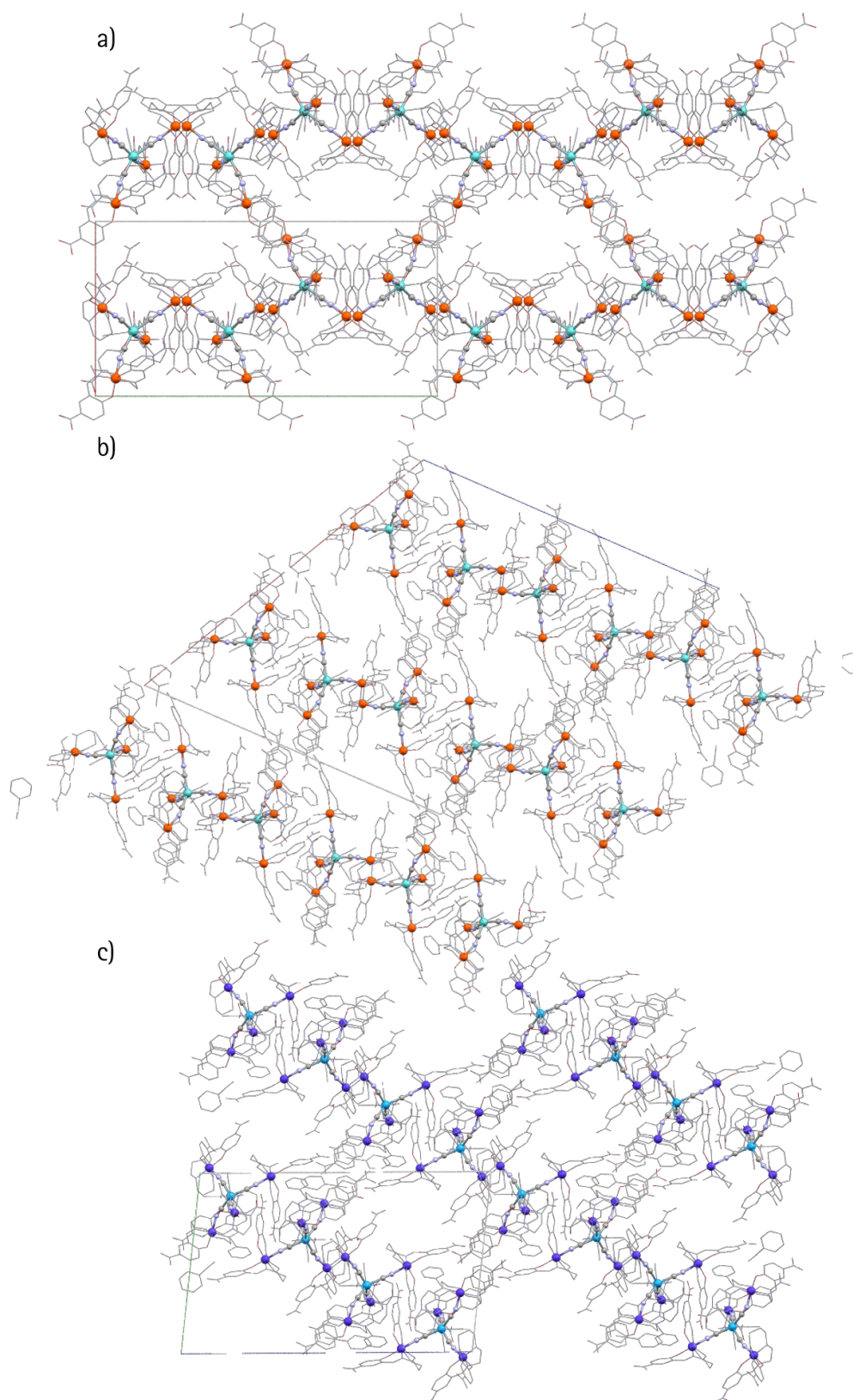


Figure 60: Packing of a) P1(acetone), b) P1 and c) P2. Mixed-valence bonds are highlighted. Hydrogen atoms have been omitted for clarity. Color code: C, gray; N, light blue; O, red; Fe, orange; Mo, light turquoise; Co, dark blue; W, dark turquoise.; a-axis, red line; b-axis, green line; c-axis, blue line.

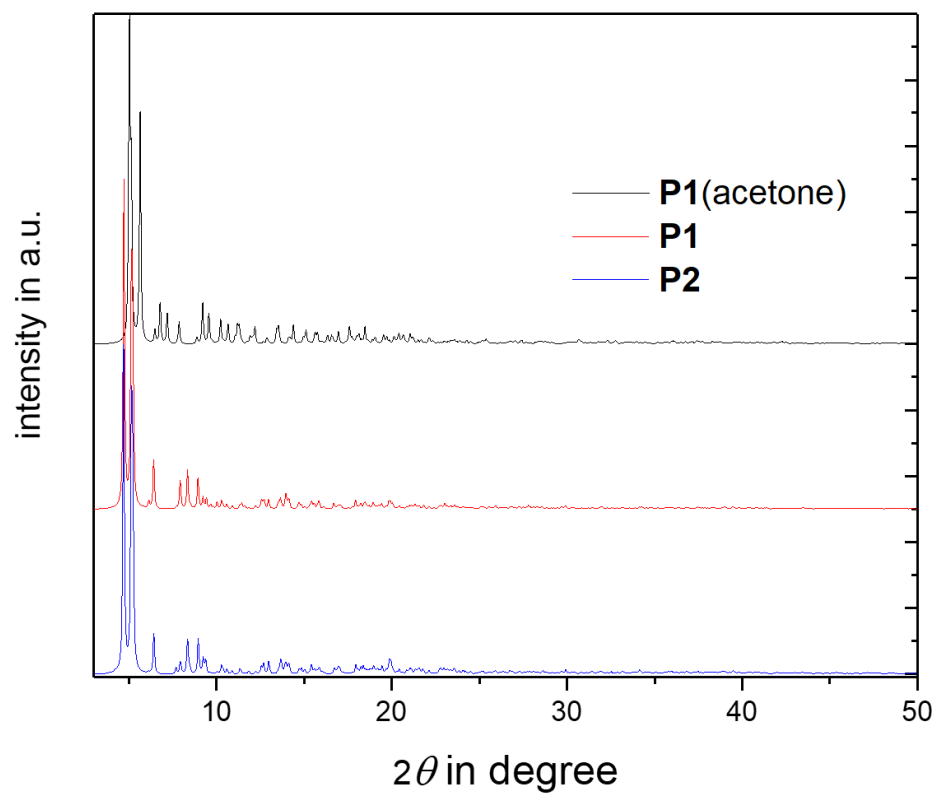


Figure 61: Powder XRD calculated from the single crystal structures of P1(acetone), P1 and P2.

Table 29: Examples of the shortest angle between the binding atom (A) of the monodentate ligand (X) and the outer carbon atom (C) of the phenyl ring inside [M(salpet)X] mono- and multinuclear complexes (Figure 23). The spin states are determined at the temperature the structure was measured.

compound	shortest angle C1-M-C2 in °	spin state
[Fe(salpet _{Br,C})NCS]	81.22(9)	Fe(III) HS
[Fe(salpet _{Br,C})N ₃]	103.36(5)	Fe(III) HS
[Fe(salpet _{Br,C})CN]	100.5(1)	Fe(III) LS
[Co ₂ Co]	73.4(2), 76.5(2)	Co(III) LS
[Fe(salpet _{H,H})CN] ^[26]	83.53(6)	Fe(III) LS
{[Fe(salpet _{H,H})] ₂ CN}ClO ₄ ^[26]	74.2(1), 76.9(1)	Fe(III) HS, Fe(III) LS (SCO)
{Ni(CN) ₄ [Fe(salpet _{tert-butyl,Me})] ₂ } ^[26]	77.79 (4)	Fe(III) HS
{Fe ^{II} (CN) ₅ (NO)[Fe(salpet _{H,H})] ₂ } ^[26]	67.24(8), 68.52(8)	Fe(III) HS (SCO)
{Co ^{III} (CN) ₆ [Fe(naphet)] ₃ } ^[71]	89.9(2), 101.7(2), 101.7(2)	Fe(III) LS (SCO)
{Fe ^{II} (CN) ₆ [Fe(salpet _{H,H})] ₆ }Cl ₂ ^[69]	92.3(3) – 108.2(2)	Fe(III) HS (SCO)
{Fe ^{II} (CN) ₆ [Fe(salpet _{OMe,H})] ₆ }Cl ₂ ^[70]	106.9(1) – 106.94(8)	Fe(III) HS
{[Co(salpet _{OEt,H})CN][Fe(salen)]Cl} ^[134]	78.20(8)	Co(III) LS
{[Co(salpet _{OEt,H})CN][Mn(salen)]Cl} ^[79]	77.1(1)	Co(III) LS
{[Co(salpet _{OEt,H})CN] ₂ [Mn(salen)]} ^[79]	71.8(1), 77.5(1)	Co(III) LS

naphet: 1-((Z)-((3-((2-((E)-((2-hydroxynaphthalen-1-yl)methylene)amino)ethyl)-amino)propyl)imino)methyl)naphthalen-2-ol; salen: *N,N'*-bis(salicylidene)ethane-1,2-diamine

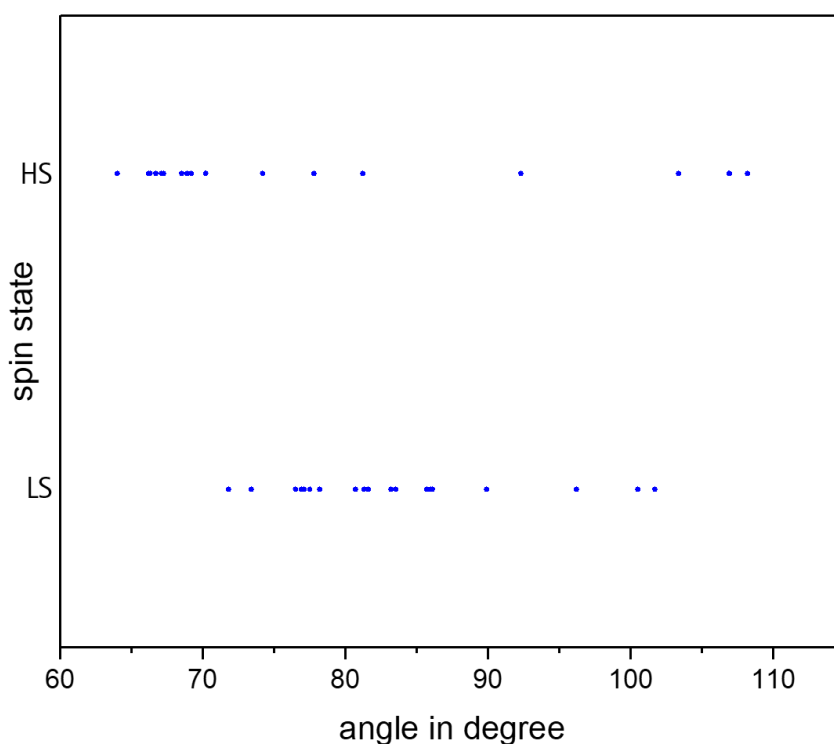


Figure 62: A-M-C angle (Figure 23) in dependency to the spin stated of P1(acetone), P1, P2, and further examples (Table 29).

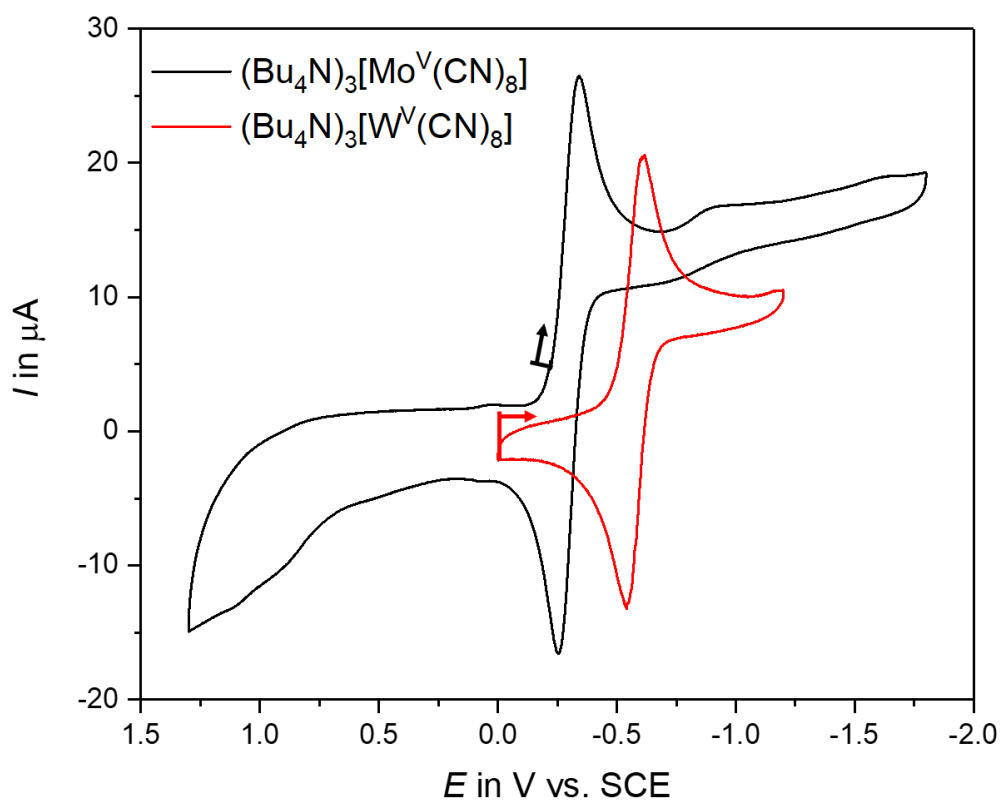


Figure 63: CV of $(\text{Bu}_4\text{N})_3[\text{Mo}^{\text{V}}(\text{CN})_8]$ and $(\text{Bu}_4\text{N})_3[\text{W}^{\text{V}}(\text{CN})_8]$ in acetonitrile vs. SCE. The electrolyte was Bu_4NPF_6 , the counter electrode was a platinum wire, with a glassy Carbon working electrode and a scan rate of 0.1 V/s.

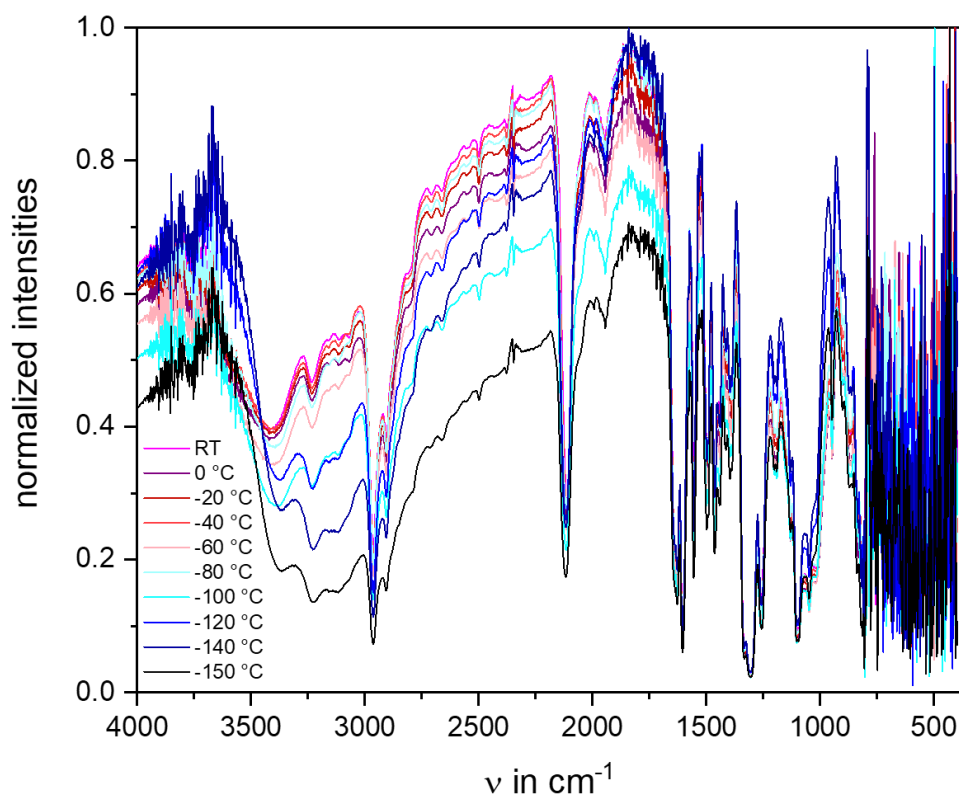


Figure 64: Temperature-dependent IR spectra of P2.

8.3 Co-Crystallization of Tetranuclear [Fe₂Co₂]-Complexes

Solid state hydrogen bond alterations in a [Co₂Fe₂] complex with bifunctional hydrogen bonding donors

Supporting Information

Masayuki Nihei,^{*[a]} Yuta Yanai,^[a] Dominik Natke,^[b] Ryo Takayama,^[a] Marina Kato,^[a] Yoshihiro Sekine,^[a] Franz Renz,^[b] and Hiroki Oshio^{*[a]}

[a] Graduate School of Pure and Applied Sciences, University of Tsukuba, Tennodai 1-1-1, Tsukuba, Ibaraki 305-8571, Japan

[b] Institut für Anorganische Chemie, Leibniz University Hannover, Callinstr. 9 D-30167 Hannover, Germany

chem_201901383_sm_miscellaneous_information.pdf

Syntheses

All reagents were obtained from commercial suppliers and were used without further purification. $(\text{Bu}_4\text{N})[\text{Fe}(\text{CN})_3\text{tp}^*]$ and $\text{Co}(\text{OTf})_2 \cdot 6\text{H}_2\text{O}$ were synthesized according to the literature methods.^[S11, S12]

$[\text{Co}_2\text{Fe}_2(\text{CN})_6(\text{tp}^*)_2(\text{bpy}^*)_4](\text{PF}_6)_2 \cdot 2\text{ABA} \cdot 4\text{BN} \cdot 2\text{PE}$ (**SQ1**_{solv}).

The reaction of $\text{Co}(\text{OTf})_2 \cdot 6\text{H}_2\text{O}$ (11.9 mg, 0.026 mmol) with bpy^* (9.7 mg, 0.053 mmol) in benzonitrile (BN) (10 ml) gave a pale yellow solution. After stirring for 5 minutes, $(\text{Bu}_4\text{N})[\text{Fe}(\text{CN})_3(\text{tp}^*)]$ (16.5 mg, 0.025 mmol) was added followed by the addition of 4-aminobenzoic acid (ABA) (0.302 g, 2.2 mmol) and Bu_4NPF_6 (19.9 mg, 0.051 mmol). The mixture was stirred for 10 minutes and the resulting red solution was filtered. Diisopropyl ether (PE) was added to the filtrate and red plate crystals of **SQ1**_{solv} were obtained after standing the solution at 5 °C. Yield: 24.1 mg (33%). Anal Calcd. for $\text{C}_{105}\text{H}_{111}\text{N}_{29}\text{B}_2\text{Co}_2\text{F}_{12}\text{Fe}_2\text{O}_4\text{P}_2$ ($[\text{Co}_2\text{Fe}_2(\text{CN})_6(\text{tp}^*)_2(\text{bpy}^*)_4](\text{PF}_6)_2 \cdot 2\text{ABA} \cdot 1\text{BN}$); C, 52.89; H, 4.69; N, 17.04%. Found: C, 53.08; H, 4.77; N, 16.88%.

Crystal structural analyses

Single crystals of **SQ1**_{desolv}, suitable for crystal structural analysis were obtained by standing the crystal of **SQ1**_{solv} for 1 night at room temperature. Single crystal was mounted with epoxy resin on the tip on a glass fiber. Measurements were performed at 100 and 250 K for **SQ1**_{solv} and 100 and 270 K for **SQ1**_{desolv}, respectively. Diffraction data were collected using a Bruker SMART APEX II diffractometer equipped with a CCD type area detector. A full sphere of data was collected with graphite-monochromated Mo-K α radiation ($\lambda = 0.71073$ Å). The data frames were integrated using the SAINT program and merged to give a unique data set for structure determination. An absorption correction was performed using SADABS.^[S13] The structure was solved by direct methods and refined on F^2 by the full-matrix least-squares methods using SHELXTL package (Bruker Analytical X-ray systems). Non hydrogen atoms were refined with anisotropic thermal parameters. Hydrogen atoms were included in calculated positions and refined with isotropic thermal parameters riding on those of the parent atoms. CCDC 1864631-1864634 contain the supplementary crystallographic data for this paper. These data can be obtained free of charge via www.ccdc.cam.ac.uk/conserv/trieving.html (or from the Cambridge Crystallographic Data Centre, 12, Union Road, Cambridge CB21EZ, UK; fax: (+44)1223-336-033; or deposit@ccdc.cam.ac.uk). Crystallographic parameters are summarized in Table S1.

Physical measurements

Magnetic susceptibility data were collected using a Quantum Design MPMS-5S SQUID magnetometer. Temperature dependence was measured at 5.0 K increments in the settle mode with an applied magnetic field of 20 kOe in the temperature range of 5 - 400 K. The temperature scan rate was fixed

to 3.0 K/min, and each measurement was performed 30 seconds after the temperature had stabilized. Magnetic data were corrected for the diamagnetism of the sample holder, and for the diamagnetism of the sample using Pascal's constants. For the photomagnetic experiments, light from a DPSS laser (808 nm; 20mW, Intelite I808-120G-CAP) was guided via a flexible optical fiber (Newport F-MBD; 3 m length, 1.0 mm core size, 1.4 mm diameter) into the SQUID magnetometer. Irradiation was performed on the ground sample inside the SQUID sample chamber at 5 K. One end of the optical fiber was located 40 mm above the sample and the other was attached to the laser coupler (Body; Newport M-F-916T and lens; M-10X). Temperature dependence of magnetic susceptibilities after light irradiation was measured using an applied magnetic field of 20kOe and a scan rate at 0.3 K/min in the scanning mode. Powder X-ray diffraction (PXRD) measurements were performed on the microcrystalline samples using Bruker D8 ADVANCE diffractometer. Infrared absorption spectra were measured on KBr pellet samples using a SHIMADZU IR Affinity-1 spectrometer. The temperature dependence of infrared absorption spectra was measured on KBr pellet samples using a SHIMADZU IR Affinity-1 spectrometer equipped with UNISOKU USP-203-A cryostat. Thermogravimetric (TG) analysis was performed using Hitachi High-Technologies TG/DTA7300 thermogravimetric analyser.

References

- [S11] D. Li, S. Parkin, G. Wang, G. T. Yee, S. M. Holmes, *Inorg. Chem.* **2006**, *45*, 1951.
- [S12] S. H. John, R. S. John, C. T. Robwer, *Can. J. Chem.* **1981**, *59*, 669.
- [S13] G. M. Sheldrick, *SADABS: An Empirical Absorption Correction Program*, Bruker Analytica X-ray Systems, Madison, WI, 1996.

8. Appendix

Table S1. Crystallographic Parameters of SQ1_{solv} and SQ1_{desolv}

	SQ1 _{solv}		SQ1 _{desolv}	
	100 K	250 K	100 K	270 K
Temperature	100 K	250 K	100 K	270 K
Formula	C ₁₃₈ H ₁₅₄ B ₂ Co ₂ Fe ₂ F ₁₂ N ₃₂ O ₆ P ₂		C ₉₈ H ₁₀₆ B ₂ Co ₂ Fe ₂ F ₁₂ N ₂₈ O ₄ P ₂	
Mr [g mol ⁻¹]	2898.04		2282.22	
Space group	Triclinic $P\bar{1}$		Triclinic $P\bar{1}$	
<i>a</i> [Å]	14.6738(17)	14.8765(14)	13.98(7)	13.85(8)
<i>b</i> [Å]	15.7057(19)	16.0305(16)	14.97(8)	14.82(9)
<i>c</i> [Å]	18.750(2)	19.0127(19)	15.90(8)	16.08(10)
α [°]	79.5990(17)	77.9349(16)	63.37(5)	117.10(5)
β [°]	67.9420(14)	77.9349(16)	69.20(5)	105.13(6)
γ [°]	62.3350(14)	67.6284(13)	83.72(6)	95.09(6)
<i>V</i> [Å ³]	3546.9(7)	3716.8(6)	2775(24)	2751(29)
<i>Z</i>	1	1	1	1
μ [mm ⁻¹]	0.534	0.510	0.670	0.678
Reflection Collected	15568	16415	8384	9793
Independent reflections	11023	9171	7792	8070
<i>R</i> 1 (<i>I</i> > 2 σ <i>I</i>)	0.0718	0.0745	0.1546	0.1390
<i>wR</i> 2 (<i>I</i> > 2 σ <i>I</i>)	0.1747	0.1872	0.3361	0.3346
GOF on <i>R</i> ²	1.019	1.017	1.439	1.025

Table S2. X-ray Structural Parameters of SQ1_{solv} and SQ1_{desolv}

	SQ1 _{solv}		SQ1 _{desolv}	
	100 K	200 K	100 K	270 K
Spin state	LS	HS	LS	HS
<i>av.</i> <i>d</i> _{Co-N} (Å)	1.929(3)	2.126(4)	1.96(2)	2.12(2)
<i>av.</i> <i>d</i> _{Fe-C.N} (Å)	1.965(4)	1.960(4)	1.99(2)	1.95(2)
<i>d</i> _{C-O(ABA)} (Å)	1.230(8)	1.248(6)	1.31(3)	1.24(4)
	1.328(8)	1.291(6)	1.37(4)	1.34(4)
<i>d</i> _{N(CN)···N(ABA)} (Å)	2.948(8)	3.083(6)		
<i>d</i> _{N(CN)···O(ABA)} (Å)			2.85(3)	2.85(3)

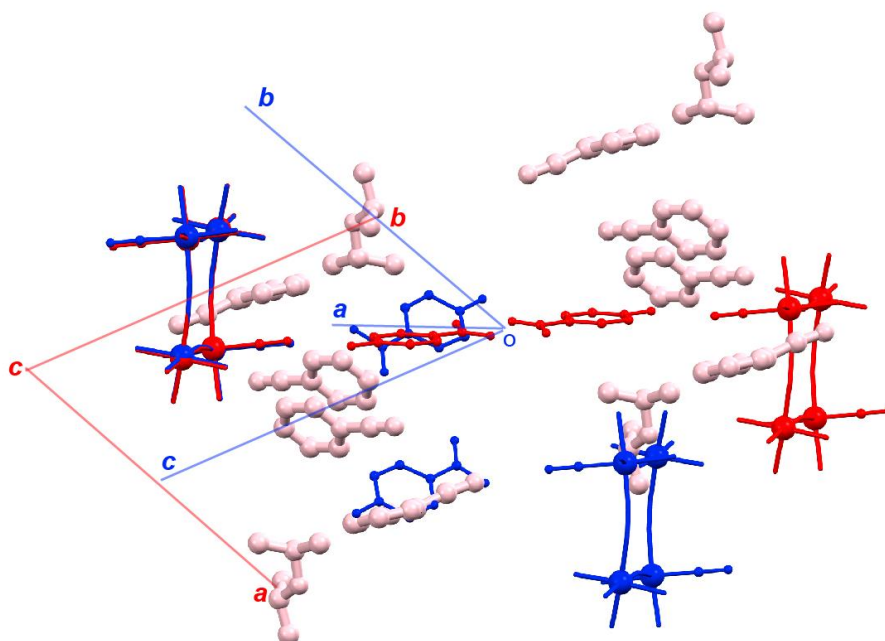


Figure S1. An overlay diagram of crystal packings of SQ1_{solv} (red) and $\text{SQ1}_{\text{desolv}}$ (blue). Capping ligands of $[\text{Co}_2\text{Fe}_2]^{2+}$ cations, hydrogen atoms, and counter anions were omitted for clarity.

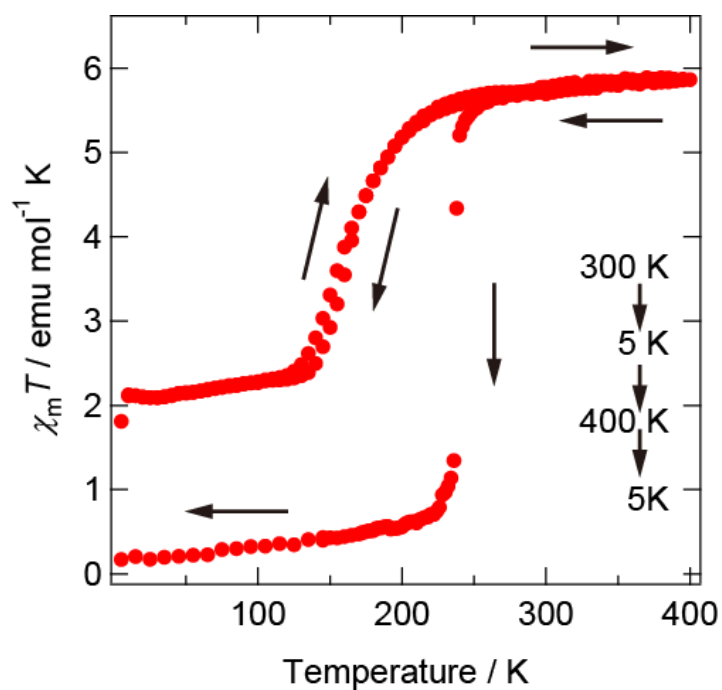
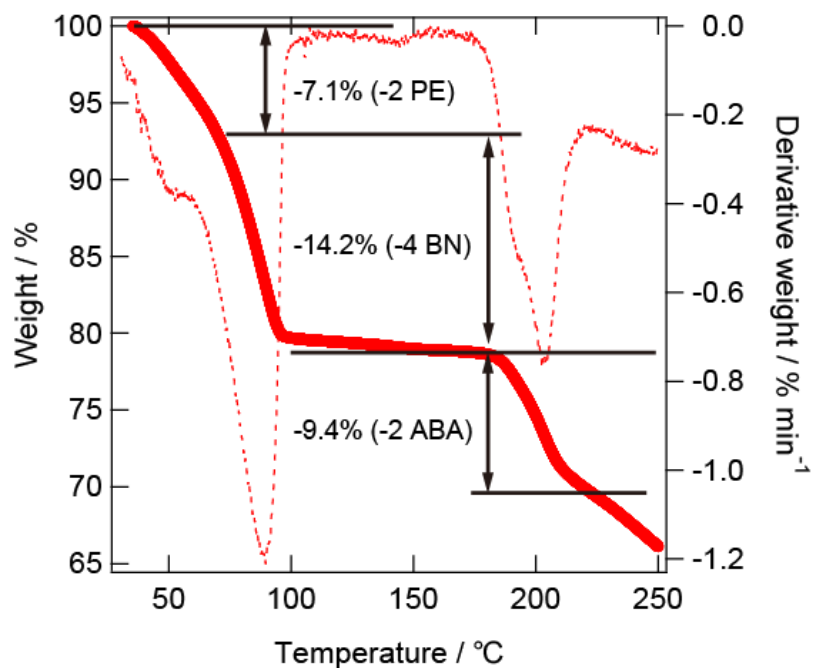
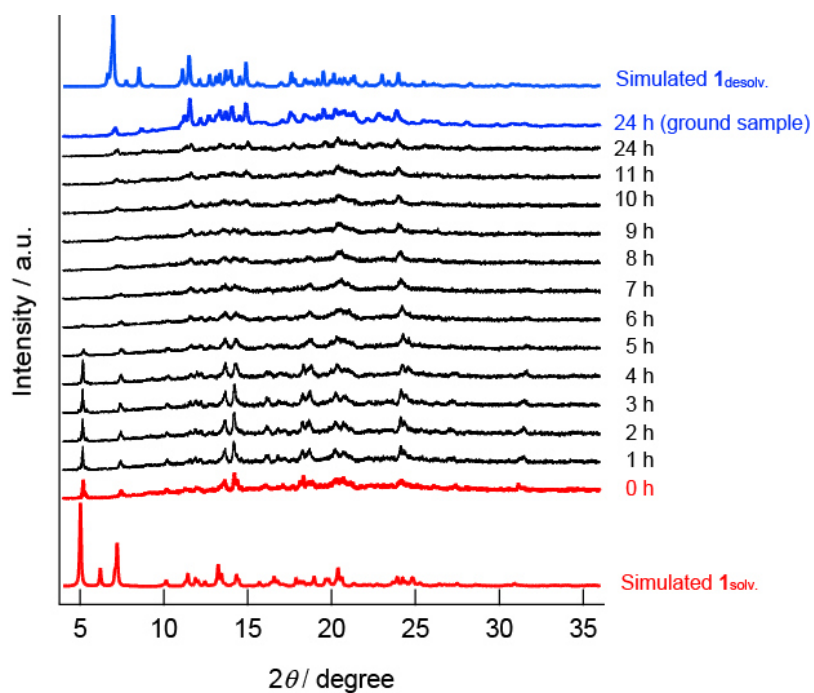


Figure S2. mT - T plot for partially desolvated SQ1_{solv} upon heating and cooling processes

Figure S3. Thermogravimetric curve of SQ1_{solv}.Figure S4. Time course change of PXRD patterns of SQ1_{solv} standing at room temperature.

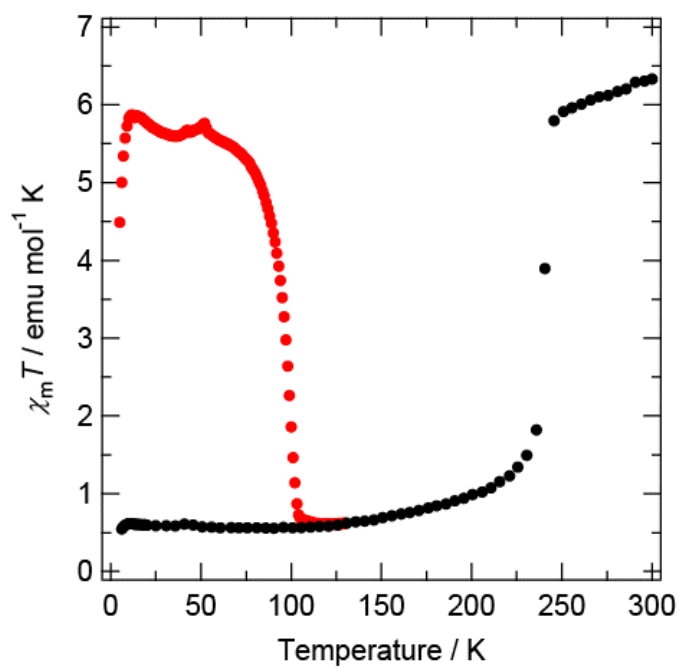


Figure S4. $\chi_m T$ - T plot for $\text{SQ1}_{\text{desolv}}$ before (black) and after (red) light irradiation.

8.4 Framework Structures of Fe, Co, and Ni with $[\text{Bi}(\text{SCN})_6]^{3-}$

Thiocyanate-Based Coordination Compounds with Co, Fe, and Ni

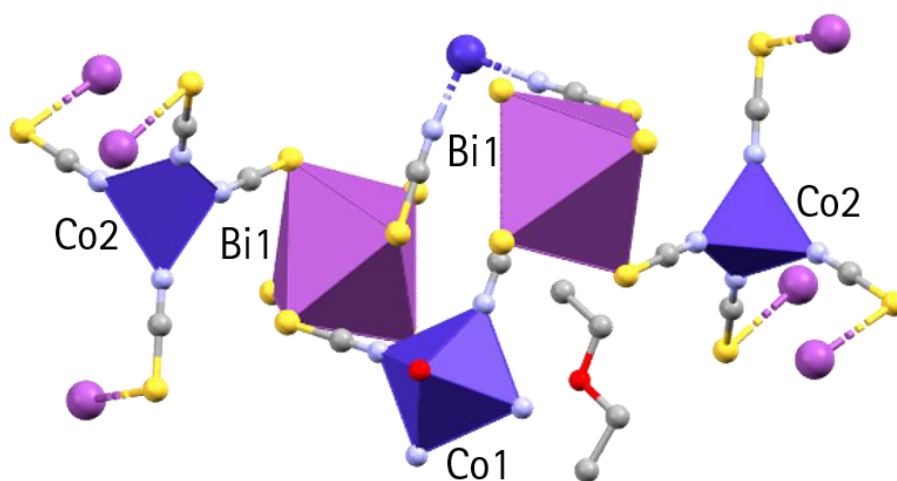


Figure 65: Highlighted coordination polyhedrons within the crystal structure of **B1**. Color code: C, gray; N, light blue; O, red; Co, dark blue; Bi, magenta; S, yellow. Hydrogen atoms have been omitted for clarity.

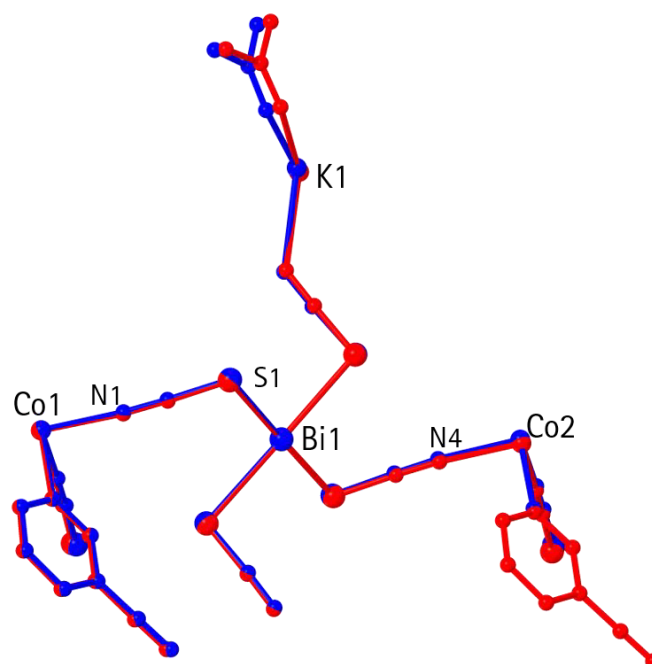


Figure 66: Comparison of the asymmetric unit of **B2** at 100K (blue) and 273 K (red). Hydrogen atoms have been omitted for clarity.

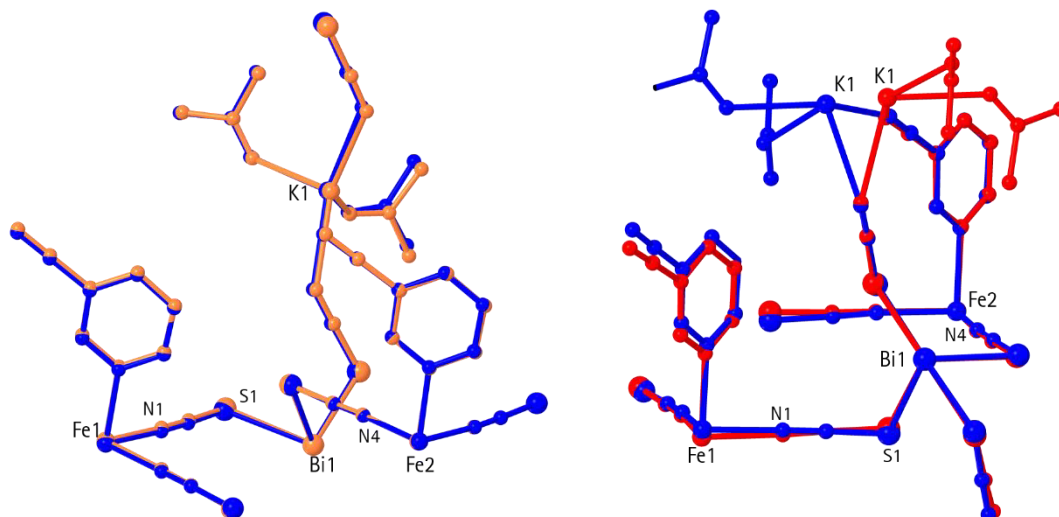


Figure 67: Comparison of the asymmetric unit of **B5** at 100K (blue), 223 K (pink) and 273 K (red). Hydrogen atoms have been omitted for clarity.

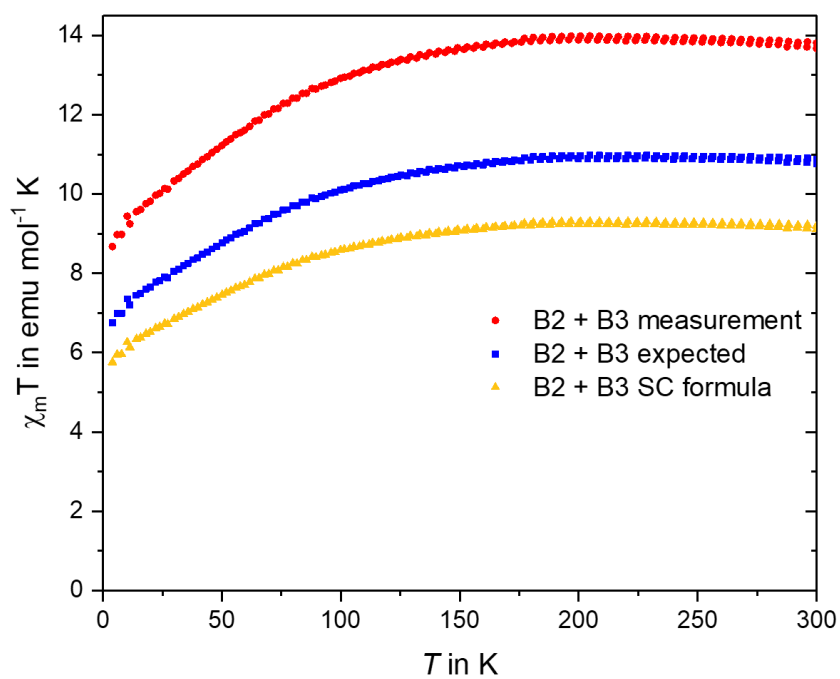


Figure 68: Temperature-depending magnetic measurements of **B2 + B3**. The red points represent the calculated $\chi_m T$ values according to the formula determined by the elemental analysis and TG measurements, the blue points represent the expected values based on the measurement data and the yellow points represent the calculated $\chi_m T$ values according to the formula determined by the crystal structure without impurities.

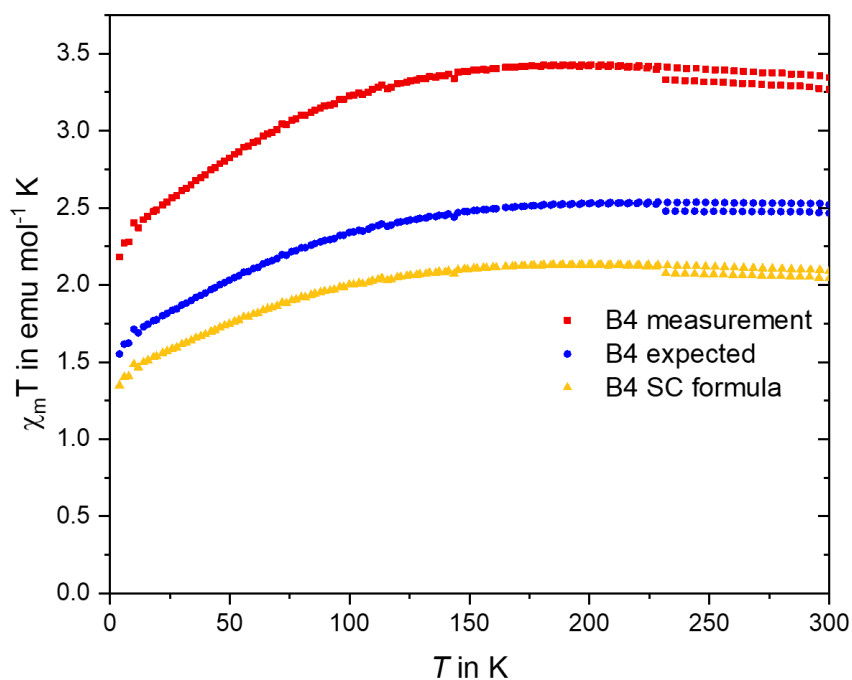


Figure 69: Temperature-depending magnetic measurements of **B4**. The red points represent the calculated $\chi_m T$ values according to the formula determined by the elemental analysis and TG measurements, the blue points represent the expected values based on the measurement data and the yellow points represent the calculated $\chi_m T$ values according to the formula determined by the crystal structure without impurities.

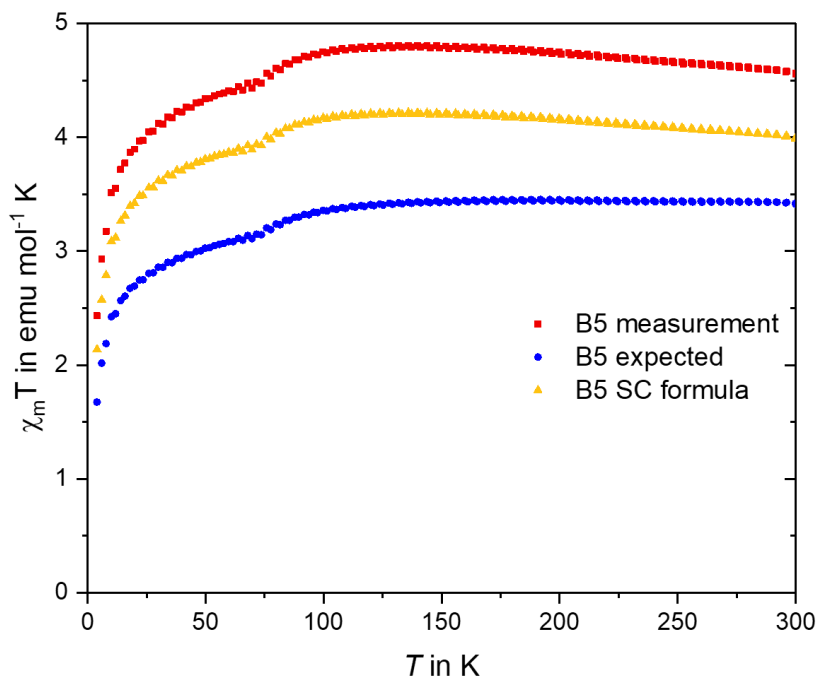


Figure 70: Temperature-depending magnetic measurements of **B5**. The red points represent the calculated $\chi_m T$ values according to the formula determined by the elemental analysis and TG measurements, the blue points represent the expected values based on the measurement data and the yellow points represent the calculated $\chi_m T$ values according to the formula determined by the crystal structure without impurities.

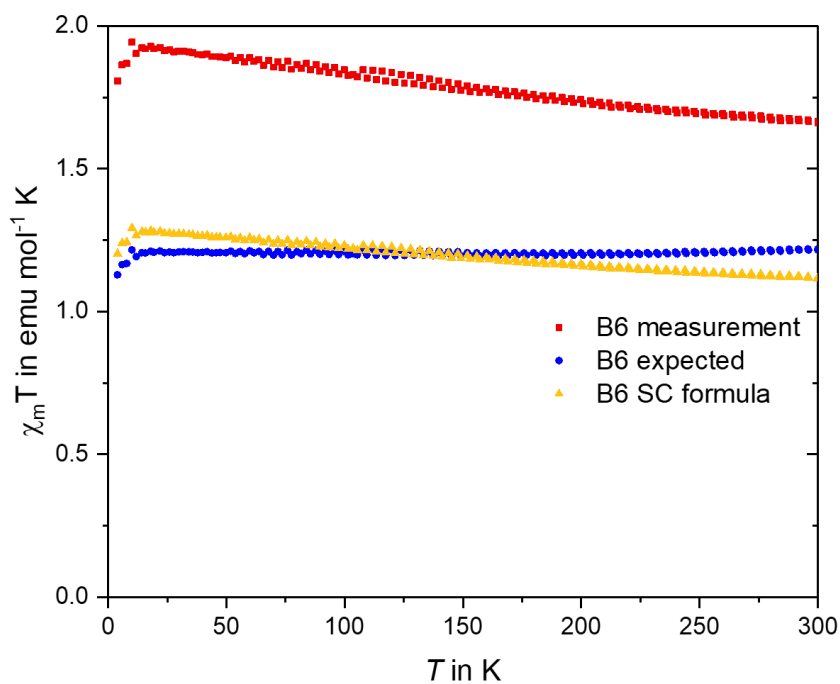


Figure 71: Temperature-depending magnetic measurements of **B6**. The red points represent the calculated $\chi_m T$ values according to the formula determined by the elemental analysis and TG measurements, the blue points represent the expected values based on the measurement data and the yellow points represent the calculated $\chi_m T$ values according to the formula determined by the crystal structure without impurities.

New Structures of Bi-NCS Coordination Polymers

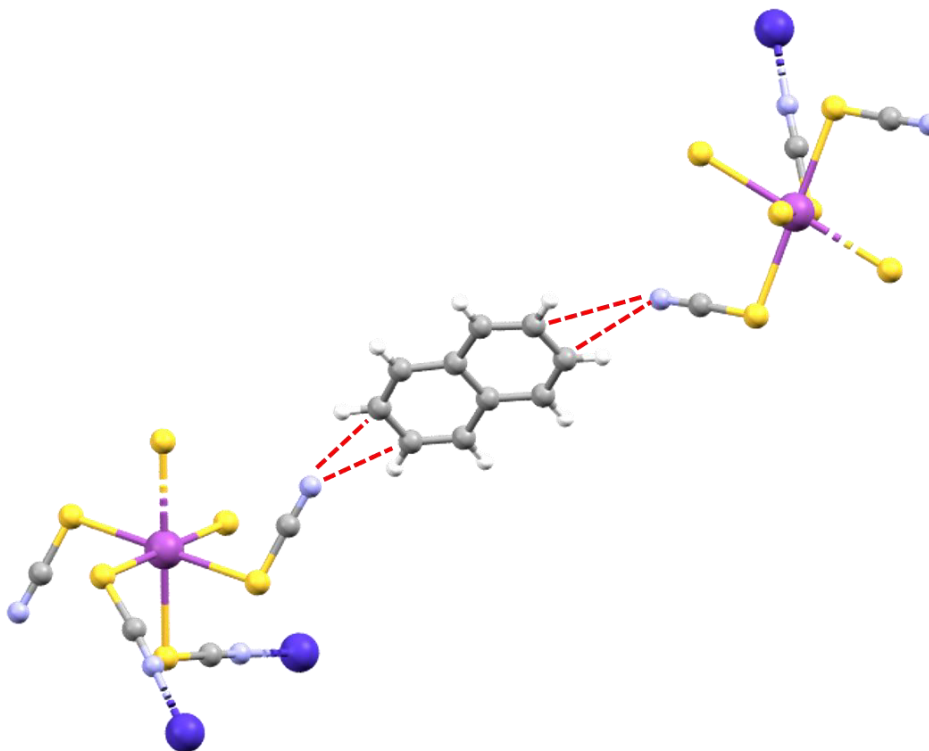


Figure 72: Interplane connection of **SB5**. Color code: C, gray; N, light blue; Co, dark blue; Bi, magenta; S, yellow. The red dotted lines visualize the interacting between parts of the planes and the protonated isoquinoline. The N atom of the (*H*-isoquinoline)⁺ ion is not displayed and shown as grey C atom.

9. References

- [1] IBM, "Deep Blue," can be found under <https://www.ibm.com/ibm/history/ibm100/us/en/icons/deepblue/>, 2021.
- [2] D. M. Fleetwood, *IEEE Trans. Nucl. Sci.* 2021, 68, 5, 509–545..
- [3] S. A. Chambers, *Mater. Today* 2002, 5, 34–39.
- [4] T. Jungwirth, J. Sinova, A. Manchon, X. Marti, J. Wunderlich, C. Felser, *Nat. Phys.* 2018, 14, 200–203.
- [5] A. S. Sidorenko, *Beilstein J. Nanotechnol.* 2020, 11, 1704–1706.
- [6] K. S. Kumar, M. Ruben, *Angew. Chemie Int. Ed.* 2021, 60, 7502–7521.
- [7] F. Renz, *J. Phys. Conf. Ser.* 2010, 217, 012022.
- [8] P. Gütlich, A. B. Gaspar, Y. Garcia, *Beilstein J. Org. Chem.* 2013, 9, 342–391.
- [9] M. Nihei, T. Shiga, Y. Maeda, H. Oshio, *Coord. Chem. Rev.* 2007, 251, 2606–2621.
- [10] A. Bousseksou, G. Molnár, L. Salmon, W. Nicolazzi, *Chem. Soc. Rev.* 2011, 40, 3313–3335.
- [11] G. Molnár, S. Rat, L. Salmon, W. Nicolazzi, A. Bousseksou, *Adv. Mater.* 2018, 30, 1703862.
- [12] M. D. Manrique-Juárez, F. Mathieu, A. Laborde, S. Rat, V. Shalabaeva, P. Demont, O. Thomas, L. Salmon, T. Leichle, L. Nicu, G. Molnar, A. Bousseksou, *Adv. Funct. Mater.* 2018, 28, 1–7.
- [13] A. B. Gaspar, V. Ksenofontov, M. Seredyuk, P. Gütlich, *Coord. Chem. Rev.* 2005, 249, 2661–2676.
- [14] O. Kahn, *Science*, 1998, 279, 44–48.
- [15] M. Nihei, *Chem. Lett.* 2020, 49, 1206–1215.
- [16] Y. S. Meng, O. Sato, T. Liu, *Angew. Chemie - Int. Ed.* 2018, 57, 12216–12226.
- [17] C. Q. Jiao, Y. S. Meng, Y. Yu, W. J. Jiang, W. Wen, H. Oshio, Y. Luo, C. Y. Duan, T. Liu, *Angew. Chemie - Int. Ed.* 2019, 58, 17009–17015.
- [18] M. Nihei, Y. Sekine, N. Suganami, K. Nakazawa, A. Nakao, H. Nakao, Y. Murakami, H. Oshio, *J. Am. Chem. Soc.* 2011, 133, 3592–3600.
- [19] M. Nihei, Y. Yanai, I.-J. Hsu, Y. Sekine, H. Oshio, *Angew. Chemie Int. Ed.* 2017, 56, 591–594.

- [20] T. Matsumoto, G. N. Newton, T. Shiga, S. Hayami, Y. Matsui, H. Okamoto, R. Kumai, Y. Murakami, H. Oshio, *Nat. Commun.* **2014**, *5*, DOI 10.1038/ncomms4865.
- [21] S. Ohkoshi, S. Takano, K. Imoto, M. Yoshikiyo, A. Namai, H. Tokoro, *Nat. Photonics* **2014**, *8*, 65–71.
- [22] N. Hoshino, F. Iijima, G. N. Newton, N. Yoshida, T. Shiga, H. Nojiri, A. Nakao, R. Kumai, Y. Murakami, H. Oshio, *Nat. Chem.* **2012**, *4*, 921–926.
- [23] T. Liu, D.-P. Dong, S. Kanegawa, S. Kang, O. Sato, Y. Shiota, K. Yoshizawa, S. Hayami, S. Wu, C. He, C. Y. Duan, *Angew. Chemie Int. Ed.* **2012**, *51*, 4367–4370.
- [24] I.-R. Jeon, S. Calancea, A. Panja, D. M. Piñero Cruz, E. S. Koumoussi, P. Dechambenoit, C. Coulon, A. Wattiaux, P. Rosa, C. Mathonière, R. Clerac, *Chem. Sci.* **2013**, *4*, 2463.
- [25] E. S. Koumoussi, I. R. Jeon, Q. Gao, P. Dechambenoit, D. N. Woodruff, P. Merzeau, L. Buisson, X. Jia, D. Li, F. Volatron, C. Mathoniere, R. Clerac, *J. Am. Chem. Soc.* **2014**, *136*, 15461–15464.
- [26] I. Šalitraš, R. Boča, L. Dlhán, M. Gembický, J. Kozíšek, J. Linares, J. Moncol', I. Nemeč, L. Perašínová, F. Renz, I. Svoboda, H. Fuess, *Eur. J. Inorg. Chem.* **2009**, 3141–3154.
- [27] C. Krüger, P. Augustin, I. Nemeč, Z. Travnicek, H. Oshio, R. Boca, F. Renz, *Eur. J. Inorg. Chem.* **2013**, 902–915.
- [28] C. Krüger, P. Augustin, L. Dlhán, J. Pavlík, J. Moncol', I. Nemeč, R. Boca, F. Renz, *Polyhedron* **2015**, *87*, 194–201.
- [29] I. Nemeč, R. Herchel, R. Boča, Z. Trávníček, I. Svoboda, H. Fuess, W. Linert, *Dalt. Trans.* **2011**, *40*, 10090.
- [30] R. Herchel, Z. Trávníček, *Dalt. Trans.* **2013**, *42*, 16279–16288.
- [31] P. Masárová, P. Zoufalý, J. Moncol, I. Nemeč, J. Pavlík, M. Gembický, Z. Trávníček, R. Boča, I. Šalitraš, *New J. Chem.* **2015**, *39*, 508–519.
- [32] P. Augustín, R. Boča, *Nov. Biotechnol. Chim.* **2015**, *14*, 96–103.
- [33] L. Pogány, J. Moncol, M. Gál, I. Šalitraš, R. Boča, *Inorganica Chim. Acta* **2017**, *462*, 23–29.
- [34] C. Rajnák, R. Mičová, J. Moncol', L. Dlhán, C. Krüger, F. Renz, R. Boča, *Dalt. Trans.* **2021**, *50*, 472–475.

- [35] M. Nihei, K. Shiroyanagi, M. Kato, R. Takayama, H. Murakami, Y. Kera, Y. Sekine, H. Oshio, *Inorg. Chem.* **2019**, *58*, 11912–11919.
- [36] M. J. Cliffe, E. N. Keyzer, M. T. Dunstan, S. Ahmad, M. F. L. De Volder, F. Deschler, A. J. Morris, C. P. Grey, *Chem. Sci.* **2019**, *10*, 793–801.
- [37] M. J. Cliffe, E. N. Keyzer, A. D. Bond, M. A. Astle, C. P. Grey, *Chem. Sci.* **2020**, *11*, 4430–4438.
- [38] K. Tran, Master Thesis: Integration von Schaltenden Berlinerblau Analoga in Polymeren Verbundmaterialien, Leibniz University Hannover, **2020**.
- [39] O. S. Wenger, *Chem. Soc. Rev.* **2012**, *41*, 3772.
- [40] H. M. D. Bandara, S. C. Burdette, *Chem. Soc. Rev.* **2012**, *41*, 1809–1825.
- [41] M. Natali, S. Giordani, *Chem. Soc. Rev.* **2012**, *41*, 4010.
- [42] O. Sato, J. Tao, Y. Z. Zhang, *Angew. Chemie – Int. Ed.* **2007**, *46*, 2152–2187.
- [43] R. Boča, I. Nemeč, I. Šalitroš, J. Pavlik, R. Herchel, F. Renz, *Pure Appl. Chem.* **2009**, *81*, 1357–1383.
- [44] T. Ishii, S. Tsuboi, G. Sakane, M. Yamashita, B. K. Breedlove, *Dalt. Trans.* **2009**, 680–687.
- [45] P. Gütlich, H. A. Goodwin, **2004**, pp. 1–47.
- [46] G. Vankó, F. Renz, G. Molnár, T. Neisius, S. Kárpáti, *Angew. Chemie – Int. Ed.* **2007**, *46*, 5306–5309.
- [47] D. Unruh, P. Homenya, M. Kumar, R. Sindelar, Y. Garcia, F. Renz, *Dalt. Trans.* **2016**, *45*, 14008–14018.
- [48] M. Ohba, K. Yoneda, G. Agusti, M. C. Muñoz, A. B. Gaspar, J. A. Real, M. Yamasaki, H. Ando, Y. Nakao, S. Sakaki, S. Kitagawa, *Angew. Chemie – Int. Ed.* **2009**, *48*, 4767–4771.
- [49] R. Ohtani, K. Shimayama, A. Mishima, M. Ohba, R. Ishikawa, S. Kawata, M. Nakamura, L. F. Lindoy, S. Hayami, *J. Mater. Chem. C* **2015**, *3*, 7865–7869.
- [50] M. Ohba, K. Yoneda, S. Kitagawa, *CrystEngComm* **2010**, *12*, 159–165.
- [51] M. Seredyuk, K. O. Znovnyak, J. Kusz, M. Nowak, M. C. Muñoz, J. A. Real, *Dalt. Trans.* **2014**, *43*, 16387–16394.

- [52] T. Shiga, R. Saiki, L. Akiyama, R. Kumai, D. Natke, F. Renz, J. M. Cameron, G. N. Newton, H. Oshio, *Angew. Chemie - Int. Ed.* **2019**, *58*, 5658–5662.
- [53] D. Müller, C. Knoll, M. Seifried, J. M. Welch, G. Giester, M. Reissner, P. Weinberger, *Chem. - A Eur. J.* **2018**, *24*, 5271–5280.
- [54] O. Roubeau, *Chem. - A Eur. J.* **2012**, *18*, 15230–15244.
- [55] M. . Carmen Muñoz, J. Antonio Real, in *Spin-Crossover Mater.*, John Wiley & Sons Ltd, Oxford, UK, **2013**, pp. 121–146.
- [56] M. Giménez-Marqués, M. L. García-Sanz de Larrea, E. Coronado, *J. Mater. Chem. C* **2015**, *3*, 7946–7953.
- [57] B. Dreyer, D. Natke, S. Klimke, S. Baskas, R. Sindelar, G. Klingelhöfer, F. Renz, *Hyperfine Interact.* **2018**, *239*, 2–9.
- [58] I. A. Gural'skiy, V. A. Reshetnikov, A. Szebesczyk, E. Gumienna-Kontecka, A. I. Marynin, S. I. Shylin, V. Ksenofontov, I. O. Fritsky, *J. Mater. Chem. C* **2015**, *3*, 4737–4741.
- [59] S. Bonhommeau, P. G. Lacroix, D. Talaga, A. Bousseksou, M. Seredyuk, I. O. Fritsky, V. Rodriguez, *J. Phys. Chem. C* **2012**, *116*, 11251–11255.
- [60] C. Lochenie, K. Schötz, F. Panzer, H. Kurz, B. Maier, F. Puchtler, S. Agarwal, A. Köhler, B. Weber, *J. Am. Chem. Soc.* **2018**, *140*, 700–709.
- [61] R. C. Stoufer, D. H. Busch, W. B. Hadley, *J. Am. Chem. Soc.* **1961**, *83*, 3732–3734.
- [62] I. Krivokapic, M. Zerara, M. L. Daku, A. Vargas, C. Enachescu, C. Ambrus, P. Tregenna-Piggott, N. Amstutz, E. Krausz, A. Hauser, *Coord. Chem. Rev.* **2007**, *251*, 364–378.
- [63] P. N. Martinho, B. Gildea, M. M. Harris, T. Lemma, A. D. Naik, H. Müller-Bunz, T. E. Keyes, Y. Garcia, G. G. Morgan, *Angew. Chemie - Int. Ed.* **2012**, *51*, 12597–12601.
- [64] N. Bridonneau, J. Long, J.-L. Cantin, J. von Bardeleben, S. Pillet, E.-E. Bendeif, D. Aravena, E. Ruiz, V. Marvaud, *Chem. Commun.* **2015**, *51*, 8229–8232.
- [65] O. Stefańczyk, A. M. Majcher, M. Rams, W. Nitek, C. Mathonière, B. Sieklucka, *J. Mater. Chem. C* **2015**, *3*, 8712–8719.
- [66] H. Schiff, *Ann. der Chemie und Pharm.* **1864**, *131*, 118–119.
- [67] W. Qin, S. Long, M. Panunzio, S. Biondi, *Molecules* **2013**, *18*, 12264–12289.

9. References

- [68] N. Matsumoto, S. Ohta, C. Yoshimura, A. Ohyoshi, S. Kohata, H. Okawa, Y. Maeda, *J. Chem. Soc. Dalton Trans.* **1985**, *44*, 2575.
- [69] R. Boča, I. Šalitraš, J. Kožíšek, J. Linares, J. Moncol, F. Renz, *Dalt. Trans.* **2010**, *39*, 2198.
- [70] I. Šalitraš, R. Boča, R. Herchel, J. Moncol, I. Nemeč, M. Ruben, F. Renz, *Inorg. Chem.* **2012**, *51*, 12755–12767.
- [71] J. Pavlik, P. Masárová, I. Nemeč, O. Fuhr, M. Ruben, I. Šalitraš, *Inorg. Chem.* **2020**, *59*, 2747–2757.
- [72] A. Panja, *Dalt. Trans.* **2014**, *43*, 7760.
- [73] D. D. Narulkar, A. K. Srivastava, R. J. Butcher, K. M. Ansy, S. N. Dhuri, *Inorganica Chim. Acta* **2017**, *467*, 405–414.
- [74] G. N. Newton, M. Nihei, H. Oshio, *Eur. J. Inorg. Chem.* **2011**, 3031–3042.
- [75] H. Oshio, O. Tamada, H. Onodera, T. Ito, T. Ikoma, S. Tero-Kubota, *Inorg. Chem.* **1999**, *38*, 5686–5689.
- [76] H. Oshio, H. Onodera, O. Tamada, H. Mizutani, T. Hikichi, T. Ito, *Chem. – A Eur. J.* **2000**, *6*, 2523–2530.
- [77] R. Herchel, R. Boča, M. Gembický, J. Kožíšek, F. Renz, *Inorg. Chem.* **2004**, *43*, 4103–4105.
- [78] R. Herchel, Z. Trávníček, *Dalt. Trans.* **2013**, *42*, 16279.
- [79] I. Nemeč, R. Herchel, Z. Trávníček, T. Šilha, *RSC Adv.* **2016**, *6*, 3074–3083.
- [80] O. Sato, T. Iyoda, A. Fujishima, K. Hashimoto, *Science*, **1996**, *272*, 704–705.
- [81] O. Sato, Y. Einaga, A. Fujishima, K. Hashimoto, *Inorg. Chem.* **1999**, *38*, 4405–4412.
- [82] V. Escax, A. Bleuzen, C. Cartier dit Moulin, F. Villain, A. Goujon, F. Varret, M. Verdagner, *J. Am. Chem. Soc.* **2001**, *123*, 12536–12543.
- [83] C. P. Berlinguette, A. Dragulescu-Andrasi, A. Sieber, J. R. Galán-Mascarós, H. U. Güdel, C. Achim, K. R. Dunbar, *J. Am. Chem. Soc.* **2004**, *126*, 6222–6223.
- [84] N. Shimamoto, S. Ohkoshi, O. Sato, K. Hashimoto, *Inorg. Chem.* **2002**, *41*, 678–684.
- [85] A. B. P. Lever, *Inorg. Chem.* **1990**, *29*, 1271–1285.
- [86] S. S. Fielder, M. C. Osborne, A. B. P. Lever, W. J. Pietro, *J. Am. Chem. Soc.* **1995**, *117*, 6990–6993.

- [87] A. J. L. Pombeiro, *Eur. J. Inorg. Chem.* **2007**, 1473–1482.
- [88] P. V. Bernhardt, B. P. Macpherson, M. Martinez, *J. Chem. Soc. Dalton Trans.* **2002**, 1435.
- [89] T. Shiga, T. Tetsuka, K. Sakai, Y. Sekine, M. Nihei, G. N. Newton, H. Oshio, *Inorg. Chem.* **2014**, *53*, 5899–5901.
- [90] D. Li, R. Clérac, O. Roubeau, E. Harté, C. Mathonière, R. Le Bris, S. M. Holmes, *J. Am. Chem. Soc.* **2008**, *130*, 252–258.
- [91] D. Garnier, J. R. Jiménez, Y. Li, J. Von Bardeleben, Y. Journaux, T. Augenstein, E. M. B. Moos, M. T. Gamer, F. Breher, R. Lescouëzec, *Chem. Sci.* **2016**, *7*, 4825–4831.
- [92] M. Nihei, Y. Okamoto, Y. Sekine, N. Hoshino, T. Shiga, I. P. C. Liu, H. Oshio, *Angew. Chemie – Int. Ed.* **2012**, *51*, 6361–6364.
- [93] C. P. Berlinguette, A. Dragulescu-Andrasi, A. Sieber, J. R. Galán-Mascarós, H. U. Güdel, C. Achim, K. R. Dunbar, *J. Am. Chem. Soc.* **2004**, *126*, 6222–6223.
- [94] C. P. Berlinguette, A. Dragulescu-Andrasi, A. Sieber, H.-U. Güdel, C. Achim, K. R. Dunbar, *J. Am. Chem. Soc.* **2005**, *127*, 6766–6779.
- [95] Y. Sekine, M. Nihei, H. Oshio, *Chem. Lett.* **2014**, *43*, 1029–1030.
- [96] Y. Z. Zhang, P. Ferko, D. Siretanu, R. Ababei, N. P. Rath, M. J. Shaw, R. Clérac, C. Mathonière, S. M. Holmes, *J. Am. Chem. Soc.* **2014**, *136*, 16854–16864.
- [97] J. X. Hu, L. Luo, X. J. Lv, L. Liu, Q. Liu, Y. K. Yang, C. Y. Duan, Y. Luo, T. Liu, *Angew. Chemie – Int. Ed.* **2017**, *56*, 7663–7668.
- [98] D. Aguilà, Y. Prado, E. S. Koumoussi, C. Mathonière, R. Clérac, *Chem. Soc. Rev.* **2016**, *45*, 203–224.
- [99] C. Mathonière, *Eur. J. Inorg. Chem.* **2018**, 248–258.
- [100] K. Zhang, S. Kang, Z. S. Yao, K. Nakamura, T. Yamamoto, Y. Einaga, N. Azuma, Y. Miyazaki, M. Nakano, S. Kanegawa, O. Sato, *Angew. Chemie – Int. Ed.* **2016**, *55*, 6047–6050.
- [101] Y. Arimoto, S. ichi Ohkoshi, Z. J. Zhong, H. Seino, Y. Mizobe, K. Hashimoto, *J. Am. Chem. Soc.* **2003**, *125*, 9240–9241.
- [102] S. Ohkoshi, Y. Hamada, T. Matsuda, Y. Tsunobuchi, H. Tokoro, *Chem. Mater.* **2008**, *20*, 3048–3054.

- [103] N. Ozaki, H. Tokoro, Y. Hamada, A. Namai, T. Matsuda, S. Kaneko, S. I. Ohkoshi, *Adv. Funct. Mater.* **2012**, *22*, 2089–2093.
- [104] Y. Miyamoto, T. Nasu, N. Ozaki, Y. Umeta, H. Tokoro, K. Nakabayashi, S. Ohkoshi, *Dalt. Trans.* **2016**, *45*, 19249–19256.
- [105] R. Podgajny, S. Chorazy, W. Nitek, M. Rams, A. M. Majcher, B. Marszałek, J. Żukrowski, C. Kapusta, B. Sieklucka, *Angew. Chemie* **2013**, *125*, 930–934.
- [106] J. Jiménez, J. Glatz, A. Benchohra, G. Gontard, L. Chamoreau, J. Meunier, A. Bousseksou, R. Lescouëzec, *Angew. Chemie Int. Ed.* **2020**, *59*, 8089–8093.
- [107] P. Schinnerling, U. Thewalt, *J. Organomet. Chem.* **1992**, *431*, 41–45.
- [108] L. Alcázar, G. Aullón, M. Ferrer, M. Martínez, *Chem. – A Eur. J.* **2016**, *22*, 15227–15230.
- [109] C. Krüger, H. Sato, T. Matsumoto, T. Shiga, G. N. Newton, F. Renz, H. Oshio, *Dalt. Trans.* **2012**, *41*, 11270.
- [110] Y. Zhang, D. Li, R. Clérac, M. Kalisz, C. Mathonière, S. M. Holmes, *Angew. Chemie Int. Ed.* **2010**, *49*, 3752–3756.
- [111] D. Siretanu, D. Li, L. Buisson, D. M. Bassani, S. M. Holmes, C. Mathonière, R. Clérac, *Chem. – A Eur. J.* **2011**, *17*, 11704–11708.
- [112] A. Mondal, Y. Li, M. Seuleiman, M. Julve, L. Toupet, M. Buron-Le Cointe, R. Lescouëzec, *J. Am. Chem. Soc.* **2013**, *135*, 1653–1656.
- [113] J. Mercuriol, Y. Li, E. Pardo, O. Risset, M. Seuleiman, H. Rousselière, R. Lescouëzec, M. Julve, *Chem. Commun.* **2010**, *46*, 8995–8997.
- [114] M. Nihei, Y. Sekine, N. Suganami, H. Oshio, *Chem. Lett.* **2010**, *39*, 978–979.
- [115] Y. Sekine, M. Nihei, H. Oshio, *Chem. – A Eur. J.* **2017**, *23*, 5193–5197.
- [116] S. Cobo, G. Molnár, J. A. Real, A. Bousseksou, *Angew. Chemie Int. Ed.* **2006**, *45*, 5786–5789.
- [117] J. R. Galán-Mascarós, E. Coronado, A. Forment-Aliaga, M. Monrabal-Capilla, E. Pinilla-Cienfuegos, M. Ceolin, *Inorg. Chem.* **2010**, *49*, 5706–5714.
- [118] S. Liu, K. Zhou, T. Yuan, W. Lei, H.-Y. Chen, X. Wang, W. Wang, *J. Am. Chem. Soc.* **2020**, *142*, 15852–15859.

- [119] F. Prins, M. Monrabal-Capilla, E. A. Osorio, E. Coronado, H. S. J. Van Der Zant, *Adv. Mater.* **2011**, *23*, 1545–1549.
- [120] M. Cavallini, I. Bergenti, S. Milita, G. Ruani, I. Salitros, Z.-R. Qu, R. Chandrasekar, M. Ruben, *Angew. Chemie Int. Ed.* **2008**, *47*, 8596–8600.
- [121] M. Cavallini, *Phys. Chem. Chem. Phys.* **2012**, *14*, 11867.
- [122] Olikrom, "Olikrom website," can be found under <https://www.olikrom.com/en/>, **2021**.
- [123] G. Aromí, D. Aguilà, P. Gamez, F. Luis, O. Roubeau, *Chem. Soc. Rev.* **2012**, *41*, 537–546.
- [124] C.-M. Jureschi, J. Linares, A. Boulmaali, P. Dahoo, A. Rotaru, Y. Garcia, *Sensors* **2016**, *16*, 1–9.
- [125] F. Renz, P. A. de Souza, G. Klingelhöfer, H. A. Goodwin, *Hyperfine Interact.* **2002**, *139–140*, 699–704.
- [126] C. Bartual-Murgui, A. Akou, C. Thibault, G. Molnár, C. Vieu, L. Salmon, A. Bousseksou, *J. Mater. Chem. C* **2015**, *3*, 1277–1285.
- [127] J. Kim, S. Han, I.-K. Cho, K. Y. Choi, M. Heu, S. Yoon, B. J. Suh, *Polyhedron* **2004**, *23*, 1333–1339.
- [128] D. Li, S. Parkin, G. Wang, G. T. Yee, S. M. Holmes, *Inorg. Chem.* **2006**, *45*, 1951–1959.
- [129] G. M. Sheldrick, SADABS: An Empirical Absorption Correction Program, Bruker Analytica X-ray Systems, Madison, WI, **1996**.
- [130] G. M. Sheldrick, *Acta Crystallogr. Sect. C Struct. Chem.* **2015**, *71*, 3–8.
- [131] O. V. Dolomanov, L. J. Bourhis, R. J. Gildea, J. A. K. Howard, H. Puschmann, *J. Appl. Crystallogr.* **2009**, *42*, 339–341.
- [132] P. Van Der Sluis, A. L. Spek, *Acta Crystallogr. Sect. A* **1990**, *46*, 194–201.
- [133] I. Nemeč, R. Herchel, R. Boča, Z. Trávníček, I. Svoboda, H. Fuess, W. Linert, *Dalt. Trans.* **2011**, *40*, 10090–10099.
- [134] I. Nemeč, P. Zoufalý, R. Herchel, Z. Trávníček, *Inorg. Chem. Commun.* **2013**, *35*, 50–53.
- [135] D. J. Harding, P. Harding, W. Phonsri, **2016**, *313*, 38–61.
- [136] L. Pogány, J. Moncol, J. Pavlík, I. Šalitroš, *New J. Chem.* **2017**, *41*, 5904–5915.
- [137] L. Pogány, B. Brachňáková, J. Moncol, J. Pavlík, I. Nemeč, Z. Trávníček, M. Mazúr, L. Bučinský, L. Suchánek, I. Šalitroš, *Chem. – A Eur. J.* **2018**, *24*, 5191–5203.

- [138] J. G. Leipoldt, L. D. C. Bok, P. J. Cilliers, *Zeitschrift für Anorg. und Allg. Chemie* **1974**, *409*, 343–344.
- [139] J. R. Shapley, *Inorganic Syntheses*, John Wiley & Sons, Inc., Hoboken, NJ, USA, **2004**.
- [140] D. Matoga, J. Szklarzewicz, M. Mikuriya, *Inorg. Chem.* **2006**, *45*, 7100–7104.
- [141] F. Renz, P. Kerep, *Hyperfine Interact.* **2004**, *1*, 371–377.
- [142] S. Ohkoshi, S. Ikeda, T. Hozumi, T. Kashiwagi, K. Hashimoto, *J. Am. Chem. Soc.* **2006**, *128*, 5320–5321.
- [143] W. Kläui, W. Eberspach, P. Gütllich, *Inorg. Chem.* **1987**, *26*, 3977–3982.
- [144] E. R. King, G. T. Sazama, T. A. Betley, *J. Am. Chem. Soc.* **2012**, *134*, 17858–17861.
- [145] A. Mondal, L. M. Chamoreau, Y. Li, Y. Journaux, M. Seuleiman, R. Lescouëzec, *Chem. – A Eur. J.* **2013**, *19*, 7682–7685.
- [146] A. Bannwarth, S. O. Schmidt, G. Peters, F. D. Sönnichsen, W. Thimm, R. Herges, F. Tuczek, *Eur. J. Inorg. Chem.* **2012**, *2012*, 2776–2783.
- [147] S. O. Schmidt, H. Naggert, A. Buchholz, H. Brandenburg, A. Bannwarth, W. Plass, F. Tuczek, *Eur. J. Inorg. Chem.* **2016**, *2016*, 2175–2186.
- [148] F. Shen, W. Huang, D. Wu, Z. Zheng, X. C. Huang, O. Sato, *Inorg. Chem.* **2016**, *55*, 902–908.
- [149] V. Grippo, M. Mojovic, A. Pavicevic, M. Kabelac, F. Hubatka, J. Turanek, M. Zatloukalova, B. A. Freeman, J. Vacek, *Redox Biol.* **2021**, *38*, 101756.
- [150] M. Nihei, Y. Yanai, D. Natke, R. Takayama, M. Kato, Y. Sekine, F. Renz, H. Oshio, *Chem. – A Eur. J.* **2019**, *25*, 7449–7452.
- [151] S. Ohkoshi, M. Yoshikiyo, A. Namai, K. Nakagawa, K. Chiba, R. Fujiwara, H. Tokoro, *Sci. Rep.* **2017**, *7*, 8088.
- [152] Y. Matos-Peralta, M. Antuch, *J. Electrochem. Soc.* **2020**, *167*, 037510.
- [153] W. Li, C. Han, G. Cheng, S. Chou, H. Liu, S. Dou, *Small* **2019**, *15*, 1900470.
- [154] H. Tabe, M. Matsushima, R. Tanaka, Y. Yamada, *Dalt. Trans.* **2019**, *48*, 17063–17069.
- [155] T. Nakanishi, Y. Hori, S. Wu, H. Sato, A. Okazawa, N. Kojima, Y. Horie, H. Okajima, A. Sakamoto, Y. Shiota, K. Yoshizawa, O. Sato, *Angew. Chemie – Int. Ed.* **2020**, *59*, 14781–14787.

- [156] D. Natke, D. Unruh, B. Dreyer, S. Klimke, M. Jahns, A. Preiss, R. Sindelar, G. Klingelhöfer, F. Renz, *Hyperfine Interact.* **2018**, *239*, 1–9.
- [157] M. Reczyński, D. Pinkowicz, K. Nakabayashi, C. Näther, J. Stanek, M. Kozieł, J. Kalinowska-Tłuścik, B. Sieklucka, S. Ohkoshi, B. Nowicka, *Angew. Chemie Int. Ed.* **2021**, *60*, 2330–2338.
- [158] P. A. Maughan, V. R. Seymour, R. Bernardo-Gavito, D. J. Kelly, S. Shao, S. Tantisriyanurak, R. Dawson, S. J. Haigh, R. J. Young, N. Tapia-Ruiz, N. Bimbo, *Langmuir* **2020**, *36*, 4370–4382.
- [159] Z. Bai, Y. Yang, D. Zhang, Y. Wang, Y. Guo, H. Yan, P. K. Chu, Y. Luo, *J. Solid State Electrochem.* **2021**, *25*, 1657–1665.

10. Curriculum Vitae and List of Publications

Dominik Aljoscha Florian Natke

Date of birth: 2nd May 1991 in Langenhagen, Germany

Nationality: German

Education and Professional Experience

Since 07/2020	Research Associate Institute of Inorganic Chemistry, Leibniz University Hannover
Since 09/2016	Ph.D. Candidate in Chemistry Institute of Inorganic Chemistry, Leibniz University Hannover
10/2016 to 09/2019	Research Associate at the Institute of Inorganic Chemistry, Leibniz University Hannover (6 months break due to research stays in Japan in 2017 and 2018)
04/2016 to 09/2016	Master Thesis in Material- and Nanochemistry University of Tsukuba, Japan Title: <i>External Stimuli-Induced Spin Transition in Cyanide-Bridged Multi-Nuclear Complexes</i>
10/2014 to 09/2016	Master's Course: Material- and Nanochemistry Leibniz University Hannover Degree: Master of Science
10/2011 to 12/2014	Bachelor's Course: Chemistry Leibniz University Hannover Degree: Bachelor of Science
10/2010 to 09/2011	Bachelor's course: Physics Leibniz University Hannover
2010	Highschool: Tellkampfschule, Hannover Degree: Abitur

International Exchange:

- 2020: 6 months as visiting scientist at the Kyushu University in Fukuoka, Japan
- 2018 + 2017: 3 months each as visiting scientist supported by the DAAD at the University of Tsukuba, Japan
- 2018 + 2017 + 2014: Scientific exchange program with the University of Ss. Cyril and Methodius in Trnava and the Slovak University of Technology in Bratislava, Slovakia

Conferences

Oral Presentations:

Solid State Afternoon, Zentrum für Festkörperchemie (ZFM), Leibniz University Hannover, 06.07.2018, Designing Molecular Switches – A Building Block Approach.

15th Koordinationschemie-Treffen (KCT), Ludwig-Maximilians-Universität München, 3.3.–5.3.2019, Verwendung mononuklearer Spin-Crossover Komplexe als Bausteine für schaltende cyanidverbrückte multinuklearer Komplexe

Poster Presentations:

15th International Conference on Molecular-Based Magnets (ICMM), Sendai, Japan, 04.09.–08.09.2016, Spin-State Switching in Cyanide-Bridged Fe^{II}-Fe^{III} Multinuclear Systems,

International Conference on the Application of the Mössbauer Effect (ICAME) 2017, St. Petersburg, Russland, 03.09.–08.09.2017, Tuning Spin Transitions of Iron(II)-DPP Systems

43rd International Conference on Coordination Chemistry (ICCC), Sendai, Japan, 30.07.–04.08.2018, Control of Electron Transfer in a Cyanide-Bridged [Co₂Fe₂] Square Complex by a Bifunctional Hydrogen Donor

Phase Transition and Dynamical Properties of Spin Transition Materials (PDSTM), Gainesville, Florida, USA, 06.05. – 10.05.2019, Spin Transition in Mixed Valence Multinuclear Complexes

4th International Conference on Functional Molecular Materials, Krakau, Polen, 25.11.–27.11.2019, Spin Transition in Mixed Valence Multinuclear Complexes

List of Publications

D. Natke, T. Enomoto, R. Boca, T. Shiga, M. Ohba, H. Oshio, F. Renz, Co(II) and Fe(II) Schiff Base Complexes in Dinuclear Prussian Blue Analogs, soon to be submitted to *ChemistryOpen*, 2021.

D. Natke, A. Preiss, S. Klimke, T. Shiga, R. Boca, M. Ohba, H. Oshio, F. Renz, Structural, Magnetic and Electrochemical Characterization of Iron(III) and Cobalt Complexes with Penta-N₃O₂-dentate Ligands, *Eur. J. Inorg. Chem.*, 2021, 15, 1498-1504.

F. Lübke, J. F. Miethe, F. Steinbach, P. Rusch, A. Schlosser, D. Zambo, T. Heinemeyer, D. Natke, D. Zok, D. Dorfs, N. C. Bigall, Patterning of Nanoparticle-Based Aerogels and Xerogels by Inkjet Printing, *Small*, 2019, 1902186.

M. Jahns, S. Klimke, D. Natke, R. Sindelar, U. Schrewe, R. Patzke, F. Renz, An Arduino based Mössbauer spectrometer, *Nucl. Instrum. Methods Phys. Res.* 2019, 940, 116-118.

M. Nihei, Y. Yanai, D. Natke, R. Takayama, M. Kato, Y. Sekine, F. Renz, H. Oshio, Solid-State Hydrogen-Bond Alterations in a [Co₂Fe₂] Complex with Bifunctional Hydrogen-Bonding Donors, *Chem. Eur. J.* 2019, 25, 7449-7452.

T. Shiga, R. Saiki, L. Akiyama, R. Kumai, D. Natke, F. Renz, J. M. Cameron, G. N. Newton, H. Oshio, A Bronstedt-Ligand-Based Iron Complex as a Molecular Switch with Five Accessible States, *Angew. Chem. Int. Ed.* 2019, 58, 5658-5662.

D. Natke, D. Unruh, B. Dreyer, S. Klimke, M. Jahns, A. Preiss, R. Sindelar, G. Klingelhöfer, R. Renz, Tuning spin transitions of iron(II)-dpp systems, *Hyperfine Interact.* 2018, 239, 12.

B. Dreyer, D. Natke, S. Klimke, S. Baskas, R. Sindelar, G. Klingelhöfer, F. Renz, Implementation of spin crossover compounds into electrospun nanofibers, *Hyperfine Interact.* 2018, 239, 8.